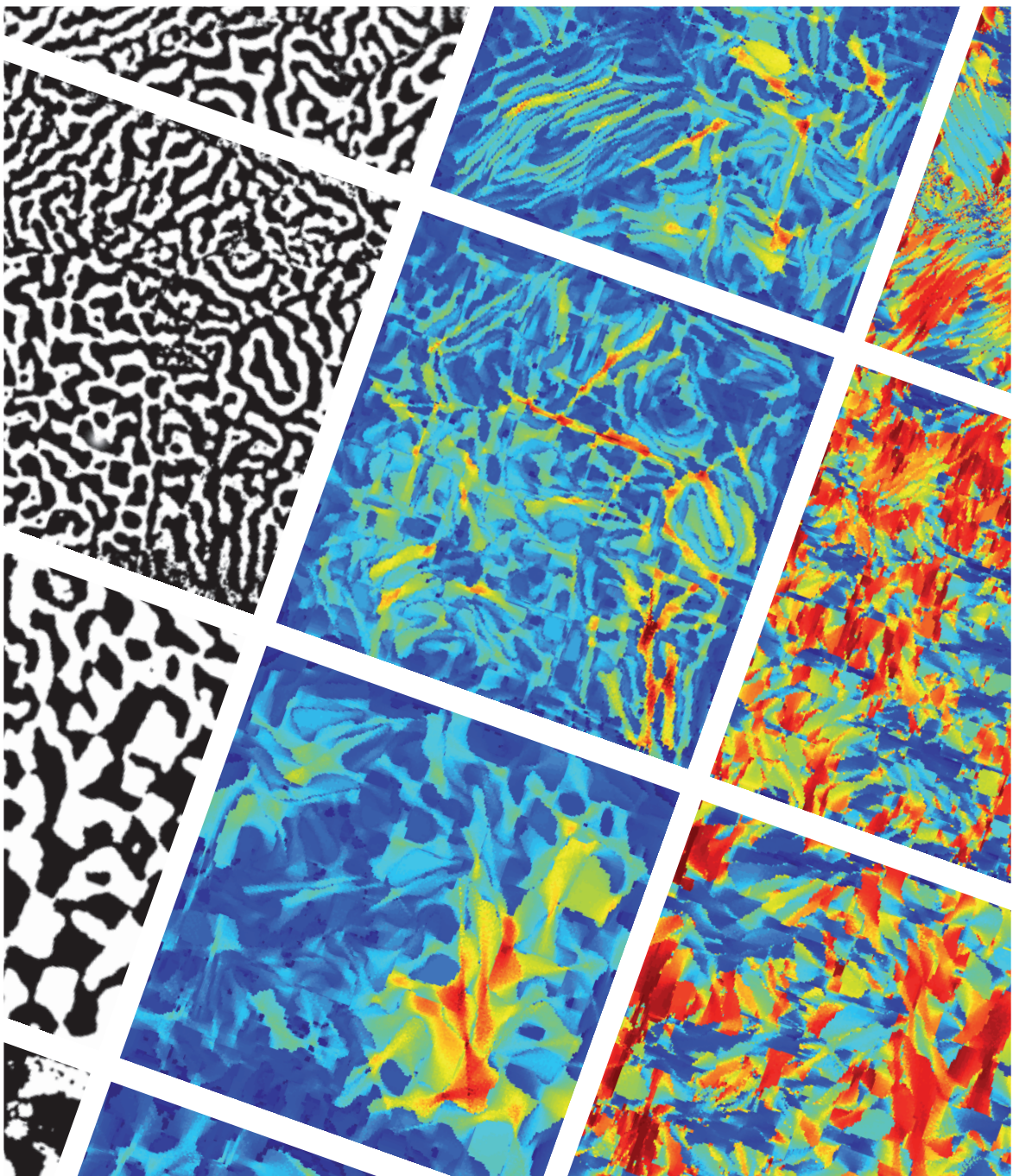


# Polar Microstructure and Nanoscale Electromechanical Behavior of Lead-Free Piezoelectric Ceramics

Thesis approved for award of the academic degree of Doctor Engineer (Dr.-Ing.) by the Faculty of Engineering of the University of Duisburg-Essen, submitted by by MSc. Danka Dittmer-Gobeljic from Belgrade. Defended on 16<sup>th</sup> July 2015 in Essen.



*Polar Microstructure and Nanoscale Electromechanical Behavior of Lead-Free Piezoelectric Ceramics*

Von der Fakultät Ingenieurwissenschaften der Universität Duisburg-Essen zur Erlangung des akademischen Grades Doktor-Ingenieur (Dr.-Ing.) genehmigte Dissertation von

MSc. Danka Dittmer-Gobeljic, geb. Gobeljic, aus Belgrad.

Datum der Einreichung: 3. Juni 2015

Datum der mündlichen Prüfung: 16. Juli 2015

Referent: Prof. Dr. rer. nat. habil. Doru C. Lupascu

Korreferent: Prof. Dr. Andrei Kholkin

*"Every science begins as philosophy  
and ends as art."*

Will Durant



# Contents

<b>Symbols and Abbreviations</b>	<b>vii</b>
<b>1 Introduction</b>	<b>1</b>
<b>2 Fundamentals and Literature Review</b>	<b>3</b>
2.1 Dielectrics . . . . .	3
2.1.1 Dielectric Properties . . . . .	3
2.1.2 Ferroelectrics . . . . .	7
2.1.3 Relaxor Ferroelectrics . . . . .	15
2.2 Lead-Free Piezoelectric Ceramics . . . . .	21
2.2.1 Potassium Sodium Niobate-Based Piezoelectric Ceramics . . . . .	21
2.2.2 Bismuth Sodium Titanate . . . . .	24
2.2.3 $\text{Bi}_{1/2}\text{Na}_{1/2}\text{TiO}_3$ -Based Pseudobinary Systems . . . . .	26
2.2.4 $\text{Bi}_{1/2}\text{Na}_{1/2}\text{TiO}_3$ -Based Pseudoternary Systems . . . . .	30
2.3 Scanning Probe Microscopy . . . . .	32
2.3.1 Piezoresponse Force Microscopy . . . . .	33
2.3.1.1 Experimental Setup . . . . .	33
2.3.1.2 Physics of PFM . . . . .	34
2.3.1.3 PFM Imaging . . . . .	35
2.3.1.4 Dynamics of Vector PFM . . . . .	38
2.3.1.5 Piezoresponse Force Spectroscopy . . . . .	38
2.3.1.6 Lock-in Amplification . . . . .	40
2.3.1.7 Lateral Resolution of PFM . . . . .	41
2.3.2 Band Excitation Piezoresponse Force Microscopy . . . . .	42
2.3.2.1 Band Excitation Switching Spectroscopy . . . . .	44
2.3.2.2 First-Order Reversal Curve Band Excitation Switching Spectroscopy . . . . .	45
<b>3 The Ferroelectric Properties of KNN-Based Piezoceramics</b>	<b>46</b>
3.1 Introduction . . . . .	46
3.2 Experimental Methods . . . . .	48
3.2.1 Material and Sample Preparation . . . . .	48
3.2.2 X-Ray Diffraction at Room Temperature . . . . .	48
3.2.3 Temperature-Dependent Dielectric Permittivity and Losses . . . . .	49
3.2.4 Temperature-Dependent Measurements of the Piezoelectric Coefficient . . . . .	49
3.2.5 Large-Signal Strain and Polarization as Function of Temperature . . . . .	50

3.2.6	Transmission Electron Microscopy at Room Temperature . . . . .	50
3.2.7	Piezoresponse Force Microscopy . . . . .	51
3.3	Experimental Results . . . . .	52
3.3.1	Macroscopic Properties . . . . .	52
3.3.1.1	Room Temperature X-Ray Diffraction . . . . .	52
3.3.1.2	Piezoelectric and Ferroelectric Properties . . . . .	53
3.3.1.3	Temperature-Dependent Dielectric Properties . . . . .	53
3.3.1.4	Large-Signal Properties as Function of Temperature . . . . .	54
3.3.1.5	Temperature-Dependent Piezoelectric Coefficient . . . . .	55
3.3.2	Microscopic Properties . . . . .	56
3.3.2.1	Domain Structure at Room Temperature . . . . .	56
3.3.2.2	Unpoled Domain Structure as Function of Temperature . . . . .	56
3.3.2.3	Poled Domain Structure as Function of Temperature . . . . .	57
3.3.2.4	Local Switching Behavior as Function of Temperature . . . . .	60
3.4	Discussion . . . . .	61
3.4.1	Macroscopic Properties . . . . .	61
3.4.1.1	Large-Signal Constitutive Behavior at Room Temperature . . . . .	61
3.4.1.2	Large-Signal Properties as Function of Temperature . . . . .	61
3.4.1.3	The Phenomenology of Temperature-Insensitive Strain . . . . .	63
3.4.2	Microscopic Properties . . . . .	65
3.4.2.1	Domain Structure at Room Temperature . . . . .	65
3.4.2.2	Domain Structure as Function of Temperature . . . . .	65
3.4.2.3	The Local Piezoelectric Response as Function of Temperature . . . . .	67
3.4.2.4	Local Switching Behavior as Function of Temperature . . . . .	67
3.5	Summary . . . . .	72
<b>4</b>	<b>Stability of Induced Ferroelectric Order in Relaxor Ferroelectric BNT-BKT-BZT</b>	<b>73</b>
4.1	Introduction . . . . .	73
4.2	Experimental Methods . . . . .	76
4.2.1	Material and Sample Preparation . . . . .	76
4.2.2	Electrical Large-Signal Measurements . . . . .	77
4.2.3	Electrical Small-Signal Measurements . . . . .	78
4.2.4	Piezoresponse Force Microscopy . . . . .	79
4.3	Influence of a <i>dc</i> -Electric Field on the Field-Induced Phase Transition . . . . .	80
4.3.1	Experimental Results . . . . .	80
4.3.1.1	Macroscopic Properties . . . . .	80
4.3.1.2	Microscopic Properties . . . . .	82
4.3.2	Discussion . . . . .	85
4.3.2.1	Macroscopic Properties . . . . .	85

---

4.3.2.2	Microscopic Properties . . . . .	88
4.4	Influence of Temperature on the Field-Induced Ferroelectric Phase . . . . .	91
4.4.1	Experimental Results . . . . .	91
4.4.1.1	Macroscopic Properties . . . . .	91
4.4.1.2	Microscopic Properties . . . . .	91
4.4.2	Discussion . . . . .	98
4.4.2.1	Macroscopic Properties . . . . .	98
4.4.2.2	Microscopic Properties . . . . .	99
4.5	Summary . . . . .	104
<b>5</b>	<b>Polar Microstructure of Relaxor-Ferroelectric Composites</b>	<b>105</b>
5.1	Introduction . . . . .	105
5.2	Experimental Methods . . . . .	109
5.2.1	Material Processing and Sample Preparation . . . . .	109
5.2.2	Electron Backscatter Diffraction . . . . .	109
5.2.3	Piezoresponse Force Microscopy . . . . .	110
5.3	Experimental Results . . . . .	111
5.3.1	Domain Structure . . . . .	111
5.3.2	EBSD Results . . . . .	113
5.3.3	Comparison Between EBSD and PFM Results . . . . .	114
5.3.4	Switching Properties . . . . .	118
5.4	Discussion . . . . .	122
5.4.1	Conventional Analysis of the Domain Structure . . . . .	122
5.4.2	Line-of-Sight Method of Spatial Domain Structure Analysis . . . . .	123
5.4.3	Autocorrelation Function Analysis . . . . .	129
5.4.4	Conventional Analysis of Switching Properties . . . . .	130
5.4.5	k-Means Clustering . . . . .	131
5.5	Conclusions . . . . .	139
<b>6</b>	<b>Conclusion</b>	<b>140</b>
<b>A</b>	<b>Appendix</b>	<b>145</b>
	<b>Bibliography</b>	<b>147</b>
	<b>List of Figures</b>	<b>176</b>
	<b>List of Tables</b>	<b>180</b>
	<b>Erklärung</b>	<b>183</b>
	<b>Acknowledgments</b>	<b>185</b>

**Curriculum Vitae**

**187**



# Symbols and Abbreviations

## Symbols

$a$	Landau coefficient
$a$	Lattice parameter
$a$	Autocorrelation parameter
$a$	Calibration constant
$A$	Area of the electrode
$A$	Amplitude of piezoresponse (PFM)
$A_{avr}$	Average domain area
$A_{\omega}$	Amplitude of the first harmonic piezoresponse (PFM)
$A_{max}$	Maximum domain area
$A_i^{max}$	Maximum amplitude at resonant frequency
$A_s$	Area of the local hysteresis loop (PFM)
$\alpha_a$	Attenuation factor (PFM)
$b$	Landau coefficient
$b$	Lattice parameter
$\beta$	Stretching exponent
$\beta$	Proportionality coefficient (PFM)
$c$	Landau coefficient
$c$	Dumping constant
$c$	Fitting parameter (PFM)
$c$	Number of data point
$C$	Tip-surface capacitance
$C$	Capacitance
$C_m$	Measurement capacitance
$C_s$	Sample capacitance
$C_{r_1, r_2}$	Autocorrelation image function
$C'_{cant}$	Capacitance gradient due to the cantilever
$C'_{cone}$	Capacitance gradient due to the conical part of the PFM tip
$C'_{sphere}$	Capacitance gradient due to the spherical part of the PFM tip
$C_x$	x-Coordinate of a polygon centroid
$C_y$	y-Coordinate of a polygon centroid
$\chi$	Electric susceptibility
$\chi$	Rotation angle
$\overline{\overline{\chi}}$	Electric susceptibility tensor
$D$	Dielectric displacement vector

---

$D$	Local piezoresponse
$D_0$	Remanent piezoresponse
$d_{33}$	Piezoelectric coefficient measured along the poling direction
$d_{33}^*$	Normalized strain $S_{max} \cdot E_{max}^{-1}$
$d_{33}^0$	Relaxed piezoelectric coefficient
$d_{33}^1$	Relaxation strength parameter
$d_{ijk}$	Piezoelectric tensor
$d_{zz}$	Piezoelectric coefficient measured along the poling direction
$D_{loc}$	Piezoresponse inside a single domain (PFM)
$D_{max}$	Maximum piezoresponse
$D_{max}^-$	Negative maximum piezoresponse
$D_{max}^+$	Positive maximum piezoresponse
$D_{rem}$	Remanent piezoresponse
$\Delta z$	Local displacement of the sample surface (PFM)
$\Delta z_\omega$	The first harmonics local displacement of the sample surface (PFM)
$\Delta z_{2\omega}$	The second harmonics local displacement of the sample surface (PFM)
$E$	Electric field
$\mathbf{E}$	Electric field vector
$E_a$	Activation energy
$E_c$	Coercive field
$E_{c,-}$	Negative coercive field
$E_{c,+}$	Positive coercive field
$E_D$	Depolarization field
$E_{dis}$	Dissipated energy
$E_{max}$	Maximum applied electric field
$E_{sat}$	Electric field at which signal saturates
$E_{th}$	Threshold electric field
$\varepsilon'$	Real part of the permittivity
$\varepsilon''$	Imaginary part of the permittivity
$\varepsilon_0$	Permittivity of the vacuum
$\varepsilon_{ik}$	Dielectric tensor
$\varepsilon_r$	Relative permittivity
$\varepsilon_{r,33}$	Relative permittivity measured along the direction of field application
$f$	Frequency
$F$	Free energy
$F$	Original image function
$f_0$	Attempt frequency in Vogel-Fulcher equation
$F_0$	Free energy of the reference state
$F_{driving}$	Driving force (PFM)

---

$F$	Object transform function
$F$	Free energy function
$h$	Roughness of a polarization interface
$I$	Image function in the Fourier space
$I_0$	Ideal image function
$J$	Minimum sum of distances
$k$	Tip-surface junction spring constant
$k$	Boltzmann constant
$k$	Cantilever stiffness
$k$	Number of clusters
$k_1$	Cantilever spring constant
$k_p$	Coupling factor for radial oscillation of a thin plate
$\lambda$	Wavelength
$m$	Cantilever mass
$M_{333}$	Electrostrictive constant
$M_x$	Moment of area along x-direction
$M_y$	Moment of area along y-direction
$\mu$	Point position ( $LoS$ )
$n$	Number of data points
$N$	Number of frequency points
$NNB$	Negative nucleation bias
$\mathbf{n}$	Surface unit normal vector
$N$	Noise function in the Fourier space
$\omega_0$	Resonant frequency of piezoresponse
$\omega$	Frequency of electric field (PFM)
$\omega_r$	Frequency of a reference signal (Lock-in amplifier)
$\omega_s$	Frequency of a response signal (Lock-in amplifier)
$P$	Polarization
$\mathbf{P}$	Polarization vector
$P_3$	Polarization measured along the direction of field application
$\mathbf{p}_{av}$	Average dipole moment
$P_d$	Dipole spontaneous polarization
$P_{max}$	Polarization at maximum electric field
$PNB$	Positive nucleation bias
$PR$	Piezoresponse (PFM)
$P_{rem}$	Remanent polarization at electric zero-field
$P_{rem,+}$	Positive remanent polarization
$P_{rem,-}$	Negative remanent polarization
$P_s$	Spontaneous polarization

---

$\varphi$	Phase angle
$\varphi$	Phase shift of the response signal (lock-in amplifier)
$\varphi$	Domain angle
$\pi_i$	Pyroelectric coefficient
$q$	Charge
$Q$	Charge
$Q$	Quality factor
$Q$	Electrostrictive constant
$Q_m$	Charge on measurement capacitor
$Q_s$	Charge on sample surface
$r$	Radius of the central peak of the autocorrelation image
$R$	Amplitude of the response signal (lock-in amplifier)
$R_0^-$	Negative remanent piezoresponse (PFM)
$R_0^+$	Positive remanent piezoresponse (PFM)
$r_{min}$	Half the minimum distance among the two cluster centers
$r_n$	Polygon centroid
$R_s^-$	Negative piezoresponse (PFM)
$R_s^+$	Positive piezoresponse (PFM)
$\rho$	Point distribution
$S$	Strain
$S$	Amplitude of the reference signal (lock-in amplifier)
$S_3$	Strain measured along the direction of applied electric field
$s_{ij}$	Strain tensor
$s_{ijkl}^E$	Elastic compliance tensor at constant electric field
$S_{max}$	Maximum strain
$S_{max}^T$	Maximum strain at temperature T
$S_{max}^{RT}$	Maximum strain at room temperature
$S_{min}$	Minimum strain
$S_{neg}$	Negative strain
$S_{rem}$	Remanent strain
$S_r$	Reference signal (Lock-in amplifier)
$S_s$	Response signal (Lock-in amplifier)
$S_{useful}$	Useful strain
$\sigma$	Polarization surface charges
$\sigma_{kl}$	Stress tensor
$\sigma_{max}$	Maximum dispersion
$t$	Sample thickness
$t$	Time
$T$	Temperature

---

$T_0$	Curie-Weiss temperature
$T_B$	Burns Temperature
$T_c$	Transition temperature
$T_{c0}$	Transition temperature during zero-field heating
$T_d$	Depolarization temperature determined from $d_{33}(T)$
$T_f$	Freezing temperature
$T_m$	Temperature of maximum permittivity
$T_{O-T}$	Orthorhombic to tetragonal phase transition temperature
$\tan\delta$	Loss tangent
$\tau$	Relaxation time
$\tau_{MW}$	Maxwell-Wagner relaxation time
$\theta_p$	Voltage pulse duration
$\theta$	Response phase at resonant frequency
$\theta$	Diffraction angle
$U_m$	Voltage drop across measurement capacitance
$V$	Bias voltage
$V_0$	Coercive voltage
$V_0^+$	Forward coercive voltage (PFM)
$V_0^-$	Reverse nucleation bias (PFM)
$V_{ac}$	Alternating current voltage (PFM)
$V_c$	Nucleation bias (PFM)
$V_c^-$	Negative coercive bias (PFM)
$V_c^+$	Positive coercive bias (PFM)
$V_{dc}$	Direct current voltage (PFM)
$v_i$	Cluster center
$V_s$	Alternating voltage on the sample surface (PFM)
$V_{sat}$	Saturation voltage
$V_{tip}$	Voltage (PFM)
$x$	Atomic percentage of second compound in a solid solution
$x$	Mole fraction of second compound in a pseudo-binary solid solution
$x$	Cantilever position
$x$	Coordinate of a polygon vertex
$X$	Output signal of lock-in amplifier
$\xi$	Correlation length
$y$	Mole fraction of third compound in a pseudo-ternary solid solution
$y$	Coordinate of a polygon vertex
$Y$	Output signal of lock-in amplifier

**Abbreviations**

<i>ac</i>	Alternating current
AF	Antiferroelectric
AFM	Atomic force microscopy
BA	Bismuth aluminate $\text{BiAlO}_3$
BAgT	Bismuth silver titanate $\text{Bi}_{1/2}\text{Ag}_{1/2}\text{TiO}_3$
BE	Band excitation (PFM)
BEPS	Band excitation piezoresponse spectroscopy (PFM)
BH	Barium hafnate $\text{BaHfO}_3$
BKT	Bismuth potassium titanate $\text{Bi}_{1/2}\text{K}_{1/2}\text{TiO}_3$
BLA	Bismuth lanthanum aluminate $\text{Bi}_{1/2}\text{La}_{1/2}\text{AlO}_3$
BLT	Bismuth lithium titanate $\text{Bi}_{1/2}\text{Li}_{1/2}\text{TiO}_3$
BMT	Bismuth magnesate titanate $\text{BiMg}_{1/2}\text{Ti}_{1/2}\text{O}_3$
BNT	Bismuth sodium titanate $\text{Bi}_{1/2}\text{Na}_{1/2}\text{TiO}_3$
BNT-100 <i>x</i> BKT-100 <i>y</i> BZT	$(1-y)((1-x)\text{Bi}_{1/2}\text{Na}_{1/2}\text{TiO}_3 - x\text{Bi}_{1/2}\text{K}_{1/2}\text{TiO}_3) - y\text{BiZn}_{1/2}\text{Ti}_{1/2}\text{O}_3$
BNT-7BT	$0.93\text{Bi}_{1/2}\text{Na}_{1/2}\text{TiO}_3 - 0.07\text{BaTiO}_3$
BNT-6BT-2KNN	$0.94\text{Bi}_{1/2}\text{Na}_{1/2}\text{TiO}_3 - 0.06\text{BaTiO}_3 - 0.02\text{K}_{0.5}\text{Na}_{0.5}\text{NbO}_3$
BT	Barium titanate $\text{BaTiO}_3$
BZ	Barium zirconate $\text{BaZrO}_3$
<i>dc</i>	Direct current
<i>DoN</i>	Degree of nonergodicity
DSP	Digital signal processing
EBSD	Electron backscatter diffraction
EDX	Energy-dispersive X-ray
EFM	Electrostatic force microscopy
ER	Ergodic relaxor
FE	Ferroelectric
FFT	Fast Fourier transformation
FORC	First-order reversal curve (BEPS)
FWHM	Full width half maximum
HP	Hot pressing
IP	In-plane (PFM)
KMC	k-means clustering
KN	Potassium niobate $\text{K}_{0.5}\text{NbO}_3$
KNN	Potassium sodium niobate $\text{K}_{0.5}\text{Na}_{0.5}\text{NbO}_3$
KNN-CZ5	$(\text{Na}_{0.49}\text{K}_{0.49}\text{Li}_{0.02})(\text{Nb}_{0.8}\text{Ta}_{0.2})\text{O}_3 - 0.05\text{CaZrO}_3$
LF4	$(\text{K}_{0.44}\text{Na}_{0.52}\text{Li}_{0.04})(\text{Nb}_{0.84}\text{Ta}_{0.10}\text{Sb}_{0.06})\text{O}_3$
LF4T	$(\text{K}_{0.44}\text{Na}_{0.52}\text{Li}_{0.04})(\text{Nb}_{0.84}\text{Ta}_{0.10}\text{Sb}_{0.06})\text{O}_3$ textured
LIA	Lock-in amplifier

---

<i>LoS</i>	Line of Sight
LPFM	Lateral piezoresponse force microscopy
LT	Lithium tantalate $\text{LiTaO}_3$
LS	Lithium antimonate $\text{LiSbO}_3$
LN	Lithium niobate $\text{LiNbO}_3$
MPB	Morphotropic phase boundary
NB	Nucleation bias
NE	Nonergodic relaxor
NN	Sodium niobate $\text{NaNbO}_3$
O–T	Orthorhombic and tetragonal phase mixture
OP	Out-of-plane (PFM)
PE	Paraelectric
PFM	Piezoresponse force microscopy
PFM-S	Piezoresponse force microscopy spectroscopy
PMN	Lead magnesium niobate $\text{Pb}(\text{Mg}_{1/3}\text{Nb}_{2/3})\text{O}_3$
PNR	Polar nano-region
PPT	Polymorphic phase transition
PR	Piezoresponse
PSD	Phase-sensitive detection
PT	Lead titanate $\text{PbTiO}_3$
PTFE	Polytetrafluoroethylene
PZN	Lead zinc niobate $\text{Pb}(\text{Zn}_{1/3}\text{Nb}_{2/3})\text{O}_3$
PZSnT	$\text{Pb}_{0.95}\text{La}_{0.018}\text{Ba}_{0.02}(\text{Zr}_{0.60}\text{Ti}_{0.10}\text{Sn}_{0.30})\text{O}_3$
PZT	Lead zirconate titanate $\text{Pb}(\text{Zr}_{1-y}\text{Ti}_y)\text{O}_3$
RF	Relaxor ferroelectric
RT	Room temperature
SBN	Strontium barium niobate $\text{Sr}_x\text{Ba}_{1-x}\text{Nb}_2\text{O}_6$
SHO	Single harmonic oscillator
SNR	Signal-to-noise ratio
SPM	Scanning probe microscopy
SPS	Spark plasma sintering
SS-PFM	Switching spectroscopy piezoresponse force microscopy
SSPM	Scanning surface potential microscopy
ST	Strontium titanate $\text{SrTiO}_3$
SZ	Strontium zirconate $\text{SrZrO}_3$
TEM	Transmission electron microscopy
VPFM	Vertical piezoresponse force microscopy
XRD	X-ray diffraction
ZFC	Zero-field cooling

ZFH

Zero-field heating



# 1 Introduction

Within the plethora of energy converters, piezoelectric materials are highly recognized due to their ability of linear, bidirectional translation of mechanical and electric energy. The piezoelectricity of these materials is, therefore, employed for countless high-tech applications from piezoelectric actuators, fuel injectors, transducers to piezoelectric motors, micro- and nanopositioning systems, and many others.

The unique range of properties of lead zirconate titanate  $\text{PbZr}_x\text{Ti}_{1-x}\text{O}_3$  (PZT) makes this material and its compounds the most prevalent, high-performance piezoelectric material. By the additional property optimization provided through chemistry and processing adjustment, the PZT-based materials gained a tremendous market dominance.

Nonetheless, the use of PZT-based materials has become seriously restricted due to concerns regarding their toxicity, which is particularly disadvantageous in material processing, machining of lead-containing devices, recycling, and post-disposal. Several European Union legislative regulations, such as RoHS and WEEE, require the limitation of consumption and eventual replacement of toxic substances in order to mitigate their adverse effect on human health and environment.<sup>1,2,3</sup> In a respond to this evolution, a rapid growth of research efforts has been encouraged in the field of lead-free piezoelectric materials, resulting in an improvement of already existing materials and the development of a variety of new non-toxic alternatives. Despite two decades of joint academic and industrial research, no compound has been reported so far that may adequately substitute PZT in its full spectrum of properties. For this reason, the replacement of lead-based materials in critical applications is not yet accomplished.<sup>4</sup>

Significant improvement in finding competitive lead-free piezoelectrics has certainly been achieved by introducing bismuth sodium titanate,  $\text{Bi}_{1/2}\text{Na}_{1/2}\text{TiO}_3$ ,<sup>5</sup> and potassium sodium niobate,  $(\text{K},\text{Na})\text{NbO}_3$  based systems.<sup>6</sup> Beside their practical merits, these classes of materials are scientifically intriguing, raising numerous questions on the physical mechanisms underlying their piezoelectric characteristics. While BNT-based materials demonstrate advanced electromechanical properties as a result of a peculiar relaxor-ferroelectric phase transition, KNN-based materials excel by a variety of morphotropic and polymorphic phase transition regions. The further enhancement of their properties requests further development of lead-free piezoelectrics through structural manipulation, chemical modification, and optimization of the microstructure. In fact, as much as 70% of the piezoelectric and dielectric properties in the widely used PZT emanates from domain wall contribution. That said, understanding of the local microstructural and electrical properties seems to be a crucial aspect to further promote the functional properties of lead-free materials.

The present work focuses on the investigation of the salient properties of three outstanding lead-free piezoceramics: First, the ferroelectric sodium potassium lithiumate–niobium tantalate–calcium zirconate with 2 wt% manganese dioxide addition  $0.95(\text{Na}_{0.49}\text{K}_{0.49}\text{Li}_{0.02})(\text{Nb}_{0.8}\text{Ta}_{0.2})\text{O}_3-0.05\text{CaZrO}_3$  with 2 wt%  $\text{MnO}_2$  (KNN-CZ5); second, the relaxor ferroelectric bismuth sodium titanate–bismuth potassium titanate–bismuth zinc titanate  $(1-y)(0.81\text{Bi}_{1/2}\text{Na}_{1/2}\text{TiO}_3-0.19\text{Bi}_{1/2}\text{K}_{1/2}\text{TiO}_3)-y\text{BiZn}_{1/2}\text{Ti}_{1/2}\text{O}_3$  (BNT-19BKT-100yBZT); third, the microstructural composite of nonergodic relaxor bismuth sodium titanate–barium titanate  $\text{Bi}_{1/2}\text{Na}_{1/2}\text{TiO}_3-0.07\text{BaTiO}_3$  (BNT-7BT) and ergodic relaxor bismuth sodium titanate–barium titanate–potassium sodium niobate  $\text{Bi}_{1/2}\text{Na}_{1/2}\text{TiO}_3-0.06\text{BaTiO}_3-0.02\text{K}_{0.5}\text{Na}_{0.5}\text{NbO}_3$  (BNT-7BT/BNT-6BT-2KNN).

Their structural, microstructural, and electrical properties, as well as their mutual interrelation are examined as a function of composition, temperature, and electric field. The conducted research is based on the interrelated observations of the materials' electromechanical behavior on different length scales, ranging from a submicroscopic to a macroscopic perspective. Within the framework of this thesis, the former one is achieved by means of piezoresponse force microscopy, a state-of-the-art scanning probe microscopy technique. The direct comparison of properties on multiple length scales affords deep insight into the fundamental mechanisms responsible for the enhanced electromechanical behavior of the investigated material systems. Furthermore, novel, advanced data analysis methods are introduced, aiming at a quantitative description of the complex domain microstructures witnessed in the materials in question. Moreover, a distinction of local polarization switching character is sought.

The following chapter provides an overview on the field of piezoceramics, lead-free materials, and the PFM method. Subsequently, one chapter is devoted to each of the three aforementioned lead-free material systems, including a detailed introduction of the related scientific questions and the experimental techniques, as well as a presentation of the results, a comprehensive discussion, and conclusions. The final chapter summarizes the key results and the most crucial findings and, finally, concludes this work.

## 2 Fundamentals and Literature Review

### 2.1 Dielectrics

#### 2.1.1 Dielectric Properties

Information included in the following chapter is based upon the text books of Waser *et al.* <sup>7</sup> and Moulson,<sup>8</sup> unless referenced otherwise. Dielectrics are electrical insulators the polarizability of which is generated in the interaction with an electric field. In response to an applied electric field, a displacement of electric charges occurs around their equilibrium positions in the unit lattice cell causing a dielectric polarization. The polarization  $P$  of matter is determined by the applied electric field  $E$ , permittivity of vacuum  $\varepsilon_0$ , and the dielectric susceptibility  $\chi$  as defined by Equation 2.1.

$$\mathbf{P} = \varepsilon_0 \cdot \overline{\chi} \cdot \mathbf{E} \quad (2.1)$$

The dielectric susceptibility defines the degree of polarization of a dielectric material in response to an electric field. It is related to the relative permittivity  $\varepsilon_r$  according to Equation 2.9.

$$\chi = \varepsilon_r - 1 \quad (2.2)$$

The electric displacement  $D$  that occurs in a dielectric medium in response to the applied electric field is defined by the following equation.

$$\mathbf{D} = \varepsilon_0 \cdot \mathbf{E} + \mathbf{P} \quad (2.3)$$

The properties of a dielectric medium are strongly determined by several polarization mechanisms. Electronic polarization appears in all dielectric media and is a result of dielectric dipoles formed between the electric-field displaced cloud of negative charges and the positively charged atom core, as shown in Figure 2.1. The electronic polarization is directly proportional to the volume of the electronic cloud, which implies that large atoms have larger polarizability. Ionic polarization forms in ionic crystals as a result of electric field-induced displacement of positive ions with respect to negative ones. Orientation polarization occurs in dielectric media with permanent built-in dipoles. At no applied electric field, these dipole moments rotate freely, but under the applied electric field the dipoles orient according to the direction of the applied electric field. Space charge polarization, also called Maxwell-Wagner polarization, occurs in dielectrics where the charge carrier densities are spatially inhomogeneously distributed. In ceramics, space charge polarization typically appears for materials with electrically conducting grains and insulating grain boundaries, but it may also form at the junction of the macroscopic electrode and the sample. This effect causes a time and frequency dependence of polarization, known as Maxwell-Wagner relaxation.

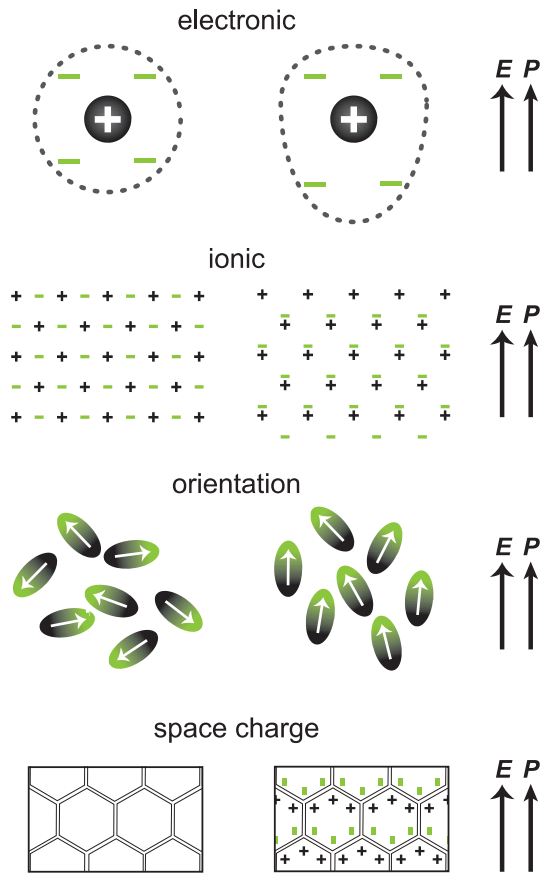


Figure 2.1: Different mechanisms of microscopic polarization.

One crucial polarization mechanism that greatly determines the dielectric properties of ferroelectric materials originates from the domain wall motion. The mechanisms of the domain wall motion under an electric field and their contribution to the dielectric properties of ferroelectrics are a subject of the following chapter where it will be introduced.

As shown in Figure 2.2, polarization mechanisms strongly depend on the frequency regime of an applied electric field for which polarization forms. The space charge, orientation, and domain wall polarizations are observed in the lower frequency ranges, while the resonance effects can be observed for electronic and ionic polarization at high frequencies.

Originating from the lattice, the electronic and ionic polarization are considered to be intrinsic polarization contributions, whereas the orientation, space charge, and domain wall polarizations are the extrinsic contributions.

Piezoelectricity is a characteristic of some dielectric materials to develop surface electric charges under an applied mechanical stress. Under this condition, electromechanical coupling becomes

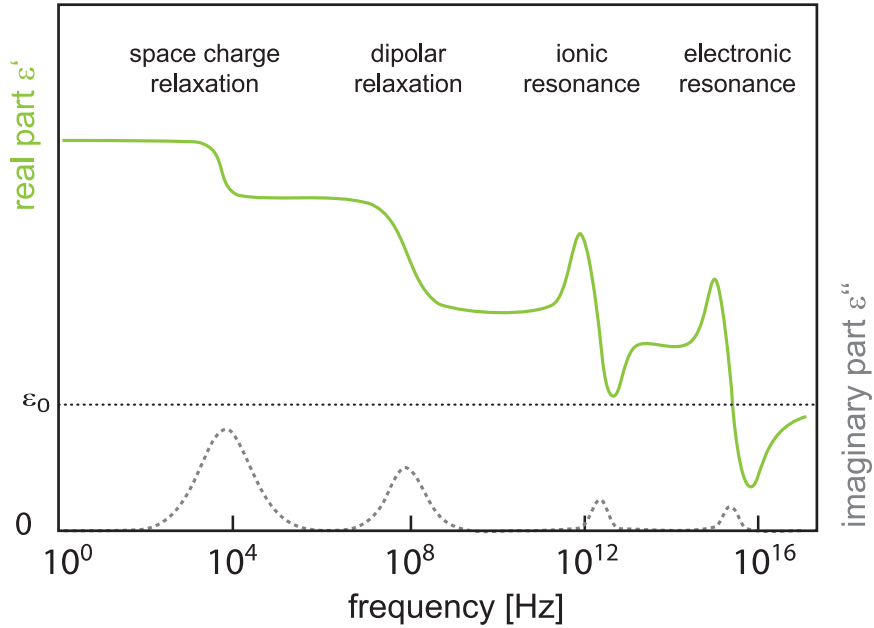


Figure 2.2: Schematic representation of the frequency dependence of the real and imaginary part of the dielectric permittivity (after Ref.[7]).

apparent which is defined by the following two equations.

$$D_i = d_{ijk} \cdot \sigma_{jk} + \varepsilon_{ik}^\sigma \cdot E_k \quad (2.4)$$

$$S_{ij} = s_{ijkl}^E \cdot \sigma_{kl} + d_{ijk} \cdot E_i \quad (2.5)$$

The direct piezoelectric effect is defined by Equation 2.4 and it describes the electrical response caused by a mechanical stimulation. The dielectric displacement  $D_i$  [C/m<sup>2</sup>] and the stress  $\sigma_{jk}$  [N/m<sup>2</sup>] are coupled by the piezoelectric tensor  $d_{ijk}$  with the units [C/N] or [m/V]. The product of electric field  $E_k$  and permittivity  $\varepsilon_{ik}$  defines the dielectric contribution.

The mechanical response to an electric stimulation is termed the converse piezoelectric effect and is described by Equation 2.5. Electric field  $E_i$  and stress  $\sigma_{kl}$  are coupled to the electromechanical strain  $S_{ij}$  via the piezoelectric tensor  $d_{ijk}$  and the compliance  $s_{ijkl}^E$  [m<sup>2</sup>/N], respectively.

Piezoelectricity occurs in dielectric materials with a non-centrosymmetric crystal structure. Out of 32 crystallographic point groups, 21 point groups are non-centrosymmetric and among them only point group 432 exhibits no piezoelectricity. Table 2.1 summarizes the point groups classified by their centrosymmetry. Among those 21 non-centrosymmetric point groups that exhibit piezoelectricity, 10 point groups are polar and belong to the pyroelectric group of materials. Pyroelectrics exhibit a spontaneous polarization  $P_s$  due to the existence of a dipole moment between the centers of negative and positive charges that do not coincide. The spontaneous polarization is defined as a dipole moment per unit volume or charge per unit area, *i.e.* the charges induced on the surfaces

Table 2.1: Crystallographic point groups in short Hermann-Mauguin notation (after Ref. [9]).

	centrosymmetric		non-centrosymmetric	
	11 non-polar		11 non-polar	10 polar
triclinic	$\bar{1}$			1
monoclinic	2/m			2, $m$
orthorhombic	$mmm$		222	$mm2$
rhombohedral	$\bar{3}, \bar{3}m$		32	3, $3m$
tetragonal	4/m, $4/mmm$		$\bar{4}, \bar{4}2m, 422$	$4mm, 4$
hexagonal	6/m, $6/mmm$		$\bar{6}, \bar{4}m2, 622$	$6mm, 6$
cubic	$m\bar{3}m, m\bar{3}$		$\bar{4}3m, 432, 23$	

perpendicular to the polarization vector. The direction of the spontaneous polarization is referred to as polar axis. The pyroelectric effect is defined as the change in the material polarization  $P_s$ , that is, charge density, on the material surface upon a change of temperature of the crystal. The temperature dependent change of polarization is defined as the pyroelectric coefficient  $p_i = \partial P_{n,i} / \partial T$ .

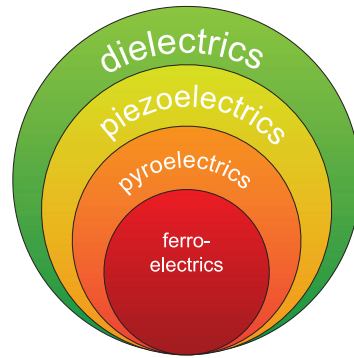


Figure 2.3: Classification of dielectrics.

Ferroelectrics are dielectrics with both piezoelectric and pyroelectric properties (Figure 2.3). A crystal is ferroelectric if the vector of the spontaneous polarization can be reoriented by an externally applied electric field. The external electric stimulation yields reorientation and alignment of electric dipoles along the poling direction. Owing to this property, ferroelectric materials are exploited in the realization of numerous practical applications. The following section introduces the characteristics of ferroelectric materials in more detail. Beside ferroelectrics, the phenomenon of polarization reversal also takes place in relaxor ferroelectrics that will be introduced thereafter.

## 2.1.2 Ferroelectrics

### a) General Information

This introduction into ferroelectrics is conceived based on work of Jaffe,<sup>10</sup> Wasing *et al.*,<sup>11</sup> Lines and Glass,<sup>12</sup> Ruschmeyer,<sup>13</sup> Waser,<sup>7</sup> Hall,<sup>14</sup> and Damjanovic.<sup>15</sup> Any reference used in addition is announced accordingly.

Ferroelectricity is the property of polar structures to exhibit a spontaneous polarization the vector of which can be switched between two or more distinct crystallographically equivalent directions upon application of a sufficiently large external electric field. The reorientation is preserved after removal of the electric stimulus.

The main properties of ferroelectrics are introduced on the example of BaTiO<sub>3</sub>. As many other ferroelectrics, it has the perovskite structure with the chemical composition always being ABO<sub>3</sub>. The high-temperature perovskite unit cell has the form of a simple cube, the corners of which are occupied by large cations (A site), the body center by a smaller cation (B site), and the centers of the faces are occupied by oxygen. The perovskite unit cell of BaTiO<sub>3</sub> is schematically presented in Figure 2.4. For the lattice of the barium titanate structure, Ba<sup>2+</sup> cations occupy the A-site, Ti<sup>4+</sup> is on the B-site, while O<sup>2-</sup> anions are placed in the face centers. The perovskite exhibits a displacive phase transition where a movement of cell atoms occurs below a critical temperature, yielding a change in crystal structure.<sup>17</sup> As shown by Figure 2.4, the crystal of barium titanate exhibits cubic symmetry at temperatures higher than  $T_c=128^\circ\text{C}$ . As a result of ionic distribution in the lattice, the centers of negative and positive charges coincide, which renders barium titanate paraelectric at temperatures above  $T_c$ .<sup>18</sup> On cooling, the cubic phase transforms into a tetragonal phase and a spontaneous polarization appears. The thermodynamics of the cubic-tetragonal phase transition can be described by the Landau-Ginzburg-Devonshire theory.<sup>19</sup> The Landau-Ginzburg-Devonshire theory defines the free energy of a unipolar crystal,  $F$  as a Taylor series expansion with polarization  $P$  as the order parameter.<sup>20</sup>

$$\Delta F = F - F_0 = \frac{1}{2}aP^2 + \frac{1}{4}bP^4 + \frac{1}{6}cP^6 - EP \quad (2.6)$$

In Equation 2.6, the higher order terms are neglected and the odd order terms are annulled due to symmetry.  $F_0$  is the energy of the reference state and parameters  $a$ ,  $b$ , and  $c$  are the Landau coefficients. The system equilibrium is established for minimized free energy. This minimum of  $F$  is found for the first derivative of  $F$  set to zero and for the positive values of its second derivative.

Applying  $\frac{\partial F}{\partial P} = 0$  and  $\frac{\partial^2 F}{\partial^2 P} = \frac{1}{\chi} > 0$ , the following equations can be derived.

$$P(a + bP^2 + cP^4) - E = 0 \quad (2.7)$$

$$\frac{1}{\chi} = a + 3bP^2 + 5cP^4 > 0 \quad (2.8)$$

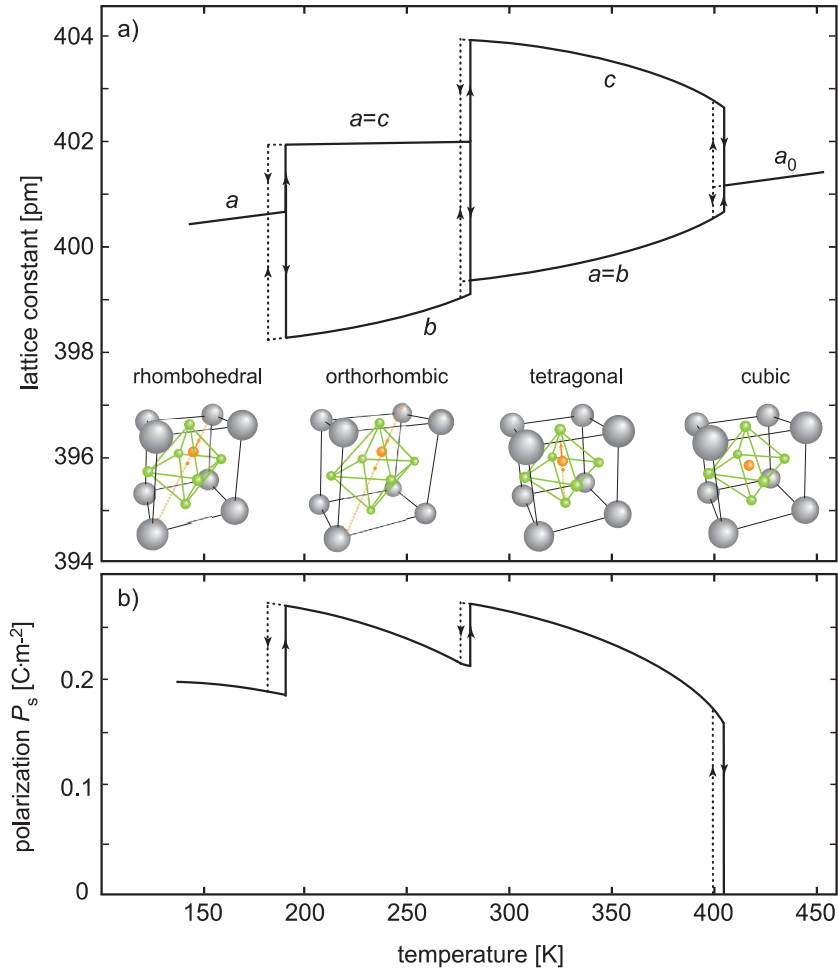


Figure 2.4: Schematic on the temperature evolution of lattice parameters, unit cell, and spontaneous polarization of barium titanate (after Ref.[16]).

In absence of electric field, the trivial solution of Equation 2.7 is  $P = 0$ . Provided so, the dielectric susceptibility is defined as follows.

$$\chi = \frac{1}{a} \quad (2.9)$$

Taking into consideration that polarization has near-zero values in the vicinity of the phase transition temperature, the higher order terms in Equation 2.7 can be neglected and the following equation applies

$$\frac{P}{E} = \frac{1}{a} = \chi. \quad (2.10)$$

The Landau-Devonshire theory assumes a linear temperature dependence of the parameter  $a$  around the Curie-Weiss temperature  $T_0$  as

$$a = a_0(T - T_0). \quad (2.11)$$



Combining Equations 2.10 and 2.11, the Curie-Weiss law can be derived.

$$\chi = \frac{C}{T - T_0} \quad (2.12)$$

For most ferroelectric systems, Equation 2.12 can be applied to describe the dielectric susceptibility in the paraelectric phase, *i.e.* when  $T > T_0$ .

In addition to the trivial solution  $P = 0$ , two more solutions of Equation 2.7 are possible. The solution  $b < 0$  and  $c > 0$  defines the first order phase transition, while the second solution  $b > 0$  implies a phase transition of second order.

For a first order phase transition, the free energy  $F(P)$  is a quadratic function at high temperatures with only one minimum at  $P = 0$  and for which a stable paraelectric phase is established. As shown in Figure 2.5(a) the free energy function obtains secondary minima at finite polarizations as temperature decreases. This assigns the establishment of the ferroelectric states. However, the en-

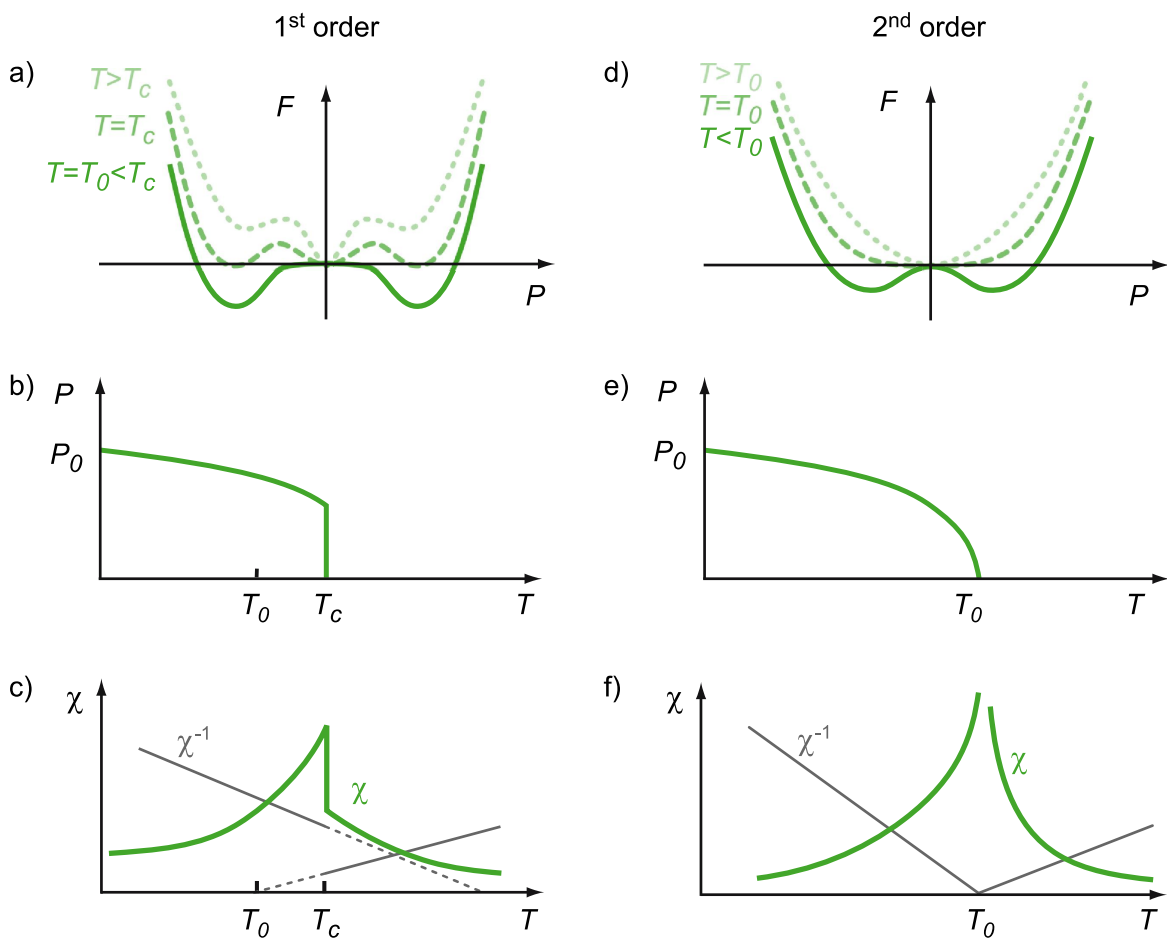


Figure 2.5: Free energy  $F(P)$ , polarization  $P(T)$ , and susceptibility  $\chi(T)$  at a first order phase transition (a, b, c) and a second order phase transition (d, e, f) (after Ref. [20]).

ergy level of the formed minima is higher than the minimum at  $P = 0$ . Therefore, the preferable, stable state is at  $P = 0$  and the polar states at finite  $P$  are metastable. At  $T = T_c$ , the minima of free energy coexist with the same energy level. Below  $T_c$ , the free energy function  $F(P)$  attains negative values and low free-energy states with finite spontaneous polarization are favorable. Throughout the temperature range between  $T_c$  and  $T_0$ , the first order phase transition to the ferroelectric state takes place. A spontaneous polarization increase to a finite value and a discontinuity in the susceptibility  $\chi(T)$  occurs (Figure 2.5(c)). With further temperature decrease, the tetragonal phase transforms first to an orthorhombic and then to a rhombohedral phase (Figure 2.4). Note that all phase transitions in  $\text{BaTiO}_3$  are first order phase transitions.

For a second order phase transition and a solution with  $b > 0$ , the free energy  $F(P)$  is a quadratic function with a parabolic shape and a minimum at  $P = 0$  for high temperatures. Here, the Curie temperature  $T_c$  coincides with the Curie-Weiss temperature  $T_0$ . At temperatures above  $T_c$ , the free energy function  $F(P)$  is a parabola with a minimum at  $P = 0$ . Starting from  $T_c$ , the  $F(P)$  continuously decays, while the ferroelectric states with finite polarizations become stable. The order parameter  $P$  continuously changes (Figure 2.5(e)), whereas the dielectric susceptibility peaks at  $T_0$ .

### b) Domain Structure in Ferroelectrics

The domains and their existence are predetermined by the electrostatics formed to minimize the free energy of the system. The formation of domains can be affected by a nonuniform strain, microscopic defects, and a thermal or electric treatment of the material. As the spontaneous polarization forms due to displacement of positive charges in respect to negative ones, a net charge density of opposite signs exists on the opposite sides of the crystal. Therefore, a depolarization field  $E_D$  is generated in response to the charge separation (Figure 2.6).

A system's tendency to minimize the electrostatic energy associated with  $E_D$  results in the crystal splitting into domains, since the free energy of a polydomain state is lower than for a single domain state. Consequently, the domains and according domain walls are created. Polarization within a domain is uniform. At domain walls, where polarization changes, polarization charges  $\sigma$  may exist and Equation 2.13 applies.

$$\sigma = (\mathbf{P}_1 - \mathbf{P}_2) \cdot \mathbf{n} \quad (2.13)$$

Here,  $\mathbf{P}_1$  and  $\mathbf{P}_2$  are the polarization vectors of two neighboring domains separated by the domain wall with  $\mathbf{n}$  being a surface unit normal vector. The elimination of the surface charges, *i.e.*  $\sigma = 0$ , occurs in two cases: For the polarization vectors being antiparallel to each other and parallel to the domain wall or for the polarization vectors under non-180° angle with a bisecting domain wall. The former case describes a 180° domain walls, while the latter applies for a non-180° domain wall. The corresponding domains are termed 180° and non-180° domains, respectively. As shown in Figure 2.6, non-180° domains are created in response to mechanical stress,

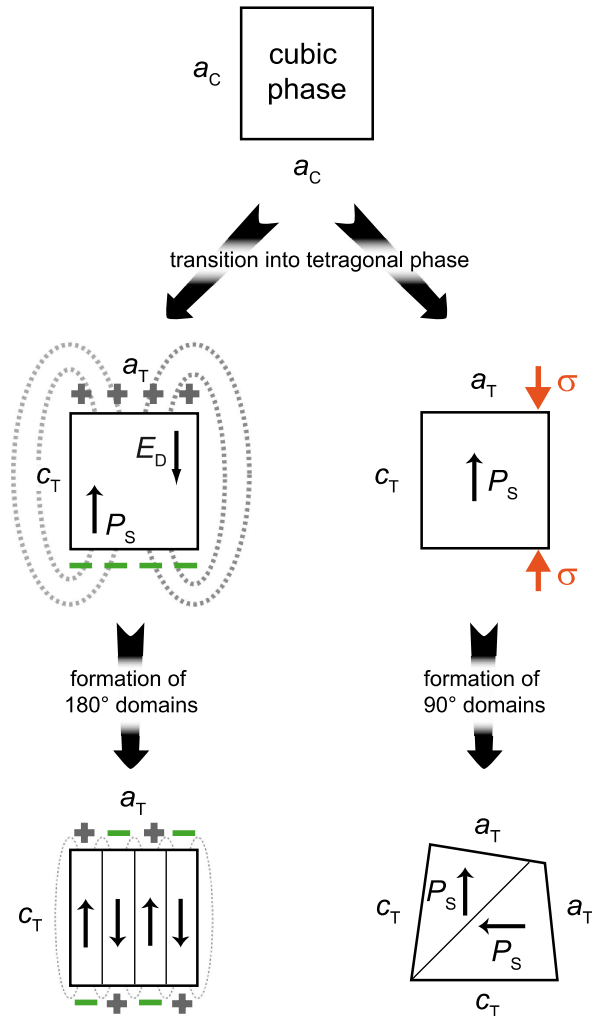


Figure 2.6: Principle of the formation of 180° and non-180° domains in a tetragonal, ferroelectric crystal (after Ref. [21]).

thus, minimizing elastic energy. The domain structure of ferroelectric ceramics consists of both 180° and non-180° domains, as the crystallites locally experience both electric and mechanical stress fields. The piezoelectricity in ferroelectrics is termed the intrinsic response as long as the domain configuration remains unaffected by the externally applied electric field or mechanical stresses.

The formation of domains in ferroelectric ceramics differs from the one in single crystals. Unlike single crystals, where the domain structures may form free of stress, the domain structure in a ceramic is formed under clamped conditions. Effectively, the formation of domains depends on the grain size. Here, grains can be deformed only by a collective motion of all neighboring grains, while their shape remains only under the condition of high internal or mechanical stresses.

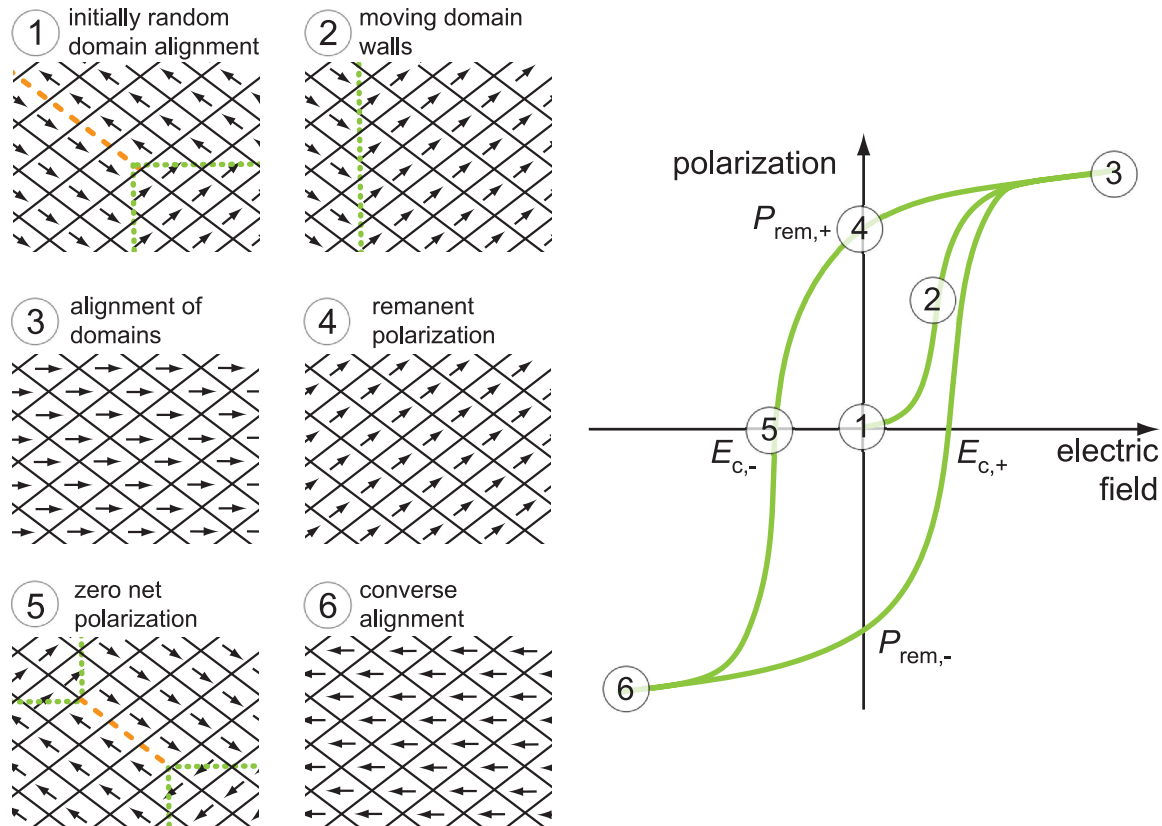


Figure 2.7: Electric field dependence of polarization and respective local domain structure (after Ref. [22]).

An external electric field or a sufficiently high mechanical stress causes the motion of domain walls. This effect contributes to the overall system piezoelectricity and is termed extrinsic piezoelectric effect.<sup>11</sup> In the initial state, the material exhibits no net polarization as the orientation of the domains is random. This is reflected in zero macroscopic polarization and corresponds to the state 1, as marked in the macroscopic polarization hysteresis loop in Figure 2.7. If an external electric field is applied to the crystal a reorganization of existing and formation of new domains may occur. By applying a small alternating electric field the domains extend in the direction of the electric field if the polarization of a domain is parallel, and contract, if the domain polarization is antiparallel with the applied electric field. For an electric field above a threshold field the polarization increases linearly with the electric field (state 2). In this low-field regime, the mechanisms contributing to piezoactivity are mostly dictated by the intrinsic ionic response and reversible domain wall vibration.

Upon further increase of the electric field, domain switching processes take place and the domains align in the direction of the applied electric field. In this regime, polarization strongly increases due to intense domain wall switching. Macroscopically, this is revealed as a nonlinear increase of

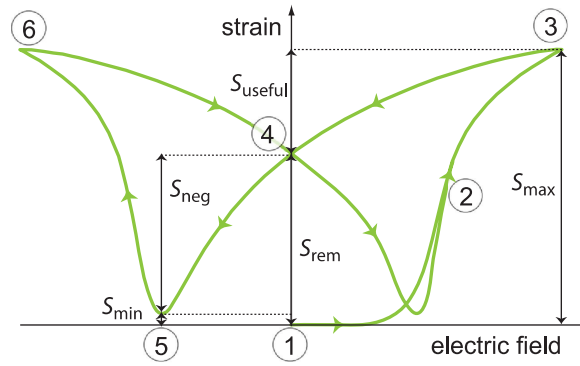


Figure 2.8: Schematic representation of the electric-field induced strain hysteresis loop. Characteristic points are inserted and labeled in accordance with Figure 2.7.

polarization followed by the polarization saturation, that is, a complete domain alignment (state 3). After the electric field is switched off, some domains reverse back as an effect of local electric and mechanical fields. At zero external electric field, the positive remanent polarization  $P_{rem,+}$  remains (state 4).

With electrical loading in the reverse direction, the polarization reverses and the formerly aligned domain structure reorganizes in respect to the negative electric field. No polarization is detectable at  $E_{c,-}$  at which only partial domain reversal is achieved (state 5). The  $E_{c,-}$  point is defined as the coercive field. For even lower electric fields, the domains are completely orientated in the direction of the negative electric field whereas polarization reaches negative saturation values (state 6). As the electric field increases again a new realignment of domains is triggered. At zero electric field, the system exhibits a negative remanent polarization  $P_{rem,-}$ . At positive coercive field  $E_{c,+}$ , the polarization is once more zero.

An electromechanical strain is generated in ferroelectric materials as an effect of the electric field. The strain hysteresis loop, referred to as butterfly curve, forms under bipolar electric loading as a consequence of the above-mentioned domain switching behavior. The typical ferroelectric  $S(E)$  curve is schematically presented in Figure 2.8. The characteristic aspects of domain switching processes are correspondingly marked as discussed previously. Characteristic parameters of the strain hysteresis curve are the maximum strain  $S_{max}$  (state 3) and the remanent strain  $S_{rem}$  (state 4). Other parameters of interest are useful strain defined as  $S_{useful} = S_{max} - S_{rem}$  and negative strain for which it applies  $S_{neg} = S_{rem} - S_{min}$ .

### c) A Physical Representation of Domain Wall Motion

The above-mentioned Landau-Devonshire theory considers no domain wall motion contribution to polarization, although their importance is decisive for the processes of polarization reversal. Assuming domain wall displacement to be quasi one-dimensional, *i.e.* no wall bending occurs,

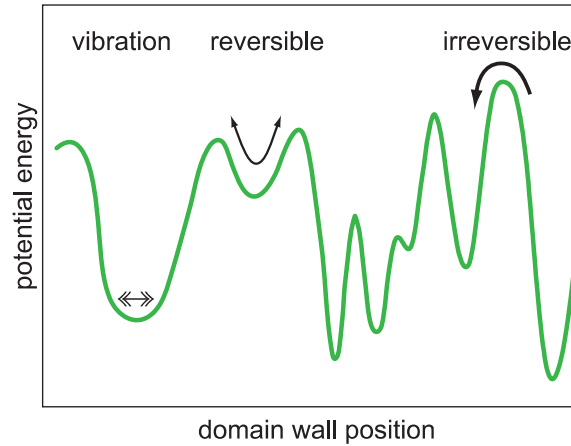


Figure 2.9: Schematic representation of the domain wall potential landscape in a ferroelectric material with randomly distributed point defects (after Ref. [15]).

the potential wall energy landscape as a function of position appears as schematically presented in Figure 2.9.

The potential energy is determined by domain walls interacting with the lattice, dislocations, point defects, and adjacent walls.<sup>23,14,11</sup> The field-induced domain wall displacement can be differentiated as processes of vibration, translation, and motion. Upon *ac* electric field application, domain walls oscillate, but their displacement is reversible and non-hysteretic at fields lower than a certain threshold field. This corresponds to the domain wall vibration and the potential energy for domain walls is symmetric. Domain wall translation is the effect of domain wall displacement over an array of pinning centers during which no changes in general domain character are made. Domain wall translation includes both reversible processes and irreversible processes in which the domain wall moves between several energy minima.

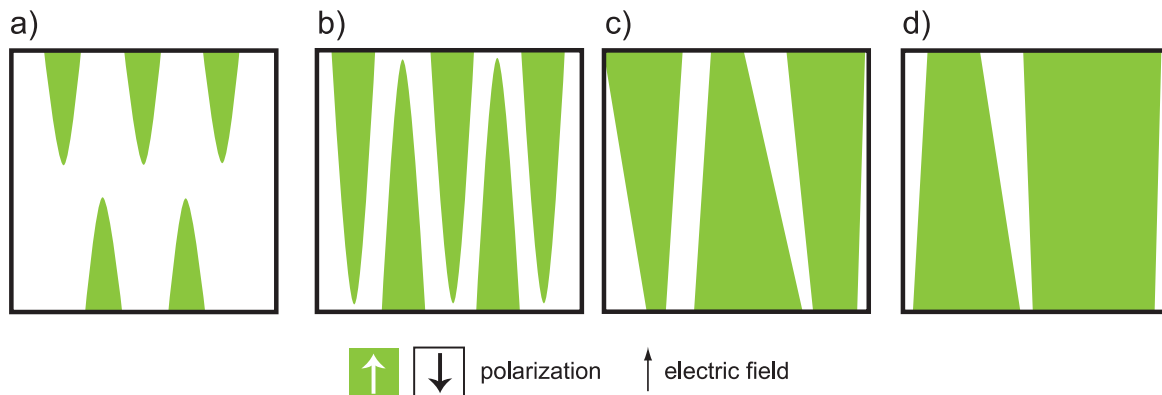


Figure 2.10: Polarization switching process: (a) domains of reverse orientation nucleate, (b) reverse domains grow, (c) domains grow sideways, and finally (d) domains coalesce (after Ref.[24]).

Domain wall motion is characterized by domain nucleation and polarization switching. Here, the domain wall motion is highly nonlinear and associated with considerable hysteretic losses. Due to the changes of the polarization vector, domain wall motion modifies the character of a domain.

The domain switching process in ferroelectrics is schematically presented in Figure 2.10. Initially, new domains nucleate and start growing in the direction of the electric field. Domains are of preferably triangular shape as the respective depolarization field is comparably small on the scale of the whole crystal. As the electric field increases, the domains grow sideways and eventually coalesce (Figure 2.10(d)).

### 2.1.3 Relaxor Ferroelectrics

#### a) General Information

If not stated otherwise, information on relaxor ferroelectrics summarized here is based on the work of Ye,<sup>25</sup> Bokov and Ye,<sup>26</sup> Kleemann,<sup>27</sup> Samara,<sup>28</sup> and Shvartsman and Lupascu.<sup>29</sup>

Originally characterized as ferroelectrics with diffuse phase transition, relaxor ferroelectrics have been discovered for the complex compositional structure perovskite  $\text{BaTiO}_3\text{-BaSnO}_3$  electroceramics by Smolenskii *et al.*<sup>30,31</sup> Featured by a strong frequency dispersion of the dielectric permittivity peak, a massive dielectric relaxation, and ferroelectric character at lower temperatures, this class of material has been differentiated from the classic ferroelectrics and named relaxor ferroelectrics. As they exhibit strong piezoelectric coupling and large electric-field induced electromechanical strain, relaxor ferroelectrics are a class of material with very strong practical importance.

A comparative representation of relaxor ferroelectrics against ferroelectrics is shown in Figure 2.11. One of the most significant differences between ferroelectrics and relaxor ferroelectrics is found in the  $P(E)$  dependence. In comparison to ferroelectric square polarization hysteresis loops with large remanent values in the low temperature regime, polarization loops of relaxor ferroelectrics may exhibit a small remanent polarization, low coercive fields and, consequently, a slim hysteresis loop. The characteristic polarization loop shape of relaxors is hypothesized to reflect the presence of small polar entities, called polar nanoregions (PNRs). The application of an electric field triggers the orientation of PNRs. Their orientation effectively contributes to a high overall polarization. Upon removal of the electric field, a polarization realignment of a majority of PNRs occurs. Their realignment is the crucial mechanism behind the low remanent polarization values. For PNRs remaining to some extent stable even at temperatures above the dynamic transition temperature  $T_m$ , the polarization in relaxors decays smoothly (Figure 2.11). In comparison, polarization of ferroelectrics vanishes above the transition temperature  $T_c$ . This polarization decay is abrupt at a first order phase transition, while being continuous for the sec-

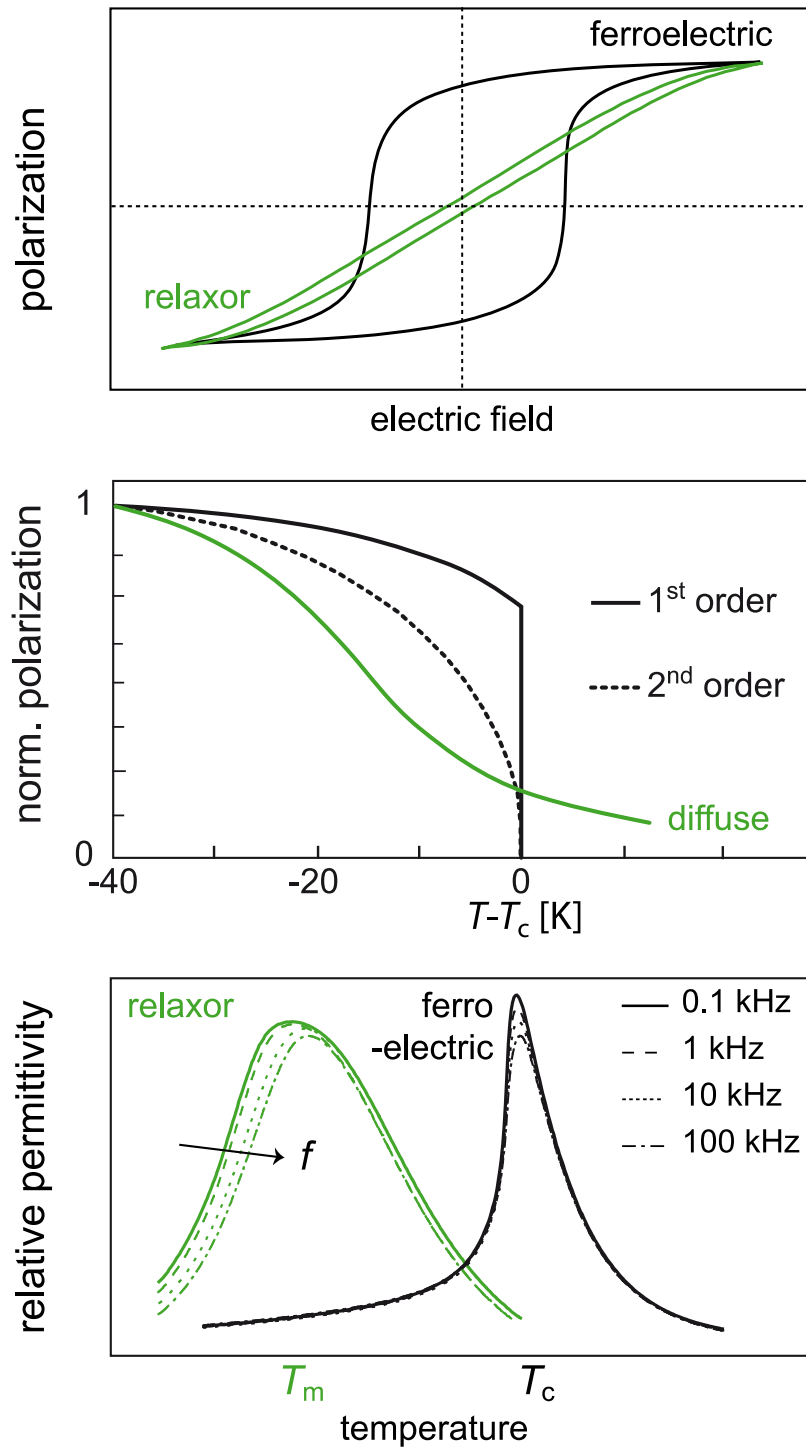


Figure 2.11: Comparison of field-induced polarization (top), temperature-dependent polarization (middle), and relative permittivity (bottom) typically observed in ferroelectrics and relaxor ferroelectrics (after Ref.[28]).



ond order phase transition. Furthermore, relaxor ferroelectrics are characterized by a very broad peak in the temperature-dependent dielectric permittivity. The magnitude of the peak permittivity as well as the temperature of maximum permittivity,  $T_m$ , strongly depend on the frequency of the poling electric field. In contrast to the sharp dielectric peak at  $T_c$  which denotes the phase transition in ferroelectrics, the dispersive dielectric maximum of relaxors indicates no structural symmetry change, but rather a slowing down of the dipolar moment dynamics. For relaxors above the transition temperature no Curie-Weiss law applies.

Although widely studied, the physical principles behind the nature of relaxor ferroelectrics are still a subject of continuous scientific discussions. Due to the challenging fundamental considerations, no unique physical model on the relaxor ferroelectricity has been adopted so far. By now, a variety of different models has been suggested, including the dipolar glass model,<sup>32</sup> superparaelectric model,<sup>33</sup> diffuse phase transition model,<sup>30</sup> random field model,<sup>34</sup> spherical random-bond-random-field model,<sup>35</sup> and random-bond-random-field model.<sup>36</sup> All models are in detail elaborated in the review paper by Bokov and Ye.<sup>26</sup>

### b) Compositional Order and Disorder

The compositional disorder, also called chemical or substitution disorder, greatly governs the properties of relaxor ferroelectrics. For perovskites, relaxor behavior is often strongly determined by the difference in the valence of cations occupying the lattice sites of the  $ABO_3$  structure, as well as by the coherence length of the chemically ordered nanoregions.<sup>37,38</sup> In the case of B-site substitution, the perovskite structure is formed as  $A(B'_{1/2}B''_{1/2})O_3$ . The  $B'$  and  $B''$  may be differently charged and of different ionic radii and, by occupying the equivalent lattice positions, determine the degree of order/disorder of the structure. In this respect, several cases can be distinguished.

If two cations on the  $B'$  and  $B''$  site are of a sufficiently large chemical difference, *i.e.* valence, they can order and form chemically ordered regions.<sup>39,40</sup> At minimized electrostatic and elastic energies, long-range order is established implying long coherence lengths of nanoregions and classical phase transitions to ferroelectric or antiferroelectric phases. If, however, the valence difference is around the critical level for the B-site order/disorder occupancy, the degree of ordering can be modified, for instance, by thermal annealing. This phenomenon was observed in systems like  $Pb(Sc_{1/2}Ta_{1/2})O_3$ .<sup>41,42</sup> An increasing degree of order increases the coherence length and a phase transition into the ferroelectric phase occurs.

A smaller chemical difference between  $B'$  and  $B''$  cations usually results in compositional disorder that cannot be changed thermally, as in the case of  $Pb(Mg_{1/3}Nb_{2/3})O_3$  (PMN). The quenched compositional disorder is established but it is incomplete and inhomogeneous. Ordered nanodomains form with a short coherence length, which is characteristic for relaxor ferroelectrics. As a result of the quenched phase fluctuations or the incomplete order-disorder phase transition, ordered nanoregions are formed within a disordered matrix. The ordered nanodomains and the positively

charged disordered matrix become a source of random electric fields. These random electric fields prevent the growth of ordered nanoentities. Random electric fields form not only as a consequence of heterovalent ions in the lattice, but also due to impurities and defects.

### c) Phase Transitions in Relaxor Ferroelectrics

At high temperatures, the relaxor ferroelectrics are in the paraelectric phase. Although the structure has a cubic symmetry with the non-polar and non-centrosymmetric  $Pm\bar{3}m$  point group, it locally exhibits significant structural and chemical disorder. Distortions of the local ion configuration can take place as ions displace from their original crystallographic lattice position. It was shown that  $Pb^{2+}$  ions in some relaxors, as  $Pb(Mg_{1/3}Nb_{2/3})O_3$ ,  $Pb(Zn_{1/3}Nb_{2/3})O_3$ , and  $Pb(Sc_{1/2}Ta_{1/2})O_3$  are permanently displaced at the sites within a sphere of 0.3 Å radius around the original lattice position. As already mentioned, the random electric fields can, among others, be caused by the random distribution of B-site heterovalent ions. The random fields trigger the creation of short-range ordered nuclei with polar symmetry. Depending on the fluctuation of the random field, the polarity of these polar dipoles is likewise random, but they are overall compensated within the relaxor so that the net polarization is zero. In this high-temperature regime, the Curie-Weiss law actually applies for relaxor ferroelectrics.

With temperature decreasing, the uncorrelated dipoles evolve into dynamic entities. This change in the character of dipoles occurs at the Burns temperature  $T_B$ . The Burns temperature is typically well above the temperature of the maximum permittivity  $T_m$  (Figure 2.12). It corresponds to a temperature where the temperature-dependent permittivity deviates from the Curie-Weiss law. The dynamic polar entities induce polarization in adjacent unit cells forming polarization clouds. Due to the increase of polarizability of the matrix with cooling, the correlation length increases, improving the dipole-dipole interaction. At  $T_B$ , the new polar regions are unstable and regions with a subcritical size disappear. Only sufficiently large nuclei grow in size. The equilibrium size of dynamic nuclei can be almost arbitrarily small, as little as only several unit cells. The spatial symmetry is conditioned by the symmetry of the surrounding matrix, therefore, remains paraelectric, although symmetry breaking occurs on the level of PNRs. The PNRs with the local spontaneous polarization  $P_d$  have randomly distributed dipole moments, so that the net average polarization is  $\sum P_d = 0$ ; in contrast,  $\sum P_d^2 \neq 0$  applies. This denotes that no macroscopic polarization can be measured, but the appearance of PNRs apparently affects those properties depending on  $P^2$ , such as electrostriction,<sup>33</sup> thermal expansion coefficient,<sup>28</sup> and refractive index.<sup>43,44</sup> The relaxor phase in which the polar regions are highly dynamic and oriented randomly is referred to as an ergodic relaxor state (ER). A more detailed description of the ergodic state will follow at a later stage.

A further decrease of temperature causes a stronger interaction between PNRs, their dynamics slow down, and they increase in size and number. The polar fraction in the nonpolar matrix increases and results in higher polarization and dielectric permittivity (Figure 2.12). Due to the randomness of PNR interaction and the broad distribution of PNR size, a broad distribution of re-

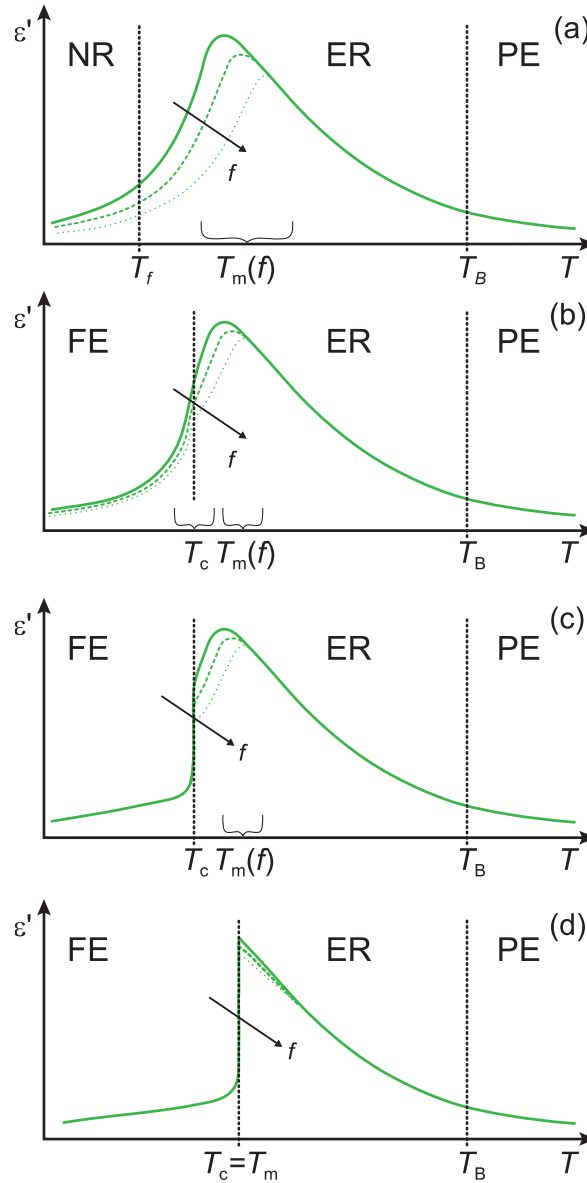


Figure 2.12: Dielectric permittivity as a function of temperature for different relaxor structures: (a) a canonical relaxor in which the ER state evolves into the NE state on cooling, (b) relaxor with a diffuse ER-FE transition at  $T_c < T_m$ , (c) relaxor with a sharp ER-FE transition at  $T_c < T_m$ , and (d) structure with ER-FE transition at  $T_c = T_m$  (after Ref.[26]).

laxation times is generated. This is clearly reflected in the frequency-dispersive permittivity peak at the frequency-dependent temperature  $T_m$ . Upon additional cooling, two possible directions in the property evolution can occur. The first case corresponds to the further growth of PNRs on cooling and eventual freezing of their dynamics at a specific temperature  $T_f$ . At this state, referred to as the nonergodic (NE) state, the correlation length of PNRs increases, implying stronger interaction between dipoles. At around  $T_f$ , the number of polar nanoregions decays due to the fact

that PNRs merge at this temperature. For this class of relaxors, termed canonical relaxors, the long-range ordered ferroelectric state can be established from the short-range ordered NE state by applying a large enough electric field<sup>45</sup> or mechanical stress.<sup>46</sup> The freezing temperature  $T_f$  can be determined from fitting the frequency-dependent permittivity peak temperature  $T_m$  to the Vogel-Fulcher law, defined in Equation 2.14.<sup>29</sup>

$$f = f_0 \cdot \exp\left(\frac{E_a}{k \cdot (T_m - T_f)}\right) \quad (2.14)$$

Here,  $E_a$  is an activation energy,  $f_0$  is an attempt frequency, and  $k$  is the Boltzmann constant.<sup>47</sup>

In the second case, the ferroelectric phase is spontaneously induced from the ergodic relaxor state at the temperature  $T_c$  (Figure 2.12 (b)-(d)). At  $T_c$ , which is below  $T_m$ , a phase transition from the cubic to a polar, long-range ordered phase occurs. The domain structure reveals micron-size domains,<sup>48</sup> while strain  $S(E)$  and polarization  $P(E)$  resemble the butterfly strain and rectangular polarization hysteresis loops of ferroelectrics. This field-induced ferroelectric state differs only slightly from the classical ferroelectric state by more diffused domain walls and dispersed dielectric peak originating from the relaxation of polarization and not from the phonon contribution.<sup>49</sup>

#### d) Electric Field-Induced Phase Transition

Numerous properties of relaxor ferroelectrics are dictated by the externally applied electric field. By applying an electric field larger than a critical value, nonergodic relaxor ferroelectrics undergo an electric field-induced phase transition to a long-range ordered phase. If the quenched random electric fields are overcome by the applied electric field, the formation of long-range ordered ferroelectric domains from PNRs is possible.

The ferroelectric phase can be induced from the relaxor state either by cooling from the ergodic phase while applying an electric field (field cooling, FC) or by applying an electric field after zero-field cooling (ZFC). Figure 2.13 represents the electric field-temperature phase diagram defined for PMN.<sup>50,51</sup> By FC, the phase transformation from an ergodic pseudocubic phase to a polar phase is induced at  $T_c$ , followed by a breaking of symmetry. In this regime,  $T_c$  is higher for higher electric fields, as assigned by line *A*. After removal of the electric field, the polarization of this field-induced ferroelectric phase remains stable down to low temperatures. For a material that is, however, zero-field heated (ZFH) above  $T_c$ , the long range-ordered ferroelectric state becomes unstable and vanishes as the material returns to the ergodic phase. The material is in a glassy-like state, *i.e.* nonergodic, at low temperatures. The glassy freezing temperature  $T_f$  separates the ergodic and nonergodic relaxor phases in the zero-field cooling regime. This indicates that the stability of the induced state strongly depends on both temperature and electric field. These two parameters are, therefore, interrelated and cannot be examined independently from each other.

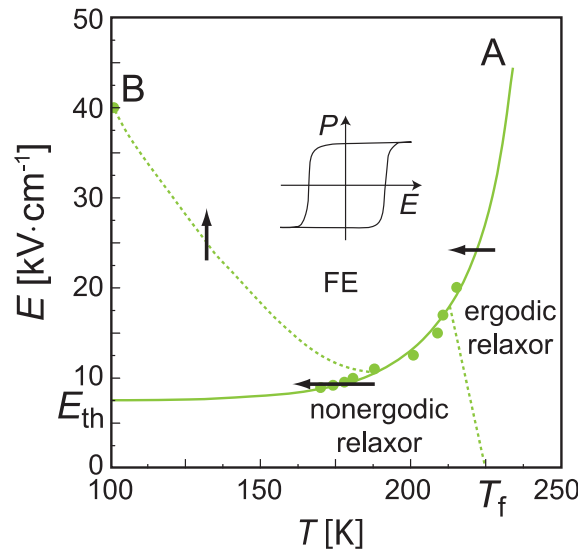


Figure 2.13: Electric field-temperature phase diagram as suggested for PMN: The ferroelectric state with reversible polarization is enclosed by an U-shape region. For temperatures above  $T_f$ , the ergodic phase is observed. At lower temperatures, either the nonergodic relaxor state (before field application) or the ferroelectric state with non-reversible polarization (at electric fields larger than  $E_{th}$ ) is established (after Ref. [51]).

## 2.2 Lead-Free Piezoelectric Ceramics

### 2.2.1 Potassium Sodium Niobate-Based Piezoelectric Ceramics

#### a) Structure and Properties

Initially reported by Shirane *et al.*,<sup>52</sup> potassium sodium niobate  $K_{1-x}Na_xNbO_3$  is a ferroelectric solid solution of ferroelectric  $KNbO_3$  (KN) and antiferroelectric  $NaNbO_3$  (NN).<sup>53</sup> The KNN solid solution exhibits several thermally induced polymorphic phase transitions (PPT) and composition dependent morphotropic phase boundaries (MPB). The KNN phase diagram suggested by Ahtee *et al.*<sup>54,55</sup> reveals a series of PPTs on the KN-rich side (Figure 2.14). There is a low-temperature rhombohedral phase, an orthorhombic phase at around room temperature, a tetragonal phase at temperatures between 225 °C and 435 °C, and a cubic phase at temperatures above 435 °C.

On the NN-rich side seven PPTs occur within a wide temperature range.<sup>56</sup> Among those, two transitions are evident for the entire compositional range. The phase transition at  $\sim 200$  °C separates the ferroelectric phases. The paraelectric phase is established at around  $\sim 400$  °C. At ambient temperature, phase boundaries are detected at 17.5 %, 32.5 %, and 47.5 % of  $NaNbO_3$  content. In the following, the abbreviation KNN will denote the  $K_{1-x}Na_xNbO_3$  composition with  $x=0.50$ .

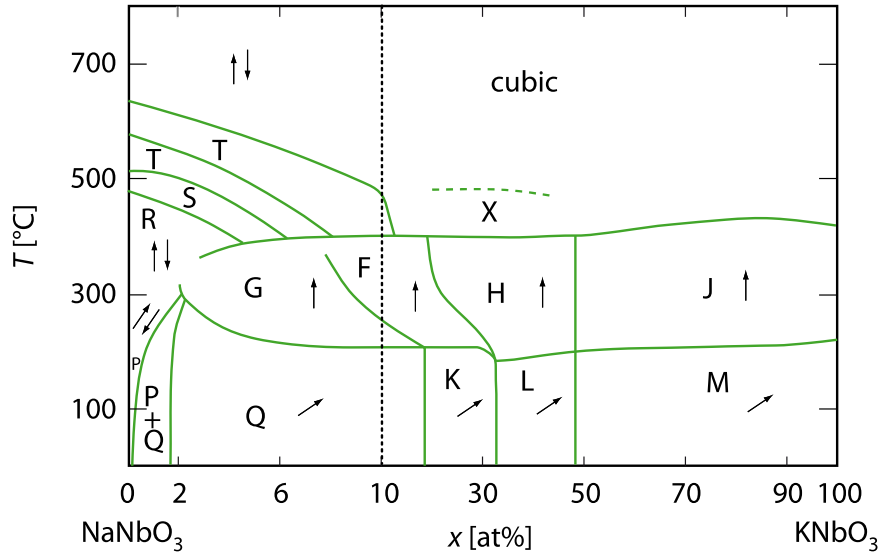


Figure 2.14: Phase diagram proposed for  $K_xNa_{1-x}NbO_3$  with monoclinic phases, regarded also as orthorhombic ferroelectric (regions marked as Q, K, L), tetragonal ferroelectric phases (regions F, H, and J), orthorhombic ferroelectric phases (regions M and G), and orthorhombic antiferroelectric phases (region P) (after Ref. [55]).

At room temperature, KNN is reported to have an orthorhombic crystal symmetry with the space group  $Amm2$ . However, Tennery *et al.*<sup>57</sup> and Tellier *et al.*<sup>58</sup> reported a monoclinic symmetry of KNN at room temperature, while Lie *et al.*<sup>59</sup> showed that the KNN primary cell is monoclinic at room temperature, but on the unit-cell level the symmetry is orthorhombic. The morphotropic phase boundary forms for approximately  $x=0.50$  between two orthorhombic phases, L and M in Figure 2.14. While some reports question the existence of the MPB,<sup>58,60</sup> other authors report its occurrence for a different KN/NN content ratio.<sup>61,57</sup> The enhancement of electric and piezoelectric properties of KNN in the vicinity of the MPB, however, is undeniable.

Typical values of spontaneous polarization reported for KNN are in the range from  $15 \mu C/cm^2$  to  $25 \mu C/cm^2$ .<sup>59</sup> Early investigations on unmodified KNN demonstrated a comparably moderate piezoelectric coefficient<sup>62</sup>  $d_{33}$  of  $80 pC/N$ , a planar coupling factor<sup>63</sup>  $k_p=0.36\%$ , and a relative permittivity of 290.<sup>64</sup> The KN/NN content optimization<sup>61</sup> and special sintering techniques, as hot pressing (HP) and spark plasma sintering (SPS) yielded an increase of the piezoelectric coefficient to  $160 pC/N$ <sup>61,65,66</sup> and  $148 pC/N$ .<sup>61,66,67,68</sup> Liquid phase sintering, moreover, enhances  $d_{33}$  up to  $180-270 pC/N$ .<sup>69</sup>

## b) Chemical Modifications of KNN

Compositional modifications of the KNN solid solution may significantly improve its piezoelectric and dielectric properties, but also alters its phase structure. The A-site of the unit cell is commonly doped with Li,<sup>70,71,72,73</sup> Ba and Ca, while Ta,<sup>74,75,76</sup> Sb,<sup>77</sup> and Zr occupy the B-site of the KNN

Table 2.2: Summary of properties of KNN and its compounds.

System	$d_{33}$ [pC/N]	$\epsilon_{r,33}$	$k_p$ [%]	$E_c$ [kV/mm]	$P_{rem}$ [ $\mu\text{C}/\text{cm}^2$ ]	$T_{O-T}$ [ $^{\circ}\text{C}$ ]	$T_c$ [ $^{\circ}\text{C}$ ]	Ref.
KNN	80	290	36	n/a	n/a	n/a	n/a	[64]
KNN (HP)	160	420	45	n/a	n/a	n/a	n/a	[65]
KNN + Li <sup>+</sup>	n/a	235	28	n/a	n/a	~RT	475	[70]
	324	n/a	n/a	1.8	15	60	475	[72]
	280	760	48	n/a	n/a	60	475	[73]
KNN + Sb <sup>5+</sup>	204	850	47	1.9	21	130	300	[77]
KNN + Ta <sup>5+</sup>	151	700	42	0.5	18	170	328	[78]
	270	917	44	0.7	16	87	208	[76]
KNN-LT	263	1290	53	n/a	n/a	40	325	[84]
	276	650	46	1.8	21.1	69	445	[85]
KNN-LS	265	1380	50	1.8	25	35	368	[86]
KNN-LN	215	530	41	1.3	20	n/a	450	[87]
KNN-LT-LS	416	1570	61	n/a	n/a	n/a	253	[6]
	400	2500	54	n/a	n/a	n/a	230	[88]
	345	1176	n/a	n/a	n/a	25	260	[79]
KNN-BZ+Li, Ta, Sb	365	3400	45	0.9	14	25	175	[89]
KNN-BT	225	1058	36	n/a	n/a	n/a	n/a	[90]
	193	1100	43	1.1	14	n/a	314	[91]
KNN-BNT	195	900	43	n/a	n/a	n/a	375	[92]
KNN-BKT	251	1260	49	n/a	n/a	n/a	376	[93]

perovskite cell. The controlled texturing methods and Li-, Ta-, and Sb- doping yielded  $d_{33}$  values as high as 400 pC/N.<sup>6</sup> In addition, different compositional modifications are often used to lower the temperature of the beneficial orthorhombic-tetragonal (O-T) phase transition in the vicinity of which KNN exhibits enhanced piezoelectric properties. The polymorphic phase transition temperature  $T_{O-T}$  is shifted from 200  $^{\circ}\text{C}$  to temperatures around room temperature.<sup>54,55</sup>

The properties are, furthermore, optimized in order to increase the Curie temperature  $T_c$ , which is particularly important for high-temperature performance requests. Unlike other dopants that decrease  $T_c$ , a Li-modification of KNN raises  $T_c$  above 400  $^{\circ}\text{C}$ , thereby preserving the rather high piezoelectric properties.<sup>78,73,72</sup> A similar effect of achieving both enhanced material properties and increased  $T_c$  is obtained by a variety of other dopants, but their implementation requires complex material doping engineering.<sup>79,80,81,82,83</sup> By complex chemical modification with Li, Ta, and Sb, a large piezoelectric coefficient  $d_{33}$  of 345 pC/N and a high Curie temperature of 260  $^{\circ}\text{C}$  were achieved, while the O-T phase transition temperature is maintained at around ambient temperature.<sup>79</sup>

The improvement of KNN-based materials entails several disadvantages. Firstly, high-temperature sintering, required for the processing of highly dense bulk material, causes strong compositional fluctuation, primarily due to the high volatility of alkali oxides, particularly those of Na and K.<sup>94,95</sup> Moreover, moderate densification,<sup>96</sup> compositional inhomogeneity,<sup>97</sup> and complex synthesis processes of high-performance KNN material<sup>6,98</sup> are critical issues that limit industrial applicability of the material. In addition, due to the present polymorphic phase transition, KNN suffers from both a phase instability and reduction of piezoelectricity, as reported for LiSbO<sub>3</sub>-,<sup>86</sup> Li-,<sup>71</sup> LiTaO<sub>3</sub>-,<sup>79</sup> and LiSbO<sub>3</sub>-modified KNN.<sup>79</sup>

The enhancement of KNN piezoelectric properties has been achieved by a plethora of different compositional modifications as by Li<sup>+</sup>, Sb<sup>5+</sup>, and Ta<sup>5+</sup>. Among the most intensively investigated systems are binary KNN-based systems formed with LiTaO<sub>3</sub> (LT), LiSbO<sub>3</sub> (LS), LiNbO<sub>3</sub> (LN), LiTaO<sub>3</sub> and LiSbO<sub>3</sub> (LT-LS), BaTiO<sub>3</sub> (BT), Bi<sub>1/2</sub>Na<sub>1/2</sub>TiO<sub>3</sub> (BNT), Bi<sub>1/2</sub>K<sub>1/2</sub>TiO<sub>3</sub> (BKT), or BaZrO<sub>3</sub> (BZ) with properties being listed in Table 2.2.

### 2.2.2 Bismuth Sodium Titanate

Bismuth-based compounds are reported to be suitable successors of Pb-based piezoelectric materials. The advanced piezoelectric properties of Bi-based solid solutions are related to the large radius of Bi<sup>3+</sup> ions and the consequently high polarizability. In addition, the special electronic structure of Bi<sup>3+</sup> ions plays an important role. Similar to Pb<sup>2+</sup>, Bi<sup>3+</sup> ions feature a lone electron pair in the outer shell. Two electrons, *i.e.* the lone pair of the outer shell, do not chemically bond, but form a dumbbell-like extrusion of the electron density on one side of the ion, which increases the polarizability and the distortion of the unit cell.<sup>99</sup> The lone pair can be easily hybridized with orbitals of oxygen ions. This reduces the distance between bismuth and the oxygen ions, yielding a distortion of the unit cell. The hybridization and the resulting displacement are decisive factors for the enhanced ferroelectric properties.

Bismuth sodium titanate, Bi<sub>1/2</sub>Na<sub>1/2</sub>TiO<sub>3</sub>, was discovered by Smolenski *et al.*. A large remanent polarization  $P_{rem}=38 \mu\text{C}/\text{cm}^2$ , relatively high coercive voltage  $E_c=7.3 \text{ kV}/\text{mm}$ , and high Curie temperature  $T_c=320 \text{ }^\circ\text{C}$  were reported.<sup>31</sup>

However, to obtain dense BNT ceramics high sintering temperatures ( $T>1200 \text{ }^\circ\text{C}$ ) are required. At this temperature, bismuth evaporates causing an increase of the oxygen vacancies. Effectively, this may lead to a high leakage current in the material eventually restricting poling of the material.<sup>100,101</sup>

BNT is a ferroelectric compound the structure of which exhibits two phase transitions. At ambient temperature, BNT has rhombohedral symmetry with a polar  $R3c$  space group.<sup>102</sup> By recent temperature-dependent X-ray and neutron diffraction studies, it was shown that the rhombohedral phase evolves into a  $P4bm$  tetragonal phase. This phase transition is strongly diffused between



225 °C and 400 °C where both phases coexist.<sup>103,104,105,106</sup> Here, the rhombohedral phase is detected in the form of clusters and they are embedded into the matrix of a tetragonal phase.<sup>106</sup> Eventually, at around 520 °C, the structure transforms from  $P4bm$  to a  $Pm\bar{3}m$  cubic phase,<sup>107</sup> where the twin boundaries of the tetragonal phase gradually disappear.<sup>108</sup>

Dielectric measurements, however, suggest a different phase structure. The dielectric permittivity of BNT exhibits two anomalies. One is in the form of a frequency-dispersive shoulder at around 200 °C, while the other one is at around 320 °C manifested as a frequency-independent broad permittivity maximum.<sup>109,110,111</sup> The first anomaly in the permittivity curve was rationalized by a ferroelectric-antiferroelectric phase transition, whereas at  $T=320$  °C permittivity peaks as a result of a structural phase transition to the paraelectric state. Nonetheless, X-ray diffraction,<sup>105</sup> Raman scattering,<sup>112</sup> and neutron scattering<sup>112</sup> studies reported no phase transition at the temperature of the permittivity maximum.

A TEM study revealed the vanishing of ferroelectric domains at around 200 °C as the rhombohedral phase attenuates.<sup>108</sup> Between 200 °C and 300 °C, a modulated phase appears within the  $R3c$  phase. Twinning planes in form of  $Pnma$  orthorhombic sheets with  $(a^-a^+a^-)$  octahedra tilting are detected. The modulated phase, assigned to an antiferroelectric phase, was hypothesized to be the origin of BNT relaxor nature, considering that the cationic displacement is strongly increased between atomic positions of the  $R3c$  phase and  $Pnma$  sheets.<sup>108</sup>

Using the neutron powder diffraction technique, Jones *et al.* revealed that Na/Bi and Ti atoms displace along the polar [111] axis yielding a rhombohedral phase up to 320 °C.<sup>103</sup> Above 320 °C, the Na/Bi and Ti atoms displace in opposite directions along the [001] axes which is characteristic for the tetragonal ( $P4bm$ ) phase. Eventually, at around 540 °C the cation displacements and tilt systems disappear to yield the ideally cubic perovskite structure.

Vakhrushev *et al.*<sup>106</sup> defined the phase of BNT between 200 °C and 320 °C as 'low temperature non-polar', followed by the ferroelectric phase on cooling below 200 °C. Based on permittivity anomalies and the disappearance of electric hysteresis loops once temperature is above 200 °C, the existence of smaller dynamic polar regions above and stable polar regions below 280 °C were reported.

On the basis of a pyroelectric and an electrostrictive strain study,<sup>113</sup> the relaxor properties of BNT were reported and rationalized by the existence of polar nanoregions. Moreover, the long-time variation of the electric permittivity observed in a time-dependent permittivity study is explained as an effect of polar nanoregions.<sup>114</sup> The anomaly in  $\epsilon_r$  is related to the variation of size and dynamics of polar entities, rather than to a phase transition. The temperature dependence of birefringence of BNT is rationalized by the interaction of dynamic polar regions and a nonpolar matrix, once more, implying that the BNT is indeed a relaxor.<sup>105</sup>

Although the properties of pure  $\text{Bi}_{1/2}\text{Na}_{1/2}\text{TiO}_3$  are not fully beneficial for an industrial application, BNT is an important end member of numerous solid solutions. Chemical modification of BNT leads to local inhomogeneities and local cation disorder, subsequently dictating relaxor-ferroelectric properties of such BNT compounds. Compositional modifications of BNT improve the properties like  $P_r$ ,  $k_p$ ,  $d_{33}$  and  $T_m$ , but generally yield a decay of the coercive field  $E_c$  and the depolarization temperature  $T_d$ .

Specific improvements of BNT solid solutions are achieved by different material doping using  $\text{BaTiO}_3$ ,<sup>5</sup>  $\text{La}_2\text{O}_3$ ,<sup>115</sup>  $\text{SrTiO}_3$ ,<sup>116,117,118,100,119</sup>  $\text{TaNaO}_3$ ,<sup>120</sup>  $\text{NiNbO}_3$ ,<sup>121</sup>  $\text{K}_{0.5}\text{Na}_{0.5}\text{NbO}_3$ ,<sup>92</sup>  $\text{Sc}_2\text{O}_3$ ,<sup>122</sup>  $\text{NaNbO}_3$ ,<sup>123,124,125,126</sup> or  $\text{Bi}_{1/2}\text{K}_{1/2}\text{TiO}_3$ .<sup>127,128,129,130</sup>

### 2.2.3 $\text{Bi}_{1/2}\text{Na}_{1/2}\text{TiO}_3$ -Based Pseudobinary Systems

An improvement of the functional properties of BNT with a special emphasis on the reduction of the high coercive voltage and an increase of electromechanical strain, is successfully achieved by compositional engineering. As a result, numerous BNT-based compounds have been suggested, out of which some of the most prominent pseudobinary BNT-based systems are introduced in the following section.

#### a) Barium Titanate Modification of $\text{Bi}_{1/2}\text{Na}_{1/2}\text{TiO}_3$ (BNT- $x$ BT)

The  $\text{Bi}_{1/2}\text{Na}_{1/2}\text{TiO}_3$ - $\text{BaTiO}_3$  (BNT- $x$ BT) solid solution is developed according to the concept of a morphotropic phase boundary, largely exploited in PZT-based compositions. The emergence of an MPB classifies BNT- $x$ BT among the best high-performance, lead-free piezoelectric materials.

The BNT- $x$ BT solid solution was for the first time introduced by Takenaka *et al.* in 1991<sup>5</sup> as a material that exhibits maximized dielectric permittivity, piezoelectric coefficient, and coupling factor for a specific  $x$  value. In comparison to the unmodified end members, the piezoelectric properties of BNT- $x$ BT are found to be enhanced for the compositions within the MPB region. Initially, the reason for the property enhancement was assigned to the existence of a strongly curved morphotropic phase boundary, as well as to the antiferroelectric phase above the depolarization temperature.<sup>5</sup> According to Takenaka,<sup>5</sup> the MPB forms between a BNT-rich rhombohedral and a BT-rich tetragonal phase and occurs at room temperature for  $0.6 \leq x \leq 0.7$  (Figure 2.15). Electrical measurements of Takenaka *et al.*<sup>5</sup> and Zhou *et al.*<sup>131</sup> revealed that compositions near the MPB exhibit relatively high piezoelectric properties. In fact, a piezoelectric coefficient  $d_{33}$  as high as 132 pC/N is obtained for 6 mol% BT doped BNT, whereas the piezoelectric coefficient of pure BNT is 72 pC/N.<sup>132</sup>

Hosono *et al.*<sup>133</sup> reported on a maximum dielectric constant and piezoelectric coupling factors of BNT- $x$ BT single crystals for  $0.05 \leq x \leq 0.09$ . Chiang *et al.*<sup>134</sup> demonstrated exceptionally high strain of 0.85 % by applying 3.8 kV/mm for a single crystal with  $x=0.055$ .

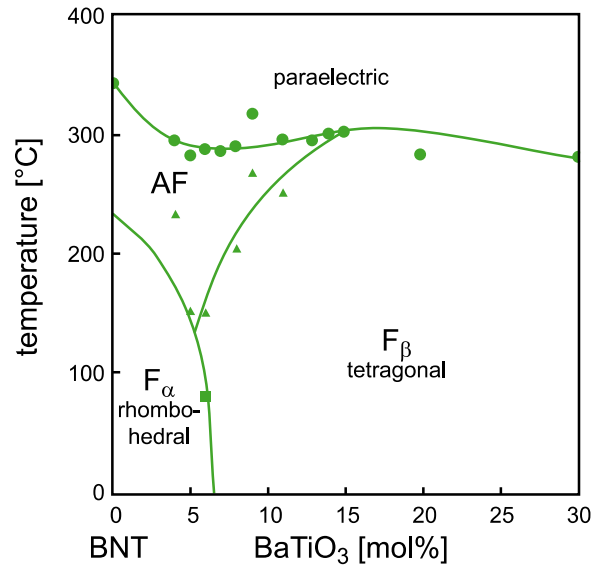


Figure 2.15: Phase diagram of BNT- $x$ BT.  $F_{\alpha}$  is the ferroelectric rhombohedral phase,  $F_{\beta}$  is the ferroelectric tetragonal phase, whereas  $AF$  represents the antiferroelectric phase (after Ref.[5]).

Structural X-ray diffraction (XRD) studies<sup>135,136</sup> of BNT-6BT describe only minor distortions from the cubic symmetry, while TEM investigations<sup>137</sup> have found no distinguishable domain morphology. Different characterizations of BNT- $x$ BT suggested a phase transformation from the non-polar to a ferroelectric phase to occur after an electric field is applied.<sup>138,135,139</sup> Later on, the phase transition and establishment of the ferroelectric phase was confirmed by acoustic emission measurements.<sup>140</sup> A neutron diffraction study of Simons *et al.*<sup>141</sup> revealed a field-induced phase transformation from the near-cubic state with weak tetragonal and rhombohedral distortions and according  $a^0a^0c^+$  and  $a^-a^-a^-$  octahedral tilting systems to a rhombohedral phase with  $a^-a^-a^-$  oxygen octahedra tilting. By contrast, Daniels *et al.*<sup>139</sup> found a pseudocubic-to-tetragonal phase transition as an effect of poling. At the same time, a featureless domain structure was found to evolve into a strongly textured one, whereas *in-situ* TEM showed that a lamellar morphology forms under an applied electric field.<sup>142</sup> According to Damjanovic *et al.*,<sup>143</sup> the BNT- $x$ BT solid solution exhibits predominantly relaxor behavior with existing polar nanoregions instead of ferroelectric domains. Direct evidence of polar nanoregions lies in the frequency dispersion of the dielectric permittivity maximum observed for compositions with  $0.07 \leq x \leq 0.09$  at and beyond ambient temperature. Several phase diagrams for BNT- $x$ BT material were proposed.<sup>148,149,5</sup> These phase diagrams are generally generated for poled BNT- $x$ BT. As pointed out by

Hiruma *et al.*,<sup>135,150</sup> the depolarization temperature does not always comply with a phase transition. Using dielectric properties and TEM-acquired local domain morphology, Ma *et al.*<sup>151</sup> generated a phase diagram for unpoled BNT- $x$ BT. The domain structure alters with the BT content from a complex rhombohedral pattern for  $0.04 \leq x \leq 0.06$ , over the short-range antiferroelectric

Table 2.3: Summary of properties for the BNT-based binary system BNT-xBT in the vicinity of the MPB.

$x$ [ % ]	$d_{33}$ [ pC/N ]	$\varepsilon_{r,33}$	$k_p$ [ % ]	$E_c$ [ kV/mm ]	$P_{rem}$ [ $\mu\text{C}/\text{cm}^2$ ]	Ref.
6	125	n/a	55	n/a	20	[5]
6	122	n/a	29	2.88	40	[144]
6	155	n/a	36	3.41	38.8	[145]
6	155	826	37	3.41	38.8	[146]
8	143	1099	23	2.92	38.7	[146]
7.5	186	990	56	2.5	22	[147]

ordered  $P4bm$  nanodomains at the MPB ( $0.06 \leq x \leq 0.11$ ), to  $P4mm$  tetragonal lamellar domains for  $x$  higher than 0.11.<sup>151</sup> Further Raman scattering detected compositions with  $0.065 \leq x \leq 0.07$  to belong to the MPB.<sup>152</sup> In addition, temperature-dependent high-resolution synchrotron XRD reveals the endurance of coexisting tetragonal-rhombohedral phases up to 200 °C.<sup>153</sup> The phase diagram of BNT- $x$ BT was reported to feature ferroelectric, relaxor and several paraelectric phases.<sup>135</sup> The origin of non-polar phases is yet debatable.<sup>154</sup> For BNT- $x$ BT, nominally tetragonal and trigonal coexisting phases, both with respective polar microdomains, were detected above  $T_d$ .<sup>155,156</sup> Yet Suchanicz *et al.*<sup>157</sup> reported tetragonal polar entities embedded into a nonpolar cubic matrix. Similarly, Xu *et al.*<sup>146</sup> suggested that the deformation of slim  $P(E)$  loops at  $T > T_d$  indicates a phase mixture with both polar and non-polar regions. Table 2.3 summarizes the properties reported for several BNT- $x$ BT compositions.

### b) Bismuth Potassium Titanate Modification of $\text{Bi}_{1/2}\text{Na}_{1/2}\text{TiO}_3$ (BNT-BKT)

BNT solid solutions modified by  $\text{Bi}_{1/2}\text{K}_{1/2}\text{TiO}_3$  (BKT) were introduced by Elkechai *et al.*<sup>158</sup> Rhombohedral BNT and tetragonal BKT form BNT- $x$ BKT with an MPB existing in the compositional range  $0.08 \leq x \leq 0.3$ .<sup>158</sup> An enhancement of piezoelectric coefficients and coupling factors with respect to both end members is achieved for compositions within the MPB region.<sup>159,158,127,160,161,162</sup>

Successive structural and dielectric studies reported different BKT concentration ranges within which the MPB appears. A study of Sasaki *et al.*<sup>127</sup> identified the MPB for  $0.16 \leq x \leq 0.2$ . In contrast, X-ray and neutron diffraction techniques revealed the absence of an MPB.<sup>159</sup> Instead, a phase transition from an  $R3c$  octahedral tilted rhombohedral phase to an  $R3m$  phase with no octahedral tilting was detected at  $x=0.45$ . Further Raman scattering study showed no MPB, but the coexistence of two phase at  $0.4 \leq x \leq 0.5$  and the occurrence of an  $R3xP - P4mm$  phase transition for higher BNT concentrations,  $0.6 \leq x \leq 0.7$ . Then again, Otonicar *et al.*<sup>163</sup> reported a narrow MPB at  $0.17 \leq x \leq 0.25$ . Pronin *et al.*<sup>164</sup> reported a pseudocubic structure for

Table 2.4: Summary of properties for the BNT-based binary BNT- $x$ BKT system.

$x$	$d_{33}$	$\varepsilon_{r,33}$	$k_p$	$E_c$	$P_{rem}$	Ref.
[ % ]	[ pC/N ]		[ % ]	[ kV/mm ]	[ $\mu\text{C}/\text{cm}^2$ ]	
7.5	186	990	56	2.5	22	[147]
8	96	1800	21	n/a	n/a	[158]
16	112	630	25	4.5	65	[162]
20	134	1140	n/a	4.4	40	[163]
20	195	1734	27	2.9	37.5	[167]
20	190	954	35	n/a	n/a	[161]
20	n/a	1030	27	3	19.9	[127]
20	157	884	54	3.6	38.4	[160]
20	167	930	54	n/a	n/a	[135]
22	126	1015	n/a	3.5	35	[163]
22	192	1007	32	n/a	n/a	[161]

$0.18 \leq x \leq 0.4$  sandwiched by rhombohedral and tetragonal phases. Nonetheless, most studies agree that the morphotropic phase boundary forms in-between the rhombohedral and tetragonal phases and occurs where the two phases coexist at approximately  $x=0.2$ .<sup>163, 127, 165, 166</sup>

The BNT-0.2BKT composition benefits from the MPB in terms of a large piezoelectric coefficient  $d_{33}$ , high maximum permittivity, and the low dielectric loss minimum at  $T_m \approx 300^\circ\text{C}$ . BNT-0.2BKT also exhibits low  $T_m$  and  $T_d$  values in comparison with other compositions.<sup>163</sup> A high normalized strain  $d_{33}^*$  of 930 pm/V is claimed for the morphotropic BNT-0.2BKT composition for a maximum electric field of 9 kV/mm.<sup>135</sup> For the same material, a giant field-induced strain of 0.38% was obtained also at a relatively low electric field of 2.4 kV/mm.<sup>167</sup>

Similar to BNT- $x$ BT, the relaxor nature of BNT- $x$ BKT has been revealed by the frequency-dispersed dielectric maximum at  $T_m$  which was related with the  $\text{Na}^+$  and  $\text{K}^+$  cation disorder at the A site.<sup>163, 168, 157</sup> Raman and X-ray spectra feature a band showing a low frequency shift and diffuse scattering, respectively, conditioned by the A-cation displacement and the presence of nanometer-sized domains.<sup>169</sup> X-ray diffraction and Raman scattering studies of Anton *et al.* confirmed no evidences for an antiferroelectric-ferroelectric phase transition related with the anomaly in the  $\varepsilon(T)$  dependence as no structural changes have been registered.<sup>170</sup> Further TEM investigations revealed a complex domain structure consisting of textured nanoscale domains and nanometer-sized antiphase domains for the morphotropic composition with  $x=0.2$ . The relaxor nature of BNT-0.24BKT was, moreover, discussed in terms of  $P(E)$  loop constrictions correlated with the electromechanical interplay of polar and nonpolar regions.<sup>167</sup>

The properties reported for some BNT- $x$ BKT materials are summarized in Table 2.4.

## 2.2.4 Bi<sub>1/2</sub>Na<sub>1/2</sub>TiO<sub>3</sub>-Based Pseudoternary Systems

### a) BNT-BT-Based Solid Solutions

In order to further enhance the electromechanical properties, in particular the field-induced strain, the BNT-*x*BT system was chemically modified by K<sub>0.5</sub>Na<sub>0.5</sub>NbO<sub>3</sub> (KNN).<sup>136</sup> High electromechanical strain as well as small remanent and negative strain were successfully achieved by doping BNT-*x*BT with a low content of orthorhombic KNN.<sup>171,172,173</sup> In fact, by applying an electric field of 8 kV/mm, an electromechanical strain of 0.45% and a  $d_{33}^* = \frac{S_{max}}{E_{max}}$  of 560 pm/V were obtained, challenging soft PZT.<sup>136</sup> Further material texturing yields a  $d_{33}$  of 479 pm/V and a strain of 0.47% at relatively low driving fields of 5 kV/mm.<sup>174</sup>

Several subsequent studies showed that a small quantity of KNN in BNT-*x*BT yields a destabilization of the field-induced long range ferroelectric order and changes the properties of undoped BNT-*x*BT from ferroelectric to relaxor.<sup>171,172,188,189,190,191,137,192</sup> For low content of KNN, ferroelectric-like square  $P(E)$  and butterfly-shaped  $S(E)$  loops are generated. Higher KNN con-

Table 2.5: Summary of properties of BNT-based ternary BNT-*x*BT-*y*X (*x,y*) systems. The field amplitude in kV/mm utilized for  $S_{max}/E_{max}$  is indicated as a corresponding footnote.

X	System	$d_{33}$ [ pC/N ]	$\epsilon_{r,33}$	$k_p$ [ % ]	$E_c$ [ kV/mm ]	$P_{rem}$ [ $\mu$ C/cm <sup>2</sup> ]	$S_{max}/E_{max}$ [ pm/V ]	Ref.
KNN	(6, 2)	30	2320	n/a	1.3	16	567 <sub>8</sub>	[137]
	(6, 1)	n/a	1370	n/a	9.7	3.7	280 <sub>5</sub>	[175]
	(6, 3)	n/a	2700	n/a	n/a	n/a	500 <sub>6</sub>	[176]
	(6, 2)	31	n/a	n/a	0.75	7	768 <sub>5</sub>	[174]
	(6, 3)	20	n/a	n/a	0.76	5.7	714 <sub>5</sub>	[174]
BZT	(6, 5)	n/a	730	n/a	3.7	36	485 <sub>5,5</sub>	[177]
BKT	(2.6, 12)	n/a	n/a	n/a	n/a	n/a	295 <sub>5</sub>	[178]
	(3.6, 8)	122	1200	30	3.6	34.4	188 <sub>8</sub>	[179]
	(3.8, 11)	220	1648	31	2.8	33.4	n/a	[180]
	(3.6, 8)	122	1200	30	3.65	34.4	188 <sub>8</sub>	[179]
	(1, 4)	191	1141	56	n/a	n/a	n/a	[181]
	(4, 8)	170	810	50	2.9	40	n/a	[182]
BZ	(6, 3)	20	n/a	10	1.5	8	542 <sub>7</sub>	[183]
	(8.5, 0.5)	147	881	n/a	2.4	16	n/a	[184]
ST	(6.5, 22)	9	2700	n/a	0.5	4	490 <sub>4</sub>	[185]
BLT	(6, 7.5)	208	1000	36	3.7	39.4	n/a	[186]
SZ	(6, 2)	197	2100	29.4	1.5	13.5	722 <sub>5,4</sub>	[187]

tents yield a decay in remanent polarization and remanent strain. Particularly high levels of usable strain  $S_{useful}$  in respect to maximum applied electric field  $E_{max}$  are obtained.

Even though some piezoactivity is detected, the crystal structure of BNT-BT-KNN is close to cubic<sup>55</sup> with a featureless domain structure<sup>137,171</sup> or consisting of nanoscopic domains.<sup>193</sup> Ferroelectric-like micron-sized domains can be induced upon poling, as it was confirmed by TEM,<sup>142,194</sup> *in-situ* diffraction,<sup>195</sup> and PFM<sup>171</sup> measurements. This finding means that the electric field triggers a phase transition from a nominally nonpolar phase to a ferroelectric phase. The mechanisms of the electric field-induced phase transition are still the subject of scientific investigations and discussions. Although the reported properties, such as the value of  $\frac{S_{max}}{E_{max}}$ , vary with chemical composition, the overall electric field response appears to be similar. Chemical additions of foreign elements contribute to the relaxor features by changing the level of random electric fields.<sup>196</sup> Similar systems with varying third end-members, such as  $\text{Bi}_{1/2}\text{K}_{1/2}\text{TiO}_3$  (BKT),  $\text{BaZrO}_3$ ,  $\text{BaHfO}_3$  (BH),  $\text{SrTiO}_3$  (ST),  $\text{Bi}_{1/2}\text{Li}_{1/2}\text{TiO}_3$  (BLT) have been suggested to improve the electromechanical properties of BNT-*x*BT, as shown in Table 2.5.

### b) BNT-BKT-Based Solid Solutions

The solid solutions of BNT-BKT with several mol% of A/B'O<sub>3</sub> perovskites resulted in strong structural changes and a change of field-dependent properties, particularly enlarged  $\frac{S_{max}}{E_{max}}$  values. The pronounced response was especially noted for  $\text{Bi}_{1/2}\text{Zn}_{1/2}\text{TiO}_3$  (BZT) modified BNT-BKT compositions.

In 5%BZT modified BNT-BKT a large  $\frac{S_{max}}{E_{max}}$  value of 547 pm/V was attained, while the 2%BZT composition exhibited an  $\frac{S_{max}}{E_{max}}$  of 500 pm/V.<sup>212,197</sup> Similar to the BNT-BT-KNN compounds, pseudocubic symmetry was found at ambient temperature and the relaxor nature was observed for BNT-BKT-BZT.<sup>198</sup> The character of the field-induced relaxor/ferroelectric phase transition changes from reversible to irreversible depending on the concentration of  $\text{Zn}^{2+}$  ions that substitute the B-site ion  $\text{Ti}^{4+}$ ,<sup>198</sup> frequency of the external electric field,<sup>212</sup> and temperature.<sup>141,198</sup> *In situ* X-ray diffraction measurements detected no structural changes related with the field-induced phase transition in BNT-BKT-BZT. In contrast, an increase of the  $\frac{1}{2}\{311\}_c$  superlattice reflection in the neutron diffraction pattern apparently revealed the phase transition. The phase diagram suggested by Patterson *et al.*<sup>197</sup> shows that BNT-BKT-BZT transforms from ferroelectric at low BZT concentration and low temperatures to a "pinched loops" phase with low  $P_{rem}$  and  $E_c$  as temperature and BZT content increase. The "pinched loops" phase resembles relaxor behavior. By 20% BZT or temperatures above 100-150 °C a transition to a pseudolinear behavior occurs followed by near-zero negative strain values and a parabolic shape of strain loops. The paraelectric phase is established at temperatures above 300-350 °C.

Additional improvement of properties was achieved also by using other chemical modifiers. An addition of 3%  $\text{CaZrO}_3$  permits an  $\frac{S_{max}}{E_{max}}$  of 617 pm/V as much as for  $\text{SrZrO}_3$  doping,<sup>209</sup> where

Table 2.6: Summary of properties for BNT-based ternary BNT- $x$ BKT- $y$ X ( $x,y$ ) system. The field amplitude in kV/mm utilized for  $S_{max}/E_{max}$  is indicated as a corresponding footnote.

X	System	$d_{33}$ [ pC/N ]	$\epsilon_{r,33}$	$k_p$ [ % ]	$E_c$ [ kV/mm ]	$P_{rem}$ [ $\mu$ C/cm <sup>2</sup> ]	$S_{max}/E_{max}$ [ pm/V ]	Ref.
BZT	(40, 5)	n/a	n/a	n/a	0.8	7	547 <sub>6</sub>	[197]
	(20, 2)	125	850	n/a	4	29	495 <sub>6</sub>	[198]
	(18, 7)	11	1200	n/a	1.2	7	385 <sub>7</sub>	[199]
BA	(25, 6)	17	1534	13.6	8.2	7.25	n/a	[200]
	(25, 8)	n/a	2200	n/a	6	8	484 <sub>6</sub>	[201]
	(22, 3)	n/a	1800	n/a	1.1	8	592 <sub>6</sub>	[202]
KNN	(6, 1)	23	n/a	4.5	3	6	217 <sub>6</sub>	[203]
	(20, 1)	n/a	n/a	n/a	0.8	6	575 <sub>8</sub>	[204]
	(20, 1)	25	1100	n/a	2	25	485 <sub>4</sub>	[205]
BMT	(22.5, 5)	n/a	n/a	n/a	1	6	570 <sub>5</sub>	[206]
	(40, 5)	n/a	1600	n/a	0.6	6	419 <sub>5</sub>	[207]
ST	(20, 5)	n/a	2400	n/a	0.6	4.6	600 <sub>6</sub>	[208]
SZ	(20, 3)	19	1850	n/a	1.5	10	617 <sub>6</sub>	[209]
BAGT	(79, 1)	160	1100	0.3	2.72	28.8	n/a	[210]
BZ	(18, 4)	n/a	1500	n/a	2	9	410 <sub>6</sub>	[211]
BLA	(22, 1)	n/a	n/a	n/a	9	1.1	579 <sub>7</sub>	[206]

incorporation of 5 % SrTiO<sub>3</sub> enables an  $\frac{S_{max}}{E_{max}}$  of 600 pm/V. A recently reported  $\frac{S_{max}}{E_{max}}$  of 930 pm/V was obtained for composites of BaTiO<sub>3</sub> and 6 % BiAlO<sub>3</sub> modified BNT-BKT.<sup>213</sup> The remarkable property enhancement of BNT-BKT has been achieved in a series of recent studies suggesting numerous ternary compounds of (1- $x$ - $y$ )BNT- $x$ BKT- $y$ X (see Table 2.6). The selected  $X$  end members were BiAlO<sub>3</sub> (BA), K<sub>0.5</sub>Na<sub>0.5</sub>NbO<sub>3</sub> (KNN), BiMg<sub>1/2</sub>Ti<sub>1/2</sub>O<sub>3</sub> (BMT), SrTiO<sub>3</sub> (ST), SrZrO<sub>3</sub> (SZ), BaTiO<sub>3</sub> (BT), BaZrO<sub>3</sub> (BZ), Bi<sub>1/2</sub>La<sub>1/2</sub>AlO<sub>3</sub> (BLA), or Bi<sub>1/2</sub>Ag<sub>1/2</sub>TiO<sub>3</sub> (BAGT).

## 2.3 Scanning Probe Microscopy

If not stated differently, the description of piezoresponse force microscopy within this chapter is based upon the book chapters by Shvartsman and Kholkin,<sup>214</sup> Ebert,<sup>215</sup> Szot,<sup>216</sup> Rodriguez,<sup>217</sup> the review articles by Kholkin *et al.*,<sup>218</sup> and Kalinin *et al.*,<sup>219</sup> and the journal articles by Kalinin,<sup>220</sup> Jesse *et al.*,<sup>221</sup> and Kalinin and Bonnell.<sup>222</sup>

Scanning Probe Microscopy (SPM) is one of the most relevant techniques of nanoscience allowing for noninvasive imaging and manipulation of the material structure on nanometer and atomic scales. Efforts to understand the material functionality and interactions employ different types of



SPM used for the characterization of electrical, topographic, magnetic, mechanical, and optical properties of the surface at the scale of several of tens of nanometers.

The working principle of SPM is based on the interaction between a scanning probe and the surface of interest. Depending on the nature of the probe-surface interaction, different response signals of different nature are measured (electric, magnetic, etc). Variations in probe-surface interactions, that is, changes in detected response signals on the surface, can be spatially resolved and mapped.

Among all SPM techniques, one of the most frequently used approaches for the sample surface investigation is the atomic force microscopy (AFM). The surface scanning methods differ depending on whether the AFM operates in contact or non-contact scanning mode. In the non-contact mode, the dominant forces are van der Waals, electrostatic, magnetic, or capillary forces. By contrast, ionic repulsion forces dominate in the contact mode. As no current between the probe and the surface of interest is necessary, AFM can be used for the characterization of non-conductive materials, such as glasses, biological materials, and ceramics. Among many others, the most commonly used AFM techniques are electrostatic force microscopy (EFM), scanning surface potential microscopy (SSPM), and piezoresponse force microscopy (PFM). Within this work, the investigation of piezoelectric materials is to a great extent performed by piezoresponse force microscopy. In the following, the basic working principles of PFM are presented.

### 2.3.1 Piezoresponse Force Microscopy

Piezoresponse force microscopy is one of the most widely used SPM techniques for local imaging of ferroelectric materials. Owing to its easy implementation, high resolution, and relative insensitivity to surface topography, PFM allows the investigation of thin films, single crystals, and polycrystalline structures in terms of selective surface poling, temporal and thermal evolution of domain morphologies, and local hysteresis measurements.

#### 2.3.1.1 Experimental Setup

A typical experimental setup of PFM is schematically shown in Figure 2.16. Beside a standard scanning probe microscope, a function generator, lock-in amplifiers, and a conductive tip are the basic components of a PFM. An alternating voltage  $V_{ac}$  is generated by the function generator and applied to the sample surface through a conductive tip, that performs as a top electrode. Based on the converse piezoelectric effect, the electric field induces deformation of the sample surface, causing cantilever deflection. The deformation of the cantilever is subsequently detected by an optical level method. This method employs a four-quadrant photodetector which captures the changes in the relative position of the laser beam that is reflected from the deflected cantilever.

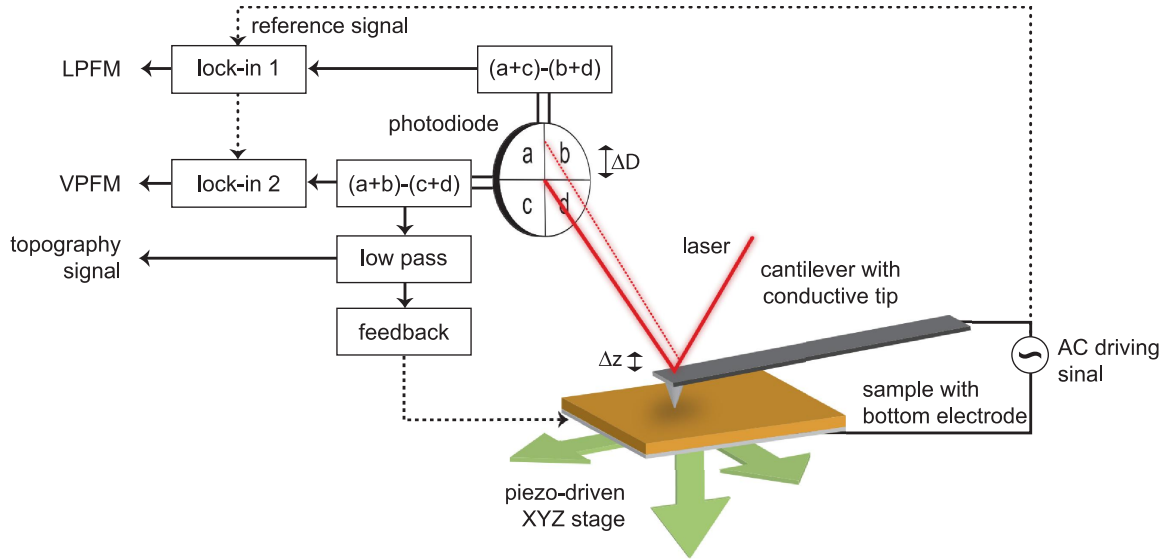


Figure 2.16: Experimental setup of piezoresponse force microscope (after Ref.[218]).

### 2.3.1.2 Physics of PFM

The mechanical motion of the PFM cantilever caused by the electric-field induced deformation of a surface is determined by two general contributions, namely the electromechanical response and the electrostatic force. The electrostatic force forms between the sample and the tip/cantilever set, whereas the electromechanical contribution is a result of converse piezoelectric and electrostrictive effects.

#### Electromechanical Forces

An applied voltage  $V_{tip}$  consists of  $dc$  and  $ac$  fractions, as defined in Equation 2.15.

$$V_{tip} = V_{dc} + V_{ac} \cdot \cos(\omega t) \quad (2.15)$$

Due to the applied electric field, a piezoelectric strain is induced in the material in accordance with the converse piezoelectric effect. The sample surface is locally displaced by  $\Delta z$ . The vertical displacement of the ferroelectric sample surface, poled along the  $z$ -direction, can be defined as

$$\Delta z = d_{33}V + \frac{M_{333}}{t}V^2. \quad (2.16)$$

Here,  $V$  is the bias voltage,  $t$  is the sample thickness,  $d_{33}$  is the piezoelectric coefficient, and  $M_{333}$  is the electrostrictive constant. Equation 2.16 defines the electromechanical response by defining the converse piezoelectric signal via the first term and the electrostrictive component of the electromechanical response by the second term.

Combining Equations 2.15 and 2.16, it follows that

$$\Delta z = \left( d_{33}V_{dc} + \frac{M_{333}}{t}(V_{dc}^2 + \frac{1}{2}V_{ac}^2) \right) + \left( d_{33}V_{ac} + 2\frac{M_{333}}{t}V_{dc}V_{ac} \right) \cos(\omega t) + \left( \frac{1}{2}\frac{M_{333}}{t}V_{ac}^2 \right) \cos(2\omega t) \quad (2.17)$$

Three different components of the surface displacement  $\Delta z$  can be distinguished. The first term in Equation 2.17 describes *dc*-part  $\Delta z_{dc}$ , whereas the second and third terms correspond to the first harmonics signal  $\Delta z_{\omega}$  and the second harmonics signal  $\Delta z_{2\omega}$ , respectively.

In contrast to the converse piezoelectric signal, the electrostrictive effect is comparably small and usually undetectable if no *dc* field is applied to the sample. Its in-field values do not influence the polarization direction imaging, but form a constant signal background.

### 2.3.1.3 PFM Imaging

The relative orientation of the spontaneous polarization vector  $\mathbf{P}$  and the vector of the applied electric field  $\mathbf{E}$  determine the sign of the converse piezoelectric signal and, finally, the contrast of corresponding PFM images.

For  $\mathbf{E}$  and  $\mathbf{P}$  vectors being parallel and of the same direction, the converse piezoelectric signal is positive and the sample surface expands locally. The applied electric field  $E$  and the first harmonic surface displacement  $z_{\omega}(t)$  are in phase,  $\varphi = 0$ . By contrast, sample contractions occur in the case of antiparallel  $\mathbf{P}$  and  $\mathbf{E}$  vectors. The phase shift between the piezoelectric signal  $z_{\omega}(t)$  and the electric field is  $\varphi = 180^\circ$ , that is, they are out of phase (Figure 2.17). Due to sample shrinking, the cantilever lowers down and the measured displacement is negative.

The phase of the electromechanical surface response,  $\varphi$ , yields information on the polarization direction under the tip. The piezoresponse amplitude,  $A = A_{\omega}/V_{ac}$  [nm/V], with  $A_{\omega}$  being the amplitude of the first harmonic response, corresponds to the local piezoelectric activity of the surface.<sup>223</sup> It strongly depends on the material properties and the tip-surface junction geometry. Moreover, the amplitude signal is greatly influenced by the long-range electrostatic forces existing at the interface between the conductive tip and the sample surface. These electrostatic forces consist of the local contribution of the tip apex and the nonlocal contribution due to the cantilever.<sup>224</sup> The PFM signal is usually represented by means of the polarization amplitude  $A$  and phase  $\varphi$ . The polarization distribution can be also mapped in a vector form using vector PFM imaging mode. A local spontaneous polarization with an arbitrary vector direction provokes the cantilever to move along with the vertical or a shear deformation of the sample at the same time.<sup>225</sup> An in-plane sample surface displacement occurs when a bias voltage is applied to the surface which is locally in-plane polarized (Figure 2.18).

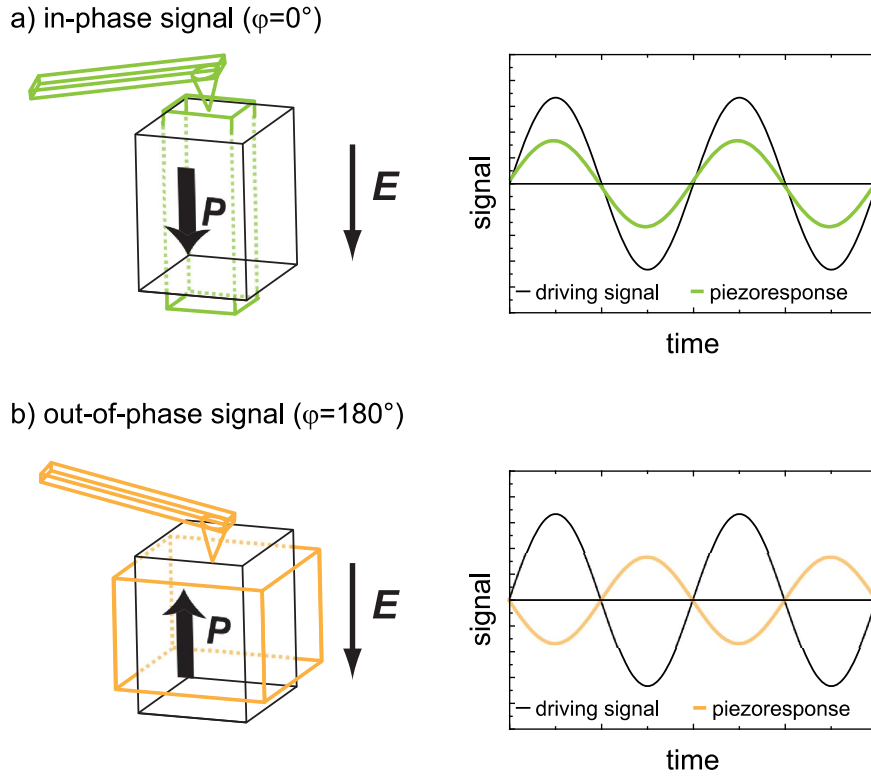


Figure 2.17: In-phase (a) and out-of phase (b) piezoresponse signal.

As mentioned, vertical surface displacement is proportional to the longitudinal piezoelectric coefficient,  $d_{33}$ . This displacement of the surface is detected as vertical PFM (VPFM) signal. A shear deformation is determined by the shear piezoelectric coefficient  $d_{51}$ . These deformations are lateral deformations which are detected as the lateral PFM (LPFM) signal. Vector PFM combines VPFM and two orthogonal LPFM signals. It is important to mention that the in-plane component of the arbitrary polarization vector is completely detected only after acquiring the LPFM signal and its orthogonal variant obtained after the sample is rotated by  $90^\circ$  around the z-axis. For the phase of  $180^\circ$  between domains of opposite polarities, the polarization distribution can be experimentally represented also as  $PR = aA_\omega \cos\varphi / V_{ac}$  in units [V]. Here,  $a$  is the calibration constant defined by the detector sensitivity and lock-in settings. The color of vector PFM maps reveals the orientation, while the intensity indicates the magnitude of the piezoelectric response.

The acquisition of amplitude and phase signals is a sensitive operational mode. By contrast, vector PFM shows good imaging stability and is, therefore, preferable for experimental use. This holds true especially for samples with a pronounced surface roughness, *e.g.*, in bulk ceramic samples with notable porosity. In general, the vertical and lateral sensitivities of a PFM are different and for their calibration several approaches have been proposed.<sup>226</sup>

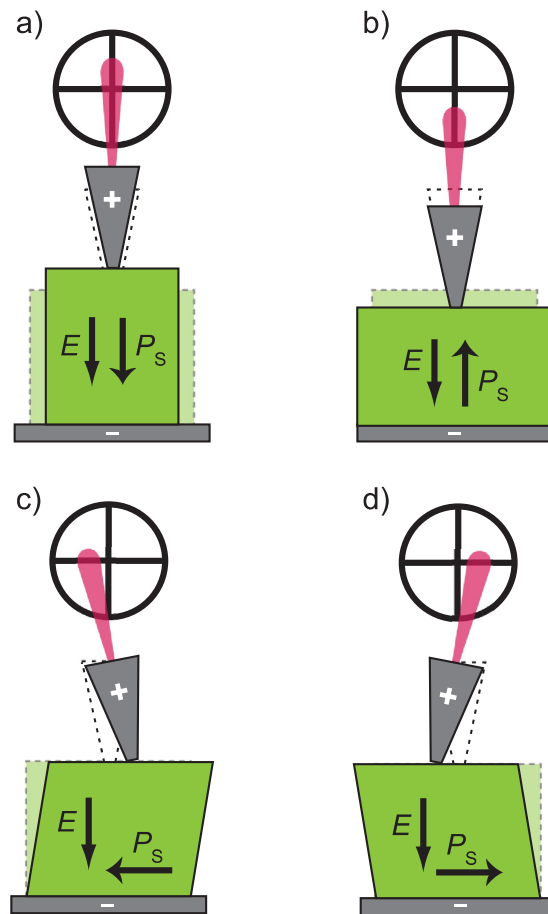


Figure 2.18: Piezoelectric effect investigated by PFM: (a) and (b) vertical cantilever displacement for parallel or antiparallel vectors of electric field and polarization; (c) and (d) in-plane displacement for perpendicular vectors of electric field and polarization (after Ref.[214]).

PFM imaging is commonly performed at driving frequencies well above the bandwidth of the topographic feedback loop ( $>1-3$  kHz) that allows that the bias-induced surface deformations are not compensated by the feedback-loop. Low-frequency PFM imaging employs frequencies from the frequency window well below the first resonant frequency of the cantilever. The high-frequency and resonance-frequency imaging, however, operate at or above the probe resonant frequencies. PFM scanning at resonant frequency yields an enhancement of weak local piezoelectric response utilizing the cantilever tip-surface contact resonance. However, the disadvantage of the resonant-frequency PFM imaging lies in tip-surface contact stiffness variations inducing a strong topographic crosstalk, causing a significant coupling between the topography and the PFM signal. Effectively, the high-resonance imaging suffers from surface-dependent frequency shifts ( $\sim 10-100$  kHz), while the driving frequency below the first resonant frequency of the tip requires comparably large driving amplitudes. To circumvent limitations of both high amplitude imaging and topographic cross-talk high frequency spectroscopy, frequency tracking methods, such as the

band excitation (BE) PFM approach were developed. More details on the operational methods of advanced BE techniques will be exposed later.

### 2.3.1.4 Dynamics of Vector PFM

The formation of a PFM image in vector PFM mode has been recently described by Jesse *et al.*<sup>227</sup> as a process that is determined by several mechanisms. Provided that the material is transversely isotropic with displacement vector and tip axis being normal to the surface, the piezoelectric response in the low-frequency regime is defined as follows.

$$PR = \frac{d_{1\omega}}{V_{ac}} = \alpha_a(h)d_{33}\frac{k_1}{k_1 + k} + \frac{C'_{sphere} + C'_{cone}}{k_1 + k}(V_{dc} - V_s) + \frac{C'_{cant}}{2k}(V_{dc} - V_{av}) \quad (2.18)$$

The electromechanical response is defined by the first term in Equation 2.18, where  $d_{33}$  is the effective piezoelectric coefficient,  $k$  is the tip-surface junction spring constant,  $k_1$  is the cantilever spring constant, and  $\alpha(h)$  is an attenuation factor describing the potential drop between the sample surface and the tip separated by the gap of height  $h$ . The attenuation  $\alpha(h)$  can be caused by, for example, an adsorbent layer on the surface of interest preventing a good tip-surface junction, the depletion phenomenon or by a subsurface layer of low permittivity. The electrostatic tip-surface contribution is described by the second term of Equation 2.18, while the third term defines the cantilever-surface interaction.  $C'_{sphere}$  and  $C'_{cone}$  are the capacitance gradients due to the spherical and conical parts of the tip, respectively, while  $C'_{cant}$  is the capacitance gradients due to the cantilever. The electrostatic effect can significantly contribute to the piezoresponse in the vicinity of the phase transition temperature in the condition of maximized dielectric permittivity. By using a stiff cantilever ( $k \gg 1$ ) and high contact forces (10-1000 nN), however, the effect of the electrostatic contribution on PFM imaging can be diminished.<sup>222</sup>

### 2.3.1.5 Piezoresponse Force Spectroscopy

PFM spectroscopy (PFM-S) is the method by which the switching behavior is probed at single positions of a sample surface. The local hysteresis loops are hereby collected by applying a sequence of *dc* voltage pulses to the sample surface through the conductive tip. An *ac* voltage is superimposed to the *dc*-bias voltage pulses in order to simultaneously measure the local piezoresponse. The operating principle of PFM spectroscopy is schematically presented in Figure 2.19. The collected hysteresis loop reflects bias-induced domain switching that occurs in the sample area below the PFM tip.

In ferroelectrics, the domain growth starts by domain nucleation after which the domain grows in all directions (Figure 2.19 (b)). Reverse bias, however, initiates a shrinking of the domain and subsequent nucleation of a domain with opposite polarity. If hysteresis loops are acquired while the *dc*-bias is switched on, the detected signal is strongly affected by the electrostatic component

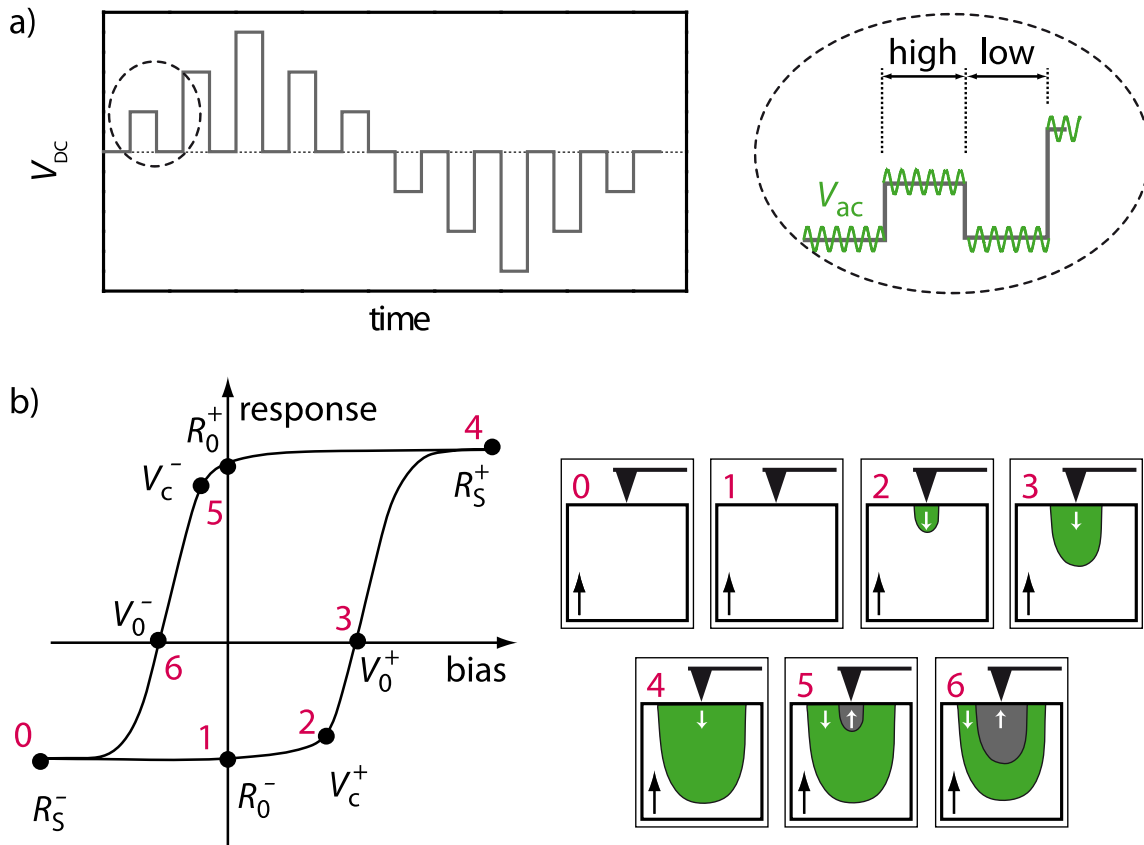


Figure 2.19: Piezoresponse force spectroscopy. (a) Bias waveform applied to the PFM tip in PFM-S mode, (b) Schematic local hysteresis loop with marked characteristic switching parameters and concurrent evolution of domain nucleation (after Ref.[229]).

due to the presence of the  $dc$ -field. Therefore, hysteresis loops collected in the off-field regime are more often considered since the electrostatic contribution is minimized.<sup>228,217</sup> The local hysteresis loops obtained in the off-field regime, however, may be linked to a relaxed state of domain polarization, as its acquisition is performed after the electric poling field is switched off. In contrast to macroscopically measured hysteresis loops, during which nucleation, growth, and interaction of multiple domain occurs, the PFM-S allows a local manipulation of polarization, that is, only at the tip-surface junction. Although fundamentally different mechanisms govern macroscopic and local PFM switching, several authors showed a good correlation between the hysteresis loops collected at different scales.<sup>230</sup> Using the first-order reversal curve diagram approach, Ricinchi *et al.*<sup>231,232,233</sup> have recently reported that the local switching parameters can be extracted from the second derivative of the macroscopic polarization in respect to the reversal and actual electric field.

Characteristic parameters of a local hysteresis loop are marked in Figure 2.19(b). The onset of switching, *i.e.* domain nucleation below the tip, occurs at nucleation biases,  $V_c^-$  and  $V_c^+$ . The

saturated positive and negative response values of the local loop are labeled as  $R_s^+$  and  $R_s^-$ , respectively. At zero bias voltages, a remanent piezoresponse  $R_0^+$  and  $R_0^-$  remains. Forward,  $V_0^+$ , and reverse coercive,  $V_0^-$ , voltages are bias values at which piezoresponse is zero. The work of switching, *i.e.* energy losses during switching, are often defined by the area enclosed by the local hysteresis curve,  $A_s$ .

Switching spectroscopy PFM (SS-PFM) allows monitoring of spatial variability of measured local PFM loops. By SS-PFM, local hysteresis loops are collected over a spatially resolved two-dimensional grid, after which a three-dimensional data array is generated.

### 2.3.1.6 Lock-in Amplification

Lock-in amplifiers are used for the detection and acquisition of *ac* signals of very small magnitude. In PFM, the amplitude of the bias-induced local piezoelectric deformation of the surface is extremely small, on the order of a few picometers. In order to be detected, the piezoresponse signal is read out using the lock-in amplifier (LIA) technique. In addition, LIA can be successfully employed in the detection of PFM signals that are significantly smaller than the noise component. The lock-in amplifier method, also known as phase-sensitive detection (PSD) technique, allows the extraction of solely one signal component at a particular frequency of the reference signal. Thus, the noise signal, the frequency of which differs from the reference signal, is eliminated while not affecting the measured signal.

The principle working scheme of a lock-in amplifier is shown in Figure 2.20. LIA combines the response signal coming from the PFM detector and the reference signal, which is generated by the function generator of the PFM setup. In LIA, the reference *ac* signal  $S_r = R \cdot \sin(\omega_r t)$  is multiplied by the response signal  $S_s = S \cdot \sin(\omega_s t + \varphi)$ . Here,  $\omega_r$  and  $\omega_s$  are the frequencies of reference and response signals, respectively,  $S$  and  $R$  are their amplitudes, while  $\varphi$  is the phase shift of the response signal in respect to the reference signal.

The LIA combination of two signal yields the following.

$$S_{PSD} = \frac{1}{2}S \cdot R \cdot \cos[(\omega_r - \omega_s)t + \varphi] - \frac{1}{2}S \cdot R \cdot \cos[(\omega_r + \omega_s)t + \varphi] \quad (2.19)$$

As Equation 2.19 shows, PSD generates two output *ac* signals with frequencies  $(\omega_r - \omega_s)$  and  $(\omega_r + \omega_s)$ . After filtering the final signal through the low pass filters, no *ac* signal passes. However, if  $\omega_r$  and  $\omega_s$  are equal, the final signal (Equation 2.19) consists of a *dc* component and an *ac* component with a frequency  $2\omega$ . After the PSD final signal is filtered by the low-pass filter, the high frequency component is removed. The residual signal is defined as follows.

$$S_{PSD} = \frac{1}{2}S \cdot R \cdot \cos(\varphi) \quad (2.20)$$



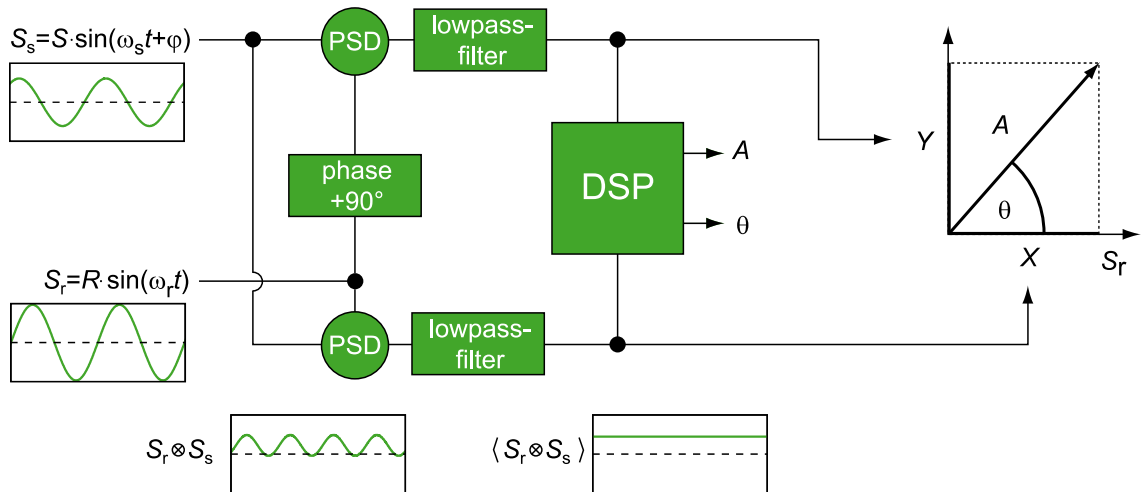


Figure 2.20: Working principle of a lock-in amplifier. The measuring signal  $S_s$  is separately multiplied with the reference signal  $S_r$ , as well as with the signal  $90^\circ$  phase shifted in respect to the reference signal. Both output signals of phase-sensitive detectors (PSD) are subsequently low-pass filtered. Two orthogonal output signals,  $X$  and  $Y$ , can be used for generating phase  $\varphi$  and amplitude  $A$  signals. DSP stands for digital signal processing (after Ref.[234]).

Finally, several signals can be generated at the output of the LIA.  $X$  is one of the output signals and is defined by Equation 2.20, while the generated  $Y$  signal is phase shifted by  $90^\circ$  with respect to  $X$ . For the  $Y$  signal it applies  $Y = S \cdot R \cdot \cos(\varphi + \frac{\pi}{2}) = S \cdot R \cdot \sin(\varphi)$ . What is particularly important for the PFM measurements is that the signals  $X$  and  $Y$  contain information on the phase  $\varphi$  and the amplitude  $A$  of a detected signal. They can be derived according to Equation 2.21.

$$A = \sqrt{X^2 + Y^2} \quad , \quad \varphi = \arctan(Y/X) \quad (2.21)$$

It is apparent from the previous equation that the amplitude signal  $A$  can be measured as independent from the phase between reference and response signals. By filtering a noise of many frequencies with far bigger amplitudes out, the signal-to-noise ratio (SNR) is improved, since only signals with frequencies at the reference signal frequency are considered.<sup>235</sup>

### 2.3.1.7 Lateral Resolution of PFM

Due to the fact that the sample thickness (tens of micrometers) is notably larger than a tip-sample contact area (5-20 nm), the electric field beneath the PFM conductive tip is strongly inhomogeneous and yields a piezodeformation of a very small volume below. Therefore, the PFM technique detects the signal with a high spatial resolution. Kalinin *et al.*<sup>220</sup> analyzed the resolution of the PFM using the transfer function approach. The measured image  $I(x)$  with  $x$  sets of spatial coordinates is defined as a convolution of an ideal image  $I_0(x - y)$  and the resolution function  $F(y)$ . If applying fast Fourier transform (FFT) for the equivalent of  $I(t)$  in the frequency space the

following applies.

$$I(q) = I_0(q)F(q) + N(q) \quad (2.22)$$

In Equation 2.22,  $F(q)$  is the object transform function, which can be determined from the ratio of the fast Fourier transformation intensity of the experimental image and the ideal image;  $N(q)$  is the FFT of the noise function  $N(x)$  that contributes to the experimental image.

In the calibration process, if the ideal image  $I_0(q)$  is known, the object transfer function  $F(q)$  and thus the resolution function  $F(y)$  can be directly determined. Knowing the resolution function the ideal image  $I_0(x)$  for any PFM acquired image and any arbitrary sample can be determined.

While the ideal image in PFM represents the distribution of piezoelectric and stiffness constants that correlate with the domain morphology, the resolution image depends on the tip geometry, tip-surface junction conditions, and lock-in amplifiers settings. In noisy surrounding, the minimum feature size is detectable at the information limit  $N(q) = F(q)$ . Under this condition, however, the intensity of the PFM signal starts to scale with the object size that leads to the inability to resolve information about the material properties. More information on the described method can be found in Ref. [220]. In addition, the information limit of PFM is found to be significantly smaller than the resolution defined by the Rayleigh two-point resolution criterion by which two features of similar intensity can be distinguished if the intensity at the midpoint between them is less than 81% of the peak intensity.<sup>220</sup>

The resolution of the PFM was shown to depend on the tip size and sample properties such as thickness, tip material etc.<sup>236</sup> By now, the domain wall thicknesses measured by PFM are in-between 5 nm and 50 nm.<sup>220</sup> This is considered to reflect the microscopy spatial resolution and not the real intrinsic width of a ferroelectric domain wall, estimated to be of the order of one to two unit cells ( $\sim 1$  nm).<sup>237</sup> If using a tip with a radius of 15 nm, a domain wall thickness of only 17 nm can be detected. A domain width as small as 3 nm has been measured in the liquid environment, as an effective screening of electrostatic interaction at the tip-surface junction can be achieved in the liquid solution.<sup>238</sup>

### 2.3.2 Band Excitation Piezoresponse Force Microscopy

The main disadvantage of single frequency PFM is the fundamental inability to entirely determine the conservative and dissipative tip-surface interactions, using the four independent parameters: resonance frequency  $\omega_0$ , amplitude and phase at resonance, and the quality-factor  $Q$ . The amplitude and the phase signals depend on the driving force, the resonance frequency depends of the stiffness of the cantilever and the tip-surface force gradient, while the  $Q$ -factor corresponds to the degree of dissipation in the system. Using a lock-in amplifier, the standard single-frequency PFM allows the determination of only amplitude and phase of the cantilever at the drive frequency.

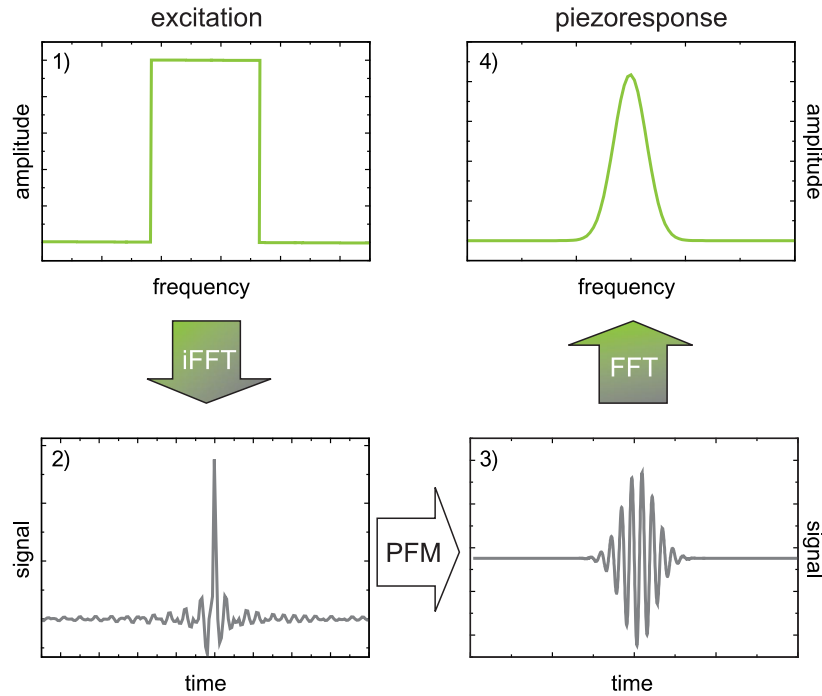


Figure 2.21: Schematic representation of band excitation piezoresponse force microscopy (after Ref.[239]).

Hence, the complete determination of the system response is limited. By using the band excitation piezoresponse force microscopy, the above-mentioned limitations can be circumvented.

Band excitation piezoresponse force microscopy utilizes resonance enhancement to trace the contact resonant frequency of the cantilever. In such a manner, BE-PFM decouples effects related to the local contact resonant frequency dependence on the sample surface condition and applied bias from a real piezoelectric response. A digitally synthesized signal with a finite spectral density in a band of frequencies centered on the predetermined cantilever resonance excites the system. The system response is simultaneously captured within the same frequency band using high speed data acquisition and then converted to the frequency domain using fast Fourier transform (Figure 2.21). The detection process is performed at each point of the scanned area. The detected data is stored in 3D  $\{A, \theta\}(x, y, \omega)$  data arrays. The amplitude and the phase of the response  $\{A, \theta\}$  and frequency  $\omega$  are detected at the spatial position  $(x, y)$ .

In contrast to the single frequency PFM where data processing is performed by the lock-in technique, BE employs data fitting in accordance with a physical model of the system. The model used to describe the cantilever dynamics under the excitation signal is the driven damped simple harmonic oscillator (SHO). The sum of the cantilever mass and acceleration is equal to the sum of

all forces on the cantilever as follows.

$$F_{driving}(t) - c \frac{dx(t)}{dt} - kx = m \frac{d^2x(t)}{dt^2} \quad (2.23)$$

The damping force is defined by the second term of Equation 2.23, where  $c$  is the damping constant and  $k$  is the cantilever stiffness used to describe elastic forces. The cantilever position depends on its deflection and is expressed by  $x$ . The driving force in PFM is defined as follows

$$F_{driving}(t) = \frac{q(t)}{d_{zz}} = \frac{C \cdot V(t)}{d_{zz}} = \beta \cdot V(t) \quad (2.24)$$

In Equation 2.24,  $q$  is the charge,  $V$  is the tip bias,  $d_{zz}$  is the material piezoelectric coefficient, and  $C$  is the tip-surface capacitance.

After Equations 2.23 and 2.24, the cantilever motion can be described by Equation 2.25.

$$m\ddot{x}(t) + c\dot{x}(t) + kx(t) = \beta \cdot V(t) \quad (2.25)$$

If this equation of motion is Fourier transformed into the frequency space and provided the interaction between tip and sample is almost linear,<sup>240</sup> the amplitude-frequency response of the cantilever in contact with the sample surface can be described as follows.<sup>241</sup>

$$A_i(\omega) = \frac{A_i^{max} \omega_{i0}^2 / Q_i}{\sqrt{(\omega_{i0}^2 - \omega^2)^2 + (\omega \omega_{i0} / Q_i)^2}} \quad (2.26)$$

In Equation 2.26,  $A_i^{max}$  is the signal at the  $i^{\text{th}}$  resonant frequency  $\omega_{i0}$  and  $Q_i$  is the Q-factor. The spatial distribution of each parameter is displayed as 2D image.

In contrast to the standard lock-in detection where the required time for the complete amplitude-frequency curve acquisition is  $NQ/\omega$ , with  $N$  being the number of frequency points, the BE method allows detection of all frequencies in parallel. The BE acquisition time depends neither on the width of the frequency band nor on the number of frequency points. This shortens the acquisition time, allows detection of relevant system response features, and accurately probes the behavior near a single resonant frequency.

### 2.3.2.1 Band Excitation Switching Spectroscopy

The mapping of polarization dynamics can be extensively explored by band excitation switching spectroscopy. This method combines the SS-PFM and BE methods, and is, therefore, named as BE SS-PFM (BEPS). The large excitation waveforms generate 4D data sets that represent 2D voltage-frequency spectra obtained for each spatial point of the 2D sample surface. Similar to PFM-S, an  $ac$  signal with a chirp pulse centered at the cantilever resonant frequency is applied

along with a *dc* train of voltage pulses of increasing magnitude. A bias-on step is used for the local polarization switching, while the system response is read-out in the bias-off state using the BE waveform. The BEPS measurements generate the amplitude  $A(\omega)$  and phase  $\theta(\omega)$  response curves acquired at each point of the sample position  $(x, y)$  as a function of the *dc* voltage magnitude,  $V_{dc}$ . The acquired data is stored in 4D data arrays of  $\{A, \theta\}(x, y, \omega, V_{dc})$ . The subsequent analysis of the 4D data sets yield the voltage dependence of material properties. The local piezoresponse,  $Q$ -factor, and resonance frequency are derived from the SHO-fits of the frequency response curve  $\{A, \theta\}(\omega)$  at each spatial and voltage point  $(x, y, V_{dc})$ . Finally, the local PFM hysteresis loops can be extracted by integrating the resonance amplitude peak. They reflect a bias-variation of the electromechanical response. After the local loop analysis, the remanent piezoresponse, nucleation and coercive voltages, and work of switching can be mapped two-dimensionally. Local maps of elastic and dissipative material properties can also be plotted if the  $Q$ -factor and the resonant frequency are bias-independent. Otherwise, the bias-dependent variations of  $Q$  and  $\omega$  within a cycle and between cycles give an access into the polarization- and voltage-related changes in local contact mechanics and dissipation.

### 2.3.2.2 First-Order Reversal Curve Band Excitation Switching Spectroscopy

First-Order Reversal Curve Band Excitation Switching Spectroscopy (FORC-BEPS) is a variant of band excitation switching spectroscopy. It probes the polarization switching mechanisms and allows an exploration of the field history of the remanent states by monitoring the evolution of the switching signal.

The FORC excitation waveform is defined as a sequence of triangular pulses with progressively increasing *dc* amplitude at a constant time interval. As for BEPS measurements, the bias pulse is used for the polarization switching and is referred to as a write-step. The response is simultaneously measured over a range of frequencies using the BE method during the interval between two pulses. This step is the read-step. The frequency band of a chirp function is, as mentioned, predefined as sufficiently broad to accommodate the variation of the contact resonance frequency of the cantilever across the surface.

In FORC, the sequence of triangular waves with different maximum amplitudes is repeated at a single point. A corresponding response for each applied waveform is recorded. When performed over a 2D grid of points, FORC-BEPS generate a 5D data set. In this case, the response depends on frequency, applied bias, the FORC sweep number (number of triangular waves), and the spatial coordinates  $(x, y)$ . A sequence of responses at a specific position at each bias point in the sweep cycle can be generated. Therefore, the output of the FORC measurements is strongly effected by the pre-existing polarization states of the material.

## 3 The Ferroelectric Properties of KNN-Based Piezoceramics

An in-depth study on lead-free potassium sodium niobate (K,Na)NbO<sub>3</sub> (KNN)-based materials performed on both the macroscopic and the microscopic scale is presented. The enhanced properties of the examined material, including high unipolar strain of 0.16 % at room temperature, high average piezoelectric coefficient  $d_{33}$  of about 300 pC/N, and enhanced local piezoelectric properties are reported and discussed. Particularly important for this class of materials is the achieved temperature stability of field-induced strain with less than 10 % value variation with increasing temperature. The piezoresponse force microscopy demonstrates the particular role of the orthorhombic-tetragonal phase transition and allows to understand mechanisms underlying the enhanced material properties in the vicinity of the transition temperature. The influence of the polymorphic phase transition is revealed. Despite its presence, a big step forward is made in the improvement of KNN-based materials and particularly of their properties employed for temperature-stable piezoelectric actuator applications.

### 3.1 Introduction

A significant contribution to the development of high-performance lead-free piezoelectrics has been made by introducing the KNN-based piezoelectric materials more than 50 years ago.<sup>64</sup> Although the pure KNN ceramics have an inferior piezoelectric coefficient  $d_{33}$  of 80 pC/N,<sup>64</sup> for the highly textured Li, Ta and Sb-doped KNN-based ceramics values as high as 416 pC/N have been reported.<sup>6</sup> This corresponds to  $d_{33}$  values obtained for soft PZT ceramics. The succeeding material studies were directed toward the doped compounds, aiming at an enhancement of  $d_{33}$ . The LiNbO<sub>3</sub>-, LiTaO<sub>3</sub>- doped solid solutions were reported to have  $d_{33}$  values between 200 pC/N and 300 pC/N.<sup>242, 70, 243</sup> The special material processing procedures yield a high  $d_{33}$  of 300 - 400 pC/N obtained at room temperature.<sup>244, 79, 245, 246</sup>

Early studies on KNN-based materials have reported that Li, Ta and Sb dopants contribute to the formation of a morphotropic phase boundary (MPB) providing a property enhancement, as known from PZT ceramics.<sup>70, 243</sup> However, later on, the property improvement has been related to the existence of a polymorphic phase transition (PPT), instead of an MPB contribution. On heating, pure KNN undergoes several phase transitions: to an orthorhombic phase at approximately room temperature, to a tetragonal phase at around 220 °C, and eventually to a cubic phase at approximately 420 °C.<sup>246</sup> According to PPT theory, the enhancement of material properties is promoted by the dopants-generated temperature shift of the orthorhombic-tetragonal phase transition  $T_{O-T}$

from 220 °C to room temperature.<sup>242,247,248,249</sup> For a KNN system with rather monoclinic than orthorhombic symmetry<sup>250,58,251,252</sup> the importance of a PPT is undeniable. As its presence may cause a strong temperature-instability of properties, a PPT is often less application favorable than an MPB.<sup>79,247,191,71</sup>

In addition to the small-signal piezoelectric coefficient  $d_{33}$ , the large-signal piezoelectric coefficient  $d_{33}^* = \frac{S_{max}}{E_{max}}$  is also considered as relevant for actuator applications. For LiSbO<sub>3</sub>-doped KNN ceramics,  $d_{33}^*$  decays significantly from 355 pm/V at room temperature (RT) to around 250 pm/V already at 50 °C, while the coupling factor,  $k_p$ , decreases linearly on sample heating.<sup>247</sup> For Li-modified KNN, Hollenstein *et al.*<sup>71</sup> reported a 30 % decay of room-temperature  $d_{31}$  and  $k_p$  values after the first heating cycle up to 140 °C.

To meet high-temperature stability requirements, two potential methods have been suggested. One includes shifting of  $T_{O-T}$  to well below room temperature by material doping,<sup>248,191,253</sup> while the other suggests synthesis of highly textured ceramics.<sup>6,98</sup> The chemical modification affords the establishment of a single tetragonal phase between room and Curie temperature. By doing so, the PPT-related problems are avoided but certain piezoactivity is sacrificed considering that some compositions perform very well at around PPT. On the other side, the complex synthesis of the highly textured KNN ceramics is not adopted to mass production due to the high costs for the texturization process. All this impedes the development of KNN-based materials with good high temperature stability of electromechanical properties.

How the local properties and dynamics contribute and determine the excellent electromechanical qualifications of (Na<sub>0.49</sub>K<sub>0.49</sub>Li<sub>0.02</sub>)(Nb<sub>0.8</sub>Ta<sub>0.2</sub>)O<sub>3</sub>-0.05CaZrO<sub>3</sub> with 2 wt% MnO<sub>2</sub> (CZ5) is investigated here by piezoresponse force microscopy. Domain structure, local piezoelectric properties, and polarization switching in the temperature range of interest are directly studied. Considering the PPT in the examined structure, a strong temperature dependence of domain morphology is expected, while the establishment of several ferroelectric states and their eventual collapse at high temperatures is hypothesized. Currently, only a few PFM studies on KNN-based materials have been carried out.<sup>254,255,256,257,258,259</sup> A recent domain imaging study of Li-, Ta-, Sb-doped KNN at room temperature has revealed the orthorhombic and tetragonal domain coexistence inside a single grain.<sup>256</sup>

Not only enhanced piezoelectric properties, but also a high temperature stability would increase the potential applicability of this KNN-based material. Therefore, in addition to room temperature macroscopic and microscopic properties, the high-temperature performance and the interrelation between macroscopic properties and locally assessed, nanoscopic characteristics are discussed.

This study has been performed in a collaboration with Prof. Dr. Ke Wang from School of Materials Science and Engineering, Tsinghua University, Beijing, China. The material synthesis and

macroscopic measurements presented below have been carried out by Prof. Dr. Ke Wang. The outcome of this study was published in two separate articles.<sup>254,260</sup>

## 3.2 Experimental Methods

### 3.2.1 Material and Sample Preparation

Ceramic samples with composition  $(1-x)(\text{Na}_{0.49}\text{K}_{0.49}\text{Li}_{0.02})(\text{Nb}_{0.8}\text{Ta}_{0.2})\text{O}_3-x\text{CaZrO}_3$  with addition of 2 wt%  $\text{MnO}_2$  were prepared in accordance with the standard oxide route. The oxides or carbonates of the respective elements, namely  $\text{NaCO}_3$  (99.5 % purity),  $\text{Li}_2\text{CO}_3$  (99.0 %),  $\text{K}_2\text{CO}_3$  (99.0 %),  $\text{Ta}_2\text{O}_5$  (99.0 %),  $\text{Nb}_2\text{CO}_5$  (99.9 %),  $\text{CaCO}_3$  (99.5 %),  $\text{ZrO}_2$  (99.5 %), and  $\text{MnO}_2$  (99.5 %) (all Alfa Aesar GmbH & Co. KG, Karlsruhe, Germany), were mixed in accordance with their stoichiometric formula. The powders were mixed with ethanol as a milling medium. The slurries were subsequently mixed in a planetary mill (Pulverisette 5, Fritsch GmbH, Idar-Oberstein, Germany) for 24 h within custom-made polyamide containers together with zirconia milling balls (Mühlheimer GmbH, Bärnau, Germany). After milling, the slurries were dried in an oven at 100 °C. In the following step, the powders were pestled and calcined for 4 h at 900 °C in covered alumina crucibles (Morgan Technical Ceramics W. Haldenwanger Technische Keramik GmbH & Co. KG, Waldkraiburg, Germany) using a box furnace (L9/KM, Nabertherm GmbH, Lilienthal, Germany). The calcined powders were once more milled afterwards for 24 h and then dried. They were manually sieved using a polymer sieve (Linker Industrie-Technik GmbH, Kassel, Germany) the mesh size of which was 160  $\mu\text{m}$ . To form the approximate sample shape, the powders were uniaxially pressed into pellets of 10 mm diameter. The sample pellets were afterwards placed into rubber sheaths which were then evacuated using a water jet pump and closed by a string. The samples were then exposed to 300 MPa of cold isostatic pressure (KIP 100E, Paul-Otto Weber GmbH, Remshalden, Germany). In the next step, the samples were sintered in air at 1080-1120 °C for 2 h using a box furnace (L16/14, Nabertherm GmbH, Lilienthal, Germany). Finally, the samples were ground down to approximately 650  $\mu\text{m}$  sample thickness. To meet requirements of PFM experiments, the surface of the sample with  $x=0.5$  (CZ5) was polished to optical quality by a polishing machine (Phoenix 4000, Jean-Wirtz GmbH & Co. KG, Düsseldorf, Germany) using polycrystalline diamond pastes (DP Paste, STRUERS GmbH, Willich, Germany) with abrasive particles of 15  $\mu\text{m}$ , 9  $\mu\text{m}$ , 3  $\mu\text{m}$ , 1  $\mu\text{m}$ , and 1/4  $\mu\text{m}$ .

### 3.2.2 X-Ray Diffraction at Room Temperature

An X-ray diffraction (XRD) pattern of the as-prepared sample was collected using a diffractometer (Rigaku, D/max 2500, Rigaku, Tokyo, Japan) with  $\text{CuK}_\alpha$  radiation with  $\lambda = 1.5405 \text{ \AA}$  measuring



in Bragg-Brentano geometry. The XRD study was performed on an unpoled bulk sample at room temperature in the  $2\theta$  range from  $20^\circ$  to  $60^\circ$  with a step width of  $0.02^\circ$ .

### 3.2.3 Temperature-Dependent Dielectric Permittivity and Losses

The temperature-dependent dielectric permittivity and dielectric losses of the poled sample were measured using an impedance analyzer (HP4192A, Hewlett Packard Japan, LTD., Kobe, Japan). A custom-built sample holder with a platinum top and bottom electrode was embedded into a box furnace (LE4/11/R6, Nabertherm GmbH, Lilienthal, Germany). The permittivity and dielectric losses were measured for temperatures up to  $450^\circ\text{C}$  at frequencies of 0.1 kHz, 1 kHz, 10 kHz, and 100 kHz with an 1 V measurement amplitude.

### 3.2.4 Temperature-Dependent Measurements of the Piezoelectric Coefficient

Before *in situ* measurement, the piezoelectric coefficient  $d_{33}$  was measured at room temperature using a Berlincourt-type quasi-static piezoelectric constant testing meter (ZJ-3A, Institute of Acoustics, Chinese Academy of Science).

The piezoelectric coefficient  $d_{33}$  as function of temperature was measured *in situ* using a custom-built apparatus that employs a laser Doppler vibrometer (OFV-505, Polytec GmbH, Waldbronn, Germany) for non-contact, interferometric displacement measurement, as shown by Figure 3.1. The sample was placed in-between a flat silver bottom electrode and a rounded top electrode, which was positioned on the sample surface using a tungsten spring. Laser light was conducted to the top electrode, the rounded silver head of which reflects the incident light on a highly polished

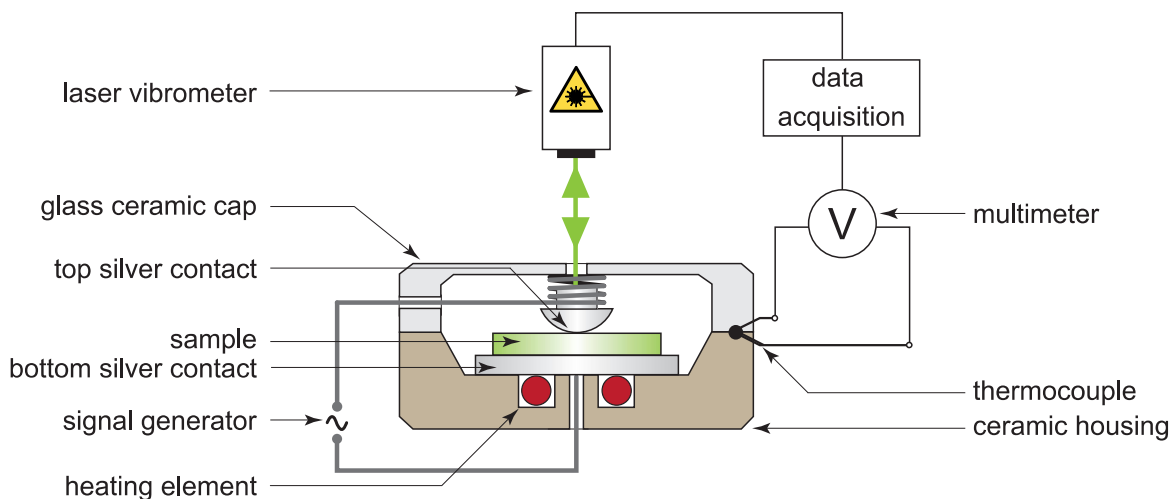


Figure 3.1: Experimental custom-built setup for *in situ* measurements of  $d_{33}(T)$ .

top surface. By this, the reflectivity necessary for interferometry was provided. The sample holder system was placed into a water-cooled furnace (TRESKOM, Institute of Physics of Condensed Systems, L'viv, Ukraine). The temperature within the furnace was regulated by a temperature controller (UTRECS K43, Institute of Physics of Condensed Systems, L'viv, Ukraine). Two thermocouples were embedded into the inner alumina part of the furnace in order to cross-check the uniformity of temperature around the sample. The laser from the vibrometer was transmitted to the sample surface through a glass window of an alumina lid.

Sample displacements were determined by the Doppler effect. The resolution of the used apparatus was limited by background noise which was  $<10$  pm. A sinusoidal AC voltage with an amplitude of  $\pm 10$  V and a frequency of 1 kHz was supplied by a functional generator (HM8131-2, HAMEG Instruments GmbH, Mainhausen, Germany). The *in situ* dielectric coefficient was acquired in the temperature range from room temperature up to 200 °C. The dielectric coefficient was computed from the measured displacement and the applied voltage.

### 3.2.5 Large-Signal Strain and Polarization as Function of Temperature

The assessed temperature dependence of the large-signal electric field-induced strain and polarization was accessed by the commercial aixPES system (aixACCT Systems GmbH, Aachen, Germany) with an integrated temperature controller. A large-signal having triangular waveform was modulated by a small-signal with a frequency of 1 kHz and an amplitude of 10 V. The polarization was measured using the virtual ground method which included an operational amplifier with a feedback resistor. Strain was measured interferometrically with a He-Ne-Laser of wavelength 633 nm. In order to measure the displacement of the sample, a mirror was placed on the sample surface using a membrane spring which was in contact with the upper electrode. As the reflectivity for interferometry was provided, the spring allowed both the displacement of the sample and the according measurements. The polarization and strain measurements were performed at temperatures increasing stepwise by 5 °C from room temperature up to 175 °C.

### 3.2.6 Transmission Electron Microscopy at Room Temperature

The sample examined by transmission electron microscopy (TEM) was mechanically polished to a thickness of about 20  $\mu\text{m}$ . The central part of the disc-shaped sample was additionally reduced by precision argon-ion milling (RES101, Leica EM, Wetzlar, Germany) at an acceleration voltage of 6 kV. The specimen was investigated using a high-resolution transmission electron microscopy (HRTEM JEOL 2011, JEOL USA, Peabody, Massachusetts, USA) operating at 200 kV and at a point resolution of 0.19 nm.

### 3.2.7 Piezoresponse Force Microscopy

Piezoresponse force microscopy was used to image and probe the local domain structure of CZ5 at room temperature as well as at elevated temperatures. The basic principles of piezoresponse force microscopy were described previously. The PFM experiments were carried out using a commercial atomic force microscopy (MFP-3D, Asylum Research, Santa Barbara, California, USA). Domain imaging was performed using single frequency PFM, by which an *ac* voltage of amplitude  $V_{ac}^+ = 5\text{--}10\text{ V}$  and frequency  $f = 50\text{ kHz}$  was applied to the sample through a conductive tip-cantilever. For this study, conductive Pt-Ir coated tip-cantilever assemblies PPP-NCHPt (Nanosensors<sup>TM</sup>, Neuchâtel, Switzerland) were used. The apex radius of the tip was less than 10 nm, with a force constant of 42 N/m and a nominal resonant frequency of about 330 kHz. The measurement frequency was chosen to be far below the resonant frequency to provide stability of the measured signals and avoid ambiguity of the experimental data.

The domain morphology at ambient temperature and its evolution with increasing temperature was imaged using vector PFM mode. Beside simultaneously recorded domain topography, two complementary PFM signals were collected, namely vertical and lateral PFM.

To study local polarization reversal, the piezoresponse hysteresis loops were measured by means of the switching spectroscopy PFM (SS-PFM) mode. In this experimental approach a train of *dc* voltage pulses with a constant duration of  $\tau_p = 100\text{ ms}$  and amplitude stepwise increasing up to 60 V and down to -60 V was applied to the PFM tip. The position of the PFM tip on the sample could be previously determined. In-between the pulses, the probing *ac* voltage was applied to record the piezoresponse which was induced by the bias voltage. Domain imaging and local polarization switching experiments were performed in the temperature range from 25 °C to 200 °C. To perform high temperature measurements, the specimen was mounted to a modular heating stage (PolyHeater, Asylum Research, Santa Barbara, California, USA), which enabled heating from ambient temperature to 250 °C. The sample was affixed to the stage using thermally conductive silver paint (Busch GmbH & Co., Viernheim, Germany) and was additionally secured using heat-isolating stage clamps. The heater stage was connected and controlled by an environmental controller (PolyHeater, Asylum Research, Santa Barbara, California, USA). The PFM data were analyzed using IgorPro (Asylum Research, Santa Barbara, CA), WSxM (Nanotec Electronica, Madrid, Spain),<sup>261</sup> and OriginLab (OriginLab Corporation, Northampton, Massachusetts, USA) software packages.

### 3.3 Experimental Results

Both macroscopic and local investigations of  $0.95(\text{Na}_{0.49}\text{K}_{0.49}\text{Li}_{0.02})(\text{Nb}_{0.8}\text{Ta}_{0.2})\text{O}_3-0.05\text{CaZrO}_3$  (CZ5) are performed in the wide temperature range from room temperature to above the Curie temperature,  $T_c=200^\circ\text{C}$ .

#### 3.3.1 Macroscopic Properties

##### 3.3.1.1 Room Temperature X-Ray Diffraction

Figure 3.2 shows the result of X-ray diffraction (XRD) performed for CZ5 confirming that the material is a solid solution with the perovskite phase structure. Beside the main reflections, small features were observed at  $2\theta \sim 20^\circ$  and  $2\theta \sim 40^\circ$ . They indicate the presence of impurities in traces related to the chemical reaction of some of the eight raw powders used for the synthesis of the material. It is important to note that at  $2\theta \cong 45^\circ$  (002) and (200) peaks of similar intensity appear. For the perovskite structure in purely tetragonal and purely orthorhombic phases the relative intensities of (002) and (200) peaks are 1:2 and 2:1, respectively. Therefore, the observation of the (002) and (200) reflections of comparable height indicates the coexistence of orthorhombic and tetragonal phases at room temperature.

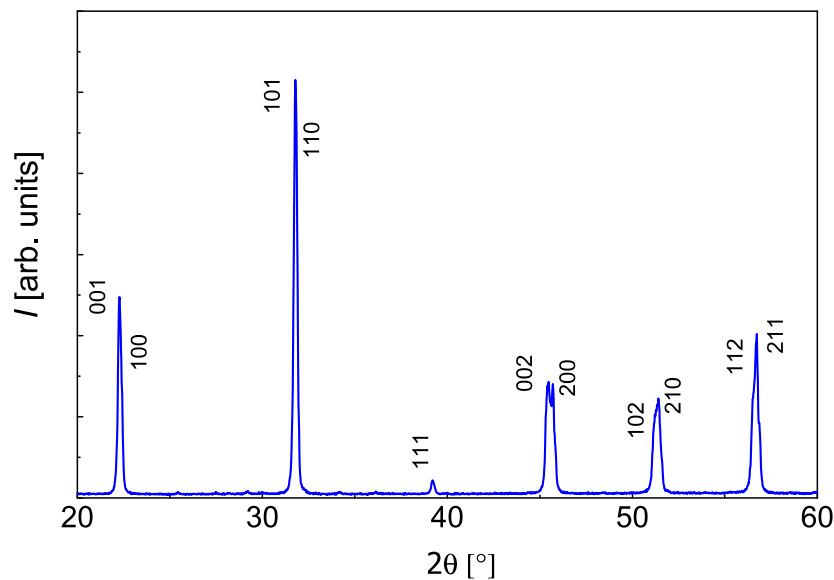


Figure 3.2: XRD diffraction pattern with intensity  $I$  as function of reflection angle  $2\theta$  for CZ5 with peak indexing adopted for a tetragonal phase (after Ref.[254]).

### 3.3.1.2 Piezoelectric and Ferroelectric Properties

Excellent piezoelectric properties are obtained for the poled CZ5 sample at room temperature. The piezoelectric coefficient  $d_{33}$  is found to be 320 pC/N, while the radial coupling coefficient is  $k_p=0.47$ . The unipolar strain  $S(E)$  as function of electric field obtained at ambient temperature is presented in Figure 3.3. For the maximum applied electric field  $E = 6$  kV/mm, a very slim strain loop with the maximum strain value of 0.16 % is observed. At all poling fields, the strain exhibits little hysteresis. The piezoelectric and electromechanical properties are comparable to soft PZT ceramics.

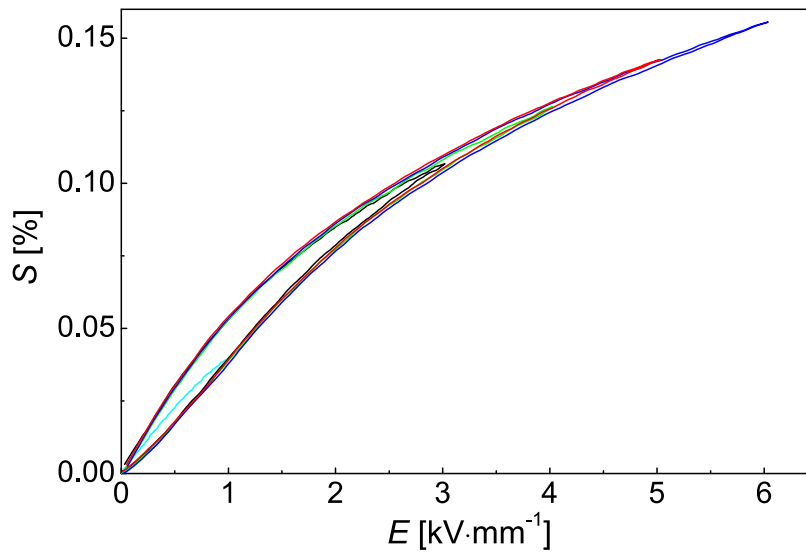


Figure 3.3: Unipolar strain as function of electric field measured at room temperature for CZ5 at a frequency of 1 Hz.

### 3.3.1.3 Temperature-Dependent Dielectric Properties

In order to identify the phase transitions in the CZ5 material, temperature-dependent dielectric permittivity measurements were performed. As shown in Figure 3.4, two anomalies are observed in both the dielectric permittivity and dielectric loss curves at around 80 °C and 192 °C. At room temperature and frequency  $f$  of 1 kHz, dielectric permittivity is measured to be 1735, while the dielectric loss tangent is 0.014.

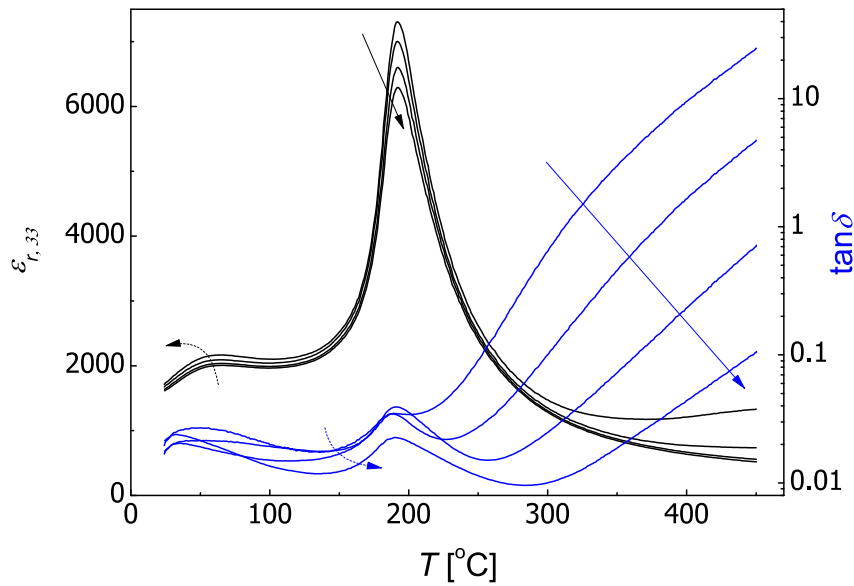


Figure 3.4: Temperature dependence of permittivity and dielectric loss for a poled CZ5 sample. The direction of solid arrows indicates increasing frequency (0.1 kHz, 1 kHz, 10 kHz, 100 kHz).

**3.3.1.4 Large-Signal Properties as Function of Temperature**

In Figure 3.5 temperature-insensitive behavior of the unipolar strain is demonstrated for temperatures between room temperature and 175 °C. In the entire temperature range, maximum strain keeps values between 0.12 and 0.13, while the generally slim loop appearance is preserved. Only

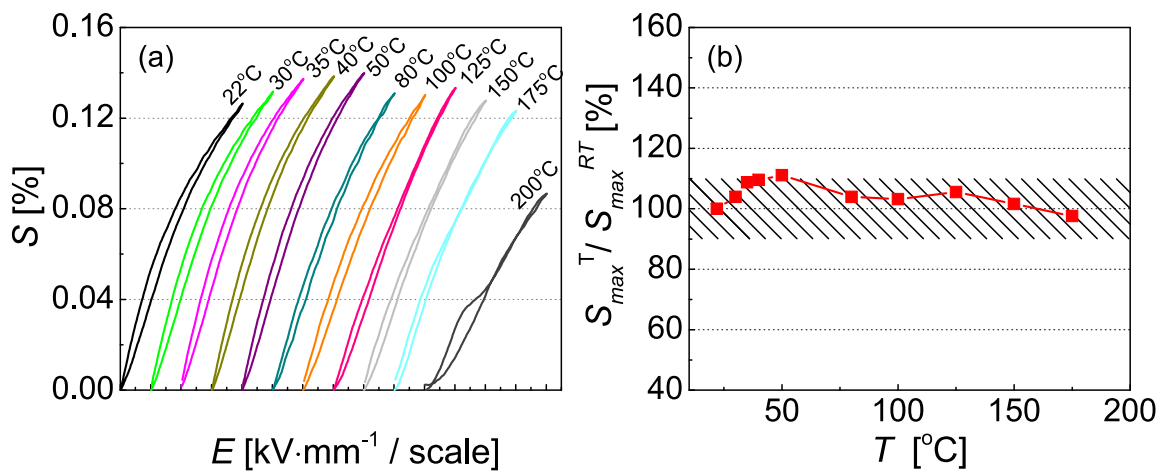


Figure 3.5: (a) Unipolar strain of CZ5 at different temperatures for an amplitude of 4 kV/mm ; (b) Temperature evolution of strain  $S_{max}^T$  normalized to its room temperature value  $S_{max}^{RT}$ .

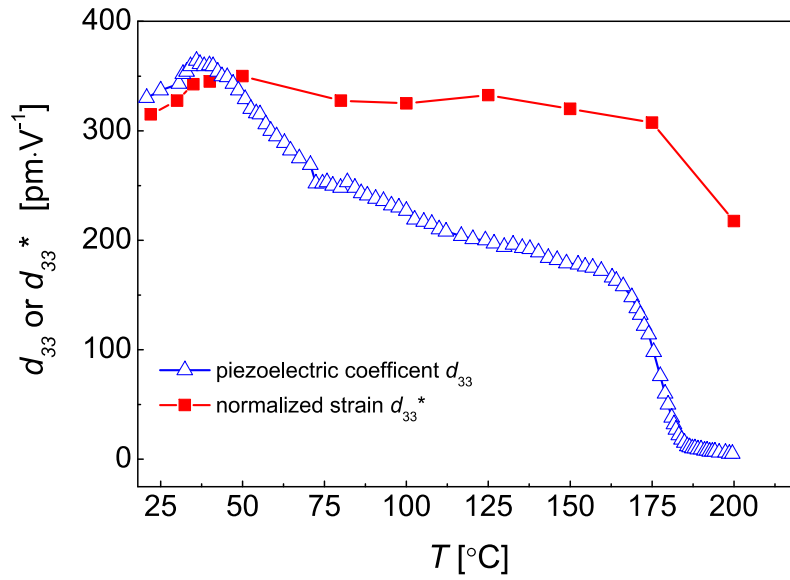


Figure 3.6: Temperature evolution of *in situ* measured small-signal  $d_{33}$  and large-signal

$$d_{33}^* = S_{max}^T / E_{max}.$$

above  $T=190^\circ\text{C}$ , the maximum strain level decays to about 0.08. Consequently, the strain normalized with its room temperature value,  $\frac{S_{max}^T}{S_{max}^{RT}}$  varies less than  $\pm 10\%$ , as marked by the shaded zone in Figure 3.5(b). All strain loops are obtained at maximum electric field amplitude  $E_{max}=4\text{ kV/mm}$ .

### 3.3.1.5 Temperature-Dependent Piezoelectric Coefficient

The temperature stability of the small-signal piezoelectric coefficient  $d_{33}$  of CZ5 is further investigated. As a matter of fact,  $d_{33}$  vs.  $T$  is rarely reported for alkali-niobate based piezoceramics due to the lack of appropriate commercial equipment.

Within this study,  $d_{33}(T)$  is measured *in situ* by a custom-designed experimental setup. At room temperature, the piezoelectric coefficient  $d_{33}$  is in the range 300-320 pm/V (Figure 3.6). These values are comparable to the room temperature value, that was mentioned previously and measured by a Berlincourt-type meter. With sample heating, the  $d_{33}(T)$  curve demonstrates an increase of  $d_{33}$  values at about  $36^\circ\text{C}$ , seen as a broad maximum peak around this temperature. At even higher temperatures,  $d_{33}$  gradually decreases to significantly lower values. In the vicinity of the Curie temperature, near-zero  $d_{33}$  values are measured.

### 3.3.2 Microscopic Properties

#### 3.3.2.1 Domain Structure at Room Temperature

In order to rationalize the superior properties that CZ5 exhibits, possibly related to the coexistence of the two phases,<sup>79</sup> the material microstructure is examined by transmission electron microscopy (TEM) and PFM. Figure 3.7 demonstrates the microstructure observed at room temperature. Both PFM and TEM studies show the presence of a complex local domain structure. The TEM measurement reveals the existence of typical stripe-like ferroelectric domains with a characteristic width of several hundred nanometers, as seen for the area (a) in Figure 3.7(a). Nanosize domains of irregular shape are sporadically distributed within some grains, as in areas (b) and (c) of Figure 3.7(a). Meanwhile, PFM demonstrates similar results. The vertical and lateral PFM images, presented by Figure 3.7(b) and (c), respectively, represent the domain structure at room temperature. Relatively large  $180^\circ$  domains are present and organized in stripe-like, quasi-periodical structures with a characteristic period of 50-100 nm (the area (d) in Figure 3.7). Nevertheless, the variations in the domain structure depend on the size of the grain. Bigger grains generally contain large, more regular domains, whereas small, irregularly shaped features are located in the fine grains.

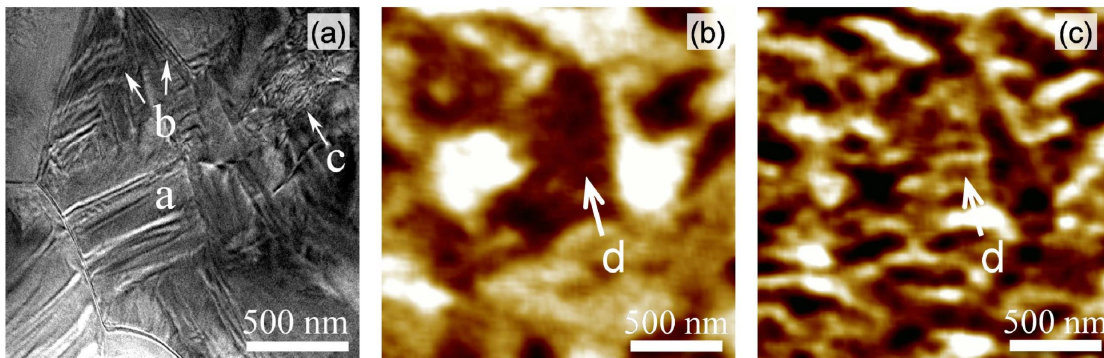


Figure 3.7: (a) TEM image, (b) vertical piezoresponse force microscopy (VPFM) image, and (c) lateral piezoresponse force microscopy (LPFM) image of CZ5 domain structure.

#### 3.3.2.2 Unpoled Domain Structure as Function of Temperature

The change in the local domain structure with an increasing temperature is examined by means of PFM. How the domain structure of unpoled CZ5 evolves with the increase of temperature from  $30^\circ\text{C}$  up to  $210^\circ\text{C}$  is shown in Figure 3.8. Both VPFM and LPFM images indicate a disordered domain structure which exhibits a strong reorganization particularly in the range between  $140^\circ\text{C}$



and 160 °C. At 160 °C, the strong changes in domain contrast are observed in both PFM images. In addition, new features of various size appear throughout the structure.

Further temperature increase, however, causes the domains to vanish, as apparent at 179 °C (Figure 3.8). At this temperature, strong PFM contrast is observed only for the larger domains, whereas almost no piezoactivity is observed for the smaller ones. Finally, at 210 °C, the overall piezoresponse is almost zero. Both VPFM and LPFM demonstrate the absence of bright and dark domain features.

### 3.3.2.3 Poled Domain Structure as Function of Temperature

The domain structure of poled CZ5 is further examined as function of temperature. It is evident that macroscopic poling influences the local domain structure. On the one side, the VPFM image shows unipolar contrast at room temperature and reveals a nearly ideal uniform poling. Its uniform contrast indicates that the domains are well aligned with respect to the poling field vector (Figure 3.9). The unipolarity of the VPFM contrast remains up to the Curie temperature. Then again, the magnitude of the VPFM signal decays as function of increasing temperature and finally completely fades away as approaching  $T_c$ .

The LPFM signal demonstrates a more peculiar domain morphology. As Figure 3.9 shows, the local domain structure experiences strong changes as the temperature increases to 127 °C. The variations in the magnitude of the piezoresponse are accomplished by the change in the sign, that is, the polarity of the local piezoresponse, in most grains. At temperatures higher than 160 °C, the contrast of the LPFM vanishes. Only small residual nanodomains around the grain boundaries are observed.

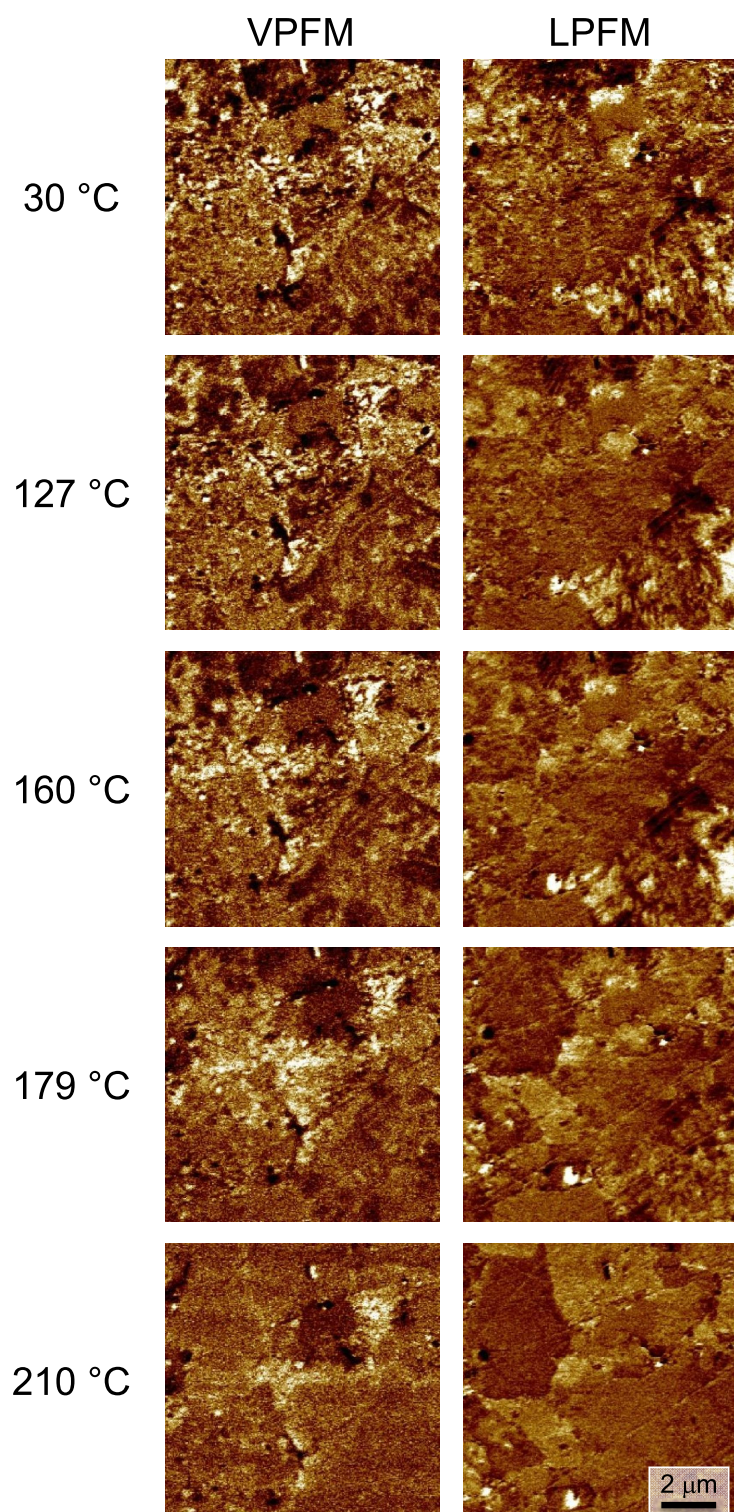


Figure 3.8: Piezoresponse force microscopy images of the unpoled CZ5 domain structure at different temperatures.

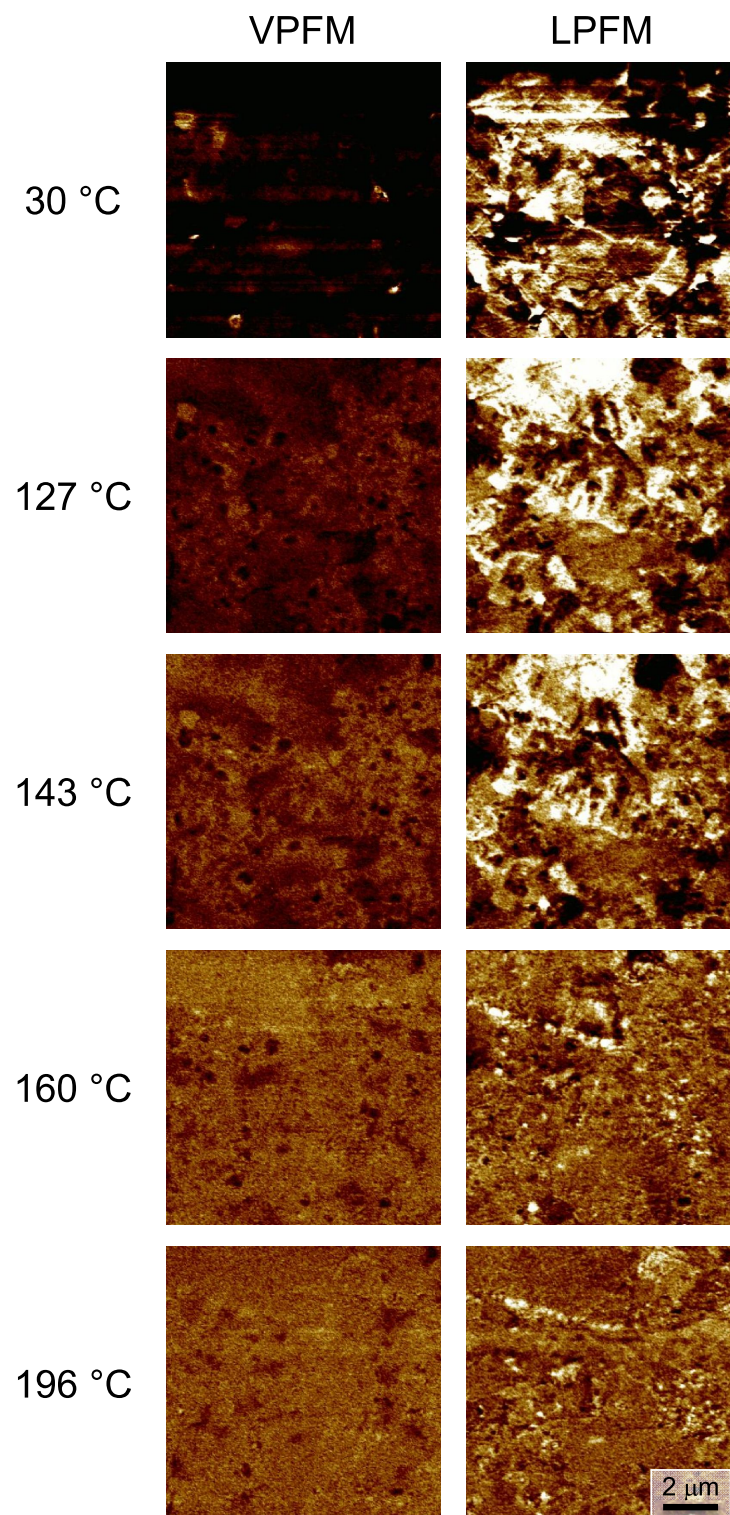


Figure 3.9: VPFM and LPFM images of the poled CZ5 sample as function of temperature. The sample was macroscopically poled in the vertical direction at room temperature using a silver-paste electrode that was removed before PFM experiments.

### 3.3.2.4 Local Switching Behavior as Function of Temperature

Local polarization switching properties are investigated by switching spectroscopy PFM. Figure 3.10 depicts the piezoresponse versus electric field captured for the CZ5 sample at characteristic temperatures. Phenomenologically similar behavior was observed for different local hysteresis loops collected within various grains of CZ5. A typical hysteresis loop obtained for CZ5 at room temperature is shown in Figure 3.10(a). During the hysteresis loop acquisition two consecutive hysteresis loops are collected at each point. As both loops demonstrate the same field dependence, only the second cycle loops are plotted. At room temperature, a typical ferroelectric, square-like hysteresis loop is obtained. The increasing positive bias voltage applied to a domain with a negative piezoresponse induces a rapid decrease of the signal magnitude. Therefore, for the applied 6 V the piezoresponse of a poled grain reaches a near-zero value. The nucleation bias is relatively small and the reverse domain nucleation occurs already at 6-7 V. The loop saturation occurs at voltages around 40 V. After the bias voltage drops to 0 V only a slight decrease of the maximum piezoresponse is achieved. This means that the polarization after removal of the electric field is comparably stable and, therefore, the remanent piezoresponse is relatively high

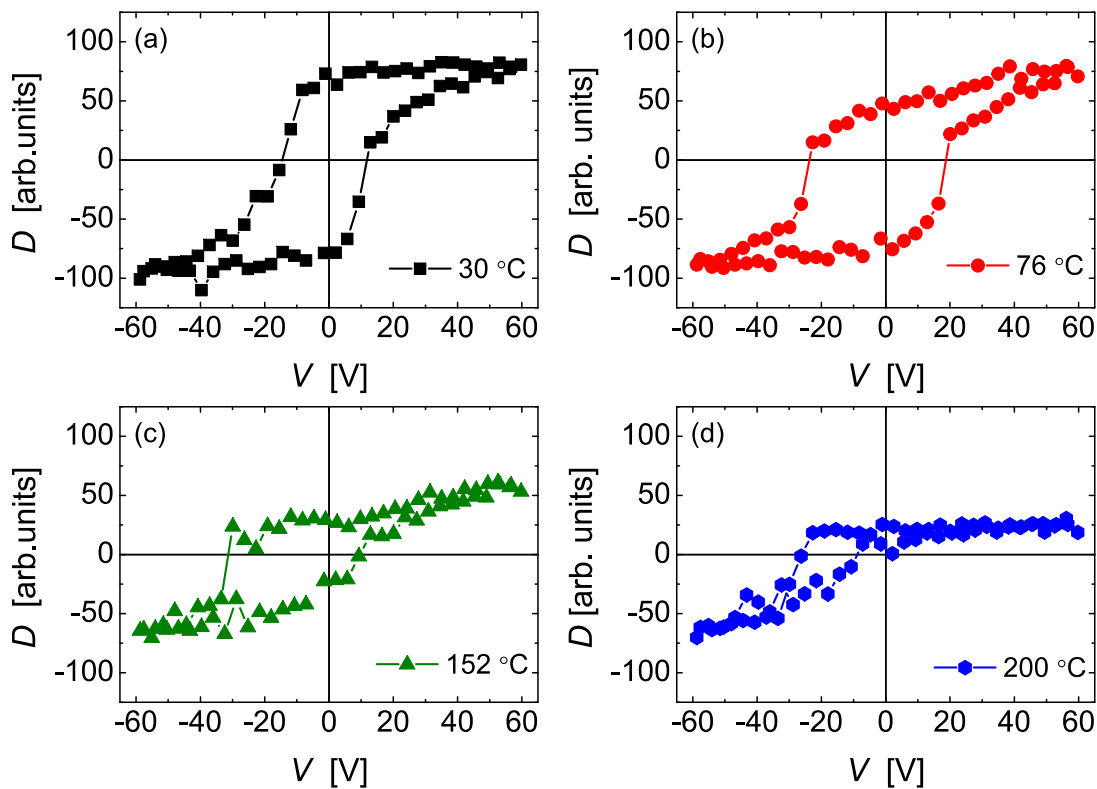


Figure 3.10: A local VPFM hysteresis loop at different temperatures at the same location of the CZ5 sample.

with respect to the piezoresponse at the maximum bias voltage. For the reverse bias voltages the piezoresponse gradually decreases and changes sign at negative biases below -15 V. The room temperature hysteresis loop is slightly asymmetric in regard to the piezoresponse axis.

With heating, the sample switching behavior changes. At 76 °C, a maximum piezoresponse is obtained, that is similar to that at room temperature. However, higher voltages are required to saturate the loop. A relatively weak decay of the piezoresponse was observed as bias voltages decrease from maximum to zero. The area enclosed within the hysteresis loop grows in total, while the loop elongates at higher voltages. A strong decay of induced polarization occurs upon further heating. The polarization loops become slimmer, while lower maximum polarization values are achieved for the same bias field amplitude. At 200 °C, a strong distortion of the hysteresis loop is observed, reflected by a decay of the maximum piezoresponse and a strong loop shift towards negative bias values.

## 3.4 Discussion

### 3.4.1 Macroscopic Properties

#### 3.4.1.1 Large-Signal Constitutive Behavior at Room Temperature

The unipolar strain of 0.16% achieved at 6 kV/mm renders the CZ5 competitive to high-performance materials, such as PZT and electrostrictive  $\text{Pb}(\text{Mn}, \text{Nb})\text{O}_3\text{-PbTiO}_3$  ceramics.<sup>262</sup> The strain loop hysteresis is smaller than that registered for the Bi-based giant strain lead-free ceramics.<sup>191</sup> The loop hysteresis, *i.e.* the area enclosed by the  $S(E)$  curve, reflects the domain wall motion at lower poling electric fields, but it is almost negligible at fields  $E \geq 5$  kV/mm. In general, the area of the loop corresponds to the dissipated energy during poling and is calculated as the integral of the loop curve  $S(E)$ . Here, the loop area is small and, therefore, the level of dissipated energy  $E_{dis}$  is low. For the current sample unipolarly loaded at 3 kV/mm, the dissipated energy is as small as 21 kJ/m<sup>3</sup>. To compare, for soft PZT the dissipated energy at the same electric loading is 26 kJ/m<sup>3</sup>, while the dissipated energy of BNT-20BKT-4BZT is as high as 61 kJ/m<sup>3</sup>.<sup>198</sup> The advantage of the small strain hysteresis, *i.e.* the low dissipated energy, of CZ5 can be used for applications that request good position accuracy and low heat generation during operation, potentially extending to the high-frequency operating range.<sup>262</sup>

#### 3.4.1.2 Large-Signal Properties as Function of Temperature

The temperature insensitive strain is inconsistent with the generally accepted hypothesis that the polymorphic phase transition impedes temperature stability in randomly oriented KNN-based ce-

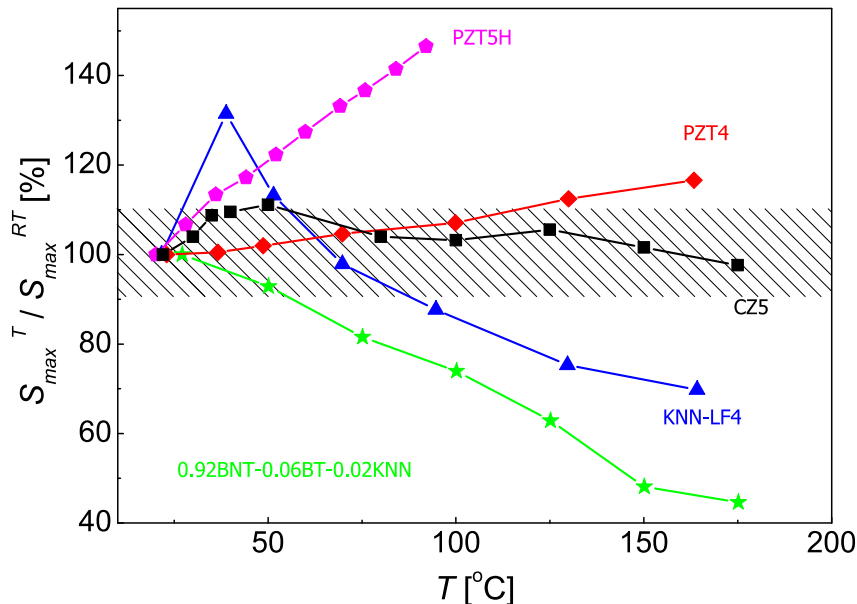


Figure 3.11: Comparison of temperature dependence of normalized strain  $S_{max}^T/S_{max}^{RT}$  for various piezoceramics. The data for PZT-5H,<sup>263</sup> PZT4,<sup>6</sup> KNN-LF4,<sup>6</sup> and BNT-BT-KNN<sup>137</sup> are plotted based on the respective references.

ramics. In CZ5, maximum strain is preserved up to 175 °C. The observed strain stability is comparable only to the strain of LF4T textured ceramics.<sup>6</sup> Figure 3.11 shows the comparison of normalized strains versus temperature for several representative piezoceramics. In respect to  $\pm 10\%$  normalized strain variation in CZ5, much stronger temperature variability has been reported for a PZT5H ceramic<sup>263</sup> with similar Curie temperature,  $T_c=200$  °C. The main disadvantage of the CZ5 system, nevertheless, is the relatively high driving field of 6 kV/mm required to obtain the high unipolar strain. In comparison, to achieve the 0.13 % strain level in PZT ceramics, an electric field of 2 kV/mm is sufficient. As demonstrated by  $\varepsilon(T)$  (Figure 3.4), CZ5 has an ideal phase structure, with small differences in the free energy between the orthorhombic and the tetragonal phase. This small free energy deviation between phases might be the cause for the diminished influence of the PPT. In addition, the temperature at which the phase transition occurs might be shifted towards lower temperatures as an effect of the applied electric field, as reported for BNT-based ceramics.<sup>264,212</sup> Moreover, the relatively high Curie temperature of CZ5 allows a stability of the tetragonal phase over a wide temperature range.

Unlike the normalized strain  $S_{max}^T/S_{max}^{RT}$ , which is rather constant up to 175 °C, the piezoelectric coefficient  $d_{33}$  on both macroscopic and microscopic scale shows a steep decay with increasing temperature. Therefore, it is important to discuss the discrepancies in the temperature stability of the normalized strain, on the one side, and  $d_{33}$  and  $D_{loc}$ , on the other side.

### 3.4.1.3 The Phenomenology of Temperature-Insensitive Strain

In order to explain the temperature insensitivity of unipolar strain, the phenomenological electrostriction relation for ferroelectrics is considered. In order to better understand this phenomenon, the polarization  $P(E)$  and bipolar strain hysteresis were measured (Figure 3.12). Figure 3.13 furthermore depicts the temperature dependence derived from the parameters of the strain and polarization hysteresis loops.

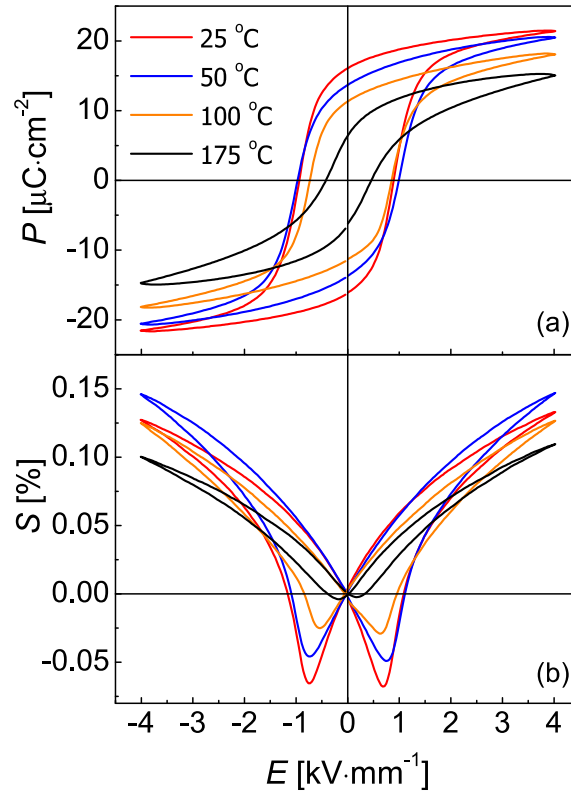


Figure 3.12: (a) Polarization and (b) bipolar strain hysteresis loops of CZ5 at different temperatures.

For tetragonal piezoelectrics,  $d_{33}$  can be defined according to the following equation.

$$d_{33} = 2Q\varepsilon_0\varepsilon_{33}P_3 \quad (3.1)$$

In Equation 3.1,  $Q$  is the electrostrictive constant which is almost invariant with temperature<sup>265</sup> and  $\varepsilon_0$  is the permittivity of vacuum,  $\varepsilon_{33}$  is the relative permittivity and, in this case, is constant below  $T_C$ , as shown by Figure 3.4. Although relation 3.1 is, strictly speaking, valid for single crystals only, it is often used to show the interrelation between the here used parameters.  $P_3$  is the polarization value along the polar axis and it is approximately of the same value as the remanent polarization  $P_{rem}$  for ferroelectric ceramics. In accordance with  $d_{33}(T)$  (Figure 3.6),  $P_3$

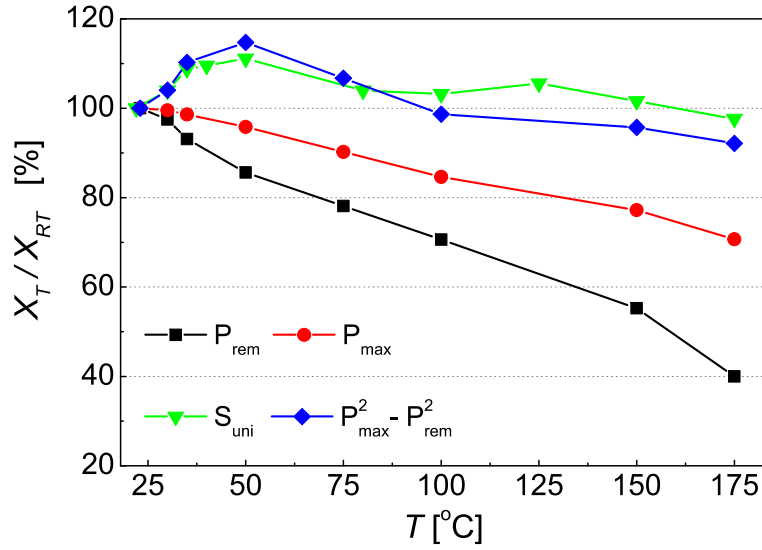


Figure 3.13: Temperature dependence of various parameters.  $X_T$  and  $X_{RT}$  correspond to  $P_{max}$ ,  $P_{rem}$ ,  $S_{uni}$  and  $P_{max}^2 - P_{rem}^2$  at temperature  $T$  and room temperature, respectively.

linearly decreases with an increasing temperature. At higher temperatures, the discrepancy between these two parameters  $P_3$  and  $P_{rem}$  becomes relevant. Then,  $P_3$ , related via Equation 3.1 to the piezoelectric coefficient  $d_{33}$ , deviates from  $P_{rem}$ , which is obtained from large-signal polarization measurements. In fact, due to thermal depoling and time-dependent relaxation,  $P_3$  drops faster than  $P_{rem}$ . As a result of the permittivity anomaly around  $T_{O-T}$ , the piezoelectric coefficient  $d_{33}(T)$  and, consequently,  $P_3(T)$  exhibits a peak. At higher temperatures,  $d_{33}(T)$  decays having a similarly decreasing trend like the remanent polarization. Eventually it suddenly drops before  $T_c$ .

The electrostrictive relation between field-induced strain  $S$  and polarization  $P$  is shown by Equation 3.2.

$$S = QP^2 \quad (3.2)$$

Apart from pure electrostrictors, this relation applies for other materials that exhibit electrostrictive behavior, including ferroelectric piezoelectrics.<sup>266</sup> The unipolar strain is defined as follows.

$$S_{uni} = S_{max} - S_{rem} \quad (3.3)$$

Combining Equations 3.2 and 3.3 yields

$$S_{uni} = QP_{max}^2 - QP_{rem}^2 = Q(P_{max}^2 - P_{rem}^2). \quad (3.4)$$

In Equation 3.4,  $P_{max}$  is the maximum value of  $P(E)$ . The values of  $P_{max}$  and  $P_{rem}$  can be extracted from experimental data shown in Figure 3.12. It is not a surprise that  $S_{uni}$  and  $P_{max}^2 - P_{rem}^2$  show the same temperature dependence. In fact, this observation confirms their relation defined before by Equation 3.4.



To summarize, the temperature-insensitive unipolar strain observed in this study is a result of the temperature-invariant difference of squared  $P_{max}$  and  $P_{rem}$  values. This applies for temperatures below the Curie point,  $T_c$ . The reduction in  $P_{max}$  with temperature can be compensated by a stronger decay of  $P_{rem}$  with temperature, resulting in the temperature-insensitive unipolar strain.

### 3.4.2 Microscopic Properties

The macroscopic properties of ferroelectric systems are strongly determined by the local domain structure. In order to understand the processes providing the property enhancement, a local investigation of the domain structure is performed. The evolution of the material piezoactivity on the local scale is observed by means of piezoelectric force microscopy. In analogy to the macroscopic approach, the domain morphology is observed at elevated temperatures. Eventually, the results of the local study are compared with the corresponding macroscopic data.

#### 3.4.2.1 Domain Structure at Room Temperature

The complex domain morphology revealed by TEM consists of stripe-like ferroelectric domains, similar to those seen in other KNN-based materials,<sup>256,72,267,268</sup> and irregular nanodomains, as observed for PZT at the MPB.<sup>269,270</sup> Similar conclusions can be derived from the nanoscopic domain features observed by PFM at room temperature. Beside theoretical evidence,<sup>271</sup> nanodomains have been reported to strongly contribute to the high piezoelectric properties of lead-based<sup>269,270,272</sup> and lead-free perovskite systems.<sup>245,70</sup>

As a matter of fact, domain size is proportional to the square root of domain wall energy,<sup>273</sup> meaning that the low domain wall energy of nanodomains allows their easy reorientation by external excitations, such as electric fields or mechanical forces. As a consequence, the piezoelectric response increases. This contributes to the enhancement of the macroscopic properties, observed as a broad peak in  $d_{33}(E)$  around room temperature.

#### 3.4.2.2 Domain Structure as Function of Temperature

The temperature-dependent investigation of the local CZ5 properties confirms the evolution of the domain structure as temperature increases. The reorganization of the domain structure is associated with the occurrence of two polymorphic phase transitions. In addition, similarities between local and macroscopic switching properties are observed. As already mentioned for poled CZ5, the strongest piezoresponse and significant rearrangement of domains occurs within the temperature range from 30 °C to 127 °C. This is followed by the changes in both the piezoresponse magnitude and its polarity in the majority of grains. At temperatures above 160 °C domains start to

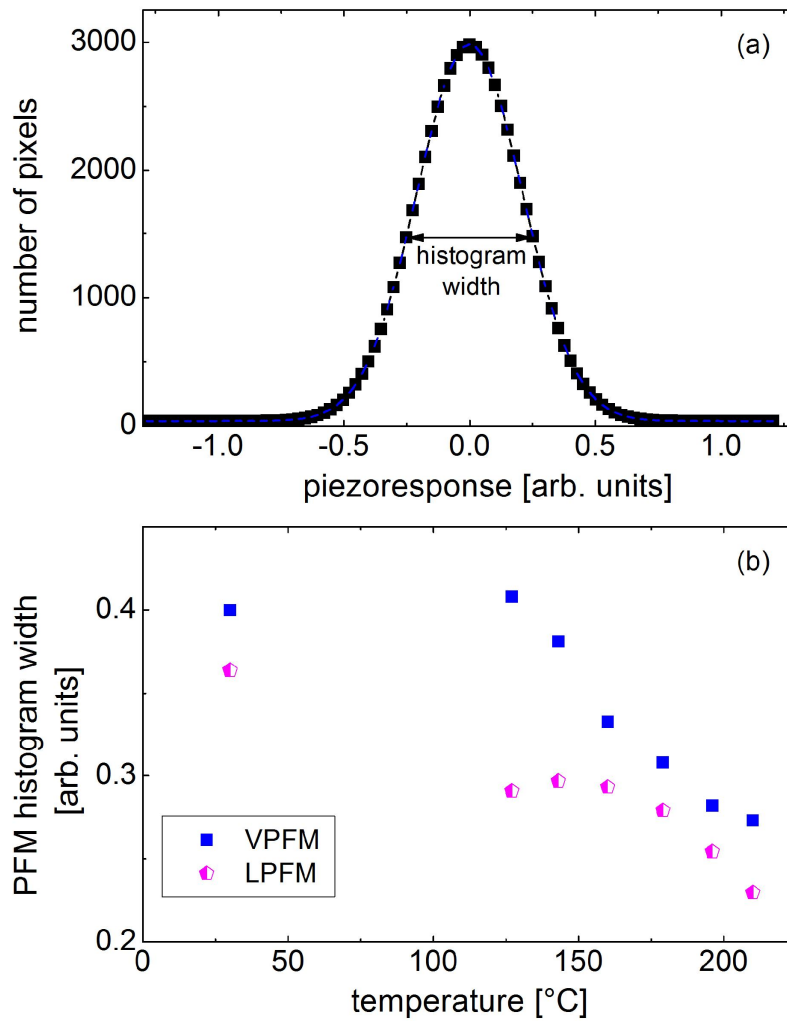


Figure 3.14: (a) A typical histogram for the VPFM signal at room temperature. (b) The width of the histograms of the VPFM and LPFM signals as function of temperature.

disappear until they finally completely vanish beyond the Curie temperature. Although the vertical component of polarization (VPFM) reveals no structural changes with increasing temperature, the in-plane polarization component rotates upon heating, as apparent in LPFM images in Figure 3.9. This polarization variation might be associated to the broad orthorhombic-tetragonal phase transition from room temperature to 80 °C.

The reorganization of the domain structure and consequential evolution of the piezoresponse with temperature can be quantified by the changes in the width of histograms of the PFM images at the respective temperatures. The histogram of the PFM image shows a statistical distribution of the measured piezoelectric signal, *i.e.* local polarization. The half-width of the histogram peak provides valuable information on the number of polarization states at the corresponding temperature.

A typical histogram of the VPFM image obtained at room temperature is shown in Figure 3.14 (a). The thermal evolution of the histogram width is depicted in Figure 3.14 (b). The narrowing of the histogram occurs after the temperature reaches approximately 120 °C, indicating the general decrease of the local piezoresponse. Some decay of the LPFM signal occurs already between room temperature and 120 °C, after which follows a similarly decaying trend as for the VPFM signal at higher temperatures.

### 3.4.2.3 The Local Piezoelectric Response as Function of Temperature

The thermal evolution of the macroscopically measured piezoelectric coefficient  $d_{33}$  is reflected in the local PFM measurements.<sup>171</sup> In order to estimate how the local piezoresponse changes with temperature, the profiling method is applied. By doing so, it is possible to calculate  $D_{loc}$ , which is directly proportional to the longitudinal piezoelectric coefficient  $d_{33}$  inside a single domain.

For CZ5, the profile method is applied to the VPFM images at different temperatures.  $D_{loc}$  is extracted for two neighboring antiparallel domains, as shown in the inset of the Figure 3.15(a).<sup>214</sup> As common for the characterization of domain interfaces in ferroelectrics, the profile of the piezoresponse is approximated by a hyperbolic tangent function, as described by Equation 3.5.

$$D(x) = D_0 + D_{loc} \cdot \tanh\left(\frac{x - x_0}{c}\right) \quad (3.5)$$

Here, the best fit parameter  $D_{loc}$  corresponds to the piezoresponse inside a single domain. Accordingly,  $D_{loc}$  is estimated for the entire temperature range. To prove consistent behavior along the entire domain structure,  $D_{loc}$  is derived for several representative domain profiles that initially demonstrated maximum VPFM signal. As shown by Figure 3.15(b),  $D_{loc}$ , that is, the local piezoresponse, decays with increasing temperature. With temperature approaching  $T_c$ , the majority of domains vanishes, which contributes to the low value of estimated local response  $D_{loc}$ .

### 3.4.2.4 Local Switching Behavior as Function of Temperature

In order to discuss local switching properties, characteristic parameters of the local hysteresis loop are labeled on a typical local hysteresis loop of CZ5 in Figure 3.16. The positive nucleation bias ( $PNB$ ) and negative nucleation bias ( $NNB$ ) are considered to correspond to the macroscopic coercive field.<sup>274</sup> At bias voltages  $V_0^+$  and  $V_0^-$ , the piezoelectric response becomes zero. In this state, the response of the newly created domains is equal to the response of still not switched volume.<sup>275</sup> The area enclosed by the local hysteresis loop,  $A_s$ , is the work of switching. The shape of local loops depends on the propagation dynamics of the switched volume underneath the PFM tip.

For the CZ5 sample, the polarization switching occurs at relatively small nucleation bias. A fast change in the piezoresponse after exceeding the nucleation bias is related to the forward and lateral

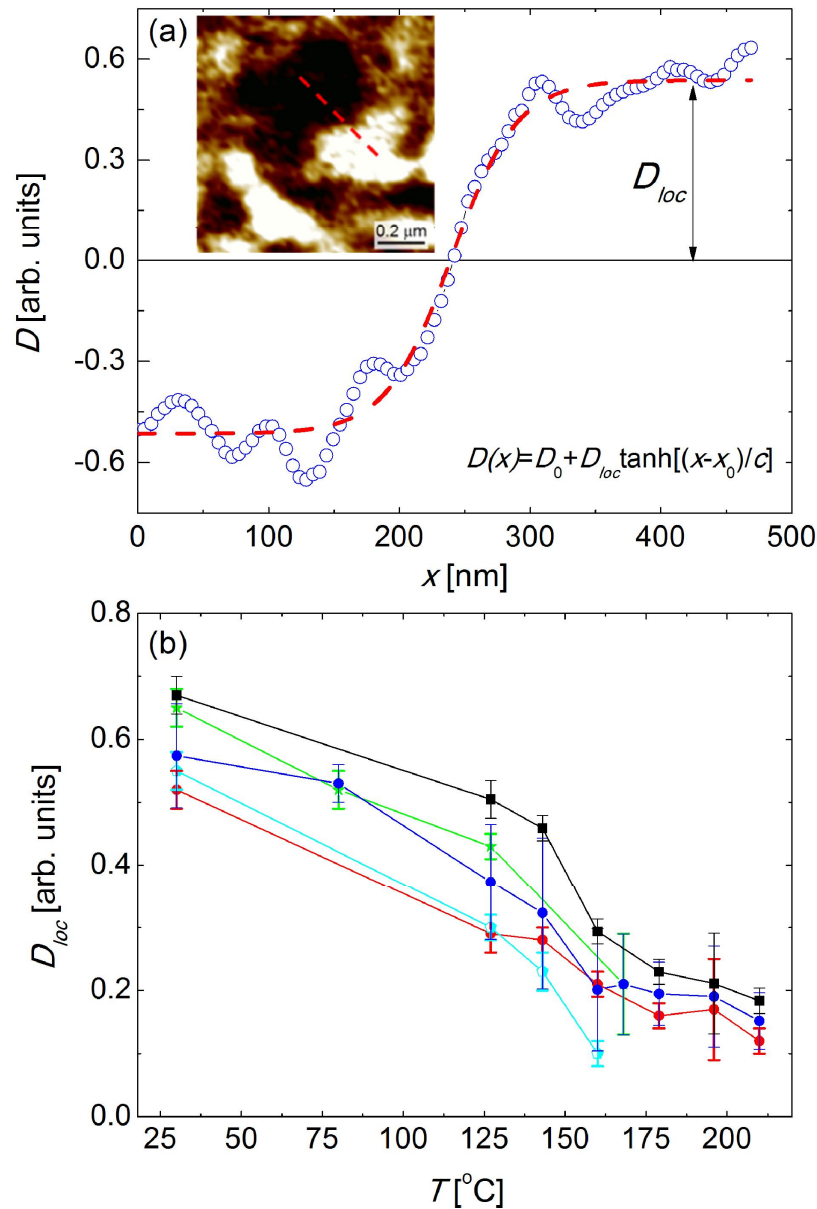


Figure 3.15: (a) The VPFM signal profile across two neighboring antiparallel domains (see inset) is approximated by a hyperbolic tangent function. Best fit (dashed line) is plotted together with experimental data (open symbols); (b) Thermal evolution of the local piezoresponse for several individual domains.

growth of the created domains, which progressively contribute to the local piezoresponse.<sup>274</sup> A weak decay of the maximum piezoresponse at decreasing bias voltages demonstrates relatively high stability of the field-induced domain.

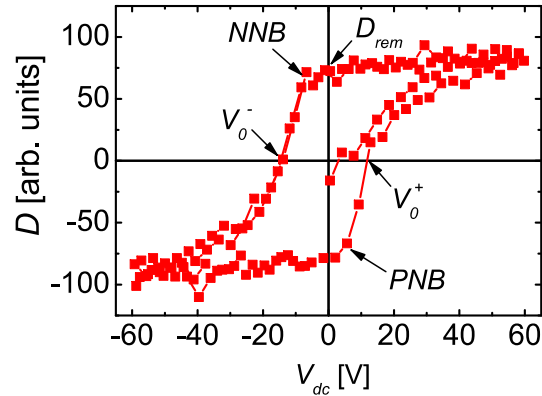


Figure 3.16: A typical hysteresis loop for CZ5 acquired at room temperature with marked parameters.

On heating, the local switching loops experience both quantitative and qualitative change. Figure 3.17 summarizes the temperature dependence of the local hysteresis parameters. The maximum piezoresponse ( $D_{max}$ ), remanent piezoresponse ( $D_{rem}$ ), work of switching ( $A_s$ ), hysteresis width ( $V_0$ ), and nucleation bias ( $NB$ ) are plotted. The maximum and remanent piezoresponse are extracted as mean values between corresponding negative and positive values. For example,  $D_{max}$  is calculated as  $D_{max} = \frac{(D_{max}^+ - D_{max}^-)}{2}$ .<sup>274</sup> Both remanent and maximum piezoresponse reach peak values at around 55 °C, while  $NB$  and  $V_0$  strongly increase at temperatures above 55 °C. These changes in the shape of the local hysteresis loops are associated with the orthorhombic-tetragonal phase transition, which, as mentioned before, occurs approximately at 65 °C.

The peak in  $D_{max}(T)$  and  $D_{rem}(T)$  at around 55 °C coincides with the anomaly seen in both  $d_{33}(T)$  and  $\varepsilon(T)$ . Beside the XRD measurements that detected orthorhombic and tetragonal phases at room temperature, the anomalies of  $d_{33}(T)$  and  $\varepsilon_{r,33}(T)$  indicate that the complete transformation to the tetragonal phase occurs at around 65 °C. Taking into consideration that the local piezoelectric coefficient is proportional to the dielectric permittivity, the anomaly in  $\varepsilon_{r,33}(T)$  mirrors an anomaly in the temperature dependence of the local piezoresponse.

The changes in the local symmetry and corresponding changes in the domain structure in this temperature range yield a modified switching kinetics. This can be observed in the remarkable broadening of the local loops for the tetragonal state. The increase in the coercive voltage upon temperature increase indicates a hardening with respect to the electric field. In addition, this hardening can be related to the smaller number of polarization variants that are available in the tetragonal phase.<sup>276</sup> The difference between temperature-dependent tendencies of coercive voltage  $V_0$  and the nucleation bias  $NB$  becomes smaller in the tetragonal phase, as shown in Figure 3.17(b). The hysteresis curve becomes steeper, implying faster propagation of the reversed domain under the tip.

At the PPT the work of switching notably increases. The increment of  $A_s$  is in principle related to the increase of pinning strength.<sup>274</sup> It was recently reported that not only the domain wall energy and spontaneous polarization of domains contribute to the shape of the local hysteresis loops, but also nucleation of new domains under the PFM tip. Provided so, it can be assumed that the nucleation of new domains contributes to the overall polarization and, consequently, to a higher maximum work of switching, remanent polarization, and maximum switchable piezoresponse.

Furthermore, the maximum switchable polarization decreases above the temperature at which the PPT occurs. This decay is in accordance with the decrease of the macroscopic piezoelectric coefficient  $d_{33}(T)$  (Figure 3.6) and with the decay of piezoresponse of the pristine domain structure,  $D_{loc}$  (Figure 3.15). The less saturated local hysteresis loops and the more pronounced difference between the maximum and remanent piezoresponse reveal an incompleteness and instability of the

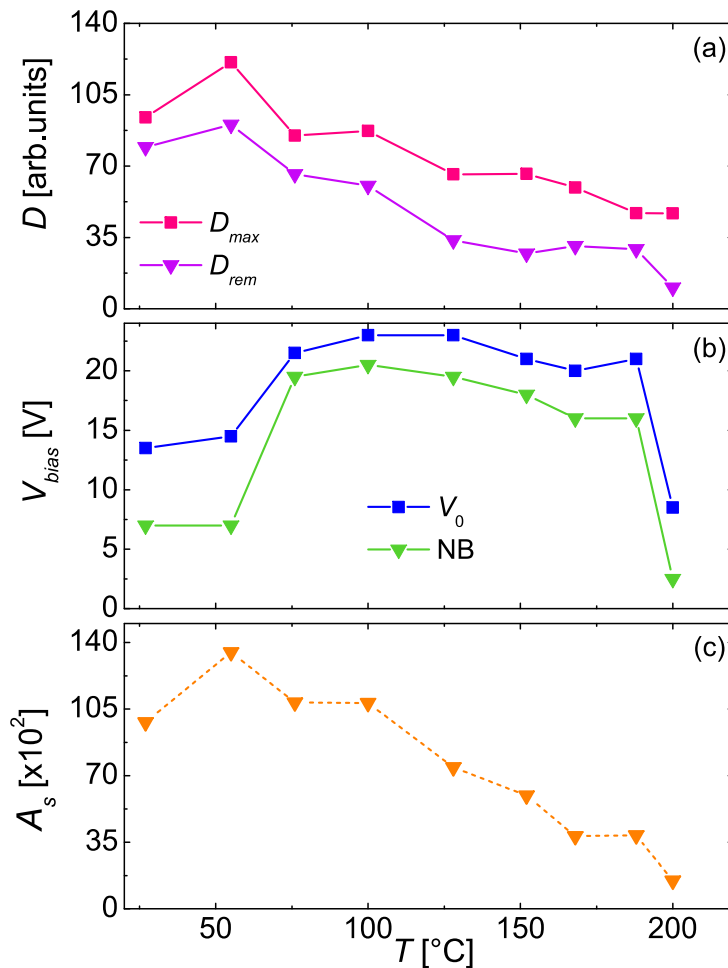


Figure 3.17: Temperature dependence of the local VPFM hysteresis loop parameters:(a) maximum and remanent piezoresponse  $D$ , (b) nucleation bias  $NB$  and loop width  $V_0$ , and (c) work of switching,  $A_s$ .

switched state. This indicates that the higher temperatures promote backswitching of the reversed domains.

At around 190 °C both  $D_{rem}$  and  $A_s$  reveal a slight peak (Figure 3.17). Similar to the anomaly in the dielectric permittivity curve at this temperature, this increase in the properties indicates the occurrence of the tetragonal-to-cubic phase transition. By this, local PFM spectroscopy confirms that the Curie temperature  $T_c$  is located at approximately 200 °C. The material becomes nonpolar which is indicated by the slimming of the local loop. While the maximum piezoresponse indicates no anomaly at this temperature, it monotonically decays starting from  $T_{O-T}$ .

Beyond the Curie temperature, the strong distortion of the hysteresis loops is manifested as a strong increase of negative asymmetry in regard to the voltage and piezoresponse axes. This loop asymmetry signifies the presence of a negative polarization offset which is induced by an internal electric field in the vicinity of the sample surface.<sup>277,278</sup> This built-in electric field may be generated by point defects accumulated at the sample surface. According to a recent study, loop shifting in ferroelectrics can be related to domain pinning caused by ionic vacancies in the perovskite structure or surface/interface defects.<sup>279,280</sup> A study of KNN-based materials has, nonetheless, suggested that the migration of highly mobile A-site vacancies<sup>244</sup> toward the sample surface is the process that generates a net positive space charge and, consequently, a large polarization field at the interface. As a consequence, a negative electric field is induced and negative domain polarization is created. Recently, a strong asymmetry of the local hysteresis loops has been reported to occur in  $Sr_{1-x}Ba_xNb_2O_6$  single crystals just above the Curie point.<sup>281</sup> It was argued that below  $T_c$  the effect of a built-in field is negligible as the long-range ferroelectric order dominates, preventing strong shifts of the hysteresis loops. In CZ5, the weak asymmetry below the Curie temperature is also observed. However, above  $T_c$ , the ferroelectric order degrades and the effect of the built-in field dominates the structure.

Finally, it would be interesting to compare the temperature dependence of properties obtained on different length scales from submicroscopic to a macroscopic one. Figure 3.18 compares the piezoelectric coefficient  $d_{33}$ , the local piezoresponse  $D_{loc}$ , and the maximum value of local hysteresis loop  $D_{max}$ . Their similar temperature trends confirm the strong correlation between microscopic and macroscopic properties. In addition, an improvement of piezoelectric properties at the orthorhombic-tetragonal polymorphic phase transition is apparent on both the macroscopic and the microscopic length scale. Finally, the monotonic decay of piezoelectricity on both scales abruptly changes as the structure transforms from tetragonal into cubic. The non-zero  $D_{loc}$  and  $D_{max}$  values at these temperatures might be rationalized by potentially incomplete depolarization of the domain structure and locally switched domains, respectively, within the experimental time range. Therefore, this comparison readily demonstrates the qualitative resemblance of the microscopic and macroscopic piezoactivity.

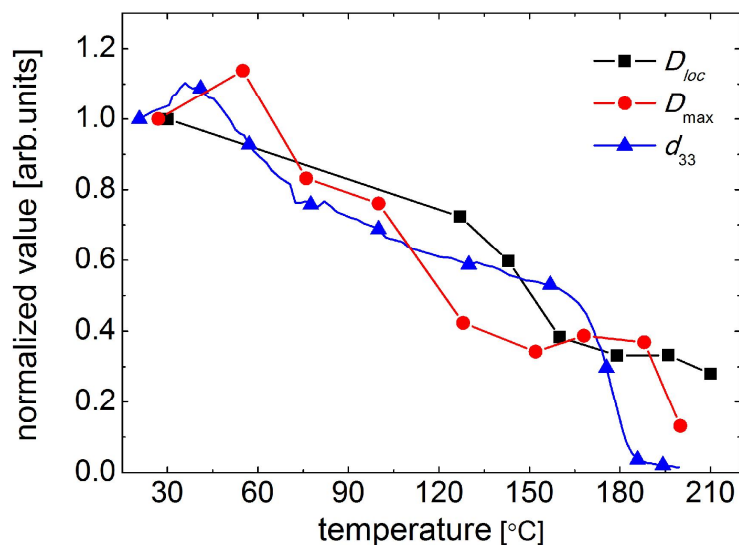


Figure 3.18: Piezoelectricity of CZ5 as function of temperature on macroscopic and microscopic length scales.

### 3.5 Summary

A new lead-free, high-performance KNN-based piezoceramic was developed with a high piezoelectric coefficient  $d_{33}$  and temperature-insensitive high unipolar strain. A maximum strain of 0.16 % is achieved at room temperature, with variation less than 10 % from 30 °C to 175 °C. The temperature stability of the unipolar strain is phenomenologically related to the temperature-stable difference of squared  $P_{max}$  and  $P_{rem}$  values. The enhanced material properties are a result of a tuned orthorhombic-tetragonal phase transition in the vicinity of room temperature.

The local PFM investigation confirms the coexistence of two ferroelectric phases at around room temperature. This is visualized by the strong PFM piezoresponse, as well as the co-presence of large, stripe-like, regular domains and small, irregularly shaped features. The increase of temperature, however, causes the rearrangement of domain morphology, related to the establishment of the tetragonal phase. Concurrently, local switching kinetics confirm that the transition to the tetragonal phase occurs with the temperature increase. Comparing to the orthorhombic phase, the nucleation of switched domains is performed at larger bias voltages and notably faster propagation of new domains is induced for the same bias field. An overall decay of piezoactivity was detected above the Curie temperature. This is evidenced as domain disappearance and the narrowing of local loops the maximum values of which are significantly lower than at lower temperatures. This study underlines the high performance of this KNN-based piezoelectric ceramic. Its excellent properties renders the investigated material as especially suitable for high-precision, temperature-stable actuator applications.



## 4 Stability of Induced Ferroelectric Order in Relaxor Ferroelectric BNT-BKT-BZT

The following chapter reports on relaxor ferroelectric  $\text{Bi}_{1/2}\text{Na}_{1/2}\text{TiO}_3\text{-}0.19\text{Bi}_{1/2}\text{K}_{1/2}\text{TiO}_3\text{-}y\text{BiZn}_{1/2}\text{Ti}_{1/2}\text{O}_3$  (BNT-BKT-BZT) ceramics with  $y=\{0.02; 0.03; 0.04\}$ . Since the reversibility of the field-induced relaxor-ferroelectric phase transition upon removal of an electric field is considered to yield outstanding electromechanical properties, its physical background is examined in terms of composition, field, and temperature on both the macroscopic and the microscopic scale. Field-dependent measurements demonstrate that an increased BZT concentration, *i.e.* a higher concentration of bivalent  $\text{Zn}^{2+}$  ions replacing the four-valent  $\text{Ti}^{4+}$  ions enhances the random electric fields and therefore ergodicity, impeding the establishment of a ferroelectric long-range order. For this reason, higher electric fields are required to induce the phase transition. An increasing temperature promotes the ergodic relaxor behavior and destabilizes the ferroelectric long-range order. At higher temperatures the initially nonergodic material demonstrates properties similar to those seen in ergodic material. The destabilization of the ferroelectric state is suggested to be a two-step process that involves an realignment of ferroelectric domains followed by their breakdown into polar nanoregions.

### 4.1 Introduction

Owing to their large electric field-induced deformation, pseudo-binary and -ternary solid solutions based on  $\text{Bi}_{1/2}\text{Na}_{1/2}\text{TiO}_3$  have been reported to provide outstanding electromechanical performance, partially competing with PZT.<sup>204, 197, 282, 202</sup> Therefore, these materials have been a subject not only of application development but also ample scientific research. The physical mechanisms yielding a large unipolar strain and its field dependence have long been discussed. Piezoresponse force microscopy studies<sup>171</sup> and diffraction methods<sup>136, 139, 141, 195, 283</sup> suggested a reversible field-induced phase transition from relaxor to ferroelectric phase, during which long-range order is established and destroyed at each field cycling.<sup>172</sup> A lack of remanence allows large strains during every cycle.<sup>197</sup>

One of the most prominent BNT-based pseudobinary solid solutions is 80BNT-20BKT which exhibits a high remanent polarization of  $0.384\text{ C/m}^2$  and good piezoelectric properties with  $d_{33} = 157\text{ pm/V}$ .<sup>160, 127</sup> After the system is modified by 4 mol%  $\text{BiZn}_{1/2}\text{Ti}_{1/2}\text{O}_3$ , a large strain is achieved upon sample poling. This class of BNT-based material was classified as a relaxor ferroelectric system that undergoes a field-induced phase transition from the relaxor state to a long-

range ordered state.<sup>198</sup> This implies that the initial polar nano-regions start growing into micron-size domains upon electric field application.

The order-disorder state is strongly conditioned by the concentration of heterovalent ions in the perovskite lattice. With increasing concentration of differently charged foreign ions distributed over equivalent crystallographic positions and consequently enhancement of random electric fields,<sup>284</sup> an initially nonergodic system evolves into an ergodic state at the same temperature. By this, the degree of nonergodicity, further discussed as  $DoN$ , may decrease.

Dittmer *et al.*<sup>198</sup> have recently shown that owing to the incorporation of  $\text{BiZn}_{1/2}\text{Ti}_{1/2}\text{O}_3$  the initially irreversible field-induced phase transition of BNT-19BKT into the ferroelectric phase comes close to a reversible transition. An influence of the chemical modification on the transition temperature at which the ergodic state evolves to a nonergodic relaxor state  $T_f$  and the degree of the nonergodicity at room temperature have been also reported.<sup>212</sup> By chemical alteration, the freezing temperature  $T_f$  can be shifted to room temperature. This is in particular beneficial for the material applicability, considering that the maximum usable strain is obtained in the vicinity of  $T_f$ .

The increasing reversibility of the field-induced phase transition, the degree of nonergodicity, and the lowering of  $T_f$  are likely entangled phenomena. Up to date, numerous questions concerning the influence of temperature and electric field on the phase transition mechanism in BNT-based relaxors have not yet been answered. It is of particular interest to assess the transition kinetics at the microscopic scale in order to allow for a better understanding of the macroscopic behavior, thus, promoting further optimization and improvement in BNT-based piezoceramics.

### Ergodicity

At this point it seems beneficial to briefly introduce the term ergodicity in more details. The term "ergodic" was derived from the Greek words for *ergon*, meaning work, and *odos* meaning path. It was introduced by Boltzmann work<sup>285</sup> in the interest to describe the energy surfaces in statistical mechanics. In the statistical frame, a process is ergodic when, under appropriate conditions, time average is equal to ensemble average. Figure 4.1 illustrates ergodicity using statistical comparisons of thrown dice. The time average, which is the average over  $6 \times 10^6$  subsequent throws of one die is equal to the ensemble average, which is the average of  $6 \times 10^6$  dice each thrown once. To have nonergodicity, however, the initial state of the  $6 \times 10^6$  dice is arranged as not random anymore. This can be achieved, for example, by having two dice faces magnetic in such a way that all "twos" are attracted by "fives" but repulsed by other "twos". By this, ergodicity is broken as the time average does not equate the ensemble average.

The concept of system ergodicity and nonergodicity has been used in solid state physics to describe the processes of magnetic spin glasses.<sup>286</sup> In these disordered systems, the system is recognized as magnetically disordered and ergodic above a temperature  $T_f$ , while at the transition

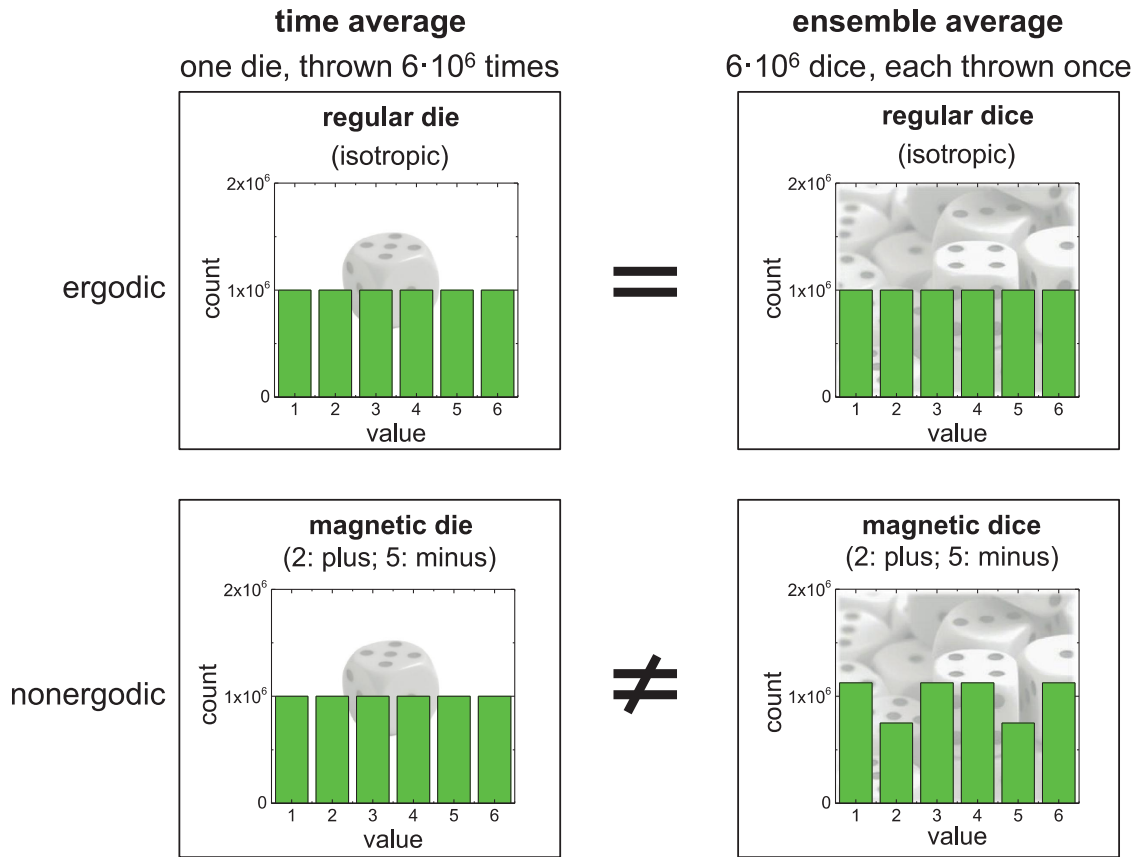


Figure 4.1: A simplified example of nonergodicity and ergodicity (after Ref. [287]).

$T_f$ , magnetic spins freeze in. Since some relaxation times diverge, ergodicity is broken and the stable ground state cannot be established in experimental time frames.

The term relaxor ferroelectrics has been suggested by Viehland *et al.*,<sup>47,32</sup> referring to disordered systems having a characteristic freezing transition similar to magnetic spin glasses. Below the Burns temperature, polar nanoregions appear in the metrically cubic structure.<sup>26</sup> As these polar entities are mainly dynamic and uncorrelated, the relaxor exhibits ergodic behavior. On cooling to  $T_f$ , PNRs start freezing and interacting. Both the growth and the appearance of new PNRs intensify their interaction and, consequently, ergodicity is broken. A glass-like character of the relaxor is created and the system becomes nonergodic. Due to the frustrated interactions, a configuration with random polarization directions is established, unlike the one with a parallel alignment as usually obtained in ferroelectrics. However, the ferroelectric state can be established from the nonergodic relaxor after a sufficiently strong electric field is applied.<sup>25</sup>

It is necessary to mention that the term "ergodic" used to describe relaxors differs from the one used in statistics where the time average and ensemble average yield the same state with a prob-

ability of 100 %. In fact, the nature of relaxor would more appropriately be discussed in terms of "quasi-ergodicity" or "varying degrees of nonergodicity".

In the following, the effect of a varying degree of nonergodicity on the functional and microstructural properties of  $(1-y)(0.81\text{BNT}-0.19\text{BKT})-y\text{BZT}$  is elaborated. In order to elucidate the peculiar field-dependent behavior, the properties of  $\text{BNT}-19\text{BKT}-y\text{BZT}$ , such as large- and small-signal behavior, as well as domain microstructure are investigated with respect to the composition, electric field, and temperature. To establish a correlation between the macroscopic and the submicroscopic mechanisms, the properties were locally investigated using PFM. The PFM technique permits *in situ* manipulation of the local polar structure and studies of the electric field-induced phase transformation at the nanoscopic scale.

The presented work is a result of a collaborative effort. The macroscopic electrical measurements and neutron diffraction experiments were performed by Dr.-Ing. Robert Dittmer, Institute of Materials Science, University of Technology Darmstadt, Germany. The obtained results have been published in two journal articles.<sup>287,288</sup>

## 4.2 Experimental Methods

### 4.2.1 Material and Sample Preparation

The material system investigated within this work is  $(1-y)(0.81\text{Bi}_{1/2}\text{Na}_{1/2}\text{TiO}_3)-0.19\text{Bi}_{1/2}\text{K}_{1/2}\text{TiO}_3-y\text{BiZn}_{1/2}\text{Ti}_{1/2}\text{O}_3$ , referred to as  $\text{BNT}-19\text{BKT}-100y\text{BZT}$  with  $y=\{0.02; 0.03; 0.04\}$ . The material processing procedure according to which the samples were prepared is in detail explained in Chapter 3. Nevertheless, the material preparation routine differs in some processing steps. In this case, the reagent raw materials  $\text{Bi}_2\text{O}_3$  (99.975 % purity),  $\text{Na}_2\text{CO}_3$  (99.5 %),  $\text{TiO}_2$  (99.9 %),  $\text{K}_2\text{CO}_3$  (99.0 %), and  $\text{ZnO}$  (99.99 %) were mixed according to the respective stoichiometric formula. After the slurry preparation and drying, the powders were calcined in covered alumina crucibles at 900 °C for 3 h. Shaped samples were compacted by hydrostatic pressure value and afterwards sintered at 1100 °C for 3 h. To minimize the loss of volatile elements during the sintering process, the samples were covered with an powder of the respective composition. For electrical measurements, the sample surface was treated by fine grinding using silicon carbide abrasive paper with a grit size of 4000 (STRUERS GmbH, Willich, Germany). Final disc-shaped samples with a diameter of 7 mm and a height of about 0.7 mm were electroded using silver paste (Gwent Electronic Materials Ltd, Pontypool, UK) and then subjected to a burn-in process at 400 °C. The surface of the specimens examined by PFM were polished down to optical quality as described previously (Chapter 2).

### 4.2.2 Electrical Large-Signal Measurements

Large-signal strain and polarization were measured in the high-electric field regime using a Sawyer-Tower circuit, schematically presented in Figure 4.2. The source of a signal with adjustable polarity, frequency, and amplitude was provided by a signal generator (Agilent 33220A, Agilent Technologies Deutschland GmbH, Böblingen, Germany) and sent to a voltage source (20/20C, TREK, Inc., Medina, NY, USA). The provided signal was of triangular waveform with a frequency of 1 Hz and an amplitude that varied from 1 kV/mm to 6 kV/mm in steps of 1 kV/mm. The electric field-induced polarization  $P$  was indirectly measured by measuring the change in charge  $Q$ . For that purpose, the sample was serially connected to a measurement capacitor  $C_m$ . The sample is considered to be an ideal capacitor of capacitance  $C_s$ . For the charge of two serially connected capacitors it applies  $Q = Q_m = Q_s$ , while the charge  $Q$  can be defined as  $Q = C \cdot V$ . Here,  $V$  is the voltage drop across the capacitor with the capacitance  $C$ . Considering this, the charge of the sample capacitor can be measured as  $Q_s = C_m \cdot V_m$  using the known capacitance  $C_m$  and the respective voltage drop  $V_m$ . The polarization was calculated in agreement to Equation 4.1.

$$P = \frac{C_m \cdot U_m}{A} \quad (4.1)$$

Here,  $A$  is the area of the sample surface. For  $C_m \gg C_s$ , the majority of the voltage drop occurs across the sample and it is of negligible value across the measurement capacitor. Since the sample capacitance was well below 10 nF, the measurement capacitance was 10  $\mu$ F. Internal resistance of the data acquisition four-channel oscilloscope (DSO6014A, Agilent Technologies, Santa Clara, USA) was increased by an operational amplifier, as shown in Figure 4.2. To apply electric fields, the samples were placed in a polytetrafluoroethylene (PTFE) container, which was filled with silicone oil (AK35 or AK200, Wacker Chemie GmbH, Munich, Germany). The electrical circle was closed by placing the sample in-between a bottom and a top point contact. Strain  $S$  was measured at the same time using an optical sensor (Figure 4.3) that detects the displacement by

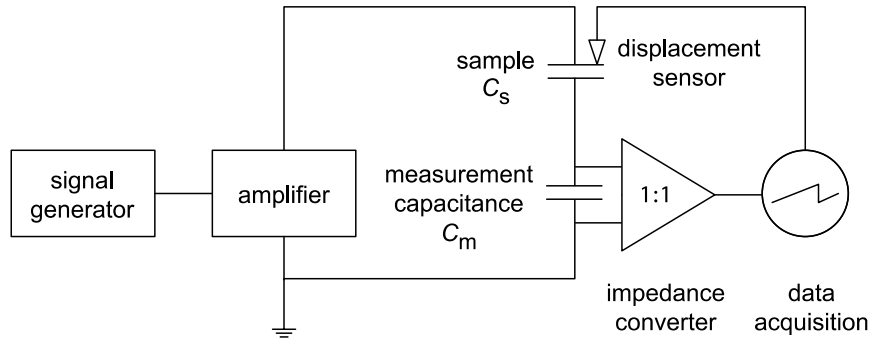


Figure 4.2: Schematic representation of the Sawyer-Tower experimental setup used for the measurements of large-signal  $P(E)$  and  $S(E)$ .

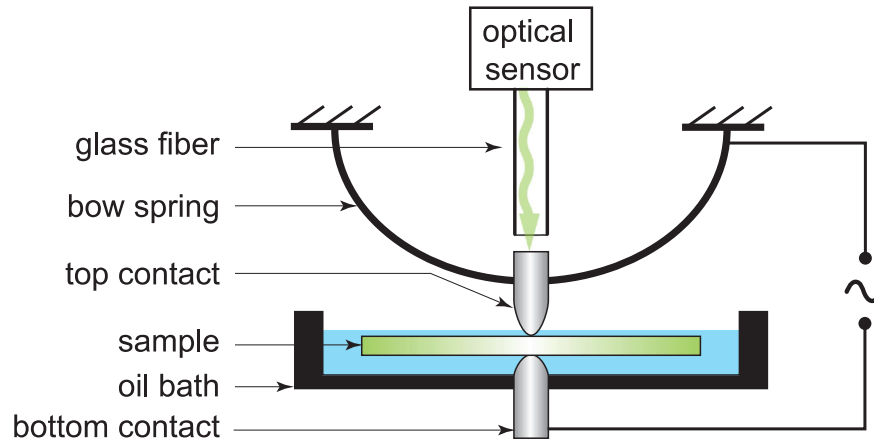


Figure 4.3: Experimental setup for the optical measurement of field-induced strain  $S(E)$  (after Ref. [289]).

sensing the intensity of reflected light. The light was conducted through a glass fiber to the upper point contact of a highly polished metal contact.

Vertical displacement of the upper electrode was enabled by a bearing using a bow spring. The displacement of the sample created a change of the distance between the upper point contact and the highly polished facet of which reflects the light. The consequential intensity changes of the reflected light were converted into the displacement signal, allowing high precision strain measurements with a resolution of up to 4 nm at 100 Hz. To monitor the amplitude-dependent evolution of the remanent strain, samples were measured from the virgin state achieved by annealing on a hot plate at 400 °C.

### 4.2.3 Electrical Small-Signal Measurements

The relative permittivity  $\epsilon_{r,33}$  and the piezoelectric coefficient  $d_{33}$  are referred to as small signal parameters, that describe the behavior of the material under small excitation fields. To assess the amplitude-dependent changes of  $\epsilon_{33}$  and  $d_{33}$ , the small-signal measurements were performed using a custom-built setup which includes the mentioned optical sensor and a LabVIEW (National Instruments Germany GmbH, Munich, Germany) program code. A step-like large-signal waveform was supplied to an amplifier (20/20C, TREK, Inc., Medina, NY, USA) using an analog-digital-converter (PCI-6221, National Instruments Corporation, Austin, TX, USA). The large signal was increased in steps of 100 V<sub>DC</sub> for 5.5 s yielding an equivalent frequency of approximately 1 mHz. Two lock-in amplifiers (SR830, Scientific Instruments, West Palm Beach, FL, USA) were used to generate the sinusoidal *ac* small-signal. Both waveforms were combined in a mixing unit and then supplied to the sample. The *ac* outgoing signal of the first lock-in amplifier being the reference

signal, the two lock-in amplifiers were employed to analyze the strain and polarization responses. Small changes in the responses were used for the measurements of  $\varepsilon_{33}$  and  $d_{33}$ . The piezoelectric coefficient was determined from the field-dependent change of strain, as described in Equation 4.2.

$$d_{33} = \frac{\Delta S_3}{\Delta E_3} \quad (4.2)$$

Assuming  $\chi \approx \varepsilon$ , the relative permittivity can be calculated by the following equation.

$$\varepsilon_{33} = \varepsilon_o \cdot \varepsilon_{r,33} = \frac{\Delta P_3}{\Delta E_3} \quad (4.3)$$

Temperature- and time-dependent assessment of the small signal piezoelectric coefficient  $d_{33}$  was achieved using the aforementioned commercially available aixPES system (aixACCT Systems GmbH, Aachen, Germany). A triangular large-signal waveform with a frequency of 50 mHz was modulated by a small-signal with a frequency of 1 kHz and an amplitude of 10 V. Prior to measurement, each BNT-19BKT-*y*BZT sample was poled for 20 s at 6 kV/mm at various measurement temperatures: 30 °C, 43 °C, 57 °C, and 71 °C. After electrical poling, the  $d_{33}$  value was measured every 5 min within a 90 min time span.

#### 4.2.4 Piezoresponse Force Microscopy

The local piezoelectric properties of BNT-19BKT-*y*BZT samples were investigated using piezoresponse force microscopy. The PFM study was accomplished using a commercial setup MFP-3D™ (Asylum Research, Santa Barbara, CA, USA). Piezoresponse force microscopy was already presented in Chapter 2. The PFM experiments were conducted as previously described in Chapter 3. Domain morphology visualization was performed in single frequency vector PFM mode, using p-doped silicon cantilevers PPP-NCHR (Nanosensors™, Neuchâtel, Switzerland) with a force constant of 42 N/m and a resonance frequency in the range of 204-497 kHz. To image the local domain structure, an *ac* voltage with amplitude  $V_{ac}=5$  V and frequency  $f=50$  kHz was applied to the tip.

In order to study the local polarization switching, poling experiments were carried out in the lithography mode by applying either positive or negative *dc* voltage,  $V_{dc}$ , up to 30 V with voltage steps of 5 V to an area of  $5 \times 5 \mu\text{m}^2$ . After each poling step, domain structure imaging was performed. To study time relaxation of the electric field-induced polarization as a function of time and temperature, an area of  $1 \times 1 \mu\text{m}^2$  was poled by *dc* bias voltage with an amplitude of 30 V. The time evolution of the piezoresponse inside the poled area was subsequently monitored by domain imaging performed in vector PFM mode. The measurements were performed at 30 °C, 43 °C, 57 °C, and 71 °C. The acquired PFM experimental results were analyzed using MatLab (The MathWorks, Inc., Natick, MA, USA) and WSxM software (Nanotec Electronica, Madrid, Spain).<sup>261</sup>

### 4.3 Influence of a *dc*-Electric Field on the Field-Induced Phase Transition

#### 4.3.1 Experimental Results

##### 4.3.1.1 Macroscopic Properties

The investigated compositions are  $\text{Bi}_{1/2}\text{Na}_{1/2}\text{TiO}_3$ - $0.19\text{Bi}_{1/2}\text{K}_{1/2}\text{TiO}_3$ - $y\text{BiZn}_{1/2}\text{Ti}_{1/2}\text{O}_3$  with  $y=0.02$ ,  $0.03$ , and  $0.04$ , referred to as 2BZT, 3BZT, and 4BZT, respectively. The electric field dependence of strain, polarization, piezoelectric coefficient  $d_{33}$ , and relative dielectric permittivity  $\varepsilon_{r,33}$  were investigated for all three composites. The strain  $S(E)$  and polarization  $P(E)$  loops are plotted as a function of the maximum electric field applied in the range from 1 kV/mm to 6 kV/mm (Figure 4.4). At electric fields lower than 2 kV/mm both strain  $S(E)$  and polarization  $P(E)$  exhibit remarkably similar behavior for all compositions. The strain hysteresis loops show only low remanent  $S_{rem}$  and negative  $S_{neg}$  strain values, while the polarization loops are of the shape of a thin ellipse with small remanent values  $P_{rem}$ . For 2BZT, the typical butterfly strain loop with large  $S_{rem}$  and  $S_{neg}$  is generated at the maximum electric field of 4 kV/mm. At further increase of the field, the polarization increases and achieves saturation at 4.7 kV/mm, which is manifested as a bending of the  $P(E)$  curve. At the same time, the strain  $S(E)$  rapidly increases with the electric field in the first half-cycle, while the slope of the strain curve significantly decreases close to the maximum field. The maximum slope  $\Delta S/\Delta E$  is achieved at about 4 kV/mm. The 3BZT com-

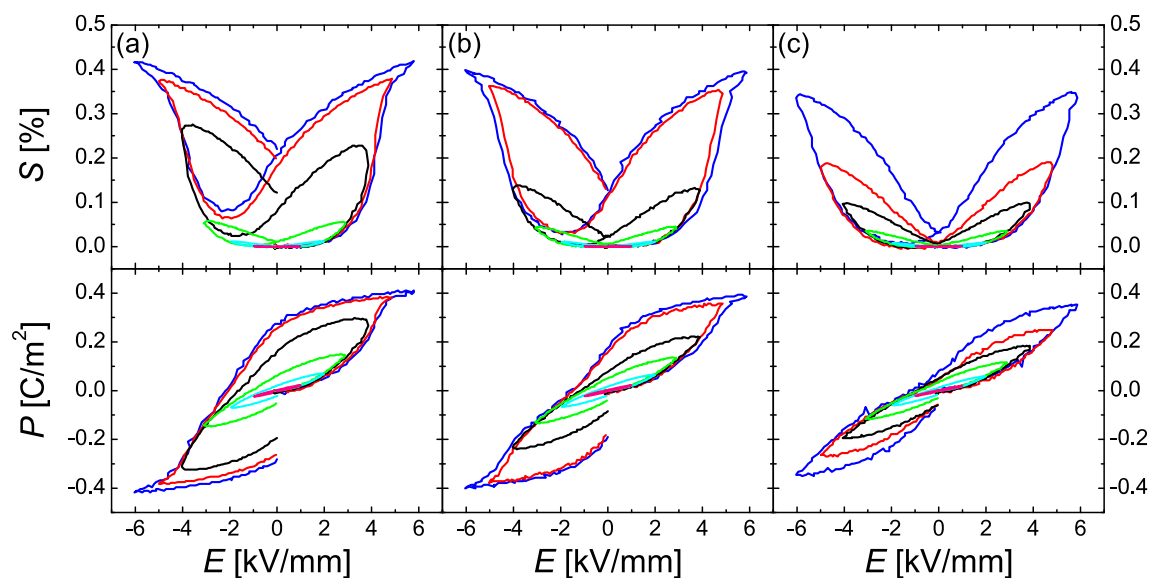


Figure 4.4: Strain  $S$  and polarization  $P$  as function of electric field for (a) 2BZT, (b) 3BZT, and (c) 4BZT measured at increasing fields.



position exhibits comparably high maximum strain that is achieved at highest maximum electric field of 6 kV/mm. It saturates at  $E_{sat} = 5.1$  kV/mm. Unlike 2BZT, significant remanent strain for 3BZT is obtained only for high electric fields. Here, usable strains achieved at electric fields larger than 5 kV/mm are found to be larger than the corresponding ones in 2BZT.

For 4BZT, "sprout"-like strain loops are obtained at each poling field. In this composition, no saturation of the strain and polarization loop was achieved at any applied electric fields. At the same time, only minute  $S_{rem}$  and  $P_{rem}$  were obtained. Nonetheless, among all compositions, 4BZT exhibits the highest useful strain  $\Delta S = S_{max} - S_{rem}$  of 0.27 % obtained at 6 kV/mm field.

Measurements of the small-signal piezoelectric coefficient  $d_{33}$  and relative permittivity  $\epsilon_{r,33}$  demonstrate similar trends for the low-field regime. Only after applying an electric field, piezoelectricity was triggered and non-zero  $d_{33}$  values were measured for all compositions. At lower electric fields,  $d_{33}(E)$  shows similar increasing trends for each composition. As Figure 4.5 shows, at 1 kV/mm the difference in  $d_{33}$  among all samples varies only by 5 %, *i.e.* 1 pC/N. At electric fields larger than 2 kV/mm, however, 2BZT exhibits the strongest increase of  $d_{33}$ . For this sample,  $d_{33}$  saturation values are reached at  $E_{sat}=3.5$  kV/mm, which is demonstrated as a bend in the  $d_{33}(E)$  curve. The saturation of  $d_{33}(E)$  in 3BZT was observed at 4 kV/mm, whereas the saturation of  $d_{33}(E)$  was not reached in 4BZT for any applied electric field but a maximum  $d_{33}$  value of 181 pC/N was achieved. The maximum piezoelectric coefficient of 2BZT and 3BZT is 157 pC/N and 170 pC/N, respectively. The highest remanent  $d_{33}$  value of 141 pC/N is measured

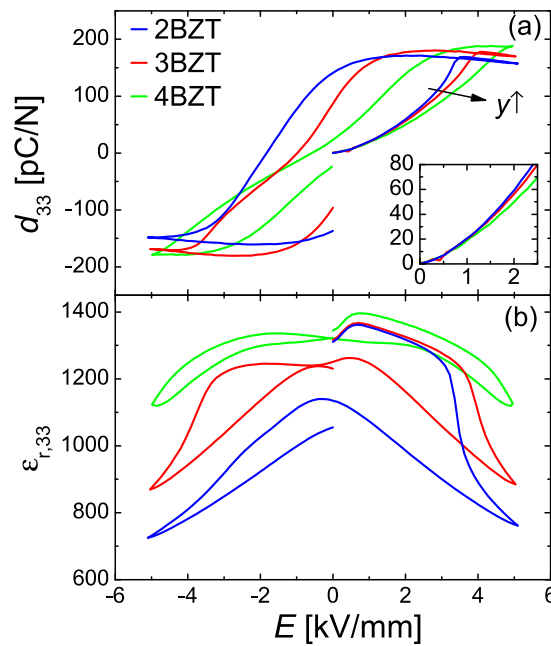


Figure 4.5: (a) Piezoelectric coefficient  $d_{33}$  and (b) relative permittivity  $\epsilon_{r,33}$  as a function of electric field.

for 2BZT. For 3BZT, the remanent  $d_{33}$  is 87 pC/N after the electric field is switched off, while for 4BZT it was measured to be 22 pC/N. The relative permittivity in the unpoled state shows no strong variations as the content of BZT changes. For 2BZT, the initial  $\varepsilon_{r,33} = 1300$  value is found to deviate less than 2 % with BZT doping increasing to 4 mol%. As already mentioned, at electric fields lower than 2 kV/mm  $\varepsilon_{r,33}(E)$  was found to be composition-invariant. Particularly strong decay of dielectric permittivity was found for 2BZT as the field increases above 2 kV/mm. For 2BZT, the lowest  $\varepsilon_{r,33}$  values were obtained below the inflection point at 3.4 kV/mm and below 3.9 kV/mm for 3BZT. For 4BZT,  $\varepsilon_{r,33}$  exhibits a weak hysteretic behavior, no abrupt decay, and no inflection point were observed. Upon poling, zero-field dielectric permittivity decays by about 20 % with respect to the unpoled state of 2BZT. This decay is measured to be about 6 % for 3BZT and only 2 % for 4BZT.

#### 4.3.1.2 Microscopic Properties

The microstructure of BNT-19BKT-*y*BZT and its compositional and field dependence were assessed by means of PFM techniques. Figure 4.6 presents the surface topography, vertical PFM, and lateral PFM images as collected for unpoled samples with different BZT contents. The topography images reveal good-quality sample surfaces the contrast of which slightly varies as an effect of grain boundaries. No strong surface defects that could affect the domain structure imaging were detected. At the same time, domain imaging reveals almost featureless domain morphology for all three compositions. The VPFM signal of the 2BZT domain structure shows relatively weak contrast variations. Piezoactive regions with a correlated piezoresponse can be distinguished, as it will be shown later in the discussion chapter. The lateral PFM signal exhibits a better signal to noise ratio. The contrast can be differentiated only at the grain boundaries. Furthermore, no contrast was observed in the VPFM image of the 3BZT domain structure. Similar to 2BZT, its lateral PFM signal displays a contrast variation only as an effect of the different crystallographic orientations of the grains. Negligible local piezoresponse of the 4BZT domain structure is demonstrated by both VPFM and LPFM. Some contrast visible in LPFM signal is probably an artifact related to the grain boundaries.

In order to induce ferroelectric long-range order locally, either a negative or a positive *dc* electric field was applied through the conductive PFM tip. For 2BZT, by applying a bias voltage of  $\mp 5V$ , macrodomains with the polarization vector parallel to the applied field were induced (Figure 4.7). The polarization inside the induced domain pattern notably increases as the bias voltage further increases, which is reflected by the stronger VPFM contrast, as shown in the top row of Figure 4.7. The increasing piezoresponse is imaged, as the voltage increases up to 20 V. At higher voltages the signal saturates.

For the composition with 3 % BZT, the vertical PFM signal shows a rather gradual increase in contrast of the written domains as the bias voltage increases. Unlike 2BZT, the response is sig-

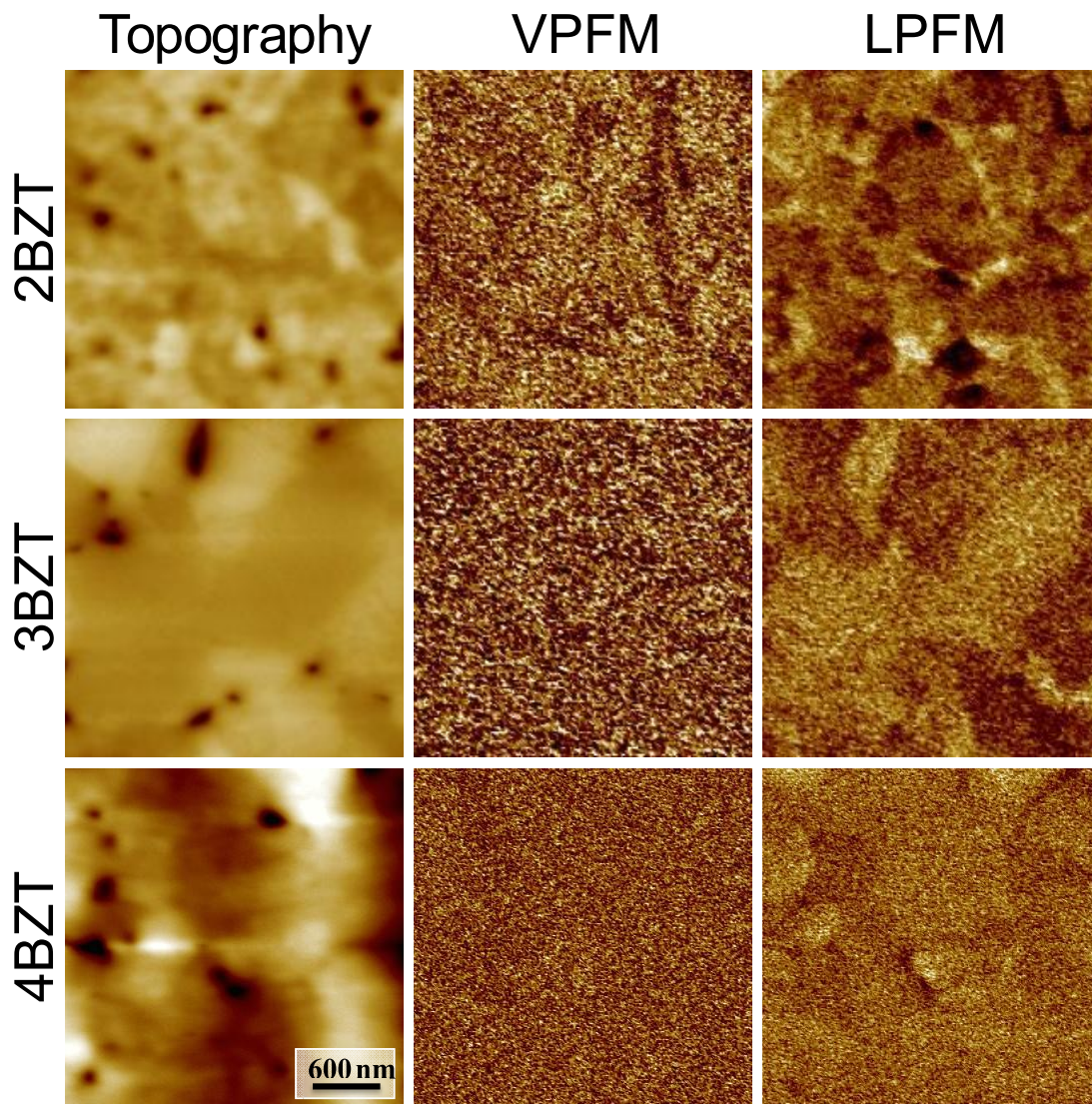


Figure 4.6: The surface topography and PFM images of unpoled BNT-BKT- $\gamma$ BZT ceramics.

nificantly weaker at 5 V and no strong pattern is formed even for biases as high as 15 V. Only at even larger voltages, the piezoresponse reaches values comparable to the piezoresponse obtained in 2BZT.

Moreover, for 4BZT no stable piezoresponse was induced at low bias voltages, while the application of voltages above  $\mp 15$  V resulted in the formation of a rather incomplete domain pattern without a clear contour. In addition, a pronounced asymmetry between the piezoresponses induced by positive and negative biases was observed. The fraction of the pattern with negative polarization exhibits piezoresponse approximately twice as high as for the positively poled region (Figure 4.7).

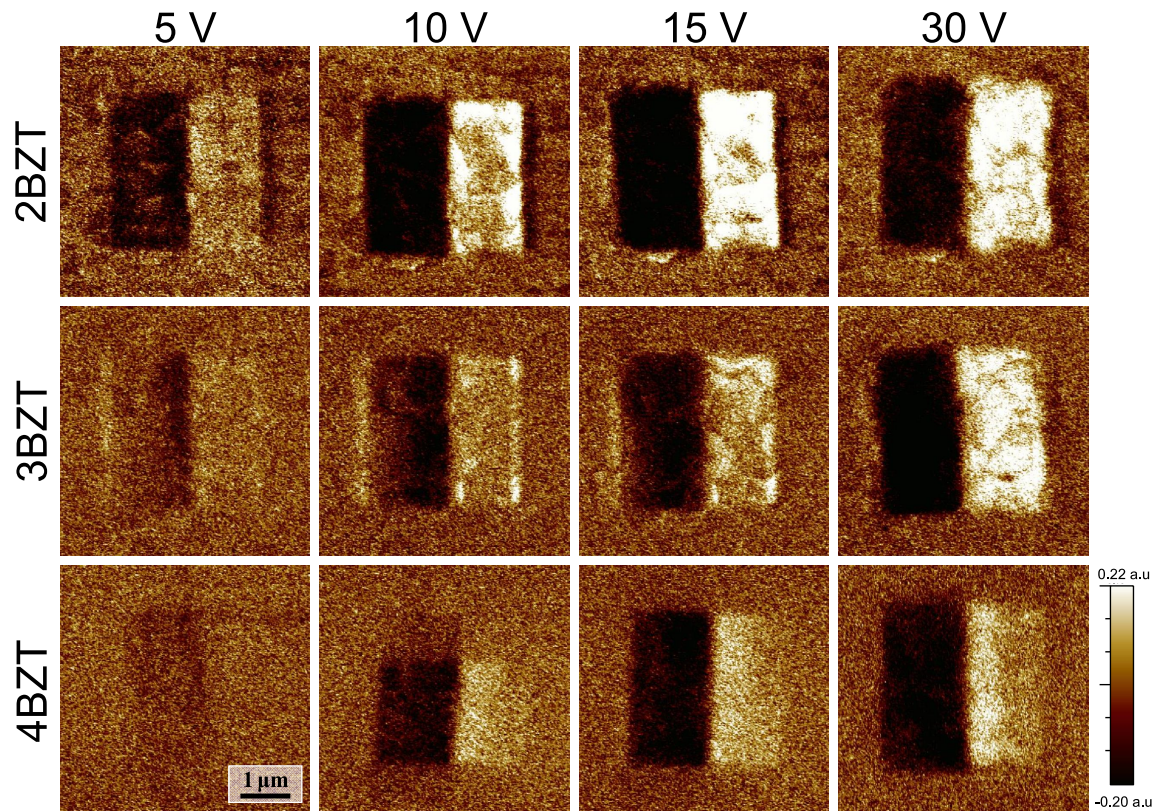


Figure 4.7: VPFM images of the BNT-BKT-BZT ceramics obtained after local poling at different bias voltages. The left and right sides of the internal square region were polarized by negative and positive bias fields, respectively.

For 3BZT, however, a less pronounced asymmetric behavior was observed, whereas for 2BZT no such asymmetry with respect to the polarity of applied bias was noted.

The simultaneously collected LPFM images are presented in the Appendix by Figure A.1. The improved signal-to-noise ratio of LPFM images allows to distinguish the grain structure, particularly apparent for 2BZT and 3BZT. The piezoresponse of the bias-formed patterns show the same general behavior with an increasing electric field as observed in the corresponding VPFM images. Therefore, field dependence of the locally induced state is in the following discussed only in terms of VPFM images.

## 4.3.2 Discussion

### 4.3.2.1 Macroscopic Properties

The  $(1-y)(0.81\text{BNT}-0.19\text{BKT})-y\text{BZT}$  material system belongs to relaxor ferroelectrics, the properties of which are generally considered to be governed by the degree of the heterovalent cation substitution.<sup>198,290</sup> For the material in question, it is the  $\text{Zn}^{2+}$  that is introduced to the B-site, previously occupied by only one ion species, that is, the four-fold positively charged titanium,  $\text{Ti}^{4+}$ . At room temperature, the composition with  $y=0.02$  exhibits characteristics of a nonergodic relaxor, resembling, for instance, the canonical PMN at low temperatures.<sup>32,26,25</sup> Therefore, by applying an electric field a coalescence of PNRs can be induced, resulting in the creation of micro-domains. Low electric fields trigger a slow increase of polarization that can be partly attributed to some PNRs merging. These PNR conglomerates are, however, mostly unstable and break up upon removal of the electric field. This is effectively seen as a zero remanent polarization in Figure 4.4. The very similar low-field behavior of  $\varepsilon_{r,33}(E)$  and  $d_{33}(E)$  for all three compositions is likely related to the fact that the polar volume fraction and the domain wall density are approximately similar. A stable long-range order is established in 2BZT only above a threshold electric field, the level of which is strongly temperature- and time-dependent.<sup>25,193</sup> With the increasing  $\text{Zn}^{2+}$  ion concentration the quenched random fields are enhanced, consequently, causing a decay of  $DoN$ . Therefore, establishing long range order in 3 % BZT requires comparably high electric fields.

The decay of  $DoN$  can be related either to the decrease of PNR correlation or with the possible coexistence of strongly correlated, frozen domains and uncorrelated dynamic PNRs. By means of phase field simulations that consider the random electric fields as introduced by the point defects, a precursory state with frozen PNRs for  $T > T_f$  was found.<sup>291</sup> This implies that a partial nonergodic state may exist even before most PNRs collectively freeze. A PFM study on the local structure of PMN-PT<sup>292</sup> demonstrated the existence of both fast and slow relaxation regions. Slow relaxation regions were identified being in a nonergodic state with frozen spatial polarization fluctuations. In both PMN and PMN-10PT static nanodomains were evidenced beyond  $T_f$ .<sup>293</sup> In addition, second-harmonic generation<sup>294</sup> and dielectric measurements<sup>284</sup> have detected the presence of partially frozen domains in relaxor SBN structure. Therefore, it may be assumed that in 3BZT the amount of static domains decreases in comparison to 2BZT. As a result, the threshold electric field in 3BZT increases to 5.1 kV/mm instead of 4.7 kV/mm as required to induce the FE state in 2BZT. Also, for fields lower than 4 kV/mm, only sprout-like strain loops with a small  $S_{rem}$  of 0.02 % were generated which indicates the formation of unstable long-range ferroelectric order.

Finally, the composition with 4 mol% of BZT is in an ergodic relaxor state. Here only dynamic and weakly correlated PNRs are present.

Figure 4.8 shows how remanent strain  $S_{rem}$  and remanent polarization  $P_{rem}$  evolve with increasing poling field for the three investigated compositions. Judging from nearly zero  $S_{rem}$

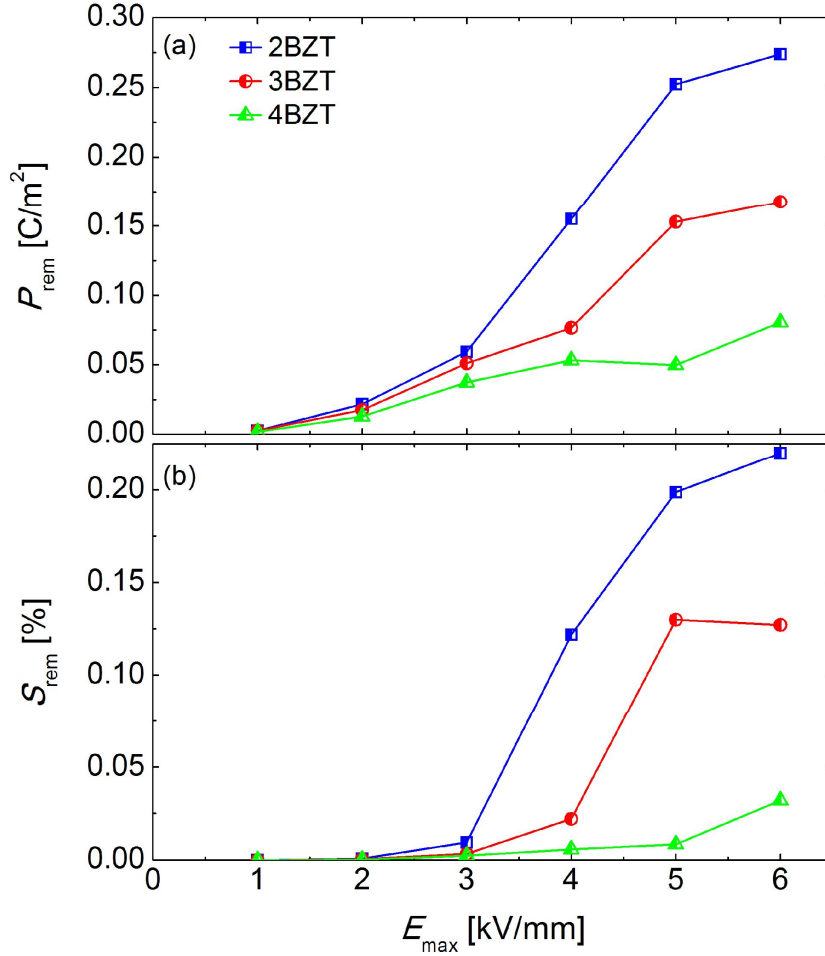


Figure 4.8: Dependence of (a) remanent polarization  $P_{rem}$  and (b) remanent strain  $S_{rem}$  on electric field amplitude  $E_{max}$ .

for  $E \leq 2$  kV/mm, it can clearly be seen that irrespective of  $DoN$ , all compositions exhibit similar electromechanical properties below the threshold field. Only at higher electric fields the influence of  $DoN$  becomes relevant as the incorporated  $Zn^{2+}$  ions effectively increase the threshold electric field required to induce the relaxor-ferroelectric phase transition. These measurements suggest that the reduction of  $DoN$  indeed strongly depends on the BZT content, that is, the concentration of heterovalent B-site ions.

Further neutron diffraction measurements revealed that the initially unpoled structures of all three compositions correspond to cubic ones, as was also well shown for other canonical relaxors.<sup>295,296</sup> Due to the small size of PNRs, any crystallographic distortions related to the PNRs have coherence length too small to be detected by diffraction. Neutron diffraction patterns in the  $2\theta$  range from  $70^\circ$  to  $110^\circ$  enclosing both the  $\{111\}_c$ - and the  $\{200\}_c$ - type reflections before and after poling are provided in the Appendix by Figure A.2. Then again, for the samples in the unpoled state the neutron diffraction technique detects weak satellite peaks at around  $2\theta$  of  $75^\circ$ . These reflections

are caused by the tilting of the oxygen octahedra. This yields a doubling of the unit cell and causes the emerging of superlattice reflections, that reveal a lower than cubic symmetry.<sup>102</sup> Application of the electric field causes vanishing of these peaks at  $2\theta \cong 75^\circ$  and the appearance of reflections of similar amplitude at  $2\theta \cong 79^\circ$ . The occurrence of the initial  $1/2\{310\}_c$ -type peaks is a result of the in-phase oxygen octahedral tilting characteristic for the tetragonal  $P4bm$  structure. It can be assumed that, although metrically cubic, all three compositions have a tetragonal-like break in symmetry that permits for this type of tilting. The pure BNT structure at high temperatures was shown to exhibit a similar type of tilting system while having tetragonal symmetry.<sup>297</sup> Then again, the emergence of the peak near the  $1/2\{311\}_c$ -type reflections after poling indicates antiphase oxygen octahedral tilting ( $a^-a^-a^-$  in Glazer notation<sup>102</sup>), which is characteristic for rhombohedral  $R3c$  and  $Cc$  structures.<sup>297,298</sup> Taking this into consideration, by applying the electric field the phase transition from a metrically cubic phase with tetragonal superlattice peaks to a phase with rhombohedral-like superlattice peaks occurs. It is important, however, to mention that the definite crystal structures for BNT-based materials cannot be unambiguously defined based only on the detection of satellite peaks.

The effect of the electric field on the structure strongly depends on the degree of nonergodicity, as shown for the  $\{111\}_c$  reflection in Figure 4.9. The most pronounced broadening of the reflection peak in nonergodic 2BZT is likely related to peak splitting due to a rhombohedral distortion.

Moreover, a notable domain texture forms with the polar axis being preferentially aligned with the electric field, *i.e.* close to  $0^\circ$  and  $180^\circ$  along  $\langle 111 \rangle$  direction. The characteristic neutron diffraction patterns of  $1/2\{311\}_c$  and  $\{111\}_c$ -type reflections for poled samples are shown in the

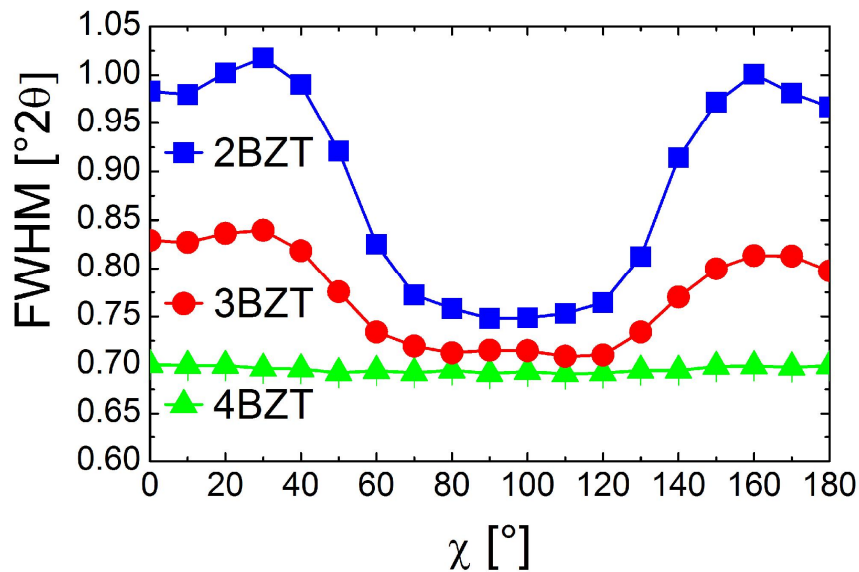


Figure 4.9: Full width at half maximum (FWHM) of the  $\{111\}_c$  neutron diffraction peak as a function of rotation angle as determined by single peak fitting.

Appendix by Figure A.3. With increasing the BZT content, the texture effect decreases and, thus, no texture is apparent for 4BZT. In addition, the satellite reflection at  $2\theta \cong 79^\circ$  is found for 2BZT and 3BZT, manifesting their angular dependence, while this reflection is not present in the 4BZT composition. This is also reflected in the near-zero remanent polarization, low  $d_{33}$  signal at zero field, and virtually no change in the relative permittivity upon field exposure. The 3% BZT-modified composition has properties that are in-between those of nonergodic 2BZT and the mainly ergodic 4BZT. Finally, it can be concluded that the structural measurements support the hypothesis of  $DoN$  varying with the BZT content and that strong altering of the electrical and structural properties consequently occurs after exposure to an electric field.

#### 4.3.2.2 Microscopic Properties

The PFM measurements were conducted to probe the microstructure at the nanoscale to support the above discussed field-dependent properties and the effect of the  $DoN$  on the material characteristics. The unpoled local microstructure of 2BZT exhibits regions of correlated piezoresponse, the spatial organization of which does not form labyrinth-like features as seen in other relaxors.<sup>48</sup> In contrast, 3BZT and 4BZT show no distinct domain structures. These observations are quantified by the autocorrelation function analysis presented in Figure 4.11. Using this analytical method an autocorrelation image  $C(r_1, r_2)$  is generated from the original PFM image using the autocorrelation transformation as stated by Equation 4.4.

$$C(r_1, r_2) = \sum D(x, y) D(x + r_1, y + r_2) \quad (4.4)$$

Here,  $D(x, y)$  represents the piezoresponse signal intensity at position  $(x, y)$ . Figure 4.10 demonstrates typical autocorrelation images obtained for 2BZT, 3BZT, and 4BZT at room temperature. For clarity, the autocorrelation images are shown in a 3D space. Their radially averaged values correspond to the values of the autocorrelation function discussed below. The shape of the autocorrelation function gives information about the symmetry and regularity of the local polarization. A strong central peak of the autocorrelation image is observed for 2BZT as reflected by a distinct average value (Figure 4.11(a)). The width of the autocorrelation peak coincides with the size of a region of correlated piezoresponse, *i.e.* local polarization.<sup>299</sup>

The autocorrelation functions obtained for 3BZT and 4BZT, however, feature a low polarization correlation, similar to a noise signal with a very narrow peak as an effect of the limited image resolution and lock-in amplifier settings. These observations confirm the evolution from a nonergodic relaxor state with frozen PNRs to a state with mainly dynamic PNRs as the BZT content increases from 2% to 4%. A featureless morphology suggests the potential existence of static and dynamic PNRs that are impossible to detect by PFM. Thus, the local PFM measurements confirm the hypothesis of varying degrees of nonergodicity with partially frozen PNRs.





Figure 4.10: Autocorrelation function image of VPFM image from Figure 4.6 obtained for (a) 2BZT, (b) 3BZT, and (c) 4BZT.

As shown earlier, a long-range ferroelectric order of varying stability could be established by the applied electric field in compositions with both nonergodic and ergodic relaxor characteristics. The switchability of polarization is confirmed by the inverted piezoresponse contrast of those regions that were exposed to either positive or negative electric field (Figure 4.7).

In addition to the macroscopic measurements that demonstrate the rise in  $P_{rem}$  and  $d_{33}$  with increasing electric field a comparable field dependence was observed at the nanoscale. The field-dependent piezoresponse averaged over the poled area is plotted in Figure 4.12 for all three com-

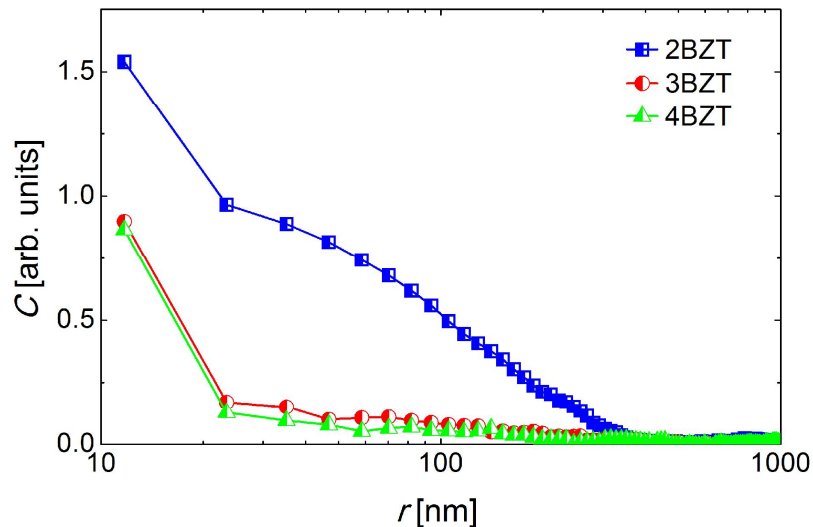


Figure 4.11: Autocorrelation function of the VPFM images obtained for the different BZT contents.

positions. Resembling behavior of the piezoelectric coefficient  $d_{33}$ , the VPFM signal increases at moderate voltages and it saturates above a certain bias value  $V_{sat}$ . The saturation voltage increases with increasing BZT content, similar to  $E_{sat}$  estimated from the macroscopic  $P(E)$ . It can be deduced that the material properties on the macroscopic level are reflected or even governed to a notable degree by the nanoscopic behavior. Unlike the less nonergodic 3BZT and 4BZT, the average piezoresponse of 2BZT increases faster with increasing voltage. In the 4BZT composition, piezoresponse is induced only above threshold bias voltages  $\sim 10V$ . These diversions can be explained by the increase in the degree of nonergodicity with increasing  $Zn^{2+}$  concentration. In fact, due to the higher  $DoN$ , higher voltages are necessary to overcome the increased random electric fields, so the long-range ferroelectric order can be established.

It is hypothesized that a lower  $DoN$  affects the stability of the field-written domains, *i.e.* the established ferroelectric long-range order. The asymmetry in the average piezoresponse, shown in Figure 4.12, underlines the importance of considering the time-dependent relaxation of the field-induced ferroelectric phase. As already mentioned, the values of piezoresponse correspond to the already relaxed state of the induced pattern, considering that they were acquired approximately 5-10 min after the bias field had been removed. As a matter of fact, the asymmetry in the piezoresponse might be assigned to the diverse relaxation dynamics between patterns formed by positive and negative bias voltages. This is particularly pronounced in the piezoresponse of 3BZT and 4BZT, where the removal of the electric field causes a strong relaxation back to a state with randomly orientated PNRs. Stronger stability of the negatively induced area might be related to the excess of negative charges at the surface. This effect could be a result of the higher mobility of

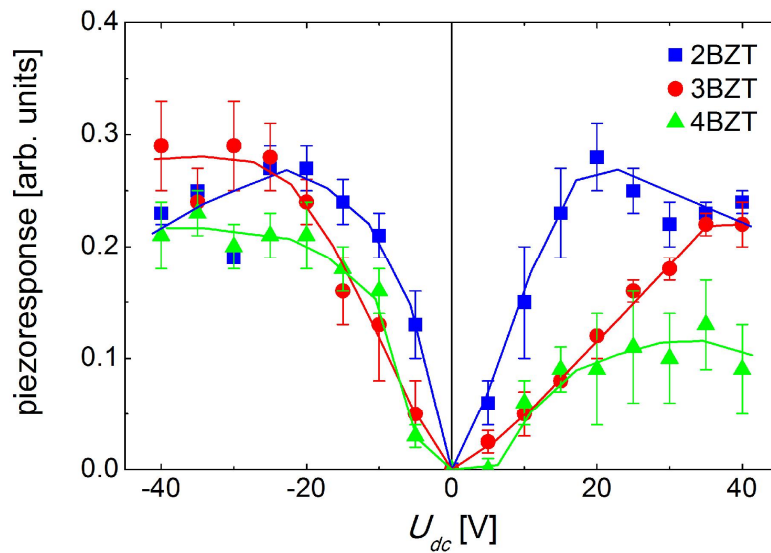


Figure 4.12: Evolution of absolute values of the average piezoresponse for the poled region with poling voltage. Lines are plotted as guide to the eye.

negative charges or a consequence of the effective n-type doping by the chemical substitution. The induced piezoresponse of nonergodic 2BZT, however, experiences minute relaxation, as it was seen for both the remanent polarization and  $d_{33}$  close to their saturation values. The piezoresponse of the induced pattern exhibits strong stability and is rather symmetric.

## 4.4 Influence of Temperature on the Field-Induced Ferroelectric Phase

### 4.4.1 Experimental Results

#### 4.4.1.1 Macroscopic Properties

The time dependence of the macroscopic small-signal piezoelectric coefficient  $d_{33}$  at 30 °C, 43 °C, 57 °C, and 71 °C was monitored for each sample after poling. The highest  $d_{33}$  value of 139 pm/V, measured at room temperature directly after sample poling, was found for the composition with 2% of BZT. In the course of 90 min,  $d_{33}(t)$  slightly decreases down to 123 pm/V, as shown in Figure 4.13. A similar time dependence is observed at 43 °C, where the  $d_{33}$  drops from 135 pm/V at  $t=0$  to 122 pm/V at  $t=90$  min. At 57 °C,  $d_{33}$  exhibits stronger changes diminishing from its initial value  $d_{33}=134$  pm/V to 107 pm/V within 90 min. The signal further decays as temperature rises to 71 °C. The initial  $d_{33}$  value of 75 pm/V was almost two times smaller than at room temperature. Besides, the signal relaxes faster and within 60 min drops to approximately 35 pm/V without notable further changes. The piezoelectric coefficient  $d_{33}$  of 3BZT was slightly lower than for 2BZT. At both 30 °C and 40 °C, the initial  $d_{33}$  value was approximately 120 pm/V. In this case, the time relaxation occurs faster and after 90 min  $d_{33}$  decays from 105 pm/V at 30 °C to 95 pm/V at 43 °C. The piezoelectric coefficient  $d_{33}(t)$  decreases and the relaxation rate increases. Consequently, the piezoelectric coefficient  $d_{33}$  drops from 92 pm/V to 65 pm/V at 57 °C, while at 71 °C that decay is from 59 pm/V to 33 pm/V.

For 4BZT,  $d_{33}$  strongly decays immediately after poling, so that the value measured at room temperature is only 18 pm/V (Figure 4.13c). This implies seven times smaller values of  $d_{33}$  than observed for 2BZT composition at the same temperature. The initial  $d_{33}$  value decays to 10 pm/V after 60 min. At both 57 °C and 71 °C  $d_{33}$  is about 5 pm/V and shows a relaxing to near-zero values within approximately five minutes.

#### 4.4.1.2 Microscopic Properties

In order to study the effect of the electric field on the local polar structure, PFM experiments were carried out. The PFM images for 2BZT, 3BZT, and 4BZT were collected after the samples were

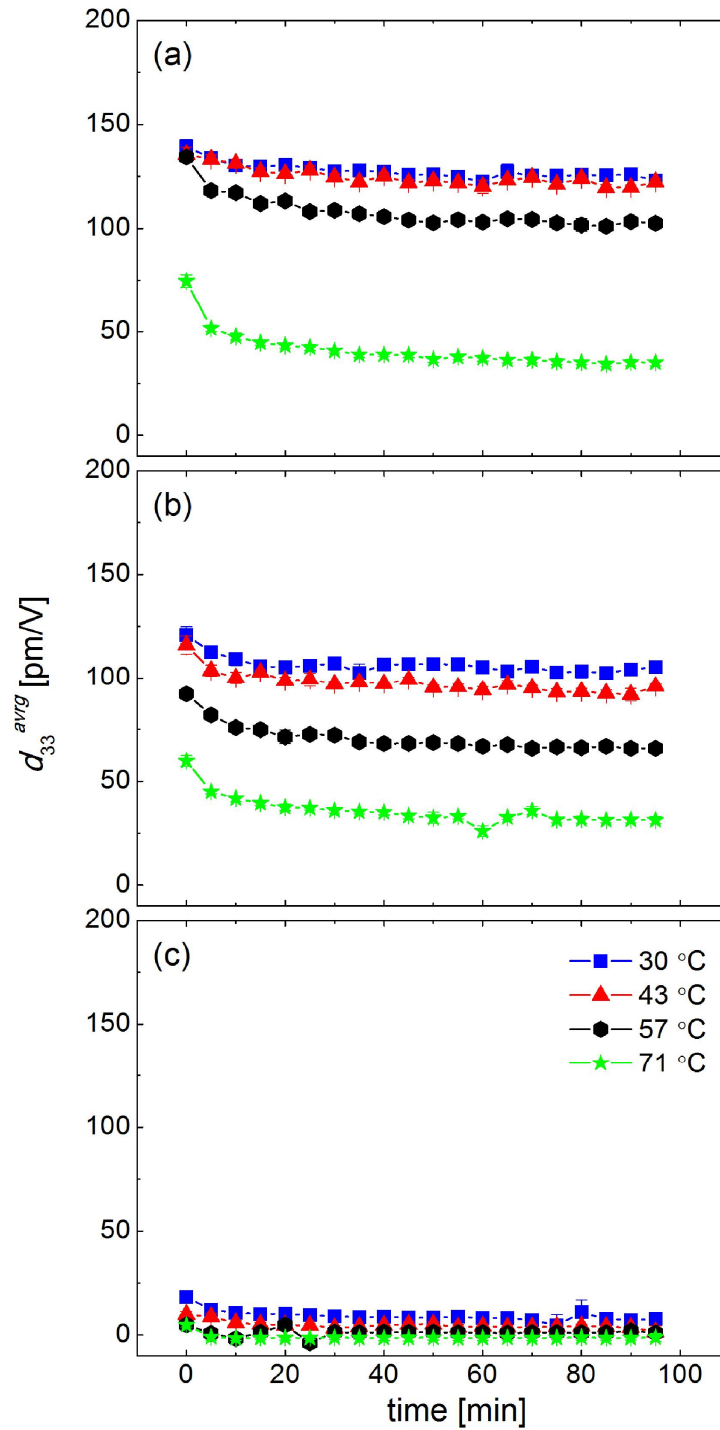


Figure 4.13: The small-signal piezoelectric coefficient  $d_{33}$  after poling with 6 kV/mm at different temperatures for (a) BNT-19BKT-2BZT, (b) BNT-19BKT-3BZT, and (c) BNT-19BKT-4BZT ceramics as function of time.

poled at different temperatures and at different time intervals. The sequence of the PFM images are presented by Figures 4.14, 4.15, and 4.16, respectively.

A *dc* voltage of +30 V was applied to a  $1\ \mu\text{m} \times 1\ \mu\text{m}$  square zone. Piezoresponse of the induced pattern was afterwards observed as a function of time. The appearing bright regions in PFM images correspond to field-induced domains with polarization aligned to the direction of the applied electric field. Here, the bright contrast implies a positive piezoresponse, meaning that the polarization vector points in upright direction normal to the image surface plane. To quantify the time-dependent evolution of the field-induced piezoresponse, the average piezoresponses of the created domain had been evaluated and visualized as a function of time in Figure 4.17.

For 2BZT, the field-induced domain with a strong piezoresponse is formed by poling at room temperature. It exhibits strong time stability, where neither a shrinkage of the written domain nor a decay of the PFM signal inside the poled area were observed (Figures 4.14(a)- 4.14(c)). Consequently, no changes are observed in the time dependence of the average piezoresponse (Figure 4.17a). Considering the time needed to acquire a single PFM scan, the first PFM image depicts the local polarization state approximately 7 min after the poling is performed. Thus, the corresponding average piezoresponse is computed for a partially relaxed state.

The poling at 43 °C creates a less uniformly poled area, with regions of weak piezoresponse. The piezoresponse furthermore decreases with time and the corresponding average piezoresponse smoothly diminishes (Figure 4.17(a)). At 57 °C, a fragmented domain pattern is created. At this temperature, the written domain shrinks fast with time (Figure 3(d)-(f)) and the average piezoresponse rapidly decays to a near-zero value. At 71 °C, only weak local poling was accomplished. The featureless microstructure was again established after 30 min (Figures 4.14(g)-(i)).

The piezoactivity of the field-induced domain in 3BZT is recorded to be lower than that of the 2BZT composition (Figure 4.17(b)). Already at room temperature, average piezoresponse showed a gradual degradation with time (Figure 4.15(a)-(c)). When the sample was heated to 43 °C, this decay was even more pronounced. At further heating, only partial poling was achieved, demonstrated by a blurry and inhomogeneous contrast (Figure 4.15(g)). Then, the piezoresponse of the poled area relaxes fast to zero values after only 20 min.

In the local structure of 4BZT a pale PFM contrast was created by poling at 30 °C and 43 °C (Figure 4.16(a) and (c)). At 30 °C no residual piezoresponse was observed after 30 min (Figure 4.16(b)-(c)), while at 43 °C complete vanishing of induced domain occurs after 10 min (Figure 4.16(e) and (f)). No written domains could be detected above 50 °C, indicating a very fast relaxation of the field-induced state (Figure 4.16(g)-(i)).

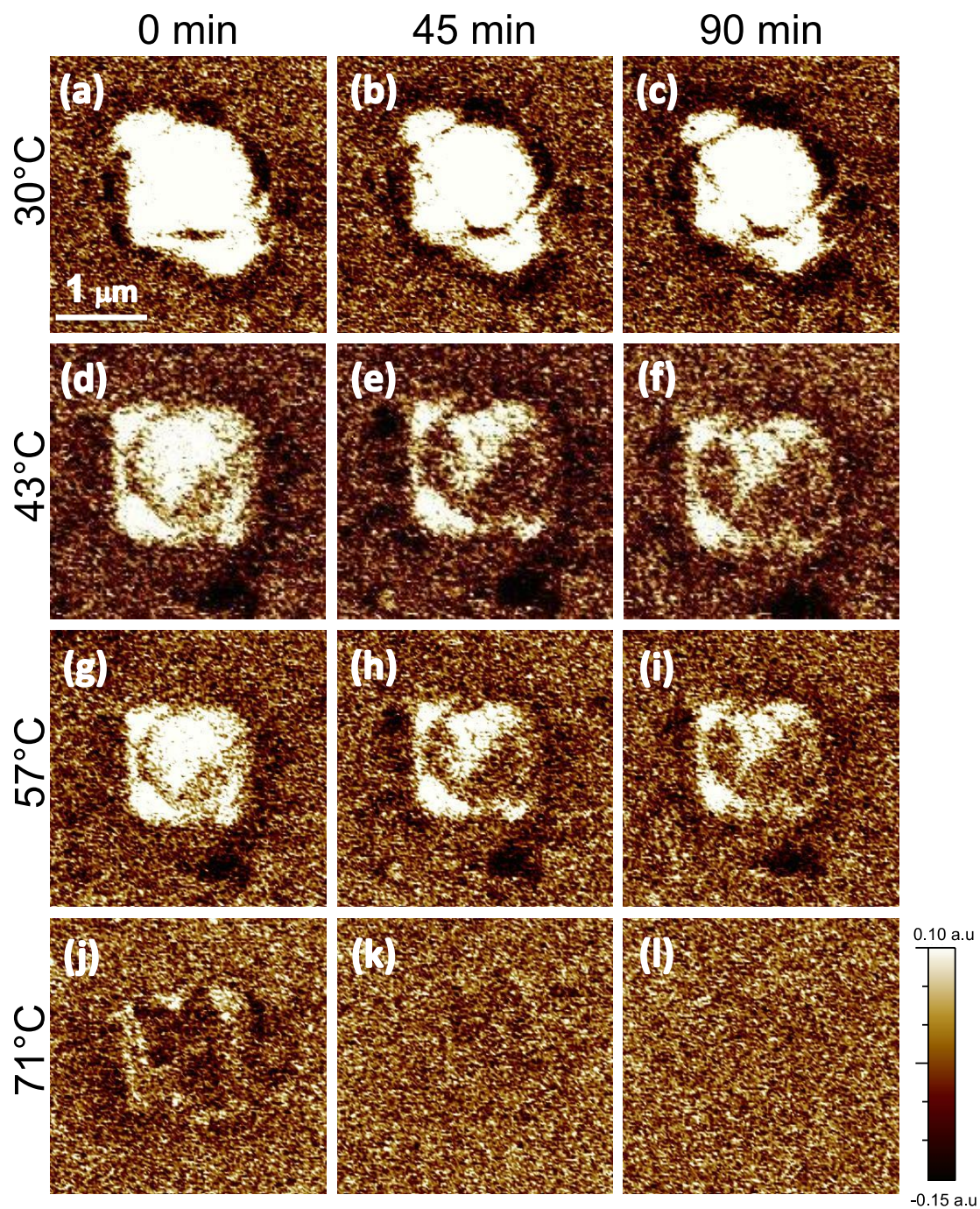


Figure 4.14: PFM images of locally poled BNT-BKT-2BZT taken at different times on heating to (a)-(c) 30 °C, (d)-(f) 43 °C, (g)-(i) 57 °C, and (j)-(l) 71 °C.

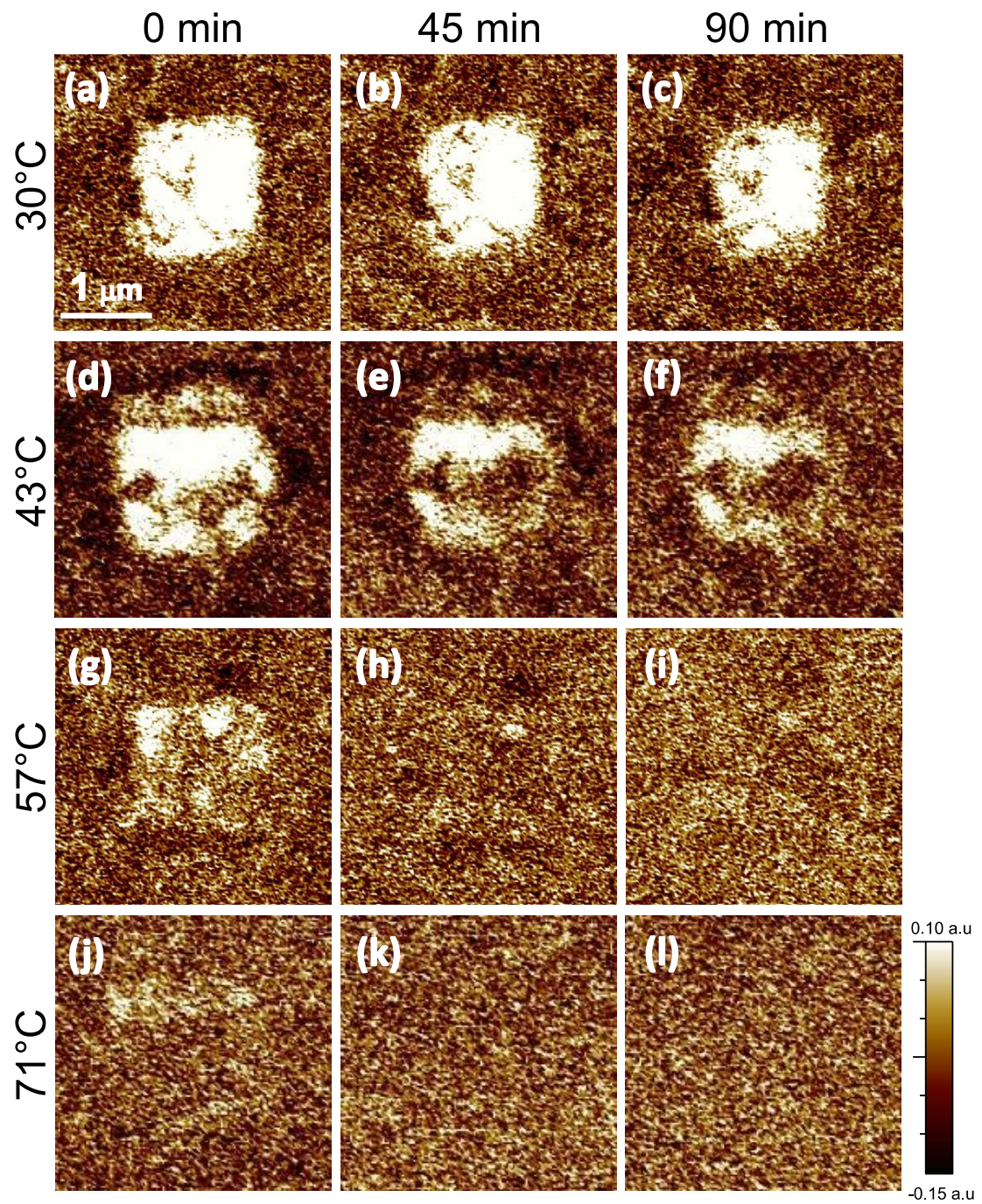


Figure 4.15: PFM images of locally poled BNT-BKT-3BZT taken at different times on heating to (a)-(c) 30 °C, (d)-(f) 43 °C, (g)-(i) 57 °C, and (j)-(l) 71 °C.

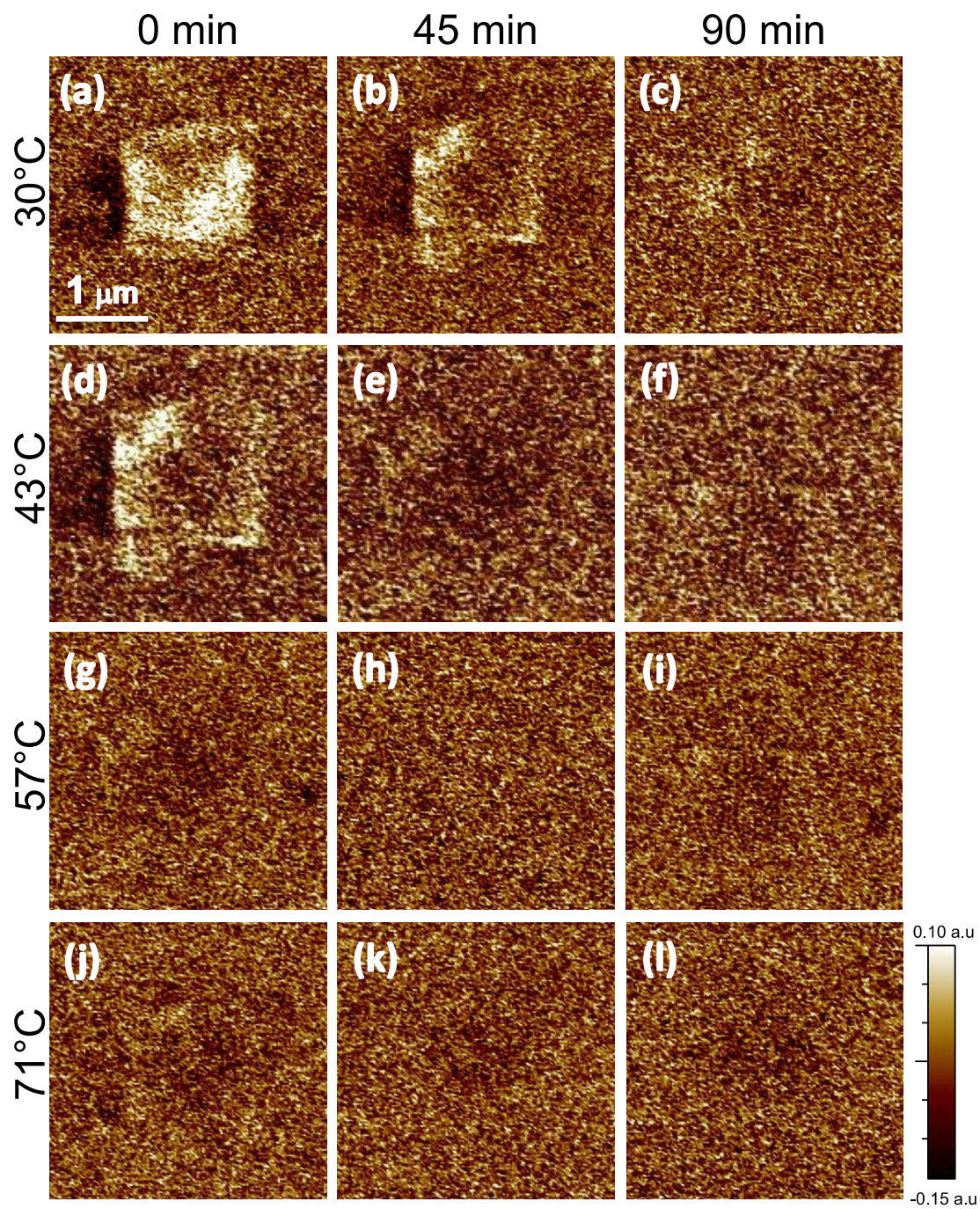


Figure 4.16: PFM images of locally poled BNT-BKT-4BZT taken at different times on heating to (a)-(c) 30 °C, (d)-(f) 43 °C, (g)-(i) 57 °C, and (j)-(l) 71 °C.



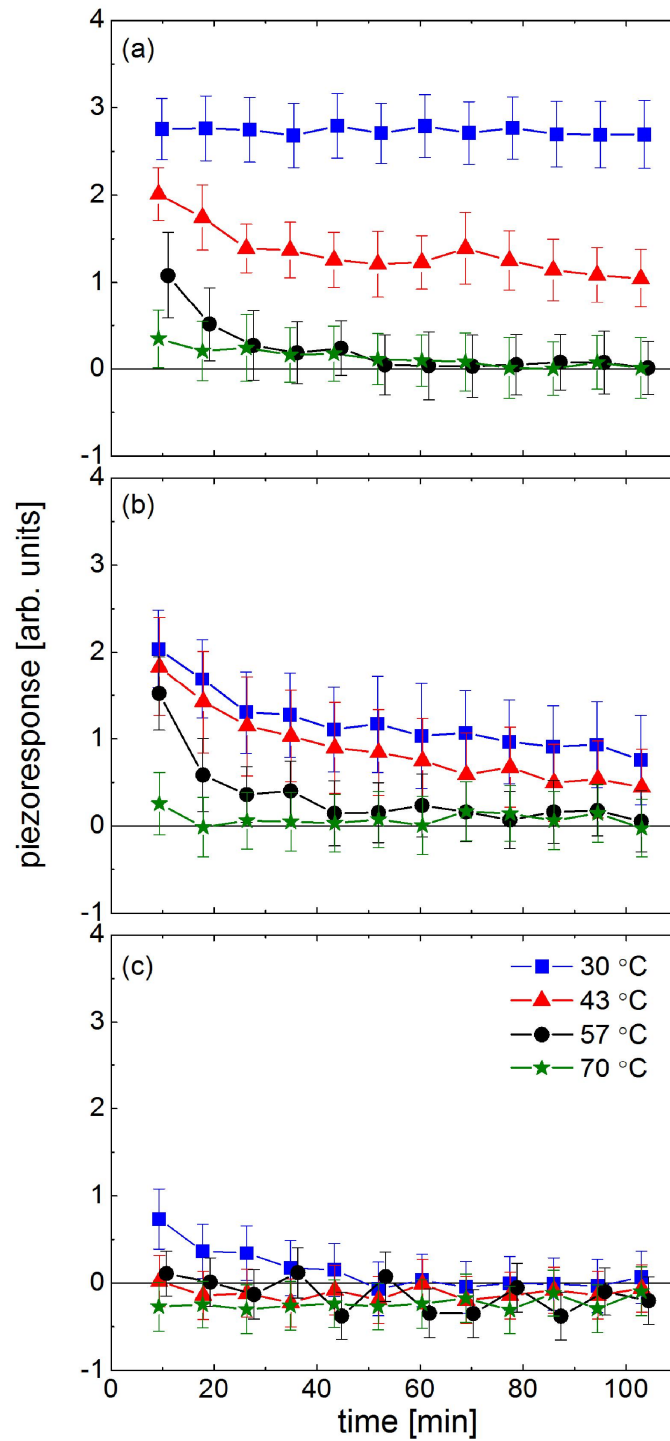


Figure 4.17: The average piezoresponse of the poled area as a function of time for (a) BNT-BKT-2BZT, (b) BNT-BKT-3BZT, and (c) BNT-BKT-4BZT.

## 4.4.2 Discussion

### 4.4.2.1 Macroscopic Properties

An in-depth investigation on the thermal and temporal stability of the field-induced ferroelectric long-range order was conducted. As mentioned before, the BNT-BKT system is considered to be a nominally nonergodic relaxor at room temperature when not or hardly chemically modified, while the nonergodicity decreases with heterovalent cation substitution. The 2BZT composition remains nominally nonergodic but ergodic relaxor properties are exhibited at room temperature in the 4BZT composition, while 3BZT exhibits intermediate behavior between 2BZT and 4BZT.

The relaxor-ferroelectric phase transition may occur in nonergodic relaxor systems as a response to an applied electric field. It has already been reported that the ferroelectric phase can be also established in the ergodic relaxor system at least at temperatures close to  $T_f$ .<sup>171,50,208</sup> Nonetheless, such an induced FE state is unstable and will return back to the ergodic state after the poling field is removed.<sup>208</sup> The relaxor-to-ferroelectric phase transition is often related to the process of coalescence of PNRs into micro-size domains prompted by the applied electric field. Moreover, establishment and reversibility of this phase transition are reported to strongly depend on the composition, applied electric field values, exposure time to it, and temperature.<sup>212,197,188</sup> An electric field applied to 2BZT at room temperature generates a ferroelectric state with a large remanent polarization, as previously demonstrated, and, consequently, a sizable piezoelectric coefficient, provided the electric field is higher than the critical value of 4 kV/mm. The macroscopic measurements show that the piezoelectric coefficient  $d_{33}$  sustains only a slight decrease of 10 % with time (Figure 4.13(a)), while at the nanoscale decay of the average local piezoresponse is smaller than statistic errors (Figure 4.17(a)). The demonstrated stability of piezoactivity denotes the irreversibility of the field-induced state for 2BZT. However, strong changes in the phase stability occur when the nonergodic-ergodic relaxor transition temperature is reached. For 2BZT, this temperature is reported to be 55 °C.<sup>212</sup> While the piezoelectric coefficient  $d_{33}$  demonstrates only a minor decay up to 57 °C, the locally induced region evolves greatly, experiencing a breakdown into nanodomains of up and down polarities already after 45 min (Figure 4.14(e) and (f)). Upon further increase of temperature, the relaxation processes change both quantitatively and qualitatively. Even the initial PFM scans reveal only disordered nanodomains that vanish rapidly with time. Eventually, an absence of any PFM contrast present after 45 min mirrors a complete transformation into the ergodic relaxor state. The very strong decay of the induced piezoresponse can be explained by the breakdown of induced domains into mainly dynamic PNRs in the absence of an ordering electric field. It might be that this degradation is the second step of a more complex relaxation process, as it was recently reported.<sup>300,264,301</sup> This scenario implies a degradation of initially induced FE order into smaller domains, as that seen at 57 °C, and subsequent decay of these nanodomains into PNRs. In this case, it appears that the first relaxation step happens relatively fast. Therefore, piezoactive nanosize domains are visualized already in the first PFM scan.

#### 4.4.2.2 Microscopic Properties

The field behavior of the 3BZT composition resembles that of 2BZT. Also in this case, the macroscopic piezoelectric coefficient  $d_{33}$  shows only minute decrease in the course of time as long as measured below the reported depolarization temperature  $T_d \approx 45^\circ\text{C}$ .<sup>171</sup> Above  $T_d$ , this decay is accelerated, but 3BZT remains partially poled at relatively high temperatures. Moreover, the locally induced domain shows no decay with time at ambient temperature. As it was already discussed in Chapter 4.3, the critical field required to induce the ferroelectric order increases as the doping concentration of  $\text{Zn}^{2+}$  ions increases. This can be considered as a contributor to both the lower degree of local poling and the lower initial value of the macroscopic piezoelectric coefficient  $d_{33}$ .

The 4BZT composition is an ergodic relaxor at room temperature, with ergodicity prompting a fast decay in both the macroscopic and the locally induced piezoresponse. At temperatures higher than  $43^\circ\text{C}$  no residual piezoresponse is recorded. At  $71^\circ\text{C}$ , the measured  $d_{33}$  is even two times smaller than for 2BZT. Here, the effect of random electric fields increases and effectively disrupts the creation of ferroelectric order.

Only weak unstable ferroelectric domains are created upon field application, and they subsequently relax to the initial featureless ergodic state after the electric field is removed (Figure 4.16(e) and (f)). These mechanisms are essential in the processes of high field-induced strain and its relapse when the electric field is switched off. The high strains are enabled by the repeated coalescence of PNRs into domains under field and their subsequent collapse back into PNRs upon field removal. As a consequence, the high poling strain can be harvested over and over again in each loading cycle. Apart from that, the here presented kinetics of relaxation are considered as essential for the severe frequency dependence of the macroscopic large-signal properties of this relaxor material.<sup>212</sup> Nucleation and growth of domains and their subsequent breakdown are strongly time-dependent processes. Therefore, the large strains achieved in this class of lead-free relaxors are assumed to diminish strongly with increasing cycling frequency. This behavior was indeed observed macroscopically.<sup>212</sup>

The relaxation processes of both macroscopic  $d_{33}$  and local piezoresponse are approximated by the stretched exponential law<sup>302,303</sup> as defined in Equation 4.5.

$$d_{33}(t) = d_{33}^0 + d_{33}^1 \exp\left(-\left(\frac{t}{\tau}\right)^\beta\right) \quad (4.5)$$

In this expression,  $d_{33}^0$  corresponds to the relaxed  $d_{33}$  value obtained after a long time period;  $d_{33}^1$  describes the relaxation strength,  $t$  is the time, while  $\tau$  is the characteristic relaxation time.  $\beta$  is the characteristic exponent and it is that  $0 \leq \beta \leq 1$ . The experimental data normalized with the corresponding initial values,  $d_{33}(t_0)$  and their best fits are plotted in Figure 4.18. All fitting

Table 4.1: Parameters of the best stretched exponential function fit of the time dependence of macroscopic  $d_{33}$  and local piezoresponse.

	$T$ [°C]	$d_{33}^l$ (normalized)		$\beta$		$\tau$	
		Macroscopic	Local	Macroscopic	Local	Macroscopic	Local
2BZT	30	0.12 ± 0.03	–	0.57 ± 0.02	–	20 ± 12	–
	43	0.10 ± 0.02	0.49 ± 0.17	0.90 ± 0.30	0.69 ± 0.16	21 ± 4	21 ± 5
	57	0.26 ± 0.03	0.95 ± 0.05	0.54 ± 0.10	0.82 ± 0.13	16 ± 5	11 ± 1
	71	0.61 ± 0.06	0.92 ± 0.03	0.38 ± 0.04	0.90 ± 0.18	13 ± 3	45 ± 7
3BZT	30	0.13 ± 0.02	0.58 ± 0.08	0.74 ± 0.27	0.85 ± 0.13	7 ± 2	23 ± 3
	43	0.18 ± 0.02	0.76 ± 0.18	0.62 ± 0.30	0.90 ± 0.08	8 ± 2	30 ± 2
	57	0.29 ± 0.02	0.93 ± 0.07	0.61 ± 0.08	0.59 ± 0.10	14 ± 2	8 ± 2
	71	0.51 ± 0.12		0.51 ± 0.16		12 ± 5	
4BZT	30	0.67 ± 0.40	0.96 ± 0.06	0.40 ± 0.30	0.93 ± 0.20	13 ± 2	18 ± 3

parameters are listed in Table 4.1. Processes which are in good agreement with the stretched exponential function have a broad relaxation time distribution. The width of the distribution is described by the  $\beta$  parameter. A single relaxation time is implied by  $\beta = 1$ , whereas  $\beta \rightarrow 0$  assigns a broad relaxation time spectrum.

For relaxation of the normalized macroscopic piezoelectric coefficient  $d_{33}$ , the fitting parameter  $\beta$  varies from  $\beta \cong 0.5$ -0.6 below  $T_d$  to  $\beta = 0.4$  above the depolarization temperature. This decrease in  $\beta$  above  $T_d$  indicates the appearance of new relaxation entities, *i.e.* dynamic PNRs. Locally, however, relaxation spectra are narrow having  $\beta \cong 0.8$ -0.91 in the entire temperature range. The discrepancy between macroscopic and the local experimental data probably originates from the difference in sample volume probed by the two approaches. The polarized state created in the PFM experiments is only of a small area with micron-size lateral dimension and presumably shallow depth. By contrast, the macroscopic investigation involves a volume several orders of magnitude larger. It is hypothesized that the larger volume is associated with a much higher variation in not only mechanical and electrical boundary conditions, but also local chemical variations, causing  $\beta$  to decrease. Consequently, the distribution of relaxation times is less pronounced at the local scale. The systematic increase of the relaxation rate with increasing temperature implies a more pronounced instability of the poled state.

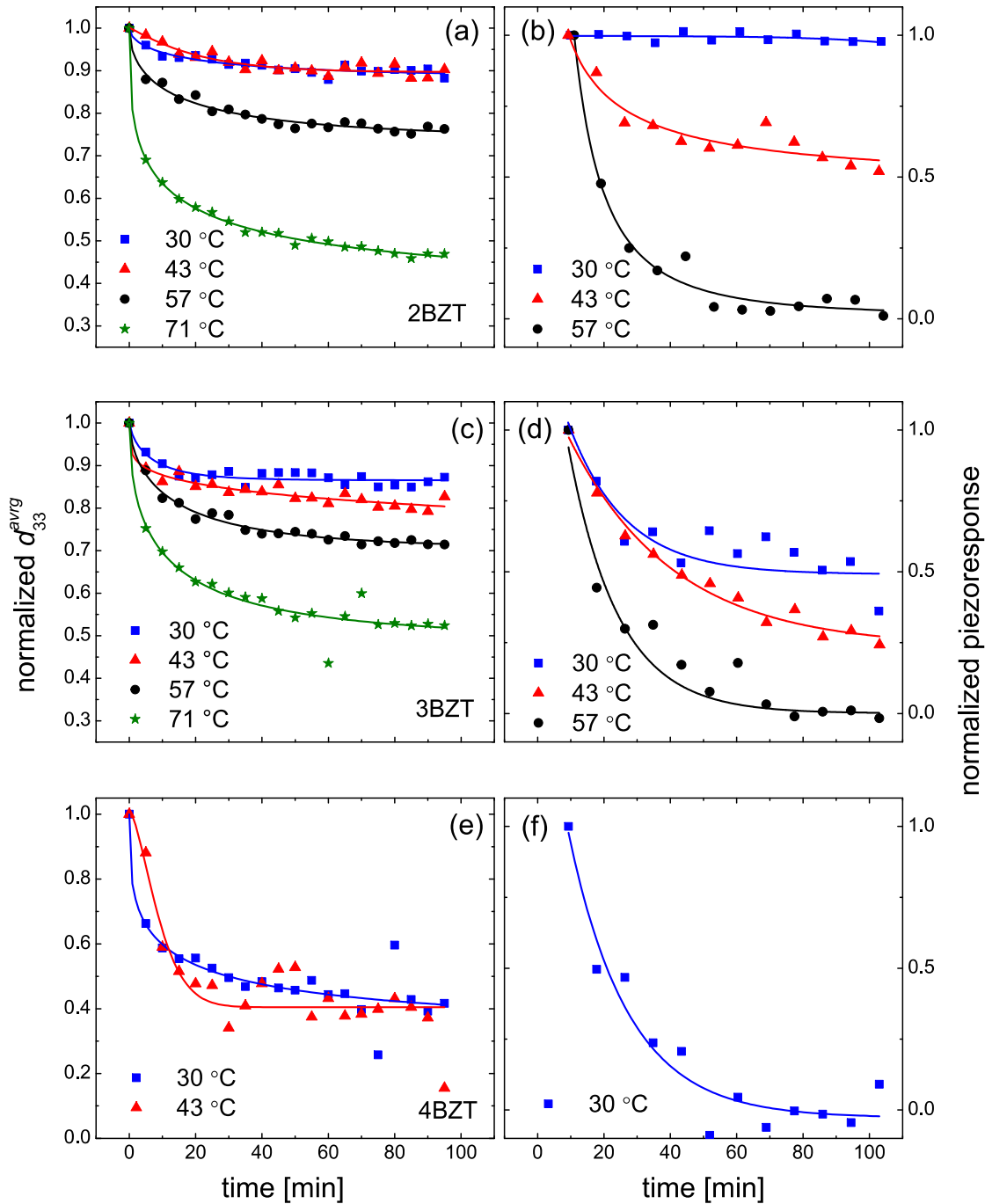


Figure 4.18: The normalized macroscopic piezoelectric coefficient  $d_{33}$  (left column) and the normalized averaged piezoresponse of the induced phase (right column) for (a, b) BNT-19BKT-2BZT, (c, d) BNT-19BKT-3BZT, and (e, f) BNT-19BKT-4BZT ceramics as a function of time after poling, performed at different temperatures. Solid lines demonstrate the best stretched exponential function fit of the experimental data.

It is interesting that the relaxation of the locally poled state occurs faster, that is, local relaxation is more efficient than for the macroscopically induced piezoactivity (Figure 4.18). Again, the difference between the macro- and microscopic data might be related to the nature of poling mechanisms that are used on two distinct length scales. In fact, contrary to the macroscopic measurements, the PFM poling creates a domain that stays in the vicinity of the sample surface and does not permeate the sample in great depth. Under these conditions, the stability of the induced domains depends on the screening conditions caused by the depolarization field which has tendency to reestablish the multidomain structure. The effect of the depolarization field can be diminished by a partial screening caused by free charge carriers localized at the domain boundaries and at the free sample surface. Therefore, since the screening of depolarization field is efficient at low temperatures, no relaxation of the induced state occurs. By contrast, the depolarization field is only partially screened at higher temperatures yielding relaxation of the local polarization. In addition, at higher temperatures the mobility of screening charges increases, meaning that the screening charges are thermally excited from shallow trap levels. These charges can be, however, towed by the scanning PFM tip and therefore the efficiency of screening can be affected. This yields stronger domain depolarization and its decay into smaller polar entities. Consequently, relaxation of the locally poled state is faster and more efficient.

It can be summarized that the relaxation mechanism above the nonergodic-ergodic phase transition is a two-step process. The decay of the induced polarization occurs by the fragmentation and realignment of the field-induced domains after the ordering electric field is removed. Similar to those ones in 2BZT at 57 °C (Figure 4.14), induced ferroelectric domains break into smaller domains, subsequently randomize, and then degrade into polar nanodomains. The macroscopic  $d_{33}$  behavior of 2BZT at this temperature contributes to the hypothesis of a two-step relaxation process. The non-zero  $d_{33}$  values at  $t=90$  min support the fact that the ferroelectric order at 57 °C does not disappear completely upon field removal. It is assumed that the grain boundaries locally stabilize the induced ferroelectric state in absence of a strong depolarization field. This two-step isothermal relaxation of the field-induced state was also observed in BNT-BT where macrodomains initially break into smaller domains, that decay into PNRs afterwards.<sup>304,264</sup>

The above discussed temporal evolution of the field-induced ferroelectric state with increasing temperature is schematically demonstrated in Figure 4.19. As a response to the applied electric field isolated PNRs coalesce and create the sharply contoured macrodomains. The polarization of the domains is aligned with the applied electric field (Figure 4.19 (a)). Ferroelectric order is established and, therefore, the material consequently exhibits a nonzero net polarization with a measurable macroscopic  $d_{33}$ . Without the electric field, the induced domains break down upon heating into smaller domains with uncorrelated polarization (Figure 4.19 (b)). This causes the decrease of the macroscopic polarization. At temperatures above  $T_d$ , uncorrelated dynamic and probably a number of static PNRs forms from the residual domains. Finally, at very high temperatures only uncorrelated PNRs reside within the relaxor until, eventually, all PNRs vanish beyond the Burn's

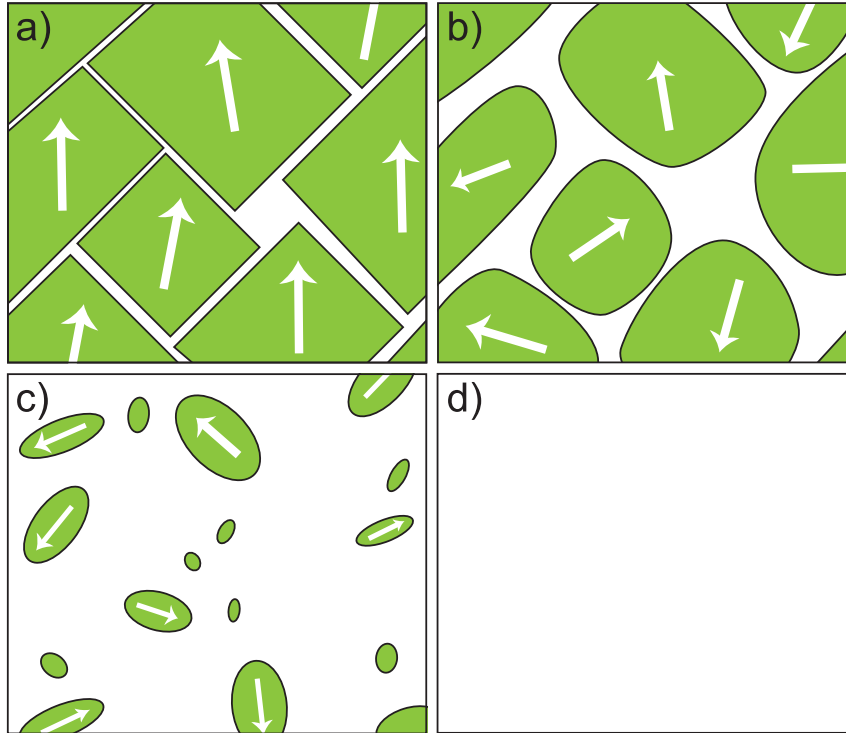


Figure 4.19: Schematic representation on the change of the field-induced state with time: (a) electric-field induced long-range order, (b) their breaking into nanodomains after electric field is turned off, (c) relaxed ergodic state with uncorrelated PNRs, and (d) paraelectric phase with no stable polar entities above Burns temperature  $T_B$ .

temperature  $T_B$ . Recently, second harmonic generation measurements have shown that the electric field creates domains which are two orders of magnitude larger than the originating PNRs.<sup>301</sup> Therefore, it should be considered that Figure 4.19 depicts the principles of the discussed thermal evolution without being in real scale with respect to the polar entities.

The conclusions derived from the conducted study confirm that the thermally driven transition from the nonergodic to the ergodic relaxor phase coincides with the depolarization temperature reported earlier from the previous macroscopic measurements.<sup>26,304</sup> In the nonergodic relaxor system, the stable ferroelectric state is obtained for electric fields above the critical value. The slight relaxation of the piezoresponse, *i.e.* polarization, occurs as an effect of the reorganization of the polar microstructure due to the mechanical and electrostatic constraints and microscopic incomplete screening of the depolarization field that destabilizes induced domains. In the ergodic relaxor phase, nonetheless, no stabilization of the field-induced phase is possible on both the local and the macroscopic scale. Here, a ferroelectric phase can be formed in part of the sample volume only in the presence of a sufficiently high electric field.

A decisive role in the establishment of the ergodic relaxor state plays the BZT doping. With an increasing BZT content, the nonergodic-ergodic transition temperature drops. Similarly to the BNT-BKT-BZT system, a crossover to the ergodic relaxor behavior by lowering the transition temperature was achieved in doped  $\text{BaTiO}_3\text{-Bi}(\text{Zn}_{1/2}\text{Ti}_{1/2})\text{O}_3$ ,<sup>305</sup>  $\text{BaTiO}_3\text{-Bi}(\text{Mg}_{1/2}\text{Ti}_{1/2})\text{O}_3$ ,<sup>306</sup> and  $\text{BaTiO}_3\text{-0.5Bi}(\text{Zn}_{1/2}\text{Ti}_{1/2})\text{O}_3\text{-0.5BiScO}_3$ .<sup>307</sup> The enhanced charge disorder and the shift of the phase transition temperature explain the pronounced instability of the field-induced ferroelectric state in 4BZT. Unlike 2BZT and 3BZT, ergodicity is particularly promoted in 4BZT as the increased BZT content further enhances random electric fields.

## 4.5 Summary

The investigation on the lead-free BNT-BKT-*y*BZT ceramics on both macroscopic and sub-micron scale demonstrated their relaxor ferroelectric nature. The increment of BZT doping influences the system nonergodicity, and, therefore, also the constitutive large-signal behavior. The drop of remanent polarization and strain with increasing  $\text{Bi}(\text{Zn}_{1/2}\text{Ti}_{1/2})\text{O}_3$  doping demonstrates the rising instability of the field-induced ferroelectric long-range order. The property field-behavior was found to be governed by the concentration of the heterovalent  $\text{Zn}^{2+}$  ions introduced by the BZT modification. Higher BZT doping promotes the charge disorder since the bivalent  $\text{Zn}^{2+}$  ions substitute the four-valent  $\text{Ti}^{4+}$  ions. Thus, the random electric fields are enhanced and the amount of dynamic PNRs in the polar structure is consequently increased. Although featureless, the domain structure of 2BZT was proposed to consist of regions with strongly correlated piezoresponse originating from static PNRs, while mainly dynamic ones are present in the structures of 3BZT and 4BZT. Neutron diffraction and PFM measurements both provide indication for the appearance of PNRs, *i.e.* increased system ergodicity as a narrowing of reflections in the neutron diffraction patterns and the instability of the locally induced FE state, respectively.

The significance of nonergodicity is identified especially for electric fields higher than 2 kV/mm in terms of electrical properties and crystal structure. Locally, 2BZT demonstrates nonergodicity through the low-field formation of a strong piezoelectric response of an induced, ferroelectric state and its temperature- and time stability.

The higher content of BZT impedes the establishment of ferroelectric order and stimulates its destabilization. Only for higher electric fields, an unstable FE state is induced in highly ergodic 4BZT. In addition, a thermally decreased degree of nonergodicity was demonstrated, reflected by the associated instability of the field-induced ferroelectric state. Destabilization of the field-established FE state was described as a complex process by which domains fragment into smaller domains and subsequently break up into dynamic polar nanoregions. Time-dependent relaxation measurements show the high-temperature decay of nonergodicity in the low-BZT compositional side, comparable to the level of that apparent in more doped compositions at room-temperature.



# 5 Polar Microstructure of Relaxor-Ferroelectric Composites

The BNT-7BT/ BNT-6BT-2KNN ceramic/ceramic composites are a new class of functional materials with peculiar local electromechanical properties and complex microstructure that challenge the conventional methods of experimental data analysis. This requires new methods of data analysis that allow identification of different phases and domain patterns on the submicron scale. Therefore, the following chapter is dedicated to a great extent, to the introduction of two methods, namely line-of-sight (*LoS*) and k-means clustering (KMC). The line-of-sight (*LoS*) method is an extensive quantitative analysis method, applied to characterize the complexity of the peculiar domain structures observed by PFM. The k-means clustering method is applied to differentiate the switching properties on the submicron scale and their correlation with the local material content and the domain morphologies.

## 5.1 Introduction

The efficient electromechanical energy conversion of ferroelectric materials is employed in a large number of technological applications, such as piezoelectric actuators, transducers, micropositioning systems, fuel injectors, and many others. Of particularly important interest for applications is the possibility of polarization manipulation by applying an external electric field. Polarization switching in ferroelectric and relaxor ferroelectric systems is a mechanism of a complex physical background. Beside a reorganization of the existing domain structure due to ferroelectric and ferroelastic domain wall motion, it involves the nucleation of new domains in the existing local domain landscape. On large scales, domain switching and domain wall motion affect physical material properties to a great extent, in particular, the dielectric permittivity, piezoelectric coefficient,<sup>308</sup> hysteretic behavior,<sup>309</sup> fatigue, and aging.<sup>310</sup>

The long-standing efforts of creating lead-free piezoelectric materials with excellent electromechanical properties have resulted in BNT-BT and KNN-based material systems and their binary and ternary mixtures. Among others, the relaxor ferroelectric pseudoternary BNT-BT-KNN system yields a giant electric field-induced unipolar strain of 0.45 %. Despite the evident large strains in this relaxor system, several major restrictions that obstruct its utilization have been distinguished. One of them is the impractically large electric field necessary to induce the giant strains, while the another one is the large  $P(E)$  hysteresis with a strong nonlinearity that indicates large losses in the material.

Several methods have been employed to improve the properties, especially concerning the mentioned drawbacks. Initial attempts suggested the realization of a 91BNT-6BT-3KNN core shell structure, where a ferroelectric core should facilitate the transition of a paraelectric shell into a ferroelectric phase, consequently mitigating the hysteretic behavior.<sup>311</sup> As reported by Lee *et al.*,<sup>312,313</sup> ceramic/ceramic composites consisting of a ferroelectric BNT embedded in a non-polar or ergodic relaxor matrix of BNKT-BiAlO<sub>3</sub>, as shown in Figure 5.1, yield a decrease in dielectric losses and a decay of the poling electric field. The large polarizability of the ferroelectric phase was hypothesized to enhance the internal electric field strength in surrounding relaxor regions as compared to the average field applied to the entire sample.

Shrout *et al.*<sup>314</sup> have studied a ceramic/ceramic lamellar heterogeneous material of alternating ferroelectric PZT and relaxor PZSnT layers, by which the advantages of both materials have been exploited. Excellent temperature stability originates from the relaxor, while large coupling factors arise from the ferroelectric component. In a subsequent work of Dausch *et al.*,<sup>315,316</sup> the model of two capacitors in series has been used to describe the effect of the ferroelectric phase in the relaxor matrix. In fact, depending on the content of the ferroelectric phase, a significant decay of the electric field required to trigger the phase transition has been achieved.

As a step forward, the realization of ceramic/ceramic material systems allows a fine optimization of the material performance by a delicate control of the volume fraction of both phases. By now, the ceramic/ceramic composite approach has yielded significant improvements of the piezoelectric and pyroelectric properties,<sup>317,318</sup> temperature stability of the dielectric permittivity,<sup>319</sup> and reliability under high electric fields loading.<sup>314</sup>

Combining an ergodic relaxor 92BNT-6BT-2KNN and a nonergodic relaxor 93BNT-7BT resulted not only in a reduction of the critical electric field, but also in a relatively high usable unipolar

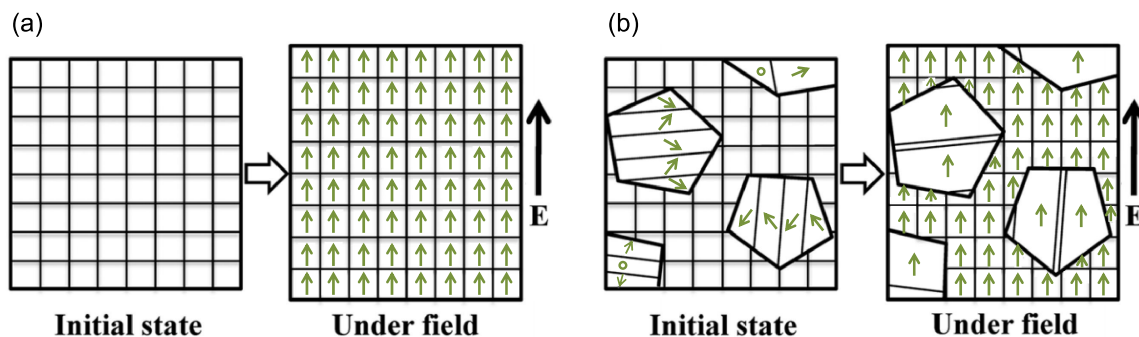


Figure 5.1: Schematic presentation of the polarization processes in polycrystalline materials exhibiting the electric field-induced phase transition (a) and polycrystalline composite materials consisting of ferroelectric large grains and non-ferroelectric small grains undergoing an electric field-induced phase transition (after Ref. [312]).

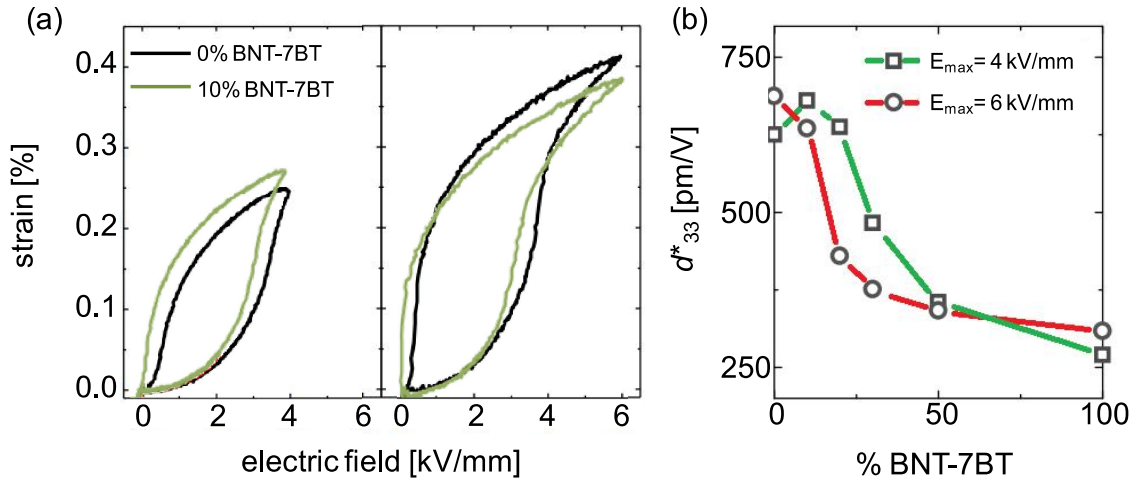


Figure 5.2: a) Unipolar strain of 0 %- and 10 %-BNT-7BT compositions at poling electric field of 4 kV/mm and 6 kV/mm. b) The effective piezoelectric coefficient  $d_{33}^* = S_{max}/E_{max}$  as a function of BNT-7BT content (after Ref. [312]).

strain of 0.38 % that can be achieved at lower electric fields for compositions with 10-30 mol% of BNT-7BT.<sup>320</sup> In the nonergodic BNT-7BT relaxor an externally applied electric field induces the irreversible phase transformation from relaxor to a ferroelectric phase. In the ergodic BNT-6BT-2KNN, however, this phase transition is reversible after the electric field switches off. The experimental data has been supported by numerical calculations,<sup>315,316,320</sup> concluding that the content of BNT-7BT in the BNT-6BT-2KNN matrix strongly determines the achievable strain level and the effective piezoelectric coefficient  $d_{33}^* = S_{max}/E_{max}$  (Figure 5.2).

However, several open questions have to be answered in order to completely understand the performance of BNT-7BT/BNT-6BT-2KNN composites. Particularly interesting are, first, the mechanism of coupling of polarization of ferroelectric-like and relaxor grains and, second, the understanding of how the field-induced phase transformation occurs within grains. An *in situ* high energy X-ray diffraction study revealed that the electric poling of relaxor grains is facilitated by the mechanical strain coupling occurring between compositionally inhomogeneous grains.<sup>321</sup> This demonstrated that the non-uniform behavior of individual grains under an applied electric field permits tuning of the macroscopic properties by incorporating grains of different phases.

On the other hand, no clear evidence for the existence of an actual composite with segregated constituents has been reported up to now. The energy-dispersive X-ray measurements revealed only a local accumulation of the relaxor phase indicated by a stronger contrast in the bright field image and a higher niobium content.<sup>320</sup> However, the crucial information on this issue can be obtained by investigating the electric-field induced polarization switching on a local scale.

The following study investigates the ceramic/ceramic composite materials with a varying volume fraction of the nominally nonergodic relaxor ferroelectric  $0.93\text{Bi}_{1/2}\text{Na}_{1/2}\text{TiO}_3\text{-}0.07\text{BaTiO}_3$  (BNT-7BT) in the ergodic relaxor ferroelectric  $0.92\text{Bi}_{1/2}\text{Na}_{1/2}\text{TiO}_3\text{-}0.06\text{BaTiO}_3\text{-}0.02\text{K}_{0.5}\text{Na}_{0.5}\text{NbO}_3$  (BNT-6BT-2KNN) matrix.

Four BNT-6BT-2KNN / BNT-7BT composite samples are investigated with the content of the nonergodic relaxor BNT-7BT being 0 %, 10 %, 30 %, or 100 %. The intragranular domain structure and the local polarization switching behavior are studied in order to examine the mutual influence of the entangled ergodic and nonergodic relaxor phases and to extrapolate from the sub-microscopic behavior to the macroscopic material performance. To find answers of interest, the relations between the chemical content, domain structure, and its spatial inhomogeneity are investigated. In addition, a comprehensive study of the peculiar domain morphologies is conducted. The line-of-sight (*LoS*) method for a quantitative analysis of the domain structure is introduced and implemented for the extensive examination of the domain structure for all composite samples. The individual grain orientation in the composite samples is investigated using the electron backscatter diffraction (EBSD) technique in order to study the effect of the crystallographic orientation on the local piezoresponse. Furthermore, the effect of phase proximity on the character of the local piezoelectric behavior is studied.

The high-resolution piezoresponse force microscopy technique significantly contributes to the investigation of both, the local domain structure in the polycrystalline materials, and their local *in situ* polarization behavior under an electric field. However, the methodological potential of the PFM technique is severely limited by, at best, the qualitative character of the acquired PFM data. A series of investigations were performed by several authors in order to quantitatively characterize the domain structure visualized by PFM. A particularly strong interest was shown for the analysis and interpretation of complex domain morphologies, such as labyrinth-like,<sup>322,323,48,324,325</sup> checkerboard-like,<sup>326</sup> stripe-like domain patterns,<sup>327,328,329</sup> and their intermixture.<sup>328,329</sup> The anisotropic stripe-like domain morphology of PMN-PT was quantitatively assessed by means of characteristic domain size and domain periodicity over a domain structure. To define the irregularity of the maze-like domain morphology of PZN-PT single crystals, fractal analysis was applied and the fractal dimension  $D$  was defined as a quantitative measure for the characteristic domain wall shape.<sup>330</sup> The average domain mean size and the preferable direction of the domain pattern are often quantitatively determined using the autocorrelation function technique.<sup>331,48</sup> The quantitative characterization of the domains in the disordered domain structures was performed in terms of domain wall roughness and effective domain dimensionality.<sup>332,309</sup>

Taking into consideration their microscopic behavior,<sup>320</sup> BNT-7BT and BNT-6BT-2KNN are below referred to as nonergodic (NE) and ergodic relaxor (ER) components, respectively.

This study was performed in collaboration with the Center for Nanophase Materials Sciences, Oak Ridge National Laboratory, Oak Ridge, Tennessee, USA (Dr. Sergei V. Kalinin, Dr. Stephen

Jesse, Dr. Alex Belianinov) and the department for materials science, University of Technology Darmstadt, Germany (Dr. Claudia Groh, Prof. Dr.-Ing. Jürgen Rödel).

## 5.2 Experimental Methods

### 5.2.1 Material Processing and Sample Preparation

The ceramic powders were prepared in accordance with the standard mixed oxides route. The  $0.93(\text{Bi}_{1/2}\text{Na}_{1/2})\text{TiO}_3\text{-}0.07\text{BaTiO}_3$  and  $0.92(\text{Bi}_{1/2}\text{Na}_{1/2})\text{TiO}_3\text{-}0.06\text{BaTiO}_3\text{-}0.02(\text{K}_{1/2}\text{Na}_{1/2})\text{NbO}_3$  constituent powders were prepared separately. The oxides or carbonates of the respective elements, namely  $\text{Bi}_2\text{O}_3$  (99.975 % purity),  $\text{BaCO}_3$  (99.8 %),  $\text{K}_2\text{CO}_3$  (99.0 %),  $\text{NaCO}_3$  (99.5 %),  $\text{TiO}_2$  (99.6 %), and  $\text{Nb}_2\text{O}_5$  (99.9 %) (all Alfa Aesar GmbH & Co. KG, Karlsruhe, Germany), were mixed in accordance with the stoichiometric formula. The preparation is similar to that one explained in Chapter 3. After ball-milling the powders in ethanol solution and drying for 24 h, the powders were calcined for 2 h at 700 °C and for another 3 h at 800 °C in covered alumina crucibles (Morgan Technical Ceramics W. Haldenwanger Technische Keramik GmbH & Co. KG, Waldkraiburg, Germany) using a box furnace (L9/KM, Nabertherm GmbH, Lilienthal, Germany). To enhance the compositional homogenization, the BNT-7BT powder is once more milled for 20 min, while BNT-6BT-2KNN is milled for additional 24 h. The powders of the composite samples BNT-7BT and BNT-6BT-2KNN were mixed in 0:100, 10:90, 30:70 and 100:0 vol% ratios, respectively, and mixed for 30 min on a rolling bank. The powders were uniaxially pressed into pellets of 10 mm diameter. After cold isostatic pressing, the sintering of the samples was performed in covered alumina crucibles at 1100 °C for 3 h. The evaporation of volatile elements is mitigated by partial coverage of the specimens with the respective powders. The created sample pellets were ground down to approximately 650  $\mu\text{m}$  thickness. Final preparation of the samples for the microscopy experiments was performed in accordance with the procedure described before.

### 5.2.2 Electron Backscatter Diffraction

Electron backscatter diffraction (EBSD) in the scanning electron microscope is a high resolution technique capable of determining the morphology of the grains yielding quantitative measurements of the grain orientations. For EBSD experiments, the sample surface was polished to optical quality down to 1/4  $\mu\text{m}$  without additional etching. EBSD was performed in a Zeiss Supra VP55 field emission scanning electron microscope. Prior to the experiments, the samples were fixed to the sample holder using carbon paste. At a working distance of 17-18 mm and a sample tilting of 20° with respect to the electron beam, it was possible to optimize the contrast of the Kikuchi patterns. EBSD data were acquired using a beam with an accelerating voltage of 20 kV at a current of 4 nA. The recording and indexing rate approaching ten points per second enabled

optimization of the contrast of the Kikuchi patterns. The acquisition with an integration time of 20 ms was performed and averaged 5-10 $\times$ . The EBSD and PFM experiments were performed for the same sample regions.

### 5.2.3 Piezoresponse Force Microscopy

The piezoresponse force microscopy experiments were performed to characterize the local properties of BNT-7BT/ BNT-6BT-2KNN composite samples with varying content of BNT-7BT component. Using single-frequency PFM, virgin domain structures of all four samples were visualized. The PFM experiments were carried out on a Cypher AFM (Asylum Research, Santa Barbara, California, USA). The cantilever tips coated with Pt/Ir (PPP-EFM-W, Nanosensors<sup>TM</sup>, Neuchâtel, Switzerland) had a resonant frequency of approximately 75 kHz and a force constant of 2.8 N/m. To avoid polarization switching, domain structures were imaged at low *ac* voltages,  $V_{ac}=2V$ . The enhanced piezoresponse was obtained by selecting the frequency of the scanning voltage to be in the vicinity of the cantilever contact resonant frequency, typically at  $f \approx 280$  kHz. The resulting PFM responses were collected in the form of 2D amplitude and phase images.

Local switching behavior was studied by collecting multiple hysteresis loops over a 2D spatial grid using combined switching spectroscopy piezoresponse force microscopy (SS-PFM) and band excitation (BE), both described previously. This set of measurements was performed at a Cypher AFM equipped with an external high voltage amplifier and a custom-built BE controller. Hysteresis loops were collected by applying a triangular waveform consisting of a sequence of voltage pulses with amplitude changing at constant time intervals. Voltage pulses were used for polarization switching (writing step), where the piezoresponse was read between two *dc* pulses (reading step). The hysteresis loops were collected over a 40 $\times$ 40 grid of points. Six triangular waveforms with gradually increasing amplitude from 5 V to 45 V were applied at each grid point. PFM data acquisition and system control were enabled by custom-made LABVIEW and MATLAB codes. Data post-processing was performed using WSxM<sup>261</sup> and MATLAB software. This PFM investigation was performed at the Center for Nanophase Materials Sciences (CNMS) within the Oak Ridge National Laboratory (ORNL, Oak Ridge, TN, USA).

## 5.3 Experimental Results

### 5.3.1 Domain Structure

The domain structures of composite samples with different contents of nonergodic relaxor phase BNT-7BT are presented in Figure 5.3. The spatial maps of domain morphologies are depicted in form of amplitude and phase PFM signals.

Grains of different size, split into domains, are clearly seen in the PFM images for all four samples. The amplitude signal corresponds to the strength of the piezoresponse that strongly depends on the grain crystallographic orientations. The phase signal represents the direction of the polarization vector of a local area underneath the PFM tip. The bright regions seen in the phase signal reveal the 'positive' polarization, *i.e.* the polarization vector directs up with respect to the image plane. In contrast, domains with 'negative' polarization are PFM mapped as dark regions with the polarization vector pointing down.

The detailed analysis of the domain structures distinguishes several characteristic features. For the pure ergodic relaxor BNT-6BT-2KNN sample (0%NE) the local microstructure features two types of domain patterns: disordered labyrinth- and distorted stripe-like domains. The labyrinth-like type of domains typically appears within grains with a strong PFM amplitude signal, as seen for grain A in Figure 5.3(a). The stripe-like domains, by contrast, are characteristic for grains with relatively weak PFM signal, as it is a case for the dark shaded grain B.

Although the content of embedded nonergodic component increases to 10 % (10%NE), no drastic changes are observed in the domain morphology. Along the entire area the labyrinth-like and quasi-stripe morphologies are dominant. A weak modification in the domain shape is the shortening of labyrinth domains. This effect is clearly observed in grain C marked in Figure 5.3(d). Significant variations in the typical domain morphology are, however, found as the content of the nonergodic constituent further increases. For 30% BNT-7BT/70% BNT-6BT-2KNN (30%NE), a new type of domain is formed appearing as checkerboard-like patterns. It is characterized by the larger feature size as presented in Figure 5.3(e)-(f). The peculiar domain structure of 30%NE demonstrates the existence of domains of various shapes, changing from labyrinth-like, as seen within grains E and G, to square-like, as featured in grain D. Interestingly, the average domain size notably increases with respect to the domains observed in samples with lower NE content.

Eventually, the domain structure of BNT-7BT (100%NE) mainly consists of checkerboard domain patterns. Here, the longitudinal and transversal domain dimensions consequently become similar. Elongated, stripe-like features are yet observed within some grains, but they seem to have larger width than in the pure relaxor sample 0%NE (Figure 5.3(g)-(h)).

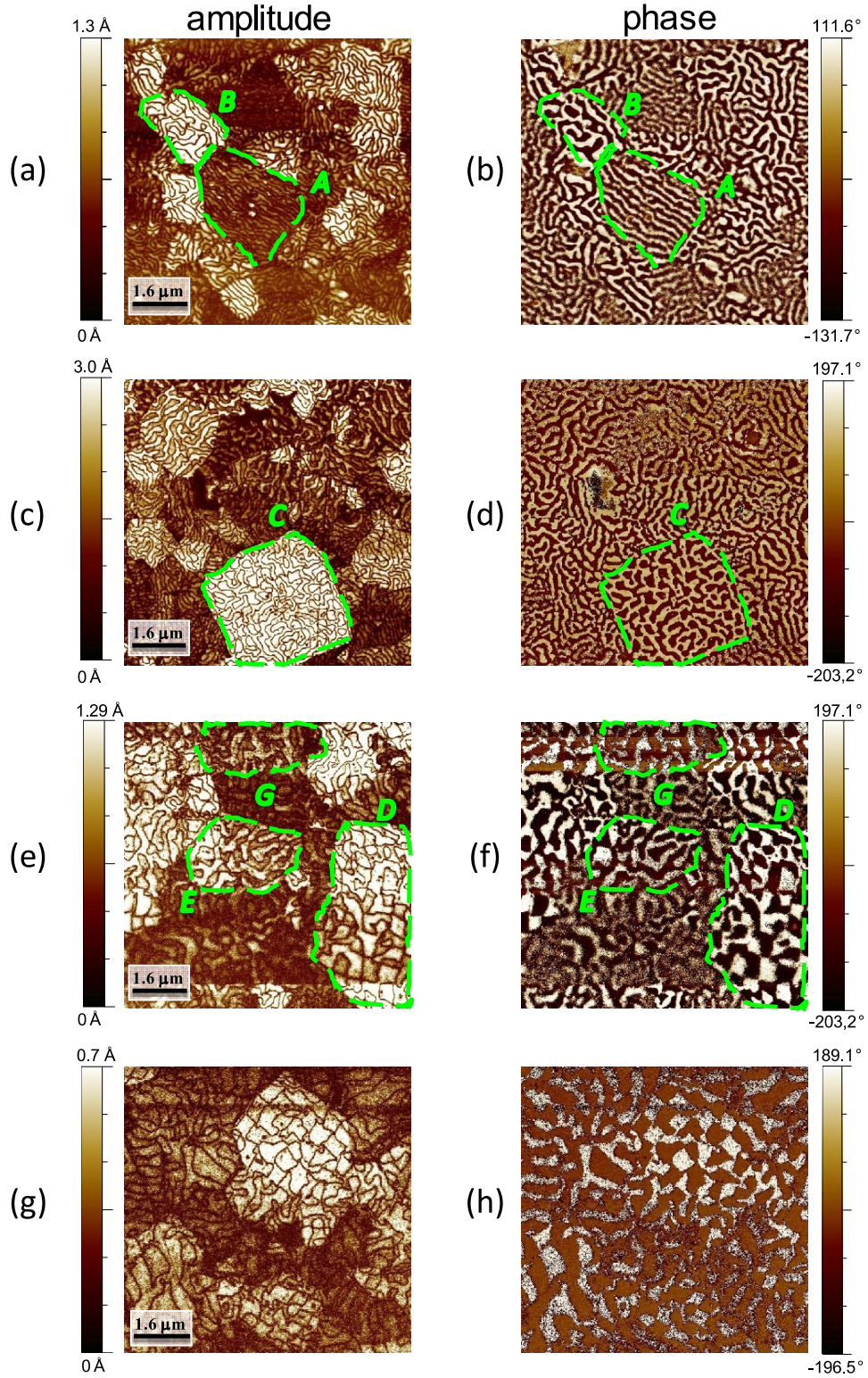


Figure 5.3: Amplitude and phase PFM images of the BNT-6BT-2KNN / BNT-7BT ceramic/ceramic composites with different content of nonergodic relaxor BNT-7BT:

0 % (a, b), 10 % (c, d), 30 % (e, f), and 100 % (g, h).



### 5.3.2 EBSD Results

To get information about the grain orientation of the composite samples the EBSD technique was applied.<sup>333,334,335,336,337</sup> The spatial distribution of the grain orientation on the sample surfaces is visualized as false color EBSD maps. The colors describe the crystallographic directions of grains which can vary between  $\langle 001 \rangle$ ,  $\langle 011 \rangle$ , and  $\langle 111 \rangle$  crystallographic directions. Typical EBSD maps generated for 0%NE, 30%NE, and 100%NE samples are presented in Figure 5.4. Note that 10%NE has been omitted from this EBSD study due to the lack of sufficient discrimination from 0%NE. The EBSD maps indicate that the orientation of grains varies all over the sample surface for each sample. Numerous grains in 0%NE are oriented along and around  $\langle 101 \rangle$  and  $\langle 111 \rangle$  directions. The largest grains have an orientation around  $\langle 001 \rangle$ . The EBSD map for the 30%NE sample confirms an increase of the average grain size. Here, the largest grains are oriented along  $\langle 101 \rangle$  and  $\langle 111 \rangle$  directions, while the small grains have different orientations. A large number of grains are oriented around the  $\langle 101 \rangle$  direction (grains colored green) as well as close to the  $\langle 111 \rangle$  direction, as indicated by the purple color. For 100%NE, significantly larger grains in respect to those in 0%NE are detected (Figure 5.4(c)). The orientation of the largest grains are mostly around the  $\langle 111 \rangle$  direction (blue and sky blue colors).

The EBSD data is furthermore utilized in combination with the PFM data obtained for the same sample regions. This is employed to investigate whether the variations in the local piezoelectric response and the characteristic domain morphologies of grains is predetermined by the specific grain orientation. The outcome of the EBSD-PFM data comparison is elaborated in more details in the discussion chapter.

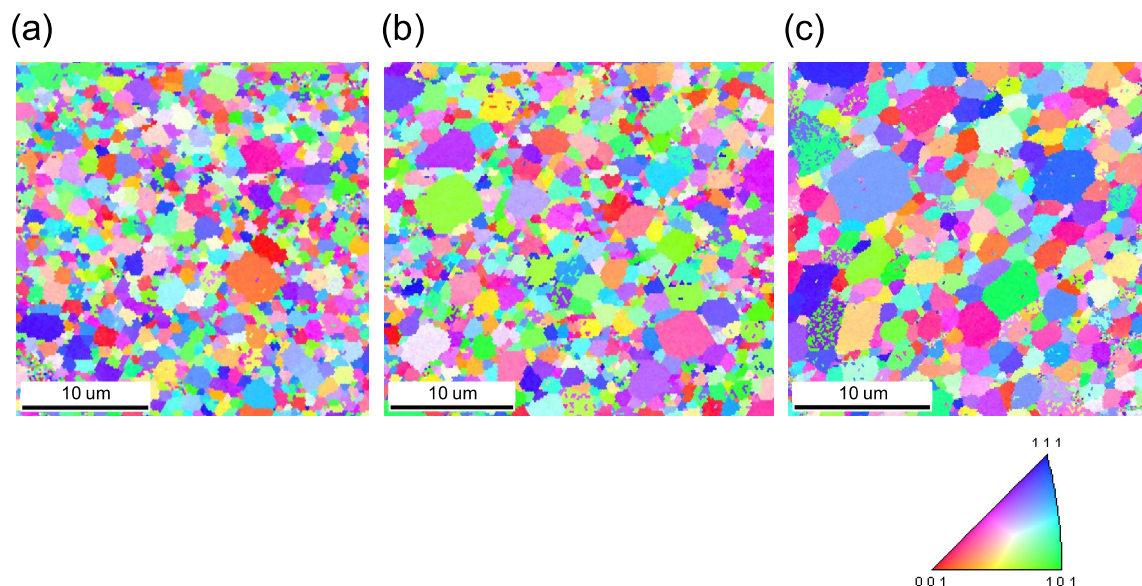


Figure 5.4: Electron backscatter diffraction diffraction images of (a) 0%NE, (b) 30%NE, and (c) 100%NE samples.

### 5.3.3 Comparison Between EBSD and PFM Results

In order to investigate the correlation between the local piezoelectric response, characteristic domain morphologies, and local grain symmetry, the EBSD and PFM measurements were performed over the same area of each sample. This was assured by the alignment of sample topographies recorded during both measurements, but also comparing the grain assemblies observed in EBSD and PFM maps.

The correlation of PFM and EBSD maps for 0%NE demonstrates different types of grains, regardless of location (Figure 5.5). The strongest PFM response (bright contrast) emanates from the grain crystallographic orientation close to the  $\langle 001 \rangle_c$  direction. Within these grains, labyrinth-like domain patterns are dominant. The grains that contain quasi-stripe domain patterns are, by contrast, oriented approximately along the  $\langle 111 \rangle_c$  direction. The PFM signal of these domains is relatively small, which can be recognized as a dark contrast in the PFM amplitude image.

Detection of the grain orientation for the 30%NE sample is particularly interesting considering it is a composite material consisting of both BNT-7BT and BNT-6BT-2KNN phases. It is hypothesized that morphologies within grains might be closely related to the crystallographic orientation of the grain. As Figure 5.6 shows, beside having high PFM piezoresponse, domains of the checkerboard-like morphology are located within the grains that are oriented around the  $\langle 001 \rangle_c$  axis. This might imply the tetragonality of the 'checkerboard' grains on the local scale. A similar checkerboard morphology has been reported to correspond to the minimum energy patterns permitted in the tetragonal system.<sup>338</sup> The bright piezoresponse of  $\langle 001 \rangle_c$  oriented grains might be related to the fact that along this direction the grains are of the maximum longitudinal response. It was recently shown that the variation in the piezoelectric contrast depends on the grain orientation, that is, on the angle between the local polarization vector and the vector of the electric field.<sup>48,339</sup>

Grains having the weakest PFM amplitude are identified to be oriented around the  $\langle 111 \rangle_c$  axis. The dominant domain morphology in this type of grains is the stripe-like one. Tsou *et al.* demonstrated that ferroelectric stripe-like domains predominantly form in structures with an  $\langle 111 \rangle_c$  crystallographic axis.<sup>338</sup> The comparison of PFM and EBSD data, furthermore, reveals that grains with dimmed piezoresponse have a crystallographic axis in plane, *i.e.* around  $\langle 101 \rangle_c$ . It is interesting that recent energy-dispersive X-ray (EDX) measurements performed for these composite materials could also distinguish different type of grains which could be assigned by their chemical content, either to BNT-7BT or BNT-6BT-2KNN.

Finally, there are two types of typical grains in 100%NE. The grains that contain checkerboard-like domain patterns have the strongest PFM signals and are typically oriented along the  $\langle 001 \rangle_c$  direction (Figure 5.7). In addition, numerous grains split into large stripe-like domains that exhibit the weakest PFM signals and are directed along the  $\langle 111 \rangle_c$  direction.

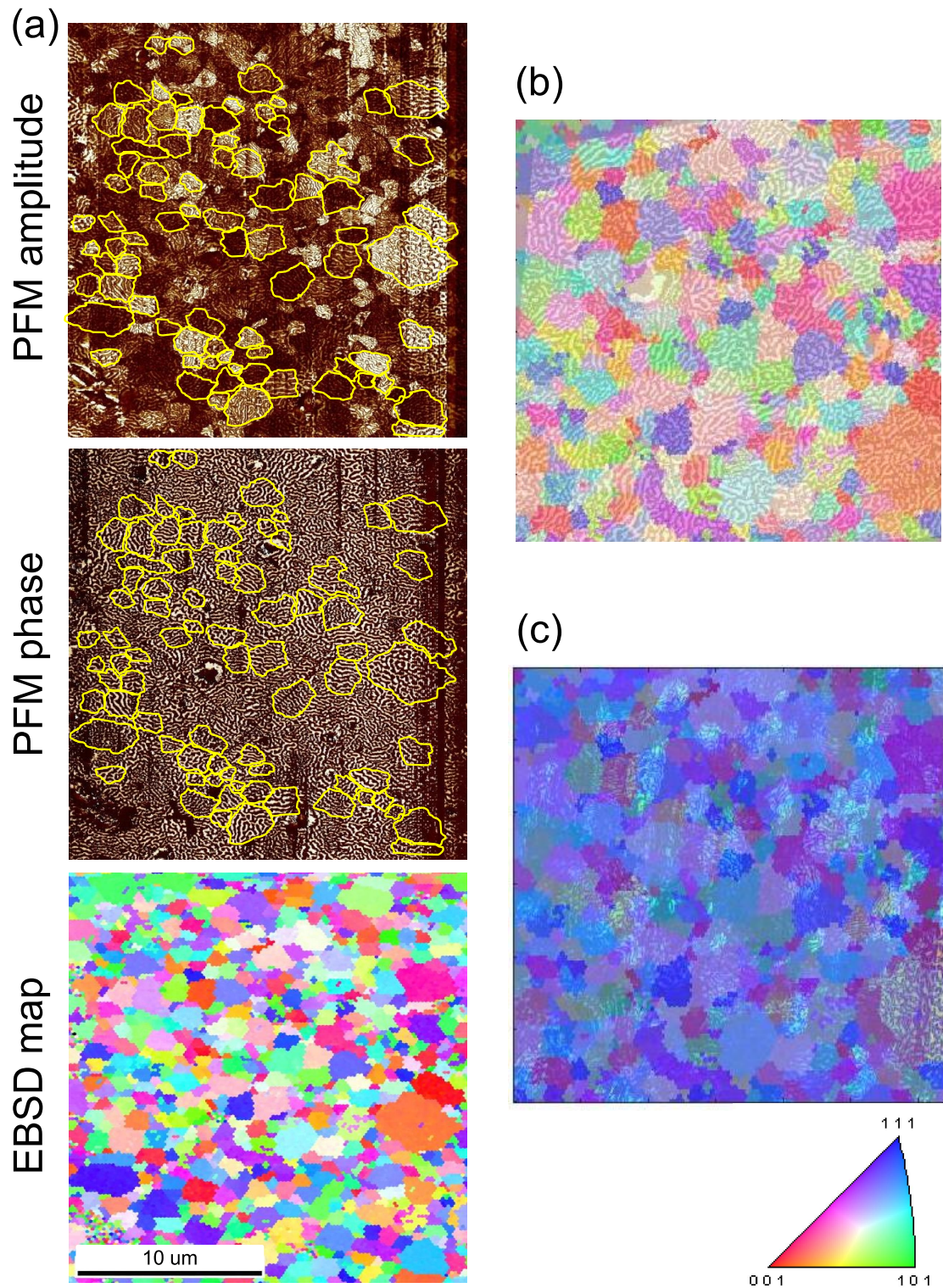


Figure 5.5: (a) PFM and EBSD images obtained at the same position for the ergodic relaxor BNT-6BT-2KNN; (b) Overlap of the PFM phase image and EBSD map; (c) Overlap of the PFM amplitude image and EBSD map. EBSD map from Figure 5.4 is shown here again to allow easier comparison.

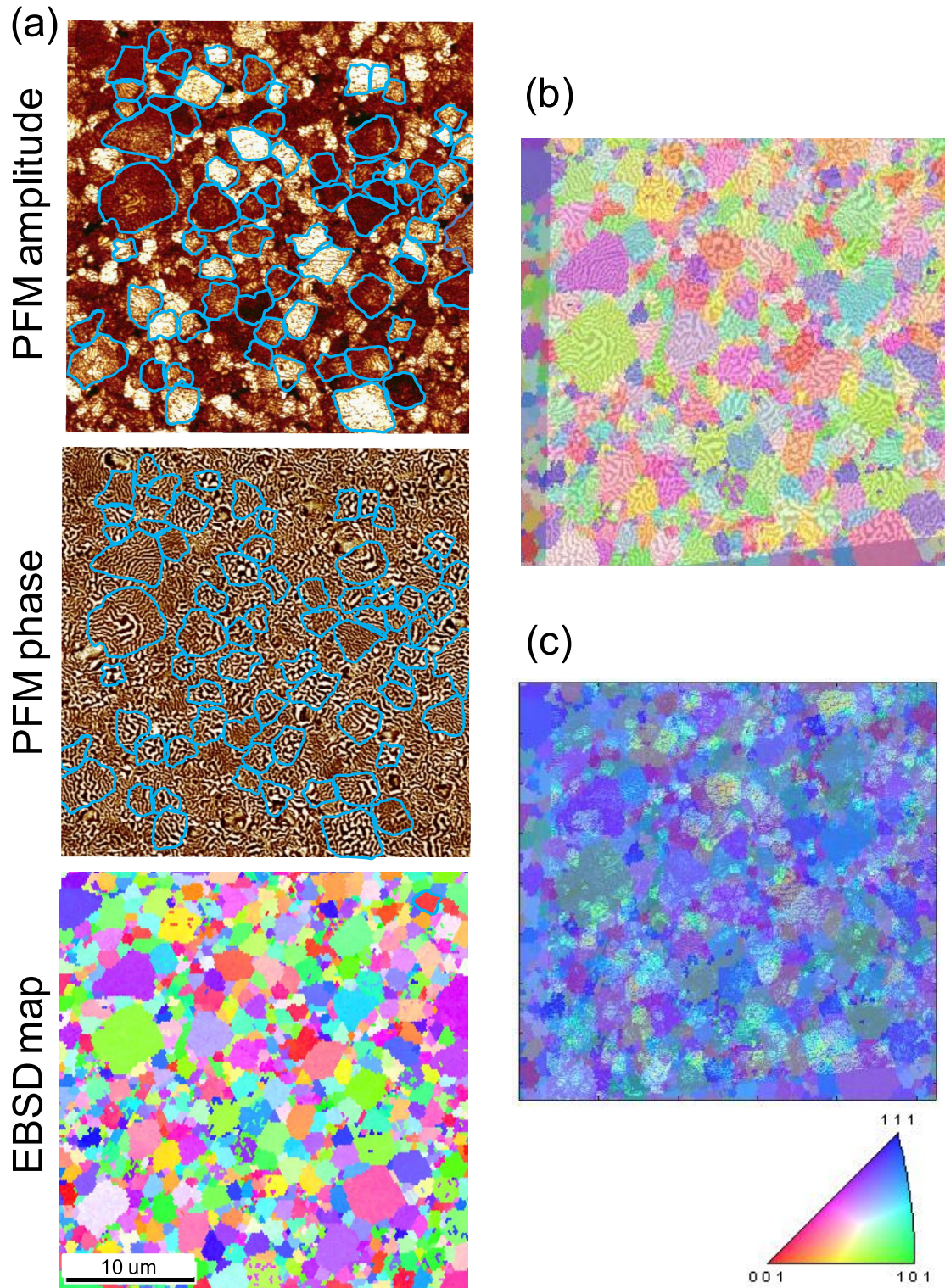


Figure 5.6: (a) PFM and EBSD images obtained at the same position for the composite ceramics with 30 % of BNT-7BT phase; (b) Overlap of the PFM phase image and EBSD map. To achieve proper alignment of the two maps, the PFM map is additionally rotated; (c) Overlap of the PFM amplitude image and EBSD map. EBSD map from Figure 5.4 is shown here again to allow easier comparison.

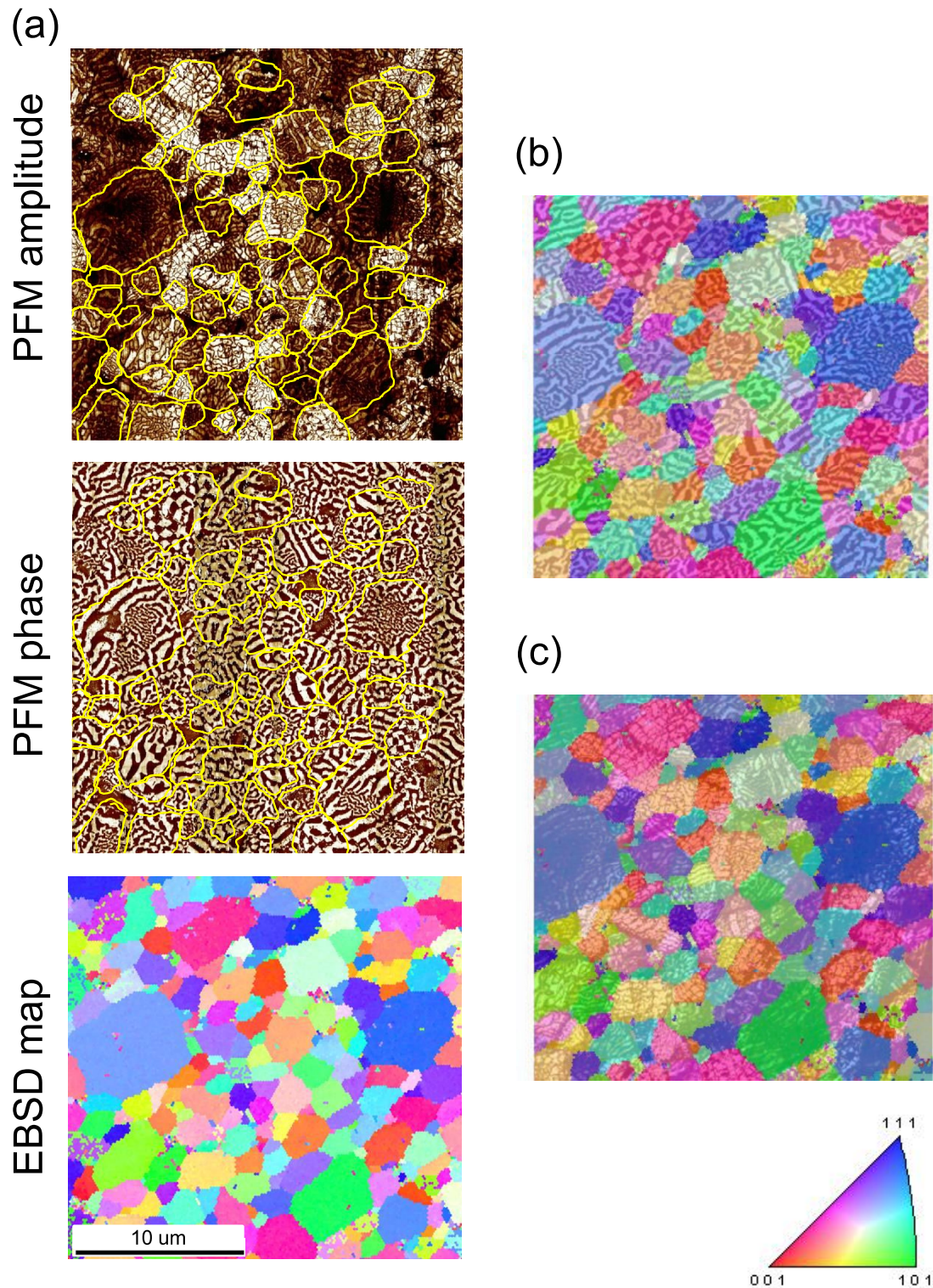


Figure 5.7: (a) PFM and EBSD images obtained at the same position for the nonergodic relaxor BNT-7BT; (b) Overlap of the PFM phase image and EBSD map. To achieve proper alignment of the two maps, the PFM map is additionally rotated; (c) Overlap of the PFM amplitude image and EBSD map. EBSD map from Figure 5.4 is shown here again to allow easier comparison.

### 5.3.4 Switching Properties

The local switching properties of ceramic/ceramic composite samples are examined from several perspectives and in respect to the content of BNT-7BT. Taking into consideration the questions opened by a recent macroscopic study concerning strain optimization by the composite approach,<sup>340,254,341</sup> the character of local switching behavior is approached on several length scales.

- (1) Average switching properties of each composite sample (compositional diversity).
- (2) Switching behavior on the single grain scale (constituent diversity). This aspect is based on the assumption that the observed labyrinth and checkerboard domain morphologies are distinctive features of ergodic or nonergodic relaxor constituents, respectively. More details on the problematic of this aspect can be found in the corresponding discussion section.
- (3) Switching behavior of a single relaxor grain as dependent on the distance from the boundary of the neighboring nonergodic grain (proximity effect).

The local switching behavior of the materials is evaluated in terms of the following characteristic parameters: maximum piezoresponse,  $D_{max}$ , remanent piezoresponse at zero bias voltage,  $D_0$ , coercive voltage,  $V_0$ , and the work of switching, *i.e.* the area within the hysteresis loop,  $A_s$ .

#### a) Compositional Diversity

1600 local hysteresis loops were collected over a  $5\mu\text{m} \times 5\mu\text{m}$  scan area for each composite sample. The effective average hysteresis loops for all four compositions are compared in Figure 5.8.

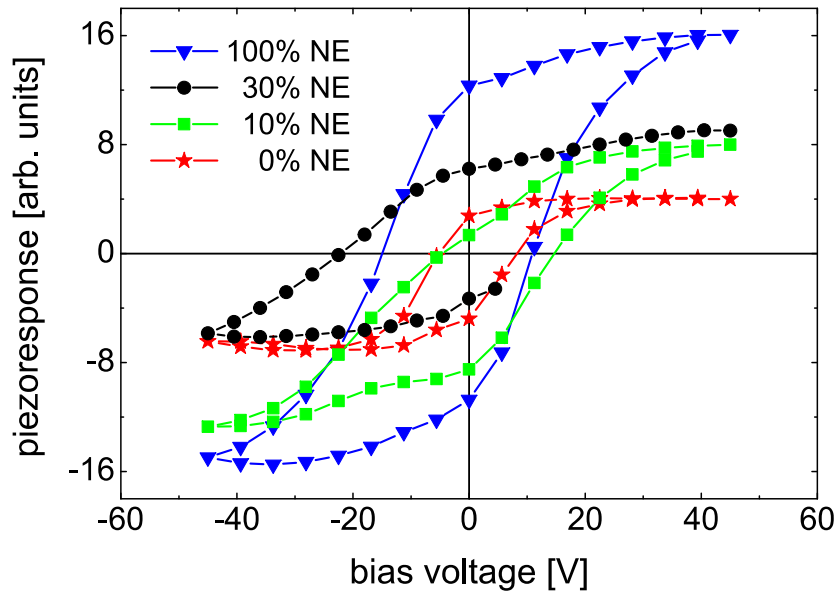


Figure 5.8: Spatially averaged local hysteresis loops for composites with different content of 93BNT-7BT (NE).

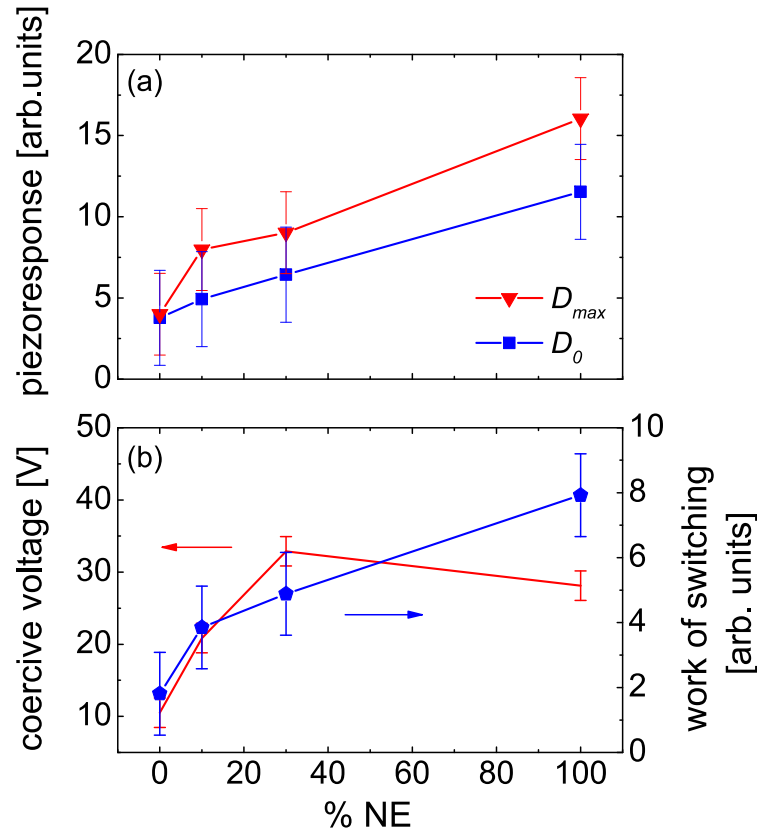


Figure 5.9: Compositional diversity: BNT-7BT content dependence of the averaged hysteresis loops parameters: maximal  $D_{max}$  and remanent piezoresponse  $D_0$  (a), coercive voltage and work of switching (b).

The plotted loops correspond to the last switching cycle local loops averaged over the entire  $40 \times 40$  grid of points and obtained at the maximum amplitude of the poling voltage. Significant variations in the average local poling behavior occur as the amount of the NE content changes. First, the 100%NE sample demonstrates typical ferroelectric properties. The square-like and symmetric hysteresis loop exhibits a very strong maximum piezoresponse  $D_{max}$  and a large remanent piezoresponse  $D_0$ . With NE content decreasing to 30 vol%, both  $D_{max}$  and  $D_0$  experience a strong decay. The average hysteresis loop of the 10%NE sample, furthermore, shows a slim hysteresis and an additional decrease in the remanent piezoresponse. An almost linear decrease of the piezoresponse is observed as the volume fraction of the NE constituent decreases (Figure 5.9(a)). It is interesting to note that for the case of 0%NE the low value of the maximum piezoresponse remains almost constant with the drop in  $dc$  bias from maximum value to zero, which is not the case for the other samples. Figure 5.9(b) compares the coercive voltages and the hysteresis areas as function of the BNT-7BT content.

It is apparent that the voltage needed to perform switching grows fast with increasing NE content and is maximized for 30%NE. Likewise, the area of the switching loop, which denotes the work of switching,<sup>274</sup> grows with NE content and it is largest for the pure NE sample.

### b) Constituent Diversity

By comparing the composite domain structures it can be assumed that the characteristic domain morphology is strongly ruled by the material content. Therefore, the character of local polarization switching is expected to be correlated with the composition of a single grain. This assumption can be verified by the evaluation of switching dynamics on the level of single grains. The constituent diversity method analyzes the switching property in a similar manner as in the compositional diversity approach. However, it compares the local hysteresis loops averaged over the entire area of grains that are assumed to be either of pure nonergodic or ergodic content. As mentioned, the checkerboard-like patterns presumably belong to a grain consisting of the nonergodic relaxor BNT-7BT (NE grain), whereas the ergodic BNT-6BT-2KNN phase is manifested as labyrinth-like domain patterns (ER grain). The local switching properties of 30%NE are analyzed. A grain with the checkerboard-like and a grain with the labyrinth-like domain morphology are considered (Figure 5.10(a)).

The average local loop of a 'checkerboard' grain demonstrates ferroelectric character with large maximum and remanent piezoresponses. In this grain, switching is successfully performed in both directions although a complete loop saturation is not achieved at the maximum applied

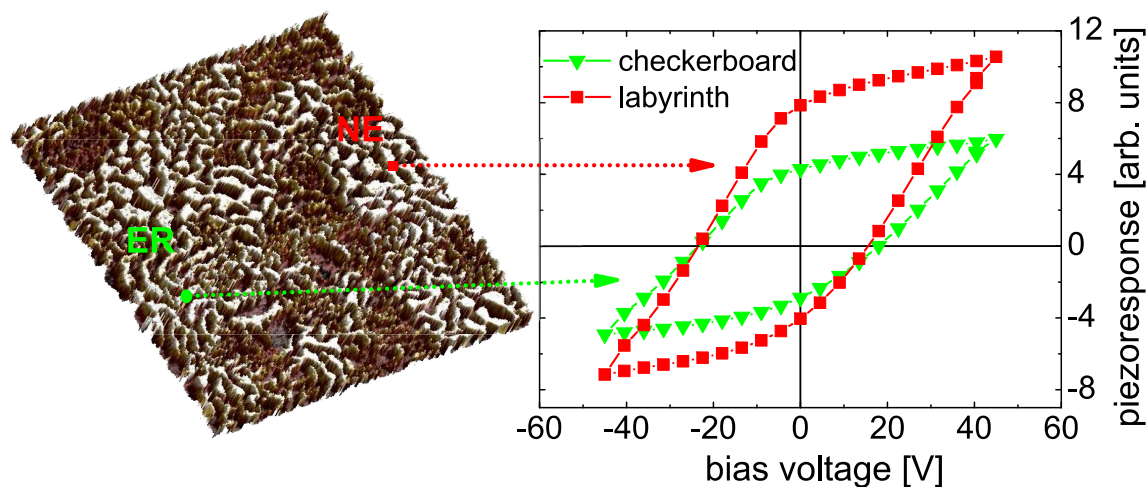


Figure 5.10: Constituent diversity: PFM phase image of the composite ceramic with 30 % of 93BNT-7BT phase (left) and intragrain averaged local hysteresis loops for grains with 'labyrinth' and 'checkerboard' domain patterns (right). The grains are marked in the left panel.



voltage. In the ER grain notably weaker piezoelectric activity is induced, although the coercive voltages are approximately the same as for the NE grain. A comparably low value of the maximum piezoresponse, which is related to the effective piezoelectric coefficient  $d_{33}$ , is observed (Figure 5.10). As seen on the large scale, the maximum piezoresponse  $D_{max}$  of the NE phase significantly drops after the bias voltage is switched off.

### c) Proximity Effect

The proximity effect approach investigates the influence of nonergodic inclusions on the properties of the surrounding ergodic relaxor matrix. At this length scale, polarization switching behavior of a 'labyrinth-like' grain is analyzed in dependence on the distance from an adjacent 'checkerboard' grain. The local loops collected at the positions marked in Figure 5.11 are extracted and further analyzed. In order to achieve better statistical accuracy, averaging over loops is performed for a narrow  $5 \times 1$  grid region that includes the points of interest. The switching parameters for a 'checkerboard' grain (position 1) are plotted for comparison. Resembling the results obtained by both compositional and constituent diversity, the largest  $D_{max}$  and  $D_0$  values are observed inside the NE grain, *i.e.* for checkerboard-like domain patterns (Figure 5.11(a)). The re-

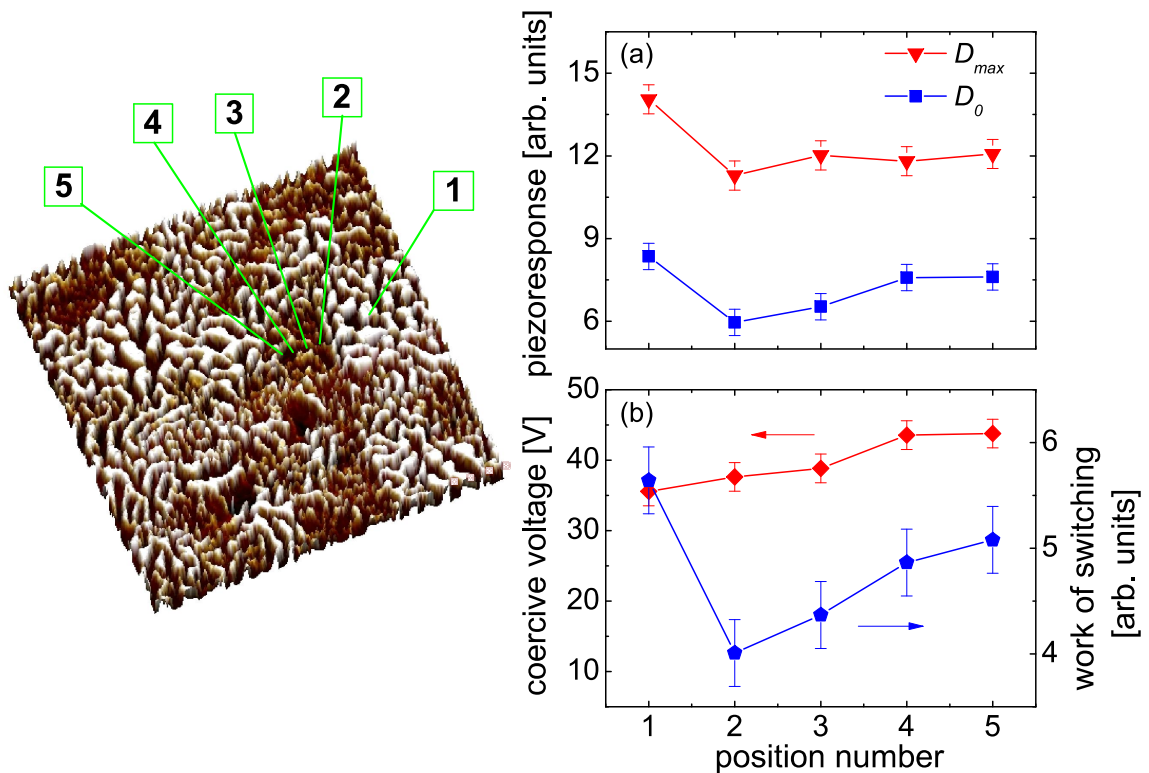


Figure 5.11: Proximity effect: variation of the hysteresis loops parameters: maximum and remanent piezoresponse (a), coercive voltage and work of switching (b) inside a relaxor grain for the composite sample with 30 % of BNT-7BT. The positions are indicated in the left panel.

manent piezoresponse of the ER grain notably decays when approaching the boundary with the NE grain, whereas the maximum piezoresponse shows only a weak change with distance. As shown in Figure 5.11(b), the loop area  $A_s$  also abruptly drops in the vicinity of a grain boundary. However, it almost linearly decreases for the positions more distant from the grain boundary. The coercive voltage, however, behaves independently of distance from the neighboring NE grain.

## 5.4 Discussion

### 5.4.1 Conventional Analysis of the Domain Structure

The PFM study of the ceramic/ceramic composite material provides an insight into the local domain structure and the sub-micron switching properties, yielding information on microscopic mechanisms that may govern the reported high, macroscopic electromechanical strain.<sup>320</sup> By now, the ceramic/ceramic composites examined within this work have been investigated in terms of macroscopic strain, *in situ* high energy XRD, microstructural energy dispersive X-ray, and transmission electron microscopy.<sup>320,321</sup> The macroscopic electromechanical strain measurements demonstrated that the high unipolar strain in the composite materials can be obtained at comparably low electric fields. The maximum strain level was, however, found to strongly depend on the amount of the BNT-7BT constituent. Modeling of these composite systems demonstrated that the two entangled ergodic and nonergodic phases permit tailoring of the high-strain material properties. The high field-induced electromechanical strain is reported to be facilitated by the NE component in the ergodic relaxor surrounding. The subsequent structural measurements contributed to a further understanding of the material properties.<sup>321</sup> Pseudocubic at zero-field state, the local structure of the material has been detected to be inhomogeneous and to experience either an irreversible or a reversible phase transition under an electric field depending on the volume percentage of the nonergodic component in the material.

This PFM study provides a new insight into the functional inhomogeneity of the composite materials by addressing the polarization and electromechanical behavior of the constituent phases separately.

By comparing the dominant domain morphologies detected in the two parent constituents (0%NE and 100%NE) and the two intermediate compositions (10%NE and 30%NE), the checkerboard-like domain patterns can be associated with the BNT-7BT phase. The crystallographic structure and the symmetry of the BNT-7BT phase are still controversial. BNT-7BT is reported to have a pseudocubic symmetry in the unpoled state, as also reported for similar lead-free relaxors.<sup>212,288,173</sup> The pseudocubic phase irreversibly transforms to the tetragonal phase upon application of a sufficiently large poling electric field.<sup>323</sup> Nevertheless, the strong local PFM response indicates that the local symmetry is not cubic even in the pristine state, at least not in the

subsurface layer probed by the PFM experiments. In addition to this, the checkerboard-like domain pattern has been previously detected to be characteristic for locally tetragonal structures.<sup>338</sup>

Unlike BNT-7BT, no grains with the checkerboard patterns are detected in the BNT-6BT-2KNN domain structure, but the labyrinth and distorted stripe patterns are found to be dominant. This type of morphology has often been reported for relaxor compounds with perovskite structure.<sup>325,342</sup> Relaxors with a composition close to the relaxor-ferroelectric boundary often exhibit fractal domain structures, whereas the labyrinth-like patterns often appear to have a single characteristic length scale.<sup>325,342</sup> Static domains and their relatively strong piezoresponse reveal that the surface breaks the ergodicity of the bulk relaxor state in BNT-6BT-2KNN and yields a non-cubic local symmetry followed by the formation of mesoscale domains. The equilibrium domain configurations are predefined by the system energetics. To minimize the total energy of the system, that is, to reduce the depolarization electric field created by the bound charges of the spontaneous polarization on the crystal surface, the crystal splits into domains. The overall domain morphology and characteristic size of domains are a result of the equilibrium between the energies of the domain walls and the depolarization field.

The domain structure of 30%NE reveals a coexistence of grains with domain patterns characteristic for the two parent constituents. Both labyrinth- and checkerboard-like patterns with notable variation in the characteristic size of domain features as observed within the parental domain structures confirm the formation of a composite with two separated phases. Judging from the sporadically distributed unique domain patterns, some intermixing of the constituents, in particularly in the vicinity of grain boundaries, is not excluded. The coexistence of disordered labyrinth and ordered checkerboard large ferroelectric domains in 30%NE may indicate that the 30%NE sample can be compositionally close to the relaxor-ferroelectric phase transition.<sup>343,344</sup>

## 5.4.2 Line-of-Sight Method of Spatial Domain Structure Analysis

### a) General Introduction of the Method

Taking into consideration that the domain structure is a material characteristic determining the overall material properties, a detailed quantitative analysis of these peculiar domain structures is performed in addition.

To face the complexity of the domain microstructures of ceramic/ceramic materials, the line-of-sight (*LoS*) domain analysis approach has been defined and applied. As the character of the local domain morphology changes with the chemical content, *LoS* is developed not only to be applied as a tool for quantitative characterization of the shape and spatial orientation of domains, but it is suggested to be utilized as a comparative tool useful for the differentiation of material properties, in this case, as dependent on the BNT-7BT content. It is important to point out that a particular

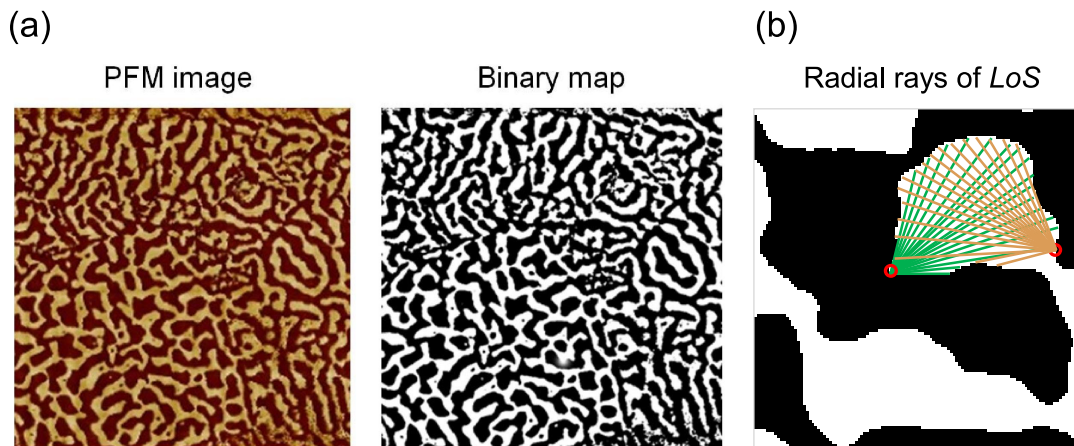


Figure 5.12: (a) Binarization of an image. Each pixel of the PFM image (left) obtains either 1 (ON) or 0 (OFF). (b) Boundary detection in *LoS* using radial rays.

merit of the *LoS* analytical approach is that it can be successfully applied in the investigation of any domain morphology.

Line-of-Sight is an edge detection algorithm. *LoS* is relatively simple for application and effective in the quantitative determination of characteristic parameters of domain morphologies. It requires an initial general thresholding and binarization of the image of interest by which the image data is improved in terms of emphasizing the local boundaries between regions of different contrasts. The image is transformed into a binary map implying that each image pixel obtains either 1 (ON) or 0 (OFF) (Figure 5.12). The binarization processing tool consequently yields additional image pixel noise, seen as roughening of the region edges previously defined by thresholding. To reduce the level of noise, a procedure of smoothing by a Gaussian function is applied. Effectively, smoothing convolves the PFM image with the Gaussian function, discarding the variation in the image intensity while preserving the relevant in-plane image information. Providing so, the accuracy of the *LoS* is significantly improved.

Effectively, the *LoS* algorithm recognizes all data points that correspond to boundaries in a binarized PFM image, interconnects them and ultimately defines all boundaries in the image plane. In the case of PFM images, these boundaries are domain walls. To detect domain walls and to geometrically approximate the domain shape, *LoS* emanates 180 evenly spaced, unbroken rays in the  $2\pi$  space from an image pixel to the first barrier, *i.e.* to pixels which have the opposite binary value (Figure 5.12(b)). The vertices of the emitted rays correspond to the boundary points, which define the contour of a domain. The interior of the contour is considered to be a domain. The domain area,  $A$ , is computed as geometrical area of the contour interior. The spatial domain orientation is closely determined by the domain angle parameter,  $\varphi$ .

For each defined polygon (domain), the inertia moments of the area in x-direction,  $M_x$ , and in y-direction,  $M_y$ , are computed. For every non-self-intersecting region a centroid,  $r_n = (C_x, C_y)$ , is defined. For a region bounded by the vertices of n number of rays, the moments of area around the x- and y-directions can be computed as follows.<sup>345</sup>

$$M_x = \frac{1}{12} \sum_{i=1}^n (C_x^{i+1} - C_x^i) \cdot (C_y^i + C_y^{i+1}) \cdot ((C_y^i)^2 + (C_y^{i+1})^2) \quad (5.1)$$

$$M_y = \frac{1}{12} \sum_{i=1}^n (C_y^{i+1} - C_y^i) \cdot (C_x^i + C_x^{i+1}) \cdot ((C_x^i)^2 + (C_x^{i+1})^2) \quad (5.2)$$

In Equations 5.1 and 5.2, it applies that  $C_x = \frac{1}{6 \cdot A} \sum_{i=1}^{n-1} (x_i + x_{i+1}) \cdot (x_i \cdot y_{i+1} - x_{i+1} \cdot y_i)$  and  $C_y = \frac{1}{6 \cdot A} \sum_{i=1}^{n-1} (y_i + y_{i+1}) \cdot (x_i \cdot y_{i+1} - x_{i+1} \cdot y_i)$ .  $A$  is the area of a polygon and  $x_i$  and  $y_i$  are the coordinates of any polygon vertex.

The spatial orientation of a polygon in  $x$ - $y$  space is computed as defined by Equation 5.3.

$$\varphi = \arctan\left(\frac{M_y}{M_x}\right) \quad (5.3)$$

In the following this parameter is discussed as a domain angle  $\varphi$ . The domain angle is considered as a difference in the angular direction of a ray relative to the direction of the  $i^{th}$  predecessor. The *LoS* generates four spatial maps for all domain descriptors  $A$ ,  $M_x$ ,  $M_y$ , and  $\varphi$ .

Figure 5.13 demonstrates the results of *LoS* obtained for simple geometrical shapes. The color assigned to each *LoS*-defined region indicates the intensity of the mapped parameter for that region. The quantitative value of each color is labeled in the corresponding adjacent colorbar. For instance, in the area map, the color indicates the size of the respective region. The domain area is calculated as a number of pixels included by the boundaries. Furthermore, within an *LoS* angle map all domains positioned along x-direction, that is, having  $0^\circ$  domain angle, are colored dark blue, whereas dark red regions are parallel to the y-axis. The color of the defined shape changes in accordance to the orientation of a domain relative to the axis. The computed angles are represented within the  $[0^\circ, 90^\circ]$  range.

Due to the major interest to qualitatively evaluate local domain structures in terms of size and spatial orientation of domains, only the domain area and domain angle maps are shown and discussed in the following.

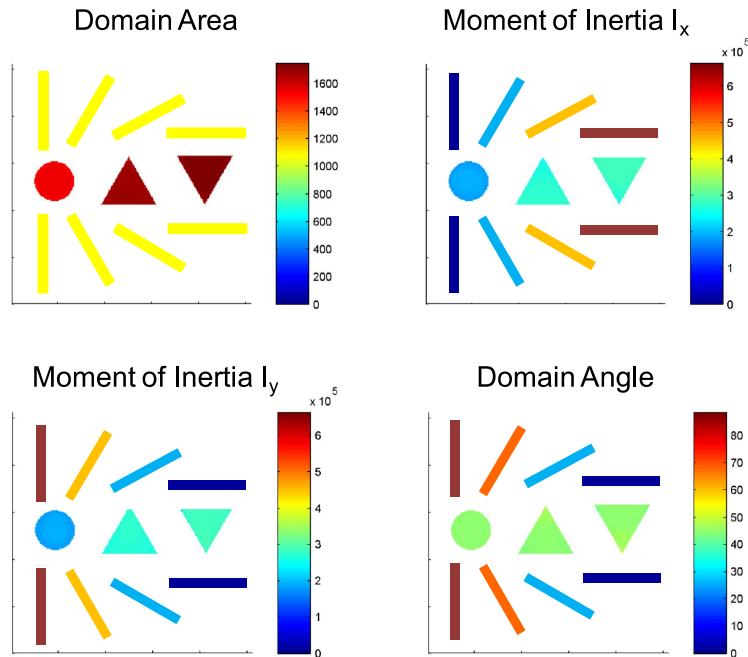


Figure 5.13: The principle of Line-of-Sight domain analysis. *LoS* is applied on simple model shapes and intensities of resulting parameters are demonstrated by corresponding color intensity.

### b) Application of *LoS*

Figure 5.14 shows PFM phase signal maps and their corresponding *LoS* area and angle maps for all composite samples. Considering that the area and angle maps are generated as  $256 \text{ px} \times 256 \text{ px}$  images of representative  $5 \mu\text{m} \times 5 \mu\text{m}$  sample areas, a single pixel occupies  $381.5 \text{ nm}^2$ . Therefore, *LoS* yields a simple calculation of the domain size. For 0%NE, the largest domain area is  $0.25 \mu\text{m}^2$  (655px) (Figure 5.14(b)). The average domain area is calculated to be as large as 187px, that is,  $0.07 \mu\text{m}^2$ . Several features with a characteristic size around  $0.15 \mu\text{m}^2$  permeate the area map. Moreover, the 10%NE map exhibits no domains larger than  $0.32 \mu\text{m}^2$  and the average domain area is computed to be  $0.075 \mu\text{m}^2$ . For 30%NE, the domain structure shows stronger variation. The domains within some grains are computed to be between  $0.34 \mu\text{m}^2$  and  $0.59 \mu\text{m}^2$ , while in others their area is not bigger than  $0.27 \mu\text{m}^2$ . The largest domain area has size of  $0.58 \mu\text{m}^2$ , whereas the average domain area is  $0.17 \mu\text{m}^2$ . As shown in Table 5.1, domains as large as  $1.14 \mu\text{m}^2$  are detected for 100%NE. For this domain structure, the average domain area is much larger than for low-NE-content samples, namely  $0.28 \mu\text{m}^2$ .

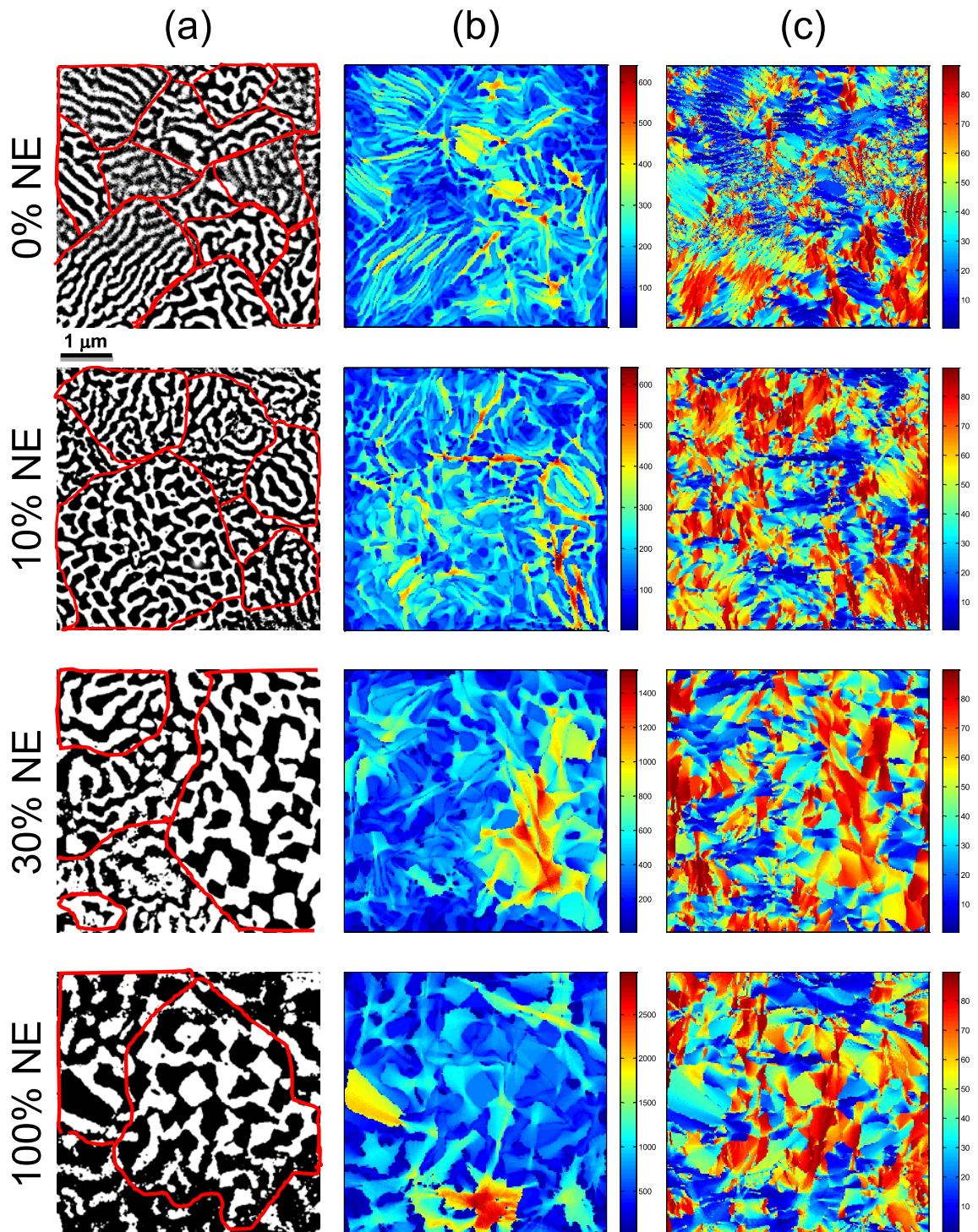


Figure 5.14: Binary PFM images (a), corresponding line-of-sight domain area maps (b), and line-of-sight domain angle maps (c) of the BNT-6BT-2KNN / BNT-7BT ceramic/ceramic composites with different content of nonergodic relaxor BNT-7BT.

Table 5.1: The largest,  $A_{max}$ , and the average,  $A_{avr}$ , domain area for the different composite samples computed by *LoS*.

	0%NE	10%NE	30%NE	100%NE
$A_{max}$ [ $\mu\text{m}^2$ ]	0.25	0.32	0.58	1.14
$A_{avr}$ [ $\mu\text{m}^2$ ]	0.07	0.075	0.17	0.28

The spatial orientation of the domains is monitored via domain angle maps, as shown in Figure 5.14(c). As a matter of fact, the angle distribution map for 0%NE domain structure detected randomly oriented labyrinth-like and relatively ordered stripe-like domains. The orientation of the domains is shown to change drastically on the inter-granular scale. The stripe-like domains are in general oriented along the same direction within the belonging grain. Some grains have all enclosed domains oriented in y-direction (colored red) and with  $0^\circ$  domain orientation (colored blue). The grains sloped  $45^\circ$  are sporadically distributed. Note that  $\varphi = (\pi - 45^\circ)$  is interpreted by *LoS* as  $\varphi = 45^\circ$ . Within some larger grains, however, several sub-groups of stripe-like domains are identified. They are found to point in several different directions within a relatively broad angle range. By contrast, *LoS* identifies labyrinth-like patterns as disordered, that is containing domains which point in various directions.

In the 10%NE domain structure, dominant domains are those with  $90^\circ$  angle. Moreover, numerous mostly single isolated domains with  $\varphi = 45^\circ$  coexist. Here, the domain angle signal shows lower uniformity within grains than in 0%NE. After correlating with the PFM image (Figure 5.14), it is evident that domains show not such a strong mutual alignment within grains as in the case of 0%NE. The uniform domain orientation is observed mostly in smaller grains. Only some domains have a zero angle orientation.

For the 30%NE sample, only smaller domains with an area up to  $0.27 \mu\text{m}^2$  show common alignment inside the grains. The domain angle for the checkerboard like features is predominantly around  $90^\circ$ . However, the majority of the stripe-like features is oriented along the  $x$ -axis.

In the 100%NE domain structure, a domain angle between  $45^\circ$  and  $90^\circ$  is computed for domains larger than 500 px (Fig 5.14 (c)). Here, the majority of square-like domains have a  $90^\circ$  domain angle and a bright PFM amplitude contrast is observed as well as a  $\langle 001 \rangle_c$  crystallographic orientation. However, comparing amplitude PFM signal and domain angle map, it is apparent that in most cases the stripe-like features with a dark PFM amplitude signal have  $\varphi = 0^\circ$ .



### 5.4.3 Autocorrelation Function Analysis

The spatial patterning of *LoS* domain maps is additionally analyzed by applying the self-correlation function analysis. The self-correlation function can be used to indicate the overall randomness and grouping of features over a domain structure in terms of size and their distribution.<sup>48,17</sup> Quantitative information is extracted by applying the self-correlation functions on domain area data sets (Figure 5.15). The autocorrelation function method transforms the original image into an autocorrelation function image according to Equation 5.4.

$$C(r_1, r_2) = \sum F(x, y)F(x + r_1, y + r_2) \quad (5.4)$$

Here,  $F(x, y)$  is an original image data set.<sup>346,220</sup> Subsequently, the 2D correlation image is radially averaged and fitted using the following function

$$C(r) = a \cdot \exp\left[\left(\frac{r}{\xi}\right)^{-2h}\right]. \quad (5.5)$$

In Equation 5.5,  $r$  is the radius of the central peak of the correlation image  $C(r)$ ,  $\xi$  is the correlation length and the exponent  $h$  is related to the roughness of a polarization interface.<sup>299,48</sup> The strongest correlation of the signal in the domain area map was obtained for 100%NE (Figure 5.15(a)). The correlation length computed for this sample is similar to the average domain size computed by *LoS*. As expected from *LoS* domain area maps, a slight decay of the correlation length for the domain area map is observed for 30%NE (Figure 5.15(b)) Significantly narrower correlation peaks are measured for samples with 10%NE and 0%NE. Hence, the strong decay of the correlation length is associated with the lower content of the NE constituent.

Interestingly, the maximum of the autocorrelation function of the 100%NE domain area map is one order of magnitude higher than for low-NE-content samples. For the central peak of the autocor-

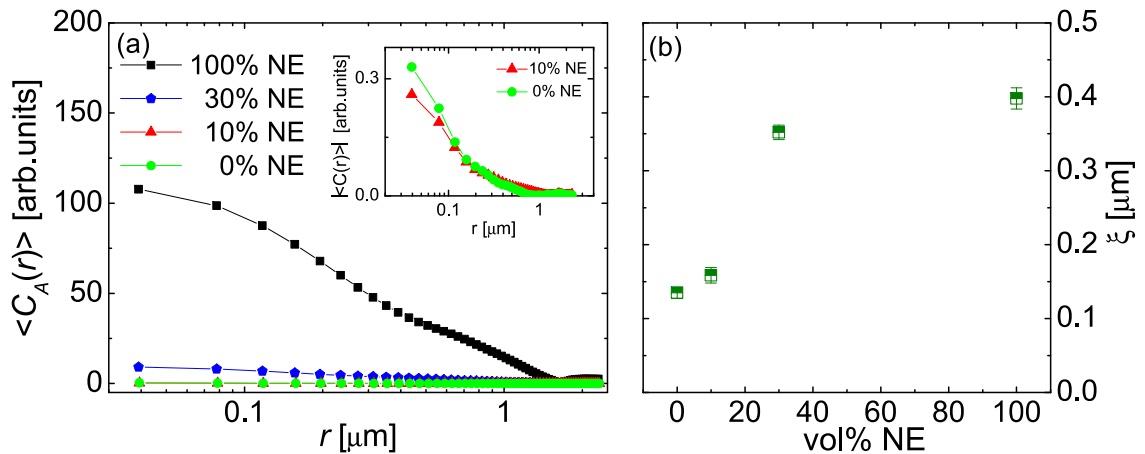


Figure 5.15: (a) The autocorrelation functions of *LoS* domain area maps. Inset: placed for clarity, the autocorrelation functions for 10%NE and 0%NE. (b) The corresponding correlation length  $\xi$  of the autocorrelation function as function of content of nonergodic relaxor BNT-7BT.

relation function  $C(0, 0) = \sum F^2(x, y)$  applies. Therefore, its height scales with signal intensity inside single pixels. In other words, more pixels of the 100%NE area map belong to larger domains than for samples with low NE-content. Although the average domain areas of 0%NE and 10%NE are the same according to *LoS*, the slightly higher  $\langle C(r) \rangle$  intensity of the 0%NE area map can be related to an overall wider distribution of domain sizes.

In ferroelectric and relaxor ferroelectric systems, the ordering of the domain structure occurs as a consequence of an increase in the long-range dipole correlation between unit cells.<sup>325</sup> Some of the accepted explanations for disordered structures, as labyrinth-like patterns, imply higher-order terms in the free energy expansion. Besides the relevant bulk energy, the influence of the long-range order correlation between next nearest neighbor domains and the correlation between nearest neighbors is included. Recently, it was reported that the labyrinth-like domain type reflects the presence of a random charge defect distribution and stresses for preventing the establishment of long-range ferroelectric order.<sup>325</sup> In addition to this assumption, the creation of disordered domains may be associated with quenched random electric fields (RFs), that are typical for relaxors.<sup>26,325</sup> In fact, nanoscale inclusions, that is, PNRs, may be embedded in the existing domains and, hence, be sources of RFs which prevent the formation of ferroelectric-like long-range ordered domains. As the content of nonergodic BNT-7BT increases, polar nanoregions associated with RFs coalesce and the formation of large, ferroelectric-like square domains becomes easier.<sup>26</sup> In the 10%NE sample, the low NE content still seems to have no strong effect on the ordering of the domain structure. The 10%NE sample is, therefore, still far away from the relaxor/ferroelectric phase transition. The situation changes as the NE content increases to 30 vol% and to 100 vol%. The sample configuration becomes closer to the relaxor-ferroelectric phase transition and disordered features may coexist with ferroelectric domains.

The labyrinthine domain structures detected by PFM for ergodic PMN-10PT have been associated with the non-cubic symmetry of the surface layer. Although similar domain morphologies were observed for the ergodic state of other relaxor systems, such as PZN-PT<sup>331</sup> and PLZT,<sup>347,48</sup> their origin is still under discussion.

#### 5.4.4 Conventional Analysis of Switching Properties

The polarization switching behavior was compared among the studied samples as a function of volume fraction of nonergodic BNT-7BT (compositional diversity). Close inspection reveals a gradual evolution of the local hysteresis loop. While the tilted slim hysteresis loops are typical for the ergodic relaxor BNT-6BT-2KNN, the rectangular and wide loops are a distinct feature of samples with higher BNT-7BT content.<sup>338</sup> Although the ergodic relaxor behavior is actually broken in the regions probed by PFM, *i.e.* domains appear, some properties common for the relaxor state are retained in the BNT-6BT-2KNN sample. This primarily refers to the rapid decay of the electric field-induced piezoresponse and a zero or even negative stability gap, indicating instability

of the tip-induced state.<sup>348</sup> The nonergodic BNT-7BT phase shows larger average piezoresponse and more stable remanent polarization, *i.e.* the stability gap is positive, which is in agreement with the macroscopic behavior.

The intermediate switching behavior due to the contribution of both phases is apparent for the 30%NE sample from the average PFM hysteresis loops. Here, the constituent diversity approach demonstrates that two different types of domain patterns are explicitly demonstrated to belong to different phases of the composite.

### 5.4.5 k-Means Clustering

#### a) General Introduction of the Method

The pronounced content-dependent diversity in the local switching behavior is further investigated by the k-means clustering (KMC) analysis. Generally speaking, the k-means clustering method complements the 'constituent approach' by employing a mathematical form to unambiguously distinguish, classify, and map data variation over a grid of points. Hereinafter, KMC will be introduced in general form and will be used afterwards for the analysis of the switching properties. KMC is especially employed to improve the detection of spatial switching diversity in the 30%NE composite and the parental 0%NE and 100%NE samples.

KMC is one of the most frequently used statistical methods, often applied in pattern recognition and classification,<sup>349</sup> data mining and knowledge discovery,<sup>350</sup> as well as in data compression and vector quantization. All cluster methods, including k-means clustering, define the subject of clustering based on different application-specified criteria. KMC specifies a real  $d$ -dimensional space,  $\mathbf{R}^d$ , in which  $n$  data points are joined to  $k$  number of clusters. Independent from their character, the k-means method 'sees' data as objects having their location in space. KMC finds a section in which data points are at the smallest distance from each other, but being as distant from objects of other clusters as possible. Each k-mean cluster is defined by its center, *i.e.* centroid, and the enclosed data points. The cluster center is determined as a point for which the sum of distances from all objects in that cluster is minimized. In the k-means iterative algorithm, locations of  $k$  cluster centers are initially suggested as random. Each data point iteratively tries to find which center is the closest one. The iterative process of defining the clusters is schematically presented in Figure 5.16.

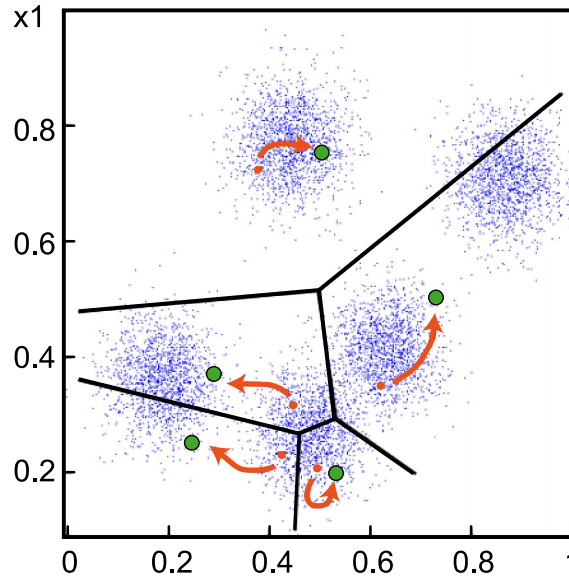


Figure 5.16: The k-means clustering method. An iterative process of defining the cluster centers and associated data. The algorithm eventually converges to a point, although it is not necessarily the minimum of the sum of squares.

The k-means iterative algorithm finds a minimum sum of distances between an associated centroid and each object over all clusters, effectively seeking to compute the following

$$J(V) = \min \sum_{i=1}^c \sum_{j=1}^{c_i} (\|x_i - v_j\|)^2. \quad (5.6)$$

In Equation 5.6,  $c_i$  is the number of data points in the  $i^{\text{th}}$  cluster,  $c$  is the number of cluster centers and  $v_i$  is the mean of points in  $V = \{V_1, V_2, V_3, \dots, V_k\}$  set of centers. The computational procedure alternates between assignment and initialization steps. After defining  $c$  cluster centers, it is necessary to establish the new connections between the data points and the nearest center of the cluster. The distance between each point and the center is calculated and each point is, correspondingly, joined to the cluster with the least distant center position than from other cluster centers. Objects are exchanged between clusters until the sum of interest is found to be minimum. In the next step, the algorithm recalculates the new cluster center according to Equation 5.7.

$$v_i = \frac{1}{c_i} \sum_{j=1}^{c_i} x_j \quad (5.7)$$

Here,  $c_i$  is the number of data points in the  $i^{\text{th}}$  cluster. It proceeds with the recalculation of the distance of data points and the newly defined cluster centers. The calculation is performed for any data point, repeating the loop above for  $c_i$  numbers of data, but stops if no data points are reassigned. Finally, each center finds the centroid of its member points and subsequently relocates to a

position of a cluster centroid. Upon placing the cluster center at the centroid of the corresponding cluster, data  $n$  are divided into  $k$  sets  $X = \{X_1, X_2, X_3 \dots X_k\}$  where  $k \leq n$ . The resulting clusters are mutually exclusive, that is, they are well defined and well separated from other ones.

By the initial suggestion of values, *i.e.* positions of the cluster centroids, and the maximum number of iterations, the k-means minimization procedure can be controlled. By a larger number of clusters a better grouping of data is possible. The disadvantage of this method is the long processing time. Generally, the long processing procedure is a consequence of the extended time needed to compute the nearest neighbors. However, the greater the separation of clusters is, the shorter is the operational time for the analysis algorithm.<sup>351</sup>

The mean and dispersion of the  $i^{\text{th}}$  cluster distribution can be defined by Equation 5.8.<sup>351</sup>

$$r_{min} = \min_{i \neq j} |\mu^{(i)} - \mu^{(j)}| \quad \text{and} \quad \sigma_{max} = \max_i \sigma^{(i)} \quad (5.8)$$

Here,  $\mu^{(i)} - \mu^{(j)}$  is the Euclidean distance of two points,  $r_{min}$  is half the minimum distance among any two cluster centers and  $\sigma_{max}$  is the maximum dispersion. For well separated clusters, it applies that  $r_{min} \gg \sigma_{max}$ . Finally, the cluster separation of the point distribution can be defined by  $\rho$ , as described in Equation 5.9.

$$\rho = \frac{r_{min}}{\sigma_{max}} \quad (5.9)$$

### b) Application of the k-Means Clustering Method

KMC is applied to analyze the variation in local PFM hysteresis loops using a specially adapted MATLAB code. The criterion by which KMC identifies, distinguishes, and plots the map of clusters is the hysteresis loop shape. By setting the number of cluster centroids to 20, k-means clustering scans the  $40 \times 40$  switching data grid, groups them into 20 different clusters ( $k = 20$ ) and generates the corresponding map of clusters. Figure 5.17(a) shows the PFM phase response and a k-means cluster map for 30%NE for which switching experiments and consequent clustering were performed. For each type of cluster recognized by KMC, a spatial map of data belonging to that cluster and a representative hysteresis loop are generated. Among 20 identified clusters, several clusters contain single data points, in which only local individual loops are unique and, therefore, are not further considered. Clusters of the same type are indicated by the same color. A color bar of k-means cluster map associates the color to each  $i^{\text{th}}$  cluster number.

As mentioned earlier, in the domain structure of the 30%NE sample the grains have either checkerboard-like or labyrinth-like domains. Thus, this material exhibits a coexistence of two different phases: a nonergodic and an ergodic one. The constituent approach revealed that the 'ergodic' grain with the labyrinth-like domain morphology exhibits smaller piezoresponse and loops that are more tilted in comparison to that of the 'nonergodic' grain (Figure 5.10).

The k-means clustering method yields further refining and statistically improves the results of the constituent approach. It differentiates two types of local loops. The first one shows small

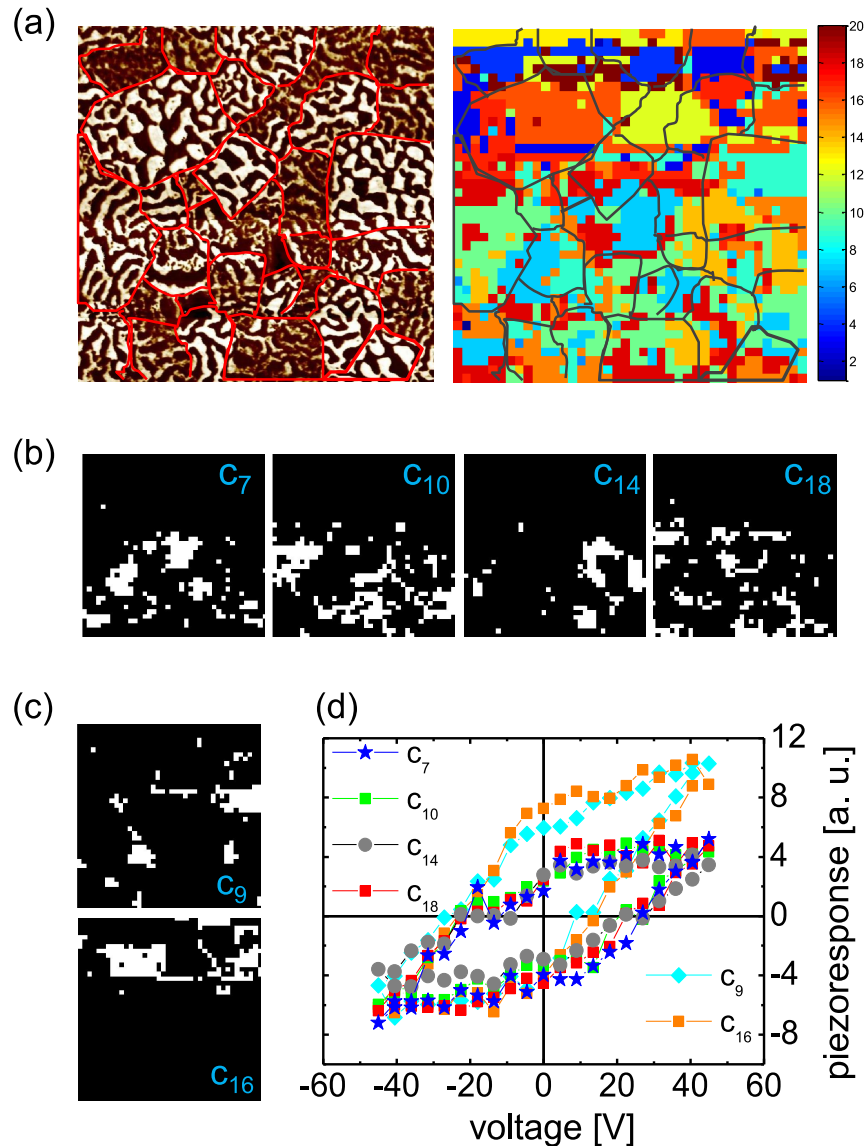


Figure 5.17: (a) The PFM phase image and the corresponding k-means clustering map for the composite ceramic with 30 % of BNT-7BT phase. The k-means clustering is performed for  $k=20$  clusters. The sample areas exhibiting the same local PFM hysteresis loop shape are distinguished and assigned to a cluster. The  $i^{\text{th}}$  representative cluster loop,  $c_i$ , is considered. Solid lines in the PFM phase image mark the grain boundaries and are depicted as a guide to the eye; (b) The k-means maps for  $c_i$  clusters with ergodic-like switching behavior; (c) The k-means maps for clusters within which the ferroelectric-like local hysteresis loops are obtained; (d) The local hysteresis loops of  $c_i$  clusters.

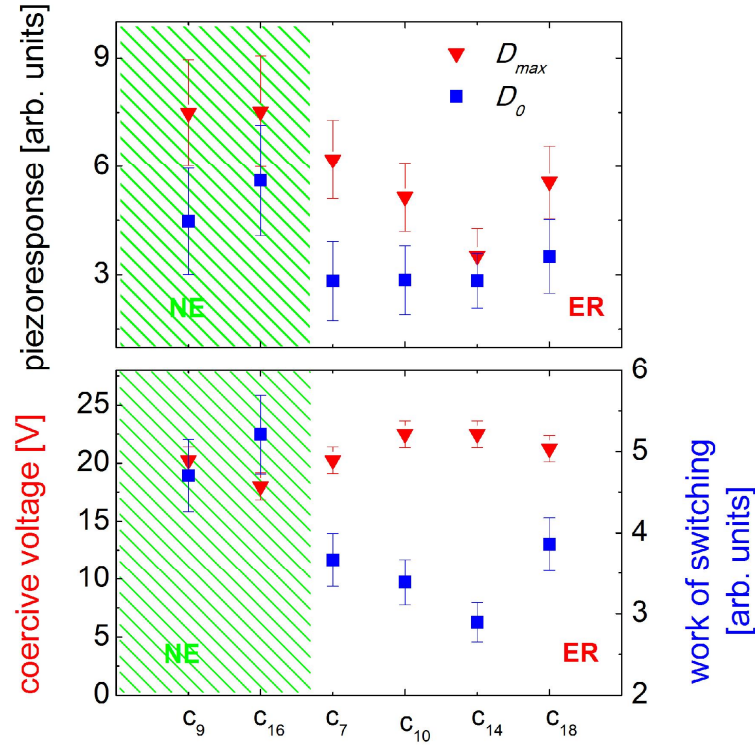


Figure 5.18: Comparison of the maximum,  $D_{max}$ , remanent piezoresponse,  $D_0$ , and coercive voltages of the different clusters  $c_i$ . The clusters  $c_9$  and  $c_{16}$  are hypothesized to be 'nonergodic' clusters, while others demonstrate ergodic-like local switching behavior.

piezoresponse, weak difference between  $D_{max}$  and  $D_0$ , small work of switching, and a large tilt (Figure 5.17(b)). This type of loop can be associated with the ergodic relaxor phase and is indeed observed mainly in grains with 'labyrinth' domains. The second type can be related to the nonergodic phase. It is observed mainly in grains with checkerboard structures and demonstrates ferroelectric-like switching with large hysteresis and high piezoresponse (Figure 5.18). The nonergodic-like local loops are detected for regions of which some are shown by cluster maps in Figure 5.17(c). The regions enclosed by the clusters  $c_7$ ,  $c_{10}$ ,  $c_{14}$ , and  $c_{18}$  confirm the ergodic-like behavior of labyrinth-like domain patterns (Figure 5.17(d)). The existence of the second phase is detected by the clusters  $c_9$  and  $c_{16}$ . The comparison of the representative local loops is shown in Figure 5.17(d). Nevertheless, intermixing of the constituents might appear particularly in the vicinity of grain boundaries. Comparison of PFM and k-means cluster maps reveals that some grains with large, but elongated domains exhibit intermediate properties; they consist of several regions belonging to different clusters (Figure 5.17(b)).

It is interesting that the hysteresis loop generated for the 'ergodic' phase on the grain-scale is broader than the average loop collected at the larger scale for the ergodic 0%NE sample. This discrepancy in the switching behavior can be related to a particular crystallographic orientation

of the chosen grain. As a matter of fact, while the polarization switching on the larger scale is a collective effect, single grain orientation directly affects the piezoactivity when probed locally.<sup>352</sup>

The ergodic relaxor behavior in the 30%NE composite might be mitigated by the vicinity of the BNT-7BT phase that, beside as macroscopic grains, may exist in the form of nanometer-sized inclusions distributed in the ergodic relaxor matrix. This fact might be a particular interest while

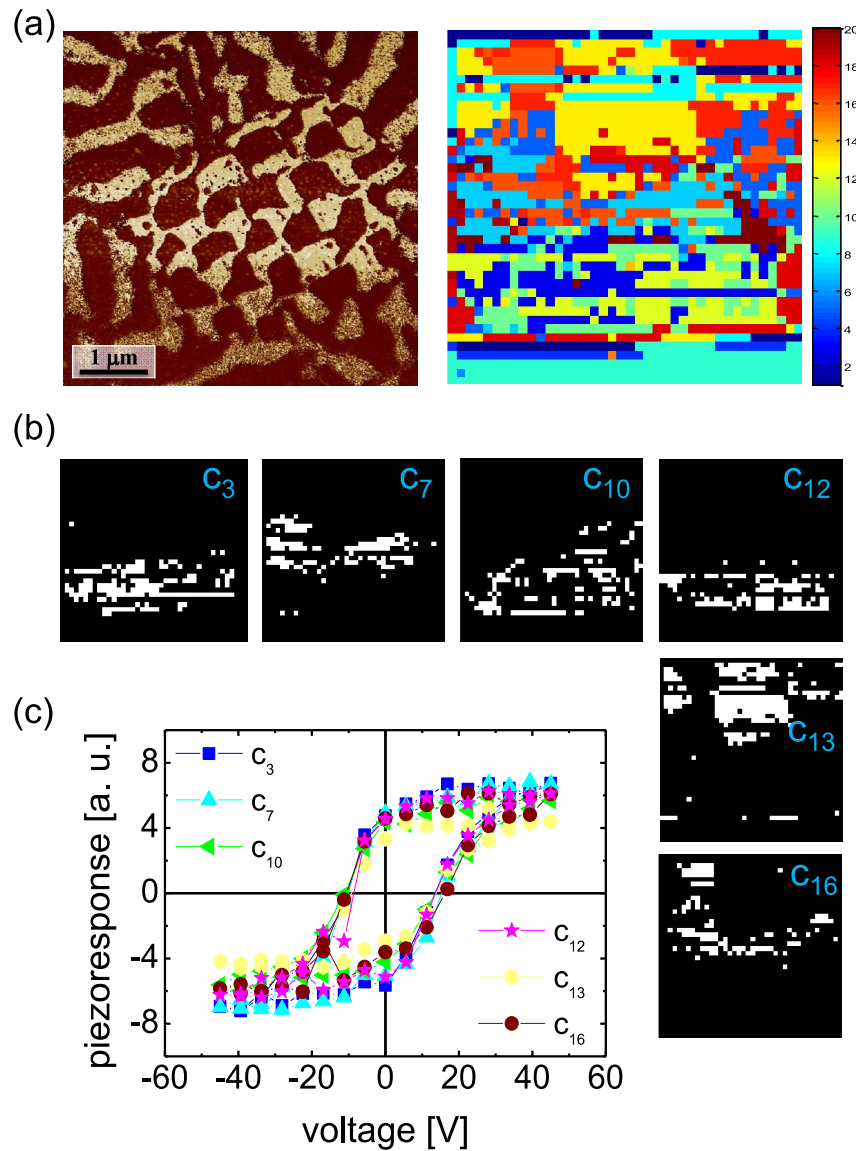


Figure 5.19: (a) The PFM phase image and the corresponding k-means clustering map for the nonergodic relaxor BNT-7BT sample. The k-mean clustering is performed for  $k=20$  clusters. The sample areas exhibiting the same local PFM hysteresis loop shape are distinguished and assigned to a cluster. The  $i^{\text{th}}$  representative cluster loop,  $c_i$ , is considered; (b) The k-means maps for the representative  $c_i$  clusters; (c) The local hysteresis loops of  $c_i$  clusters.



keeping in mind that the ferroelectric state in BNT-7BT can be induced relatively easily by an electric field. In the light of diffraction-detected compositional inhomogeneity, such ferroelectric-like inclusions are suggested to arise often in-between or within ubiquitous relaxor grains.<sup>353</sup> Nonetheless, the detection of these nano-inclusions by PFM scanning mode is severely limited as their small size is below the detection resolution limit of the technique and also as the low probing *ac* voltage is not high enough to trigger inclusions to grow.

On the other hand, a sufficiently high *dc* voltage used in the spectroscopic mode (local switching experiments) may provoke the growth of nonergodic nano-inclusions into bigger ferroelectric domains. These domains, finally, contribute to the larger field-induced piezoresponse than observed in the pure ergodic 0%NE composition. Upon poling voltage removal, the new, induced domains remain stable and effectively contribute to the remanent piezoresponse  $D_0$ , but the 'ergodic' fraction of the same grain reverses back to its pre-poling state.

In spite of the local variation in the local domain structures, k-means clustering shows no large discrepancies in the switching behavior of the parent constituents, 100%NE and 0%NE. Figure 5.19 and 5.20 demonstrate that clusters can yet be distinguished, but their corresponding local loops reveal to some extent uniform behavior.

The presence of a NE grain induces no big variations in the switching behavior of neighboring ER grains at every distance in-between. A notable decay of maximum and remanent polarization, and switching work is, however, registered close to the NE-ER interface. Also, stronger tilting of local hysteresis loops is notable at the grain boundary of interest. This decay of specific properties is assigned to an impediment of the propagation of the switched domain, which is more intense close to the interface than at the interior part of the grain. Indeed, domain wall movement can be hindered by the boundary itself, as it acts as a pinning center. Also point defects may act as pinning centers, the concentration of which is expected to be especially increased at grain boundaries.

In consideration of tailoring the properties of piezoelectric materials, it is of significant interest to review the properties of the ceramic/ceramic composites by comparing the experimental data obtained on different scales. Therefore, for simplicity, the compositional diversity approach is further on referred to as the macroscopic scale approach, whereas the proximity effect is discussed in the context of a single-point scale. Contrasting the results collected at these two scales, it can be noticed that the interior sites of the 'ergodic' grain in 30%NE on the single-point scale demonstrate properties like the 30%NE sample as whole. Besides, the average piezoresponse of 30%NE can be considered as a collective effort of the entire material, albeit inhomogeneous already on the grain length scale.

Keep in mind that the nonergodic phase undergoes an irreversible relaxor-ferroelectric phase transition, that is, it is ferroelectric-like upon poling. Consequently, it is not a surprise that the maximum values of switching work are detected for the 100%NE sample as whole and the nonergodic

grains on the single-point scale. Nevertheless, a comparison of these two values demonstrates that the work of switching, *i.e.* switching losses, is larger on the macroscale. In addition, the ergodic phase of the composite sample exhibits maximum piezoresponse on the single-point scale that is strongly improved with respect to the corresponding values in the purely ergodic sample BNT-6BT-2KNN. The higher piezoactivity can be rationalized by the proximity of the large

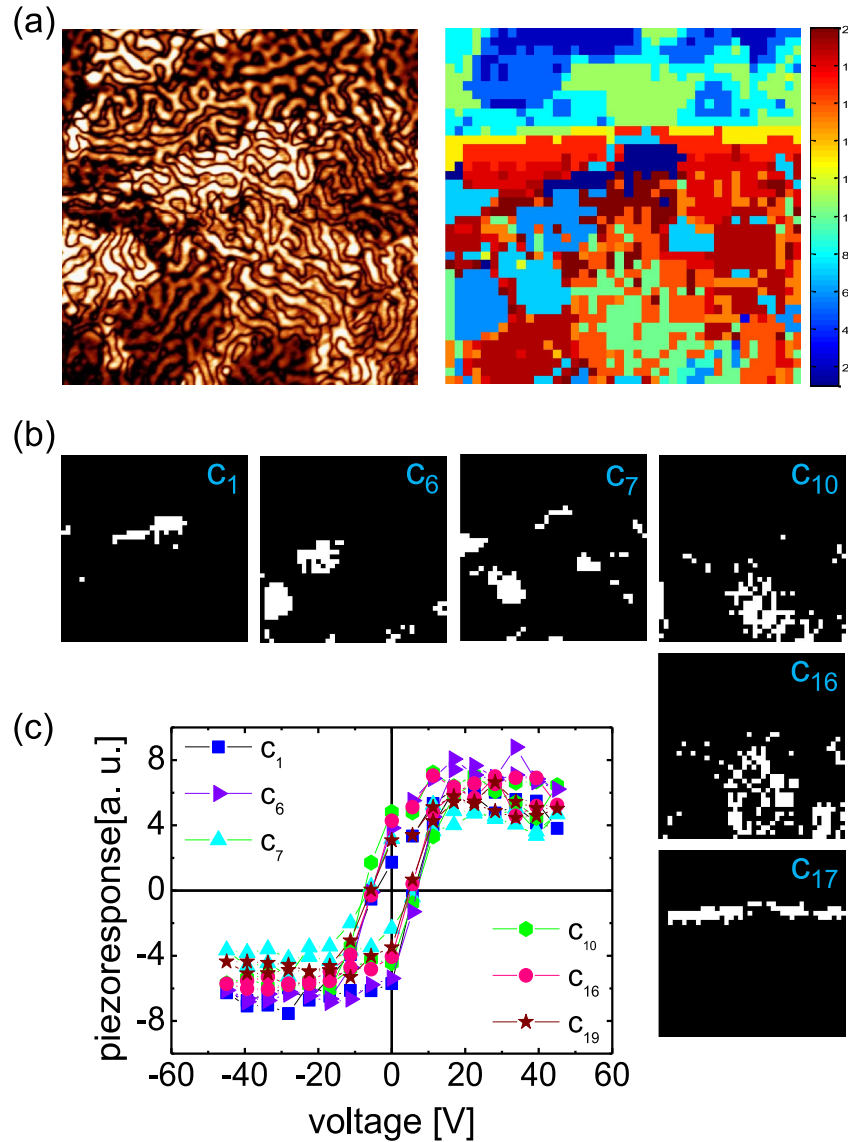


Figure 5.20: (a) The PFM phase image and the corresponding k-means clustering map for the ergodic relaxor BNT-6BT-2KNN. The k-means clustering is performed for  $k=20$  clusters. The sample areas exhibiting the same local PFM hysteresis loop shape are distinguished and assigned to a cluster. The  $i^{\text{th}}$  representative cluster loop,  $c_i$ , is considered; (b) The k-means maps for the representative  $c_i$  clusters; (c) The local hysteresis loops of  $c_i$  clusters.

BNT-7BT grain which can effectively increase the polarizability of the surrounding ergodic phase. As mentioned before, a modeling study demonstrated that the nonergodic BNT-7BT phase with a large remanent polarization relative to the ergodic matrix can facilitate the shifting of the electric field into the ergodic phase. In such a way, it allows for a local establishment of the relaxor/ferroelectric phase transition at lower electric fields.

The analysis of the hysteresis loop area further supports the fact that the switching properties of the farthest position inside the ergodic relaxor grain resemble properties seen in the 30%NE sample on the macroscopic scale. The work of switching is not as large as obtained in 100%NE on the macroscale, but also not as small as in 0%NE. Here, it can be concluded that the incorporation of grains of a different phase into the microstructure can be indeed utilized for fine adjustments of the macroscopic piezoelectric properties.

## 5.5 Conclusions

The performed piezoresponse force microscopy investigation has confirmed the formation of BNT-6BT-2KNN/BNT-7BT composites. On the microscale, grains of the BNT-6BT-2KNN phase show labyrinth and distorted stripe domain patterns, while for the BNT-7BT grains the regular checkerboard domain morphology is found to be typical. The ergodic relaxor character of pure BNT-6BT-2KNN seems to be broken at the surface, which is similar to observations in other relaxors. The line-of-sight domain analysis method has been introduced and applied to determine the size and spatial orientation of domains as well as their dependence on the content of the nonergodic constituent BNT-7BT. In addition, distinct polarization switching behavior between nominally ergodic and nonergodic constituents was registered both on the macroscopic, averaged scale and between different grains in the composite material with 30% of BNT-7BT using the k-means clustering statistical approach. An improvement of the piezoelectric response of BNT-6BT-2KNN grains in the composite sample is observed compared to the single phase ceramic. At the same time, no pronounced effect of proximity of a BNT-7BT grain on the local polarization switching in the surrounding 'ergodic' grains has been found in the composite samples. This may be related to the conditions of the used experimental approach. In fact, the local hysteresis loops are probed successively at different locations. Although macroscopic measurements revealed the opposite, local experiments demonstrated that the switching in 'ergodic relaxor' grains is rather independent from the vicinity of 'nonergodic' grains. This yields the conclusion that the influence of the more easily switched grain on the harder switched neighborhood is less pronounced than expected.

## 6 Conclusion

Encouraged by the enhanced electromechanical performance offered by a number of new lead-free piezoceramics, a comprehensive study of KNN- and BNT-based piezoelectric materials was performed on the sub-micron scale. The underlying, fundamental physical mechanisms were assessed by means of PFM for three distinct material classes: First, a ferroelectric, represented by  $0.95(\text{Na}_{0.49}\text{K}_{0.49}\text{Li}_{0.02})(\text{Nb}_{0.8}\text{Ta}_{0.2})\text{O}_3-0.05\text{CaZrO}_3$  (KNN-CZ5); second, a relaxor ferroelectric, namely  $\text{Bi}_{1/2}\text{Na}_{1/2}\text{TiO}_3-0.19\text{Bi}_{1/2}\text{K}_{1/2}\text{TiO}_3-y\text{BiZn}_{1/2}\text{Ti}_{1/2}\text{O}_3$  (BNT-19BKT-100yBZT); third, a composite material that comprises nonergodic phase fraction of  $\text{Bi}_{1/2}\text{Na}_{1/2}\text{TiO}_3-0.07\text{BaTiO}_3$  (BNT-7BT) along with an ergodic phase  $\text{Bi}_{1/2}\text{Na}_{1/2}\text{TiO}_3-0.06\text{BaTiO}_3-0.02\text{K}_{0.5}\text{Na}_{0.5}\text{NbO}_3$  (BNT-6BT-2KNN). This comprehensive approach includes the investigation of the macroscopic constitutive behavior by means of various electric characterization methods, contrasted against the sub-microscopic investigations performed via piezoresponse force microscopy.

In the light of dopant-tailored property improvement, a new, high-performance Ca-doped KNN ferroelectric material was introduced. Large- and small-signal electric measurements proved a high macroscopic unipolar strain of 0.16% with outstanding temperature insensitivity and an augmented piezoelectric coefficient  $d_{33}$  of 320 pC/N. The great advancement in electromechanical strain and piezoelectric coefficient was hypothesized to be the result of an orthorhombic-tetragonal phase transition. The coexistence of these two ferroelectric phases was indeed confirmed by the local domain structure investigation. Resembling morphotropic PZT compounds in the vicinity of the phase boundary,<sup>269,270</sup> the complex domain arrangements, consisting of large, stripe-like, regular domains and small, irregularly-shaped features, denote the presence of two phases close to room temperature.

The temperature of the orthorhombic-tetragonal phase transition shifts close to ambient temperature as an effect of doping, which is particularly beneficial for an application close to room temperature. In addition, the high unipolar strain remains stable in a wide temperature range. In fact, the field-induced strain varies less than 10% at temperatures between 25 °C and 175 °C as the tetragonality of the KNN structure is preserved within this temperature range. The origin of the remarkable temperature-insensitive unipolar strain was phenomenologically associated with the stable difference of the squared maximum and remanent polarization values. An anomaly in the temperature-dependent dielectric permittivity curve  $\varepsilon_r(T)$  experimentally indicated, that the phase transition occurs into a tetragonal ferroelectric state. Indeed, the local domain restructuring as well as the variation in the local switching kinetics confirmed the establishment of a tetragonal phase at around 50 °C.

Furthermore, temperature-dependent small-signal electrical measurements showed a decay of the piezoelectric coefficient  $d_{33}(T)$  as temperature increases. At the same time, the temperature vari-

ability of  $d_{33}$  was demonstrated by PFM to be reflected in the temperature-sensitive local piezoactivity. Both the local piezoelectric response and the piezoelectric coefficient  $d_{33}$  gradually decreased to significantly lower values. In addition,  $d_{33}(T)$  exhibits a broad maximum centered at about 36 °C, revealing the existence of a polymorphic phase transition.

Moreover, the local field-dependent behavior was studied by switching spectroscopy PFM. It was demonstrated that, unlike the orthorhombic phase, the tetragonal ferroelectric phase permits nucleation of switched domains at larger bias voltages and it allows for a notably faster propagation of newly created domains at the same level of electric field.

Eventually, a decay of overall piezoactivity was evidenced above the Curie temperature at approximately 200 °C. In the cubic phase, local piezoresponse was virtually zero due to the disappearance of domains, whereas the local hysteresis loops were narrow and exhibited low maximum and remanent values. As a result, the large-signal unipolar strain  $S(E)$  and the small-signal piezoelectric coefficient  $d_{33}$  rapidly decay upon heating beyond 175 °C.

Stepping up from a conventional ferroelectric, a lead-free relaxor ferroelectric was investigated that exhibits an inherently different temperature- and field-dependent behavior. Macroscopic studies yielded valuable information on the peculiar nature of the relaxor ferroelectric BNT-19BKT-100yBZT material system. The local domain contribution to the electromechanical properties was addressed by a complementary PFM investigation. The term "degree of nonergodicity" ( $DoN$ ) was introduced as a qualitative measure for the structural charge disorder related to the difference in the valency of ions on a unit cell level. The incorporation of heterovalent ions promotes the enhancement of random electric fields and, consequently, the formation of polar nano-regions (PNRs) in a nominally pseudocubic relaxor matrix. In the high-temperature regime, polar nanoregions are highly dynamic and the relaxor behaves in an ergodic manner. With temperature decrease, PNRs freeze and interact, thus, ergodicity is broken and the relaxor is nonergodic. By varying  $y$  in BNT-19BKT-100yBZT, charge disorder forms due to the partial  $Zn^{2+}$  substitution of  $Ti^{4+}$  ions. For low BZT contents like  $y=0.02$ , the material is hypothesized to be in the nonergodic relaxor state. With higher contents of BZT such as  $y=0.04$ , the degree of nonergodicity decreases and the material exhibits ergodic relaxor properties.

The field-dependent constitutive large-signal and small-signal behavior demonstrates that at low electric fields  $<2$  kV/mm all compositions are virtually indistinguishable in terms of electrical properties. The effect of  $DoN$  on the electrical properties becomes apparent only at higher electric fields. With the increasing concentration of  $Zn^{2+}$  ions, a rising instability of the field-induced long-range ferroelectric order was found. In fact, the large-signal, butterfly-like strain and the square-like polarization showed relatively high remanent values for BNT-19BKT-2BZT. The apparent decrease of remanence with increasing BZT content is a result of augmented random electric fields, due to which the threshold electric field necessary to induce long-range ferroelectric order increases. Small-signal  $d_{33}(E)$  and  $\varepsilon_{r,33}(E)$  behave in accordance with this observation.

At the same time, the PFM investigation of the local domain structure related the featureless domain structures to the existence of polar nanoregions. An autocorrelation function analysis demonstrated that a decay of material nonergodicity causes the character of PNR dynamics to change from strongly correlated, static PNRs for low BZT contents to weakly correlated, mainly dynamic PNRs for higher concentration of heterovalent  $\text{Zn}^{2+}$  ions. Judging from local field-dependent measurements, the macroscopic behavior reflects the submicroscopic behavior. The material with a small addition of BZT ( $y=0.02$ ) demonstrated nonergodicity by a strong piezoresponse and a ferroelectric domain morphology induced at comparably low electric fields. By contrast, the formation of the ferroelectric state is impeded for higher BZT contents. The same electric fields applied to BNT-19BKT-4BZT doped material resulted in the establishment of significantly lower piezoresponse than observed for BNT-19BKT-2BZT.

Furthermore, the influence of  $DoN$  on the thermal and temporal stability of the small-signal piezoelectric constant  $d_{33}$  and the local piezoelectric response was addressed. Similar to the compositional evolution, the system nonergodicity decreases with increasing temperature. The initially sizable  $d_{33}$  values decay at elevated temperatures as a result of an increased thermal instability of the field-induced ferroelectric phase. The time-dependent polarization relaxation indicated a decay of non-ergodicity at high temperatures in the low-BZT compositional region, which is comparable to the level of relaxation observed in BNT-19BKT-4BZT already at room-temperature.

The macroscopic polarization relaxation is reflected in a temporal decay of piezoresponse on the microscopic scale. Both processes are well described by the stretched exponential function. The broad relaxation time distribution on the macroscopic scale was shown to narrow down for sub-micron relaxation processes. This effect was found to be the result of the distinct nature of the two experimental approaches as largely varying sampling volumes are probed. The variation of  $DoN$  is visualized as a gradual degradation of the bias-induced ferroelectric phase. The destabilization of the field-induced ferroelectric long-range order was observed to be a complex two-step process. Large ferroelectric domains initially fragment into smaller domains and, ultimately, into dynamic polar nanoregions.

Eventually, the development of microstructural composites is a consequential evolution from conventional ferroelectrics or relaxors in order to further optimize the electromechanical performance of lead-free functional ceramics. This composite approach, however, adds a great degree of complexity to the domain morphology. The here presented PFM investigation of BNT-7BT/BNT-6BT-2KNN ceramic/ceramic composite materials identified that these complex domain structures and a specific local switching behavior are the very origin of the advanced macroscopic electromechanical properties.<sup>320</sup> In fact, the domain morphology of the composites confirmed the formation of ceramic/ceramic composites, proving the validity of the composite approach. According to their macroscopic behavior, the parent constituents BNT-7BT and BNT-6BT-2KNN demonstrated nominally nonergodic and ergodic relaxor ferroelectric behav-

ior, respectively. The formation of composites was shown to permit tailoring of the electromechanical material properties by varying the content ratio of the two parent constituents. In analogy, their characteristic domain morphologies gradually evolve with the increasing content of the nonergodic BNT-7BT phase in the BNT-6BT-2KNN ergodic matrix. While domains of the pure ergodic BNT-6BT-2KNN form labyrinth- and distorted stripe-like patterns, the nonergodic BNT-7BT is featured by a checkerboard-like domain morphology. The domain structures of the composite samples showed an intermixture of these two different type of domains. The disordered, stripe-like morphology of 10% BNT-7BT doped composite develops into sporadically distributed stripe- and checkerboard-like organized domains for the 30% BNT-7BT composite. Simultaneously, the characteristic domain size increases with the ordering of domains. The well-defined domain architectures of the nominally pseudocubic composites<sup>320</sup> are explained by the occurrence of symmetry breaking at the sample surface probed by PFM. The variation of domain structures and evident content-dependent domain organization allows for an identification of the two phases on the local scale.

Owing to the great complexity of the polar microstructure, new methods are required to quantify domains and their morphology. Therefore, the line-of sight (*LoS*) domain analysis method was introduced. *LoS* enables the quantitative characterization of the domain structure with respect to size and spatial orientation. Based on an image analysis algorithm of *LoS*, the resulting data was presented as *LoS* domain area maps and domain angle distribution maps. *LoS* analysis confirmed the increase of the characteristic domain size with increasing content of BNT-7BT. It was found that the average domain area of ergodic BNT-6BT-2KNN is about  $0.07 \mu\text{m}^2$ . By contrast, the average area of domains in BNT-7BT is approximately  $0.28 \mu\text{m}^2$ , as much as one order of magnitude larger than for samples with low content of nonergodic phase. With a higher fraction of nonergodic BNT-7BT, the regularity of the domain morphologies consequently increases as reflected by the *LoS* domain spatial orientation data. In addition, the correlation function analysis on the *LoS* maps of domain orientation finds a stronger data correlation for material with high BNT-7BT content.

A local polarization switching study was able to distinguish the specific switching behavior of nominally ergodic and nonergodic constituents. Local hysteresis loops show a field-induced ferroelectric-like behavior for BNT-7BT and the composite with 30% of BNT-7BT. Low maximum and remanent polarization values confirm higher ergodicity for less doped 10%BNT-7BT and the parental BNT-6BT-2KNN material. The tailoring of properties for composites reported on the macroscopic scale is supported by similar conclusions gained from the comparative local investigation by means of PFM. The 'ergodic' grain of the composite sample exhibits an improved piezoelectric response with respect to the single phase composite ceramic.

Furthermore, a novel analytical technique for the local field-dependent properties, called k-means clustering, was introduced. This method allows a study of switching properties based on the differentiation of single-point switching loop shape.

The improved KNN- and BNT-based piezoelectric materials play an important role in the struggle for high-performance, environmentally-friendly, lead-free functional materials in the vast spectrum of piezoelectric applications. Future improvements of the lead-free materials rely on a strong correlation between microstructural material properties and their manifestation on the macroscopic scale.

In this work, it is clearly demonstrated that domain morphologies in ferroelectrics, relaxors, and eventually composites can be inherently different. It was furthermore evidenced that there is a delicate balance between composition, time, temperature, and electric field yielding a multidimensional complexity. This increasing intricacy of innovative lead-free compounds on a microstructural level ultimately necessitates new methods. Only a profound, fundamental understanding of the material properties and their underlying mechanisms will promote the further improvement and development of these materials. Therefore, this work contributes to a comprehensive insight by shedding light on the local, submicrometer properties for various state-of-the-art lead-free materials. Even more importantly, new methods have been introduced, that for the first time allow for a quantification of domain properties even for most complicated domain structures. By doing so, this work strengthens the global strive to establish green alternatives for lead-containing functional ceramics.



## A Appendix

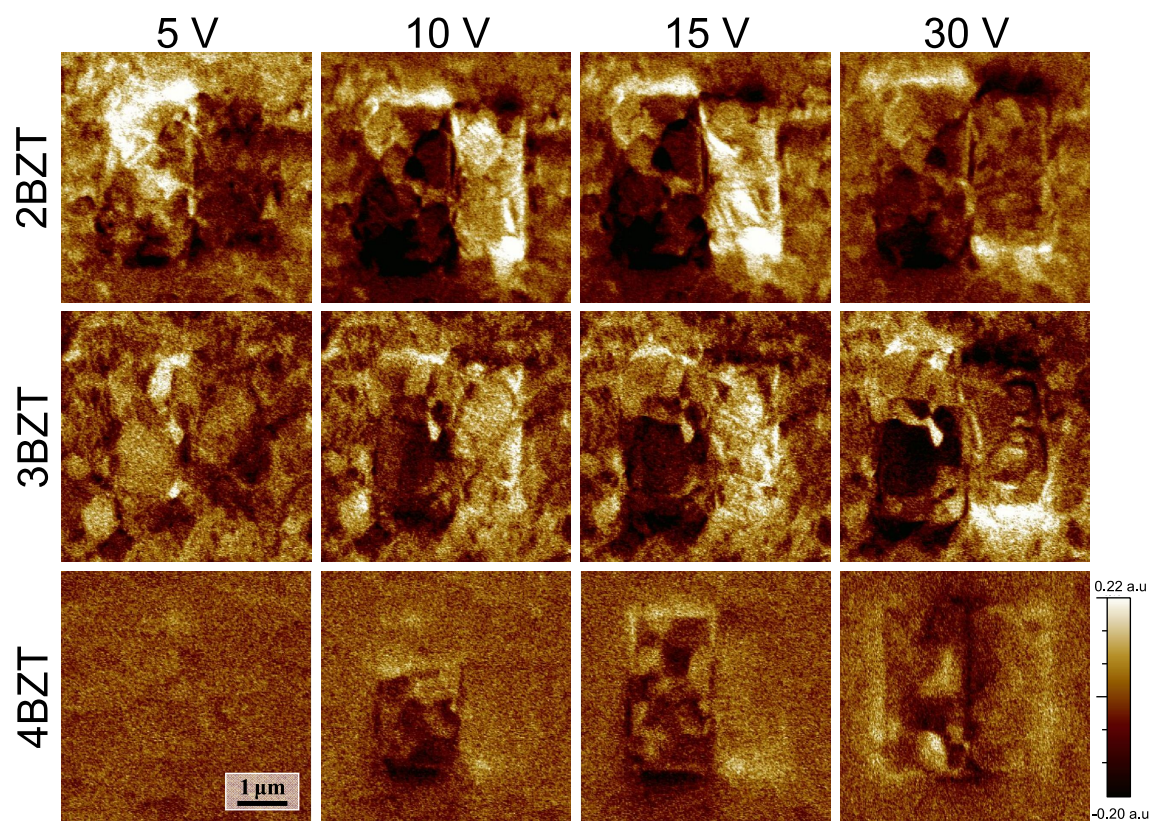


Figure A.1: LPFM images of BNT-BKT-BZT ceramics obtained after local poling.

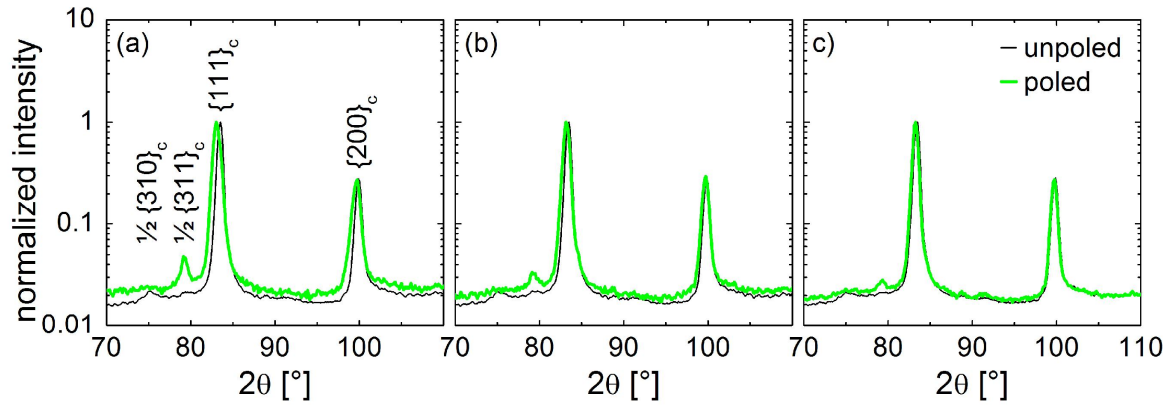


Figure A.2:  $\{111\}_c$  and  $\{200\}_c$  reflections for (a) 2BZT, (b) 3BZT, and (c) 4BZT presented with the superlattice reflections before (unpoled) and after (poled) exposure to the electric field.

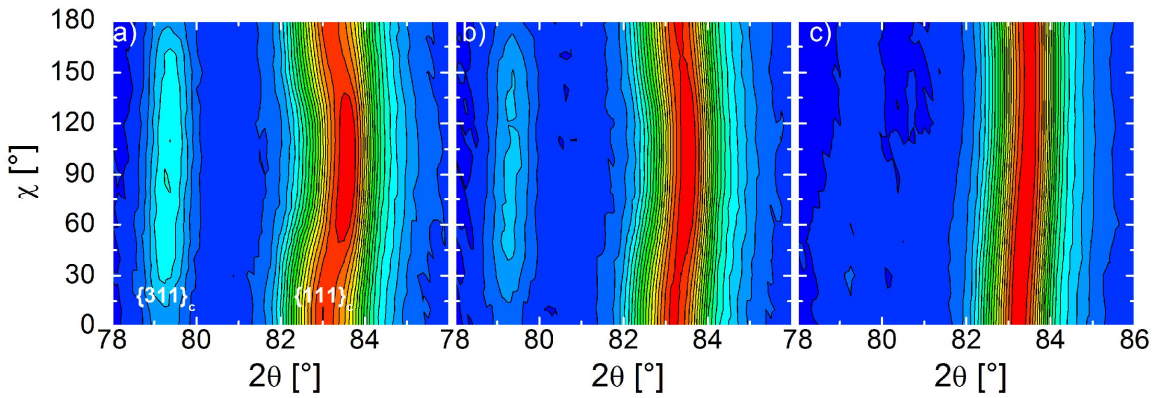


Figure A.3: Neutron diffraction patterns of the  $\frac{1}{2}\{311\}_c$  and  $\{111\}_c$ -type reflections for poled (a) 2BZT, (b) 3BZT, and (c) 4BZT in respect to angle  $\chi$ .

# Bibliography

- <sup>1</sup> EU-Commission Directive 2013/28/EU of 17 May 2013 Amending Annex II to Directive 2000/53/EC of the European Parliament and of the Council on End-of-Life Vehicles. *Official Journal of the European Union*, (L135):14–8, 2013.
- <sup>2</sup> EU-Council Directive 89/677/EEC of 21 December 1989 Amending for the Eighth Time Directive 76/769/EEC on the Approximation of the Laws, Regulations and Administrative Provisions of the Member States Relating to Restrictions on the Marketing and Use of Certain Dangerous Substances and Preparations. *Official Journal of the European Communities*, (L398):19–23, 1989.
- <sup>3</sup> EU-Commission Directive 2000/71/EC Of 7 November 2000 to Adapt the Measuring Methods as Laid Down in Annexes I, II, III and IV to Directive 98/70/EC of the European Parliament and of the Council to Technical Progress as Foreseen in Article 10 of That Directive. *Official Journal of the European Communities*, (L287):46–50, 2000.
- <sup>4</sup> J. Rödel, K. G. Webber, R. Dittmer, W. Jo, M. Kimura, and D. Damjanovic. Transferring Lead-Free Piezoelectric Ceramics into Application. *Journal of the European Ceramic Society*, 35 (6):1659–1681, 2015.
- <sup>5</sup> T. Takenaka, K. Maruyama, and K. Sakata.  $(\text{Bi}_{1/2}\text{Na}_{1/2})\text{TiO}_3\text{-BaTiO}_3$  System for Lead-Free Piezoelectric Ceramics. *Japanese Journal of Applied Physics Part 1*, 30(9B):2236–2239, 1991.
- <sup>6</sup> Y. Saito, H. Takao, T. Tani, T. Nonoyama, K. Takatori, T. Homma, T. Nagaya, and M. Nakamura. Lead-Free Piezoceramics. *Nature*, 432(7013):84–87, 2004.
- <sup>7</sup> R. Waser, U. Böttger, and S. Tiedke. *Polar Oxides - Properties, Characterization, and Imaging*. Wiley-VCH, Weinheim, 2005.
- <sup>8</sup> A.J. Moulson and J.M. Herbert. *Electroceramics*. John Wiley & Sons Ltd., Chichester, 2nd edition, 2003.
- <sup>9</sup> K. Uchino. *Materials Science and Technology - A Comprehensive Treatment*, volume 11, chapter Ferroelectric Ceramics. VCH Verlagsgesellschaft, Weinheim, 1994.
- <sup>10</sup> B. Jaffe, W.R. Cook, and H. Jaffe. *Piezoelectric ceramics*, volume 115 of *Non-metallic solids*. Academic Press London, London, 1971. 317 pp.
- <sup>11</sup> W. Wessing, Heywang, H. W. Beige, and H. Thomann. *Piezoelectricity*, chapter The Role of Ferroelectricity for Piezoelectric Materials. Springer, 2008.
- <sup>12</sup> M. E. Lines and A. M. Glass. *Application of Ferroelectrics*. Oxford University Press, New York, 2001.

- <sup>13</sup> J. Koch. *Piezokeramik : Grundlagen, Werkstoffe, Applikationen*. expert-Verlag, Renningen-Malmsheim, 1995.
- <sup>14</sup> D. A. Hall. Nonlinearity in Piezoelectric Ceramics. *Journal of Materials Science*, 36(19): 4575–4601, 2001.
- <sup>15</sup> D. Damjanovic. Ferroelectric, Dielectric and Piezoelectric Properties of Ferroelectric Thin Films and Ceramics. *Reports on Progress in Physics*, 61(9):1267–1324, 1998.
- <sup>16</sup> H.F. Kay and P. Vousden. XCV. Symmetry Changes in Barium Titanate at Low Temperatures and Their Relation to its Ferroelectric Properties. *Philosophical Magazine Series 7*, 40(309): 1019–1040, 1949.
- <sup>17</sup> F. Jona and G. Shirane. *Ferroelectric Crystals*. Pergamon Press, Oxford, 1962.
- <sup>18</sup> O. Guillon, J. Chang, S. Schaab, and S.-J. L. Kang. Capacitance Enhancement of Doped Barium Titanate Dielectrics and Multilayer Ceramic Capacitors by a Post-Sintering Thermo-Mechanical Treatment. *Journal of the American Ceramic Society*, 95(7):2277–2281, 2012.
- <sup>19</sup> A. F. Devonshire. XCVI. Theory of Barium Titanate. *Philosophical Magazine Series 7*, 40 (309):1040–1063, 1949.
- <sup>20</sup> P. Chandra and P. B.. Littlewood. A Landau Primer for Ferroelectrics. In *Physics of Ferroelectrics*, volume 105 of *Topics in Applied Physics*, pages 69–116. Springer, Berlin, 2007. ISBN 978-3-540-34590-9.
- <sup>21</sup> N. Setter. *Piezoelectric Materials in Devices*, chapter ABC of Piezoelectricity and Piezoelectric Materials. EPFL Swiss Federal Institute of Technology, Lausanne, 2002.
- <sup>22</sup> L. J. Gauckler. *Ingenieurskeramik III - Funktionskeramik*. Swiss Federal Institute of Technology Zürich, Zürich, 2001.
- <sup>23</sup> D. Damjanovic. *The Science of Hysteresis*, chapter Hysteresis in Piezoelectric and Ferroelectric Materials. Elsevier, New York, 2005.
- <sup>24</sup> V. Y. Shur. *Ferroelectric Thin Films: Synthesis and Basic Properties*, chapter Fast Polarization Reversal Process: Evolution Of Ferroelectric Domain Structure in Thin Films. Gordon and Breach, Amsterdam, 1996.
- <sup>25</sup> Z. G. Ye. Relaxor Ferroelectric Complex Perovskites: Structure, Properties and Phase Transitions. *Key Engineering Materials*, 155-156(1):81–122, 1998.
- <sup>26</sup> A. A. Bokov and Z. G. Ye. Recent Progress in Relaxor Ferroelectrics with Perovskite Structure. *Journal of Materials Science*, 41(1):31–52, 2006.

- <sup>27</sup> W. Kleemann. The Relaxor Enigma - Charge Disorder and Random Fields in Ferroelectrics. *Journal of Materials Science*, 41(1):129–136, 2006.
- <sup>28</sup> G. A. Samara. The Relaxational Properties of Compositionally Disordered ABO<sub>3</sub> Perovskites. *Journal of Physics: Condensed Matter*, 15(9):R367–R411, 2003.
- <sup>29</sup> V. V. Shvartsman and D. C. Lupascu. Lead-Free Relaxor Ferroelectrics. *Journal of the American Ceramic Society*, 95(1):1–26, 2012.
- <sup>30</sup> G. A. Smolenskii and V. A. Isupov. Segnetoelektricheskie Svoistva Tverdykh Rastvorov Stan-nata Bariya V Titanate Bariya. *Zhurnal Tekhnicheskoi Fiziki*, 24(8):1375–1386, 1954.
- <sup>31</sup> G. A. Smolenskii, V. A. Isupov, A. I. Agranovskaya, and S. N. Popov. Ferroelectrics with Diffuse Phase Transition. *Soviet Physics-Solid State*, 2(11):2584–2594, 1961.
- <sup>32</sup> D. Viehland, M. Wuttig, and L. E. Cross. The Glassy Behavior of Relaxor Ferroelectrics. *Ferroelectrics*, 120(1):71–77, 1991.
- <sup>33</sup> L. E. Cross. Relaxor Ferroelectrics. *Ferroelectrics*, 76(1):241–267, 1987.
- <sup>34</sup> M. D. Glinchuk and R. Farhi. A Random Field Theory Based Model for Ferroelectric Relaxors. *Journal of Physics: Condensed Matter*, 8(37):6985–6996, 1996.
- <sup>35</sup> R. Pirc and R. Blinc. Spherical Random-Bond-Random-Field Model of Relaxor Ferroelectrics. *Physical Review B*, 60(19):13470–13478, 1999.
- <sup>36</sup> W. Kleemann. Random Fields in Dipolar Glasses and Relaxors. *Journal of Non-Crystalline Solids*, 307-310(0):66–72, 2002.
- <sup>37</sup> C. A. Randall, A. S. Bhalla, T. R. Shrout, and L. E. Cross. Classification and Consequences of Complex Lead Perovskite Ferroelectrics with Regard to B-site Cation Order. *Journal of Materials Research*, 5(4):829–834, 1990.
- <sup>38</sup> C. A. Randall and A. S. Bhalla. Nanostructural-Property Relations in Complex Lead Perovskites. *Japanese Journal of Applied Physics Part 1-regular Papers Short Notes & Review Papers*, 29(2):327–333, 1990.
- <sup>39</sup> P. K. Davies and M. A. Akbas. Chemical Order in PMN-Related Relaxors: Structure, Stability, Modification, and Impact on Properties. *Journal of Physics and Chemistry of Solids*, 61(2):159–166, 2000.
- <sup>40</sup> M. Yoshida, S. Mori, N. Yamamoto, Y. Uesu, and J. M. Kiat. TEM Observation of Polar Domains in Relaxor Ferroelectric Pb(Mg<sub>1/3</sub>Nb<sub>2/3</sub>)O<sub>3</sub>. *Ferroelectrics*, 217(1-4):327–333, 1998.
- <sup>41</sup> C. A. Randall and R. W. Groves P. Barber, D. J. Whatmore. A TEM Study of Ordering in the Perovskite Pb(Sc<sub>1/2</sub>Ta<sub>1/2</sub>)O<sub>3</sub>. *Journal of Materials Science*, 21(12):4456–4462, 1986.

- <sup>42</sup> N. Setter and L. E. Cross. The Role of B-Site Cation Disorder in Diffuse Phase Transition Behavior of Perovskite Ferroelectrics. *Journal of Applied Physics*, 51(8):4356–4360, 1980.
- <sup>43</sup> G. Burns and F.H. Dacol. Glassy Polarization Behavior in Ferroelectric Compounds  $\text{Pb}(\text{Mg}_{1/3}\text{Nb}_{2/3})\text{O}_3$  and  $\text{Pb}(\text{Zn}_{1/3}\text{Nb}_{2/3})\text{O}_3$ . *Solid State Communications*, 48(10):853–856, 1983.
- <sup>44</sup> V. Westphal, W. Kleemann, and M. D. Glinchuk. Diffuse Phase-Transitions and Random-Field-Induced Domain States of the Relaxor Ferroelectric  $\text{PbMg}_{1/3}\text{Nb}_{2/3}\text{O}_3$ . *Physical Review Letters*, 68(6):847–850, 1992.
- <sup>45</sup> Z.-G. Ye and H. Schmid. Optical, Dielectric and Polarization Studies of the Electric Field-Induced Phase Transition in  $\text{Pb}(\text{Mg}_{1/3}\text{Nb}_{2/3})\text{O}_3$  (PMN). *Ferroelectrics*, 145(1):83–108, 1993.
- <sup>46</sup> T. Kim, J. N. Hanson, A. Gruverman, A. I. Kingon, and S. K. Streiffer. Ferroelectric Behavior in Nominally Relaxor Lead Lanthanum Zirconate Titanate Thin Films Prepared by Chemical Solution Deposition on Copper Foil. *Applied Physics Letters*, 88(26):262907, 2006.
- <sup>47</sup> D. Viehland, S. J. Jang, L. E. Cross, and M. Wuttig. Freezing of the Polarization Fluctuations in Lead Magnesium Niobate Relaxors. *Journal of Applied Physics*, 68(6):2916–2921, 1990.
- <sup>48</sup> V. V. Shvartsman, A. L. Kholkin, A. Orlova, D. Kiselev, A. A. Bogomolov, and A. Sternberg. Polar Nanodomains and Local Ferroelectric Phenomena in Relaxor Lead Lanthanum Zirconate Titanate Ceramics. *Applied Physics Letters*, 86(20):202907, 2005.
- <sup>49</sup> S. Kamba, E. Buixaderas, J. Petzelt, J. Fousek, J. Nosek, and P. Bridenbaugh. Infrared and Raman Spectroscopy of  $[\text{Pb}(\text{Zn}_{1/3}\text{Nb}_{2/3})\text{O}_3]_{0.92}-[\text{PbTiO}_3]_{0.08}$  and  $[\text{Pb}(\text{Mg}_{1/3}\text{Nb}_{2/3})\text{O}_3]_{0.71}-[\text{PbTiO}_3]_{0.29}$  Single Crystals. *Journal of Applied Physics*, 93(2):933–939, 2003.
- <sup>50</sup> X. Zhao, W. Qu, X. Tan, A. A. Bokov, and Z-G. Ye. Electric Field-Induced Phase Transitions in (111)-, (110)-, and (100)-Oriented  $\text{Pb}(\text{Mg}_{1/3}\text{Nb}_{2/3})\text{O}_3$  Single Crystals. *Physical Review B*, 75(10):104106, 2007.
- <sup>51</sup> Z. Kutnjak, B. Vodopivec, and R. Blinc. Anisotropy of Electric Field Freezing of the Relaxor Ferroelectric  $\text{Pb}(\text{Mg}_{1/3}\text{Nb}_{2/3})\text{O}_3$ . *Physical Review B*, 77(5):054102, 2008.
- <sup>52</sup> R. Shirane, G. Newnham and R. Pepinsky. Dielectric Properties and Phase Transitions of  $\text{NaNbO}_3$  and  $(\text{Na,K})\text{NbO}_3$ . *Physical Review*, 96(3):581–588, 1954.
- <sup>53</sup> E. A. Wood. Polymorphism In Potassium Niobate, Sodium Niobate, and Other  $\text{ABO}_3$  Compounds. *Acta Crystallographica*, 4(4):353–362, 1951.
- <sup>54</sup> M. Ahtee and A. M. Glazer. Lattice-Parameters and Tilted Octahedra In Sodium-Potassium Niobate Solid-solutions. *Acta Crystallographica Section A*, 32(3):434, 1976.

- <sup>55</sup> M. Ahtee and A. W. Hewat. Structural Phase-Transitions In Sodium-Potassium Niobate Solid-Solutions By Neutron Powder Diffraction. *Acta Crystallographica Section A*, 34(2):309–317, 1978.
- <sup>56</sup> V. J. Tennery. High-temperature Phase Transitions in  $\text{NaNbO}_3$ . *Journal of the American Ceramic Society*, 48(10):537, 1965.
- <sup>57</sup> V. J. Tennery and K.W. Hang. Thermal and X-ray Diffraction Studies of  $\text{NaNbO}_3$ - $\text{KNbO}_3$  System. *Journal of Applied Physics*, 39(10):4749, 1968.
- <sup>58</sup> J. Tellier, B. Malic, B. Dkhil, D. Jenko, J. Cilensek, and M. Kosec. Crystal Structure and Phase Transitions of Sodium Potassium Niobate Perovskites. *Solid State Sciences*, 11(2):320–324, 2009.
- <sup>59</sup> J. F. Li, K. Wang, F. Y. Zhu, L. Q. Cheng, and F. Z. Yao. (K,Na) $\text{NbO}_3$ -Based Lead-Free Piezoceramics: Fundamental Aspects, Processing Technologies, and Remaining Challenges. *Journal of the American Ceramic Society*, 96(12):3677–3696, 2013.
- <sup>60</sup> L. Wu, J. L. Zhang, C. L. Wang, and J. C. Li. Influence of Compositional Ratio K/Na on Physical Properties in  $\text{K}_{0.44}\text{Na}_{0.52}\text{Li}_x\text{Na}_{1-x}\text{NbO}_3$  ceramics. *Journal of Applied Physics*, 103(8):084116, 2008.
- <sup>61</sup> Y. J. Dai, X. W. Zhang, and K. P. Chen. Morphotropic Phase Boundary and Electrical Properties of  $\text{K}_{1-x}\text{Na}_x\text{NbO}_3$  Lead-Free Ceramics. *Applied Physics Letters*, 94(4):042905, 2009.
- <sup>62</sup> J. F. Nye. *Physical Properties of Crystals*. Clarendon press, 1985.
- <sup>63</sup> Kenji Uchino. *Ferroelectric Devices*. Marcel Dekker, New York, 2000.
- <sup>64</sup> L. Egerton and D. M. Dillon. Piezoelectric and Dielectric Properties of Ceramics in the System Potassium Sodium Niobate. *Journal of the American Ceramic Society*, 42(9):438–442, 1959.
- <sup>65</sup> R. E. Jaeger and L. Egerton. Hot Pressing of Potassium-sodium Niobates. *Journal of the American Ceramic Society*, 45(5):209–213, 1962.
- <sup>66</sup> J. F. Li, K. Wang, B. P. Zhang, and L. M. Zhang. Ferroelectric and Piezoelectric Properties of Fine-Grained  $\text{Na}_{0.5}\text{K}_{0.5}\text{NbO}_3$  Lead-Free Piezoelectric Ceramics Prepared by Spark Plasma Sintering. *Journal of the American Ceramic Society*, 89(2):706–709, 2006.
- <sup>67</sup> K. Wang, B. P. Zhang, J. F. Li, and L. M. Zhang. Lead-Free  $\text{Na}_{0.5}\text{K}_{0.5}\text{NbO}_3$  Piezoelectric Ceramics Fabricated by Spark Plasma Sintering: Annealing Effect on Electrical Properties. *Journal of Electroceramics*, 21(1-4):251–254, 2008.

- <sup>68</sup> R. P. Wang, R. J. Xie, T. Sekiya, Y. Shimojo, Y. Akimune, N. Hirotsuki, and M. Itoh. Piezoelectric Properties of Spark-Plasma-Sintered  $(\text{Na}_{0.5}\text{K}_{0.5})\text{NbO}_3\text{-PbTiO}_3$  Ceramics. *Japanese Journal of Applied Physics Part 1-regular Papers Short Notes & Review Papers*, 41(11B):7119–7122, 2002.
- <sup>69</sup> I. Coondoo, N. Panwar, and A. Kholkin. Lead-Free Piezoelectrics: Current Status and Perspectives. *Journal of Advanced Dielectrics*, 03(02):1330002, 2013.
- <sup>70</sup> Y. P. Guo, K. Kakimoto, and H. Ohsato. Phase transitional behavior and piezoelectric properties of  $(\text{Na}_{0.5}\text{K}_{0.5})\text{NbO}_3\text{-LiNbO}_3$  ceramics. *Applied Physics Letters*, 85(18):4121–4123, 2004.
- <sup>71</sup> E. Hollenstein, D. Damjanovic, and N. Setter. Temperature Stability of the Piezoelectric Properties of Li-Modified KNN Ceramics. *Journal of the European Ceramic Society*, 27(13-15):4093–4097, 2007.
- <sup>72</sup> K. Wang and J. F. Li. Low-Temperature Sintering of Li-Modified  $(\text{K}, \text{Na})\text{NbO}_3$  Lead-Free Ceramics: Sintering Behavior, Microstructure, and Electrical Properties. *Journal of the American Ceramic Society*, 93(4):1101–1107, 2010.
- <sup>73</sup> K. Wang, J. F. Li, and N. Liu. Piezoelectric Properties of Low-Temperature Sintered Li-Modified  $(\text{Na}, \text{K})\text{NbO}_3$  Lead-Free Ceramics. *Applied Physics Letters*, 93(9):092904, 2008.
- <sup>74</sup> Y. G. Lv, C. L. Wang, J. L. Zhang, L. Wu, M. L. Zhao, and J. P. Xu. Tantalum Influence on Physical Properties of  $(\text{K}_{0.5}\text{Na}_{0.5})(\text{Nb}_{1-x}\text{Ta}_x)\text{O}_3$  Ceramics. *Materials Research Bulletin*, 44(2):284–287, 2009.
- <sup>75</sup> Y. G. Lv, C. L. Wang, J. L. Zhang, M. L. Zhao, M. K. Li, and H. C. Wang. Modified  $(\text{K}_{0.5}\text{Na}_{0.5})(\text{Nb}_{0.9}\text{Ta}_{0.1})\text{O}_3$  Ceramics with High  $Q(m)$ . *Materials Letters*, 62(19):3425–3427, 2008.
- <sup>76</sup> M. Matsubara, T. Yamaguchi, W. Sakamoto, K. Kikuta, T. Yogo, and S. Hirano. Processing and Piezoelectric Properties of Lead-Free  $(\text{K}, \text{Na})(\text{Nb}, \text{Ta})\text{O}_3$  Ceramics. *Journal of the American Ceramic Society*, 88(5):1190–1196, 2005.
- <sup>77</sup> D. M. Lin, K. W. Kwok, H. Y. Tian, and H. W. Chan. Phase Transitions and Electrical Properties of  $(\text{Na}_{1-x}\text{K}_x)(\text{Nb}_{1-y}\text{Sb}_y)\text{O}_3$  Lead-Free Piezoelectric Ceramics with a  $\text{MnO}_2$  Sintering Aid. *Journal of the American Ceramic Society*, 90(5):1458–1462, 2007.
- <sup>78</sup> E. Z. Li, H. Kakimoto, T. Hoshina, and T. Tsurumi. A Shear-Mode Ultrasonic Motor Using Potassium Sodium Niobate-Based Ceramics with High Mechanical Quality Factor. *Japanese Journal of Applied Physics*, 47(9):7702–7706, 2008.
- <sup>79</sup> E. K. Akdogan, K. Kerman, M. Abazari, and A. Safari. Origin of High Piezoelectric Activity in Ferroelectric  $(\text{K}_{0.44}\text{Na}_{0.52}\text{Li}_{0.04})\text{-}(\text{Nb}_{0.84}\text{Ta}_{0.1}\text{Sb}_{0.06})\text{O}_3$  Ceramics. *Applied Physics Letters*, 92(11):112908, 2008.



- <sup>80</sup> H. Li, W. Y. Shih, and W. H. Shih. Effect of Antimony Concentration on the Crystalline Structure, Dielectric, and Piezoelectric Properties of  $(\text{Na}_{0.5}\text{K}_{0.5})(0.945)\text{Li}_{0.055}\text{Nb}_{1-x}\text{Sb}_x\text{O}_3$  Solid Solutions. *Journal of the American Ceramic Society*, 90(10):3070–3072, 2007.
- <sup>81</sup> J. G. Wu, D. Q. Xiao, Y. Y. Wang, J. G. Zhu, L. Wu, and Y. H. Jiang. Effects of K/Na Ratio on the Phase Structure and Electrical Properties of  $(\text{K}_x\text{Na}_{0.96-x}\text{Li}_{0.04})(\text{Nb}_{0.91}\text{Ta}_{0.05}\text{Sb}_{0.04})\text{O}_3$  Lead-Free Ceramics. *Applied Physics Letters*, 91(25):252907, 2007.
- <sup>82</sup> J. G. Wu, D. Q. Xiao, Y. Y. Wang, J. G. Zhu, and P. Yu. Effects of K Content on the Dielectric, Piezoelectric, and Ferroelectric Properties of  $0.95(\text{K}_x\text{Na}_{1-x})\text{NbO}_3-0.05\text{LiSbO}_3$  Lead-Free Ceramics. *Journal of Applied Physics*, 103(2):024102, 2008.
- <sup>83</sup> Y. H. Zhen and J. F. Li. Normal Sintering of  $(\text{K},\text{Na})\text{NbO}_3$ -Based Ceramics: Influence of Sintering Temperature on Densification, Microstructure, and Electrical Properties. *Journal of the American Ceramic Society*, 89(12):3669–3675, 2006.
- <sup>84</sup> J. L. Zhang, X. J. Zong, L. Wu, Y. Gao, P. Zheng, and S. F. Shao. Polymorphic Phase Transition and Excellent Piezoelectric Performance of  $(\text{K}_{0.55}\text{Na}_{0.45})(0.965)\text{Li}_{0.035}\text{Nb}_{0.80}\text{Ta}_{0.20}\text{O}_3$  Lead-Free Ceramics. *Applied Physics Letters*, 95(2):022909, 2009.
- <sup>85</sup> Z. Y. Shen, Y. H. Zhen, K. Wang, and J. F. Li. Influence of Sintering Temperature on Grain Growth and Phase Structure of Compositionally Optimized High-Performance Li/Ta-Modified  $(\text{Na},\text{K})\text{NbO}_3$  Ceramics. *Journal of the American Ceramic Society*, 92(8):1748–1752, 2009.
- <sup>86</sup> S. J. Zhang, R. Xia, T. R. Shrout, G. Z. Zang, and J. F. Wang. Piezoelectric Properties in Perovskite  $0.948(\text{K}_{0.5}\text{Na}_{0.5})\text{NbO}_3-0.052\text{LiSbO}_3$  Lead-Free Ceramics. *Journal of Applied Physics*, 100(10):104108, 2006.
- <sup>87</sup> H. L. Du, F. S. Tang, D. J. Liu, D. M. Zhu, W. C. Zhou, and S. B. Qu. The Microstructure and Ferroelectric Properties of  $(\text{K}_{0.5}\text{Na}_{0.5})\text{NbO}_3-\text{LiNbO}_3$  Lead-Free Piezoelectric Ceramics. *Materials Science and Engineering B-solid State Materials For Advanced Technology*, 136(2-3):165–169, 2007.
- <sup>88</sup> R. Z. Zuo, J. Fu, and D. Y. Lv. Phase Transformation and Tunable Piezoelectric Properties of Lead-Free  $(\text{Na}_{0.52}\text{K}_{0.48-x}\text{Li}_x)(\text{Nb}_{1-x-y}\text{Sb}_y\text{Ta}_x)\text{O}_3$  System. *Journal of the American Ceramic Society*, 92(1):283–285, 2009.
- <sup>89</sup> R. Z. Zuo and J. Fu. Rhombohedral-Tetragonal Phase Coexistence and Piezoelectric Properties of  $(\text{NaK})(\text{NbSb})\text{O}_3-\text{LiTaO}_3-\text{BaZrO}_3$  Lead-Free Ceramics. *Journal of the American Ceramic Society*, 94(5):1467–1470, 2011.
- <sup>90</sup> H. Y. Park, C. W. Ahn, H. C. Song, J. H. Lee, S. Nahm, K. Uchino, H. G. Lee, and H. J. Lee. Microstructure and Piezoelectric Properties of  $0.95(\text{Na}_{0.5}\text{K}_{0.5})\text{NbO}_3-0.05\text{BaTiO}_3$  Ceramics. *Applied Physics Letters*, 89(6):062906, 2006.

- <sup>91</sup> D. Lin, K. W. Kwok, and H. W. L. Chan. Dielectric and Piezoelectric Properties of  $(\text{K}_{0.5}\text{Na}_{0.5})\text{NbO}_3\text{-Ba}(\text{Zr}_{0.05}\text{Ti}_{0.95})\text{O}_3$  Lead-Free Ceramics. *Applied Physics Letters*, 91(14):143513, 2007.
- <sup>92</sup> R. Z. Zuo, X. S. Fang, and C. Ye. Phase Structures and Electrical Properties of New Lead-Free  $(\text{Na}_{0.5}\text{K}_{0.5})\text{NbO}_3\text{-(Bi}_{0.5}\text{Na}_{0.5})\text{TiO}_3$  Ceramics. *Applied Physics Letters*, 90(9):092904, 2007.
- <sup>93</sup> H. L. Du, W. C. Zhou, F. Luo, D. M. Zhu, S. B. Qu, Y. Li, and Z. B. Pei. Polymorphic Phase Transition Dependence of Piezoelectric Properties in  $(\text{K}_{0.5}\text{Na}_{0.5})\text{NbO}_3\text{-(Bi}_{0.5}\text{K}_{0.5})\text{TiO}_3$  Lead-Free Ceramics. *Journal of Physics D-applied Physics*, 41(11):115413, 2008.
- <sup>94</sup> P. Dubernet and J. Ravez. Dielectric Study of  $\text{KNbO}_3$  Ceramics over a Large Range of Frequency (10(2) -10(9) Hz) and Temperature (300 -800 K). *Ferroelectrics*, 211(1-4):51–66, 1998.
- <sup>95</sup> T. A. Skidmore and S. J. Milne. Phase Development During Mixed-Oxide Processing of a  $[\text{Na}_{0.5}\text{K}_{0.5}\text{NbO}_3]_{(1-x)}[\text{LiTaO}_3]_{(x)}$  Powder. *Journal of Materials Research*, 22(8):2265–2272, 2007.
- <sup>96</sup> H. L. Du, Z. M. Li, F. S. Tang, S. B. Qu, Z. B. Pei, and W. C. Zhou. Preparation and Piezoelectric Properties of  $(\text{K}_{0.5}\text{Na}_{0.5})\text{NbO}_3$  Lead-Free Piezoelectric Ceramics with Pressure-Less Sintering. *Materials Science and Engineering B-solid State Materials For Advanced Technology*, 131(1-3):83–87, 2006.
- <sup>97</sup> Y. Wang, D. Damjanovic, N. Klein, E. Hollenstein, and N. Setter. Compositional Inhomogeneity in Li- and Ta-Modified (K, Na) $\text{NbO}_3$  Ceramics. *Journal of the American Ceramic Society*, 90(11):3485–3489, 2007.
- <sup>98</sup> Y. F. Chang, S. Poterala, Z. P. Yang, and G. L. Messing. Enhanced Electromechanical Properties and Temperature Stability of Textured  $(\text{K}_{0.5}\text{Na}_{0.5})\text{NbO}_3$ -Based Piezoelectric Ceramics. *Journal of the American Ceramic Society*, 94(8):2494–2498, 2011.
- <sup>99</sup> D. Schütz, M. Deluca, W. Krauss, A. Feteira, T. Jackson, and K. Reichmann. Lone-Pair-Induced Covalency as the Cause of Temperature- and Field-Induced Instabilities in Bismuth Sodium Titanate. *Advanced Functional Materials*, 22(11):2285–2294, 2012.
- <sup>100</sup> H. Nagata, T. Shinya, Y. Hiruma, and T. Takenaka. Developments in Dielectric Materials and Electronic Devices. In *Ceramic Transactions*, pages 213–221, Indianapolis, Indiana, USA, 2004.
- <sup>101</sup> P. K. Panda. Review: Environmental Friendly Lead-Free Piezoelectric Materials. *Journal of Materials Science*, 44(19):5049–5062, 2009.
- <sup>102</sup> A. M. Glazer. Classification of Tilted Octahedra in Perovskites. *Acta Crystallographica Section B: Structural Science*, B 28:3384–3392, 1972.

- <sup>103</sup> G. O. Jones and P. A. Thomas. Investigation of the Structure and Phase Transitions in the Novel A-Site Substituted Distorted Perovskite Compound  $\text{Na}_{0.5}\text{Bi}_{0.5}\text{TiO}_3$ . *Acta Crystallographica Section B: Structural Science*, B58(2):168–178, 2002.
- <sup>104</sup> J. Kusz, J. Suchanicz, H. Bohm, and J. Warczewski. High Temperature X-Ray Single Crystal Study of  $\text{Na}_{1/2}\text{Bi}_{1/2}\text{TiO}_3$ . *Phase Transitions*, 70(3):223–229, 1999.
- <sup>105</sup> J. Suchanicz. Investigations of the Phase Transitions in  $\text{Na}_{0.5}\text{Bi}_{0.5}\text{TiO}_3$ . *Ferroelectrics*, 172(1):455–458, 1995.
- <sup>106</sup> S. B. Vakhrushev, V. A. Isupov, B. E. Kvyatkovsky, N. M. Okuneva, I. P. Pronin, G. A. Smolensky, and P. P. Syrnikov. Phase Transitions and Soft Modes in Sodium Bismuth Titanate. *Ferroelectrics*, 63(1):153–160, 1985.
- <sup>107</sup> S. E. Park, S. J. Chung, I. T. Kim, and K. S. Hong. Nonstoichiometry and the Long-Range Cation Ordering in Crystals of  $(\text{Na}_{1/2}\text{Bi}_{1/2})\text{TiO}_3$ . *Journal of the American Ceramic Society*, 77(10):2641–2647, 1994.
- <sup>108</sup> V. Dorcet, G. Trolliard, and P. Boullay. Reinvestigation of Phase Transitions in  $\text{Na}_{0.5}\text{Bi}_{0.5}\text{TiO}_3$  by TEM. Part I: First Order Rhombohedral to Orthorhombic Phase Transition. *Chemistry of Materials*, 20(15):5061–5073, 2008.
- <sup>109</sup> I. P. Pronin, P. P. Syrnikov, V. A. Isupov, V. M. Egorov, and N. V. Zaitseva. Peculiarities of Phase Transitions in Sodium-Bismuth Titanate. *Ferroelectrics*, 25(1):395–397, 1980.
- <sup>110</sup> K. Sakata and Y. Masuda. Ferroelectric and Antiferroelectric Properties of  $(\text{Na}_{0.5}\text{Bi}_{0.5})\text{TiO}_3$ - $\text{SrTiO}_3$  Solid Solution Ceramics. *Ferroelectrics*, 7(1):347–349, 1974.
- <sup>111</sup> J. Suchanicz, I. P. Mercurio, P. Marchet, and T. V. Kruzina. Axial Pressure Influence on Dielectric and Ferroelectric Properties of  $\text{Na}_{0.5}\text{Bi}_{0.5}\text{TiO}_3$  Ceramic. *Physica Status Solidi B-basic Research*, 225(2):459–466, 2001.
- <sup>112</sup> M. S. Zhang, J. F. Scott, and J. A. Zvirgzds. Raman-Spectroscopy of  $\text{Na}_{0.5}\text{Bi}_{0.5}\text{TiO}_3$ . *Ferroelectrics Letters Section*, 6(5):147–152, 1986.
- <sup>113</sup> J. Suchanicz, K. Roleder, A. Kania, and J. Hanaderek. Electrostrictive Strain and Pyroeffect in the Region of Phase Coexistence in  $\text{Na}_{0.5}\text{Bi}_{0.5}\text{TiO}_3$ . *Ferroelectrics*, 77(1):107–110, 1988.
- <sup>114</sup> K. Roleder, J. Suchanicz, and A. Kania. Time Dependence of Electric Permittivity in  $\text{Na}_{0.5}\text{Bi}_{0.5}\text{TiO}_3$  Single Crystals. *Ferroelectrics*, 89(1):1–5, 1989.
- <sup>115</sup> A. Herabut and A. Safari. Processing and Electromechanical Properties of  $(\text{Bi}_{0.5}\text{Na}_{0.5})((1-1.5x))\text{La}_x\text{TiO}_3$  Ceramics. *Journal of the American Ceramic Society*, 80(11):2954–2958, 1997.

- <sup>116</sup> J. R. Gomah-Petry, E. Said, P. Marchet, and J. P. Mercurio. Sodium-Bismuth Titanate Based Lead-Free Ferroelectric Materials. *Journal of the European Ceramic Society*, 24(6):1165–1169, 2004.
- <sup>117</sup> Y. Hiruma, Y. Imai, Y. Watanabe, H. Nagata, and T. Takenaka. Large Electrostrain Near the Phase Transition Temperature of  $(\text{Bi}_{0.5}\text{Na}_{0.5})\text{TiO}_3$ - $\text{SrTiO}_3$  Ferroelectric Ceramics. *Applied Physics Letters*, 92(26):262904, 2008.
- <sup>118</sup> J. K. Lee, K. S. Hong, C. K. Kim, and S. E. Park. Phase Transitions and Dielectric Properties in A-Site Ion Substituted  $(\text{Na}_{1/2}\text{Bi}_{1/2})\text{TiO}_3$  Ceramics (A=Pb and Sr). *Journal of Applied Physics*, 91(7):4538–4542, 2002.
- <sup>119</sup> S. E. Park and K. S. Hong. Variations of Structure and Dielectric Properties on Substituting A-Site Cations for  $\text{Sr}^{2+}$  in  $(\text{Na}_{1/2}\text{Bi}_{1/2})\text{TiO}_3$ . *Journal of Materials Research*, 12(8):2152–2157, 1997.
- <sup>120</sup> J. Konig, B. Jancar, and D. Suvorov. New  $\text{Na}_{0.5}\text{Bi}_{0.5}\text{TiO}_3$ - $\text{NaTaO}_3$ -Based Perovskite Ceramics. *Journal of the American Ceramic Society*, 90(11):3621–3627, 2007.
- <sup>121</sup> C. R. Zhou and X. Y. Liu. Effect of B-Site Substitution by  $(\text{Ni}_{1/3}\text{Nb}_{2/3})^{4+}$  For  $\text{Ti}^{4+}$  on Microstructure and Piezoelectric Properties in  $(\text{Bi}_{1/2}\text{Na}_{1/2})\text{TiO}_3$  Piezoelectric Ceramics. *Journal of Alloys and Compounds*, 466(1-2):563–567, 2008.
- <sup>122</sup> T. Takenaka and H. Nagata. Present Status of Non-Lead-Based Piezoelectric Ceramics. *Electroceramics In Japan I*, 157(1):57–63, 1999.
- <sup>123</sup> Y. M. Li, W. Chen, J. Zhou, Q. Xu, X. Y. Gu, and R. H. Liao. Impedance Spectroscopy and Dielectric Properties of  $\text{Na}_{0.5}\text{Bi}_{0.5}\text{TiO}_3$ - $\text{NaNbO}_3$  Ceramics. *Physica B-condensed Matter*, 365(1-4):76–81, 2005.
- <sup>124</sup> Y. M. Li, W. Chen, J. Zhou, Q. Xu, H. Sun, and R. X. Xu. Dielectric and Piezoelectric Properties of Lead-Free  $(\text{Na}_{0.5}\text{Bi}_{0.5})\text{TiO}_3$ - $\text{NaNbO}_3$  Ceramics. *Materials Science and Engineering B-solid State Materials For Advanced Technology*, 112(1):5–9, 2004.
- <sup>125</sup> S. I. Raevskaya, L. A. Reznichenko, I. P. Raevski, V. V. Titov, S. V. Titov, and J. L. Dellis. Lead-Free Niobate Ceramics with Relaxor-like Properties. *Ferroelectrics*, 340:107–112, 2006.
- <sup>126</sup> T. Takenaka, T. Okuda, and K. Takegahara. Lead-Free Piezoelectric Ceramics Based on  $(\text{Bi}_{1/2}\text{Na}_{1/2})\text{TiO}_3$ - $\text{NaNbO}_3$ . *Ferroelectrics*, 196(1-4):495–498, 1997.
- <sup>127</sup> A. Sasaki, T. Chiba, Y. Mamiya, and E. Otsuki. Dielectric and Piezoelectric Properties of  $(\text{Bi}_{0.5}\text{Na}_{0.5})\text{TiO}_3$ - $(\text{Bi}_{0.5}\text{K}_{0.5})\text{TiO}_3$  Systems. *Japanese Journal Of Applied Physics*, 38(9B):5564–5567, 1999.

- <sup>128</sup> V. A. Shuvaeva, D. Zekria, A. M. Glazer, Q. Jiang, S. M. Weber, P. Bhattacharya, and P. A. Thomas. Local Structure of the Lead-Free Relaxor Ferroelectric  $(K_xNa_{1-x})(0.5)Bi_{0.5}TiO_3$ . *Physical Review B*, 71(17):174114, 2005.
- <sup>129</sup> H. Y. Tian, K. W. Kwok, H. L. W. Chan, and C. E. Buckley. The Effects of CuO-Doping on Dielectric and Piezoelectric Properties of  $Bi_{0.5}Na_{0.5}TiO_3$ - $Ba(Zr,Ti)O_3$  Lead-Free Ceramics. *Journal of Materials Science*, 42(23):9750–9755, 2007.
- <sup>130</sup> T. Wada, K. Toyoiike, Y. Imanaka, and Y. Matsuo. Dielectric and Piezoelectric Properties of  $(A_{0.5}Bi_{0.5})TiO_3$ - $ANbO_3$  ( $A = Na, K$ ) systems. *Japanese Journal of Applied Physics Part 1-regular Papers Short Notes & Review Papers*, 40(9B):5703–5705, 2001.
- <sup>131</sup> D. X. Zhou, H. Li, S. P. Gong, Y. X. Hu, and K. Han. Sodium Bismuth Titanate-Based Lead-Free Piezoceramics Prepared by Aqueous Gelcasting. *Journal of the American Ceramic Society*, 91(9):2792–2796, 2008.
- <sup>132</sup> Y. Hiruma, H. Nagata, and T. Takenaka. Thermal Depoling Process and Piezoelectric Properties of Bismuth Sodium Titanate Ceramics. *Journal of Applied Physics*, 105(8):084112, 2009.
- <sup>133</sup> Y. Hosono, K. Harada, and Y. Yamashita. Crystal Growth and Electrical Properties of Lead-Free Piezoelectric Material  $(Na_{1/2}Bi_{1/2})TiO_3$ - $BaTiO_3$ . *Japanese Journal of Applied Physics Part 1-regular Papers Short Notes & Review Papers*, 40(9B):5722–5726, 2001.
- <sup>134</sup> Y. M. Chiang, G. W. Farrey, and A. N. Soukhojak. Lead-Free High-Strain Single-Crystal Piezoelectrics in the Alkaline-Bismuth-Titanate Perovskite Family. *Applied Physics Letters*, 73(25):3683–3685, 1998.
- <sup>135</sup> Y. Hiruma, H. Nagata, and T. Takenaka. Phase Diagrams and Electrical Properties of  $(Bi_{1/2}Na_{1/2})TiO_3$  -Based Solid Solutions. *Journal of Applied Physics*, 104(12):124106, 2008.
- <sup>136</sup> S. T. Zhang, A. B. Kounga, E. Aulbach, H. Ehrenberg, and J. Rödel. Giant Strain in Lead-Free Piezoceramics  $Bi_{0.5}Na_{0.5}TiO_3$ - $BaTiO_3$ - $K_{0.5}Na_{0.5}NbO_3$  System. *Applied Physics Letters*, 91(11):112906, 2007.
- <sup>137</sup> S. T. Zhang, A. B. Kounga, E. Aulbach, T. Granzow, W. Jo, H. J. Kleebe, and J. Rödel. Lead-free Piezoceramics with Giant Strain in the System  $Bi_{0.5}Na_{0.5}TiO_3$ - $BaTiO_3$ - $K_{0.5}Na_{0.5}NbO_3$ . I. Structure and Room Temperature Properties. *Journal Of Applied Physics*, 103(3):034107, 2008.
- <sup>138</sup> S. T. Zhang, A. B. Kounga, E. Aulbach, and Y. Deng. Temperature-Dependent Electrical Properties of  $0.94Bi_{0.5}Na_{0.5}TiO_3$ - $0.06BaTiO_3$  Ceramics. *Journal of the American Ceramic Society*, 91(12):3950–3954, 2008.

- <sup>139</sup> J. E. Daniels, W. Jo, J. Rödel, and J. L. Jones. Electric-Field-Induced Phase Transformation at a Lead-Free Morphotropic Phase Boundary: Case Study in a 93%(Bi<sub>0.5</sub>Na<sub>0.5</sub>)TiO<sub>3</sub>-7% BaTiO<sub>3</sub> Piezoelectric Ceramic. *Applied Physics Letters*, 95(3):032904, 2009.
- <sup>140</sup> E. Dul'kin, E. Mojaev, M. Roth, W. Jo, and T. Granzow. Acoustic Emission Study of Domain Wall Motion and Phase Transition in (1-x-y)Bi<sub>0.5</sub>Na<sub>0.5</sub>TiO<sub>3</sub>-xBaTiO<sub>3</sub>-yK<sub>0.5</sub>Na<sub>0.5</sub>NbO<sub>3</sub> Lead-Free Piezoceramics. *Scripta Materialia*, 60(4):251–253, 2009.
- <sup>141</sup> H. Simons, J. Daniels, W. Jo, R. Dittmer, A. Studer, M. Avdeev, J. Rödel, and M. Hoffman. Electric-Field Induced Strain Mechanisms in 94BNT-6BT. *Applied Physics Letters*, 98(8):082901, 2011.
- <sup>142</sup> J. Kling, X. Tan, W. Jo, H. J. Kleebe, H. Fuess, and J. Rödel. In Situ Transmission Electron Microscopy of Electric Field-Triggered Reversible Domain Formation in Bi-Based Lead-Free Piezoceramics. *Journal of the American Ceramic Society*, 93(9):2452–2455, 2010.
- <sup>143</sup> D. Damjanovic, N. Klein, J. Li, and V. Porokhonsky. What Can Be Expected From Lead-free Piezoelectric Materials? *Functional Materials Letters*, 3(1):5–13, 2010.
- <sup>144</sup> B.J. Chu, D.R. Chen, G.R. Li, and Q.R. Yin. Electrical Properties of Na<sub>1/2</sub>Bi<sub>1/2</sub>TiO<sub>3</sub>-BaTiO<sub>3</sub> Ceramics. *Journal of the European Ceramic Society*, 22(13):2115–2121, 2002.
- <sup>145</sup> Q. Xu, S. T. Chen, W. Chen, S. J. Wu, J. Zhou, H. J. Sun, and Y. M. Li. Synthesis and Piezoelectric and Ferroelectric Properties of (Na<sub>0.5</sub>Bi<sub>0.5</sub>)<sub>1-x</sub>Ba<sub>x</sub>TiO<sub>3</sub> Ceramics. *Materials Chemistry and Physics*, 90(1):111–115, 2005.
- <sup>146</sup> C. Xu, D. Lin, and K. W. Kwok. Structure, Electrical Properties and Depolarization Temperature of (Bi<sub>0.5</sub>Na<sub>0.5</sub>)TiO<sub>3</sub>-BaTiO<sub>3</sub> Lead-Free Piezoelectric Ceramics. *Solid State Sciences*, 10(7):934–940, 2008.
- <sup>147</sup> J. Anthoniappen, C. H. Lin, C. S. Tu, P. Y. Chen, C. S. Chen, S. J. Chiu, H. Y. Lee, S. F. Wang, and C. M. Hung. Enhanced Piezoelectric and Dielectric Responses in 92.5%(Bi<sub>0.5</sub>Na<sub>0.5</sub>)TiO<sub>3</sub>-7.5%BaTiO<sub>3</sub> Ceramics. *Journal of the American Ceramic Society*, 97(6):1890–1894, 2014.
- <sup>148</sup> C. Ma and X. Tan. Phase Diagram of Unpoled Lead-Free (1-x)(Bi<sub>1/2</sub>Na<sub>1/2</sub>)TiO<sub>3</sub>-xBaTiO<sub>3</sub> ceramics. *Solid State Communications*, 150(33-34):1497–1500, 2010.
- <sup>149</sup> J. Rödel, W. Jo, K. T. P. Seifert, E. M. Anton, T. Granzow, and D. Damjanovic. Perspective on the Development of Lead-free Piezoceramics. *Journal of the American Ceramic Society*, 92(6):1153–1177, 2009.
- <sup>150</sup> Y. Hiruma, Y. Watanabe, H. Nagata, and T. Takenaka. Phase Transition Temperatures of Divalent and Trivalent Ions Substituted (Bi<sub>1/2</sub>Na<sub>1/2</sub>)TiO<sub>3</sub> Ceramics. *Key Engineering Materials*, 350:93–96, 2007.

- <sup>151</sup> C. Ma, X. Tan, E. Dul'kin, and M. Roth. Domain Structure-Dielectric Property Relationship in Lead-Free  $(1-x)(\text{Bi}_{1/2}\text{Na}_{1/2})\text{TiO}_3-x\text{BaTiO}_3$  Ceramics. *Journal of Applied Physics*, 108(10), 2010.
- <sup>152</sup> H. Lidjici, B. Lagoun, M. Berrahal, M. Rguitti, M. A. Hentatti, and H. Khemakhem. XRD, Raman and Electrical Studies on the  $(1-x)(\text{Na}_{0.5}\text{Bi}_{0.5})\text{TiO}_3-x\text{BaTiO}_3$  Lead Free Ceramics. *Journal of Alloys and Compounds*, 618:643–648, 2015.
- <sup>153</sup> J. Anthoniappen, C.S. Tu, P.-Y. Chen, C.-S. Chen, S.-J. Chiu, H.-Y. Lee, Y. Ting, S.-F. Wang, and C.-K. Chai. Structural Phase Stability and Electric Field Induced Relaxor-Ferroelectric Phase Transition in  $(1-x)(\text{Bi}_{0.5}\text{Na}_{0.5})\text{TiO}_3-x\text{BaTiO}_3$  Ceramics. *Journal of Alloys and Compounds*, 618:120–126, 2015.
- <sup>154</sup> V. Dorcet, G. Trolliard, and P. Boullay. The Structural Origin of the Antiferroelectric Properties and Relaxor Behavior of  $\text{Na}_{0.5}\text{Bi}_{0.5}\text{TiO}_3$ . *Journal of Magnetism and Magnetic Materials*, 321(11):1758–1761, 2009.
- <sup>155</sup> Y. F. Qu, D. Shan, and J. J. Song. Effect of A-Site Substitution on Crystal Component and Dielectric Properties in  $\text{Bi}_{0.5}\text{Na}_{0.5}\text{TiO}_3$  Ceramics. *Materials Science and Engineering B-solid State Materials For Advanced Technology*, 121(1-2):148–151, 2005.
- <sup>156</sup> D. Shan, Y. F. Qu, and J. J. Song. Ionic Doping Effects on Crystal Structure and Relaxation Character in  $\text{Bi}_{0.5}\text{Na}_{0.5}\text{TiO}_3$  Ferroelectric Ceramics. *Journal of Materials Research*, 22(3):730–734, 2007.
- <sup>157</sup> J. Suchanicz, J. Kusz, H. Bohm, H. Duda, J. P. Mercurio, and K. Konieczny. Structural and Dielectric Properties of  $(\text{Na}_{0.5}\text{Bi}_{0.5})_{(0.70)}\text{Ba}_{0.30}\text{TiO}_3$  Ceramics. *Journal of the European Ceramic Society*, 23(10):S0955, 2003.
- <sup>158</sup> O. Elkechai, M. Manier, and J. P. Mercurio.  $\text{Na}_{0.5}\text{Bi}_{0.5}\text{TiO}_3\text{-K}_{0.5}\text{Bi}_{0.5}\text{TiO}_3$  (NBT-KBT) System: A Structural and Electrical Study. *Physica Status Solidi A Applications and Material Science*, 157(2):499–506, 1996.
- <sup>159</sup> J. Baek, J.-H. Kim, Z. G. Khim, C. W. Ahn, I. W. Kim, and H. W. Kim. Investigation of Lead-Free Piezoceramics  $\text{Bi}_{0.5}(\text{Na}_{1-x}\text{K}_x)_{0.5}\text{TiO}_3$  with Scanning Probe Microscope. In *Journal of Physics: Conference Series*, volume 61, page 545, 2007.
- <sup>160</sup> K. Yoshii, Y. Hiruma, H. Nagata, and T. Takenaka. Electrical Properties and Depolarization Temperature of  $(\text{Bi}_{1/2}\text{Na}_{1/2})\text{TiO}_3\text{-(Bi}_{1/2}\text{K}_{1/2})\text{TiO}_3$  Lead-Free Piezoelectric Ceramics. *Japanese Journal Of Applied Physics*, 45(5B):4493–4496, 2006.
- <sup>161</sup> Y. R. Zhang, J. F. Li, and B. P. Zhang. Enhancing Electrical Properties in NBT-KBT Lead-Free Piezoelectric Ceramics by Optimizing Sintering Temperature. *Journal of the American Ceramic Society*, 91(8):2716–2719, 2008.

- <sup>162</sup> S. C. Zhao, G. R. Li, A. L. Ding, T. B. Wang, and Q. R. Yin. Ferroelectric and Piezoelectric Properties of  $(\text{Na}, \text{K})_{0.5}\text{Bi}_{0.5}\text{TiO}_3$  Lead Free Ceramics. *Journal of Physics D-applied Physics*, 39(10):2277–2281, 2006.
- <sup>163</sup> M. Otonicar, S. D. Skapin, M. Spreitzer, and D. Suvorov. Compositional Range and Electrical Properties of the Morphotropic Phase Boundary in the  $\text{Na}_{0.5}\text{Bi}_{0.5}\text{TiO}_3$ - $\text{K}_{0.5}\text{Bi}_{0.5}\text{TiO}_3$  System. *Journal of the European Ceramic Society*, 30(4):971–979, 2010.
- <sup>164</sup> I. P. Pronin, N. N. Parfenova, N. V. Zaitseva, V. A. Isupov, and G. A. Smolenskii. Phase-Transitions in Solid-Solutions of Na-Bi and K-Bi Titanates. *Fizika Tverdogo Tela*, 24(6):1860–1863, 1982.
- <sup>165</sup> Z. P. Yang, B. Liu, L. L. Wei, and Y. T. Hou. Structure and Electrical Properties of  $(1-x)\text{Bi}_{0.5}\text{Na}_{0.5}\text{TiO}_3$ - $x\text{Bi}_{0.5}\text{K}_{0.5}\text{TiO}_3$  Ceramics Near Morphotropic Phase Boundary. *Materials Research Bulletin*, 43(1):81–89, 2008.
- <sup>166</sup> Y.K. Yan Zhao, W. H.P. Zhou and D. Liu. Morphotropic Phase Boundary Study of the BNT-BKT Lead-Free Piezoelectric Ceramics. *Key Engineering Materials*, 368 - 372:1908–1910, 2008.
- <sup>167</sup> A. Moosavi, M. A. Bahrevar, A. R. Aghaei, P. Ramos, M. Alguero, and H. Amarin. High-Field Electromechanical Response of  $\text{Bi}_{0.5}\text{Na}_{0.5}\text{TiO}_3$ - $\text{Bi}_{0.5}\text{K}_{0.5}\text{TiO}_3$  across its Morphotropic Phase Boundary. *Journal of Physics D-applied Physics*, 47(5):055304, 2014.
- <sup>168</sup> S. Said and J.P. Mercurio. Relaxor Behaviour Of Low Lead and Lead Free Ferroelectric Ceramics of the  $\text{Na}_{0.5}\text{Bi}_{0.5}\text{TiO}_3$ - $\text{PbTiO}_3$  and  $\text{Na}_{0.5}\text{Bi}_{0.5}\text{TiO}_3$ - $\text{K}_{0.5}\text{Bi}_{0.5}\text{TiO}_3$  Systems. *Journal of the European Ceramic Society*, 21(10-11):1333–1336, 2001.
- <sup>169</sup> J. Kreisel, A. M. Glazer, G. Jones, P. A. Thomas, L. Abello, and G. Lucazeau. An X-Ray Diffraction and Raman Spectroscopy Investigation of A-Site Substituted Perovskite Compounds: The  $(\text{Na}_{1-x}\text{K}_x)_{0.5}\text{Bi}_{0.5}\text{TiO}_3$  ( $0 \leq x \leq 1$ ) Solid Solution. *Journal of Physics: Condensed Matter*, 12(14):3267–3280, 2000.
- <sup>170</sup> E. M. Anton, L. A. Schmitt, M. Hinterstein, J. Trodahl, B. Kowalski, W. Jo, H.-J. Kleebe, J. Rödel, and J. L. Jones. Structure and Temperature-Dependent Phase Transitions of Lead-Free  $\text{Bi}_{1/2}\text{Na}_{1/2}\text{TiO}_3$ - $\text{Bi}_{1/2}\text{K}_{1/2}\text{TiO}_3$ - $\text{K}_{0.5}\text{Na}_{0.5}\text{NbO}_3$  Piezoceramics. *Journal of Materials Research*, 27(19):2466–2478, 2012.
- <sup>171</sup> R. Dittmer, W. Jo, J. Rödel, S. V. Kalinin, and N. Balke. Nanoscale Insight Into Lead-Free BNT-BT-xKNN. *Advance Functional Materials*, 22(12):4208–4215, 2012.
- <sup>172</sup> W. Jo, T. Granzow, E. Aulbach, J. Rödel, and D. Damjanovic. Origin of the Large Strain Response in  $(\text{K}_{0.5}\text{Na}_{0.5})\text{NbO}_3$ -Modified  $(\text{Bi}_{0.5}\text{Na}_{0.5})\text{TiO}_3$ - $\text{BaTiO}_3$  Lead-Free Piezoceramics. *Journal of Applied Physics*, 105(9):094102, 2009.



- <sup>173</sup> W. Jo, J. Rödel, J. S Lee, Y. H. Baik, and C. Park. Effect of Substitution of K for Na on the Ferroelectric Stability and Properties of  $(\text{Bi}_{1/2}\text{Na}_{1/2})\text{TiO}_3\text{-BaTiO}_3\text{-(K}_{0.5}\text{Na}_{0.5})\text{NbO}_3$ . *Functional Materials Letters*, 03(01):41–44, 2010.
- <sup>174</sup> C. M. Fancher, W. Jo, J. Rödel, J. E. Blendell, and K. J. Bowman. Effect of Texture on Temperature-Dependent Properties of  $\text{K}_{0.5}\text{Na}_{0.5}\text{NbO}_3$  Modified  $\text{Bi}_{1/2}\text{Na}_{1/2}\text{TiO}_3\text{-}x\text{BaTiO}_3$ . *J. Am. Ceram. Soc.*, 97(8):2557–2563, 2014.
- <sup>175</sup> M. Chandrasekhar and P. Kumar. Synthesis and Characterizations of BNT-BT and BNT-BT-KNN Ceramics for Actuator and Energy Storage Applications. *Ceramics International*, 41(4): 5574 – 5580, 2015.
- <sup>176</sup> E. Sapper, A. Gassmann, L. Gjødvad, W. Jo, T. Granzow, and J. Rödel. Cycling Stability of Lead-Free BNT-8BT and BNT-6BT-3KNN Multilayer Actuators and Bulk Ceramics. *Journal of the European Ceramic Society*, 34(3):653 – 661, 2014.
- <sup>177</sup> J. Glaum, H. Simons, M. Acosta, and M. Hoffman. Tailoring the Piezoelectric and Relaxor Properties of  $(\text{Bi}_{1/2}\text{Na}_{1/2})\text{TiO}_3\text{-BaTiO}_3$  via Zirconium Doping. *J. Am. Ceram. Soc.*, 96(9):2881–2886, 2013.
- <sup>178</sup> J. Shieh, Y. C. Lin, and C. S. Chen. Influence of Phase Composition on Electrostrains of Doped  $(\text{Bi}_{0.5}\text{Na}_{0.5})\text{TiO}_3\text{-BaTiO}_3\text{-(Bi}_{0.5}\text{K}_{0.5})\text{TiO}_3$  Lead-Free Ferroelectric Ceramics. *Smart Materials and Structures*, 19(9):094007, 2010.
- <sup>179</sup> S. T. Zhang, B. Yang, and W. Cao. The Temperature-Dependent Electrical Properties of  $\text{Bi}_{0.5}\text{Na}_{0.5}\text{TiO}_3\text{-BaTiO}_3\text{-Bi}_{0.5}\text{K}_{0.5}\text{TiO}_3$  Near the Morphotropic Phase Boundary. *Acta Materialia*, 60(2):469–475, 2012.
- <sup>180</sup> Y. J. Dai, X. W. Zhang, and K. P. Chen. An Approach to Improve the Piezoelectric Property of  $(\text{Bi}_{0.5}\text{Na}_{0.5})\text{TiO}_3\text{-(Bi}_{0.5}\text{K}_{0.5})\text{TiO}_3\text{-BaTiO}_3$  Lead-Free Ceramics. *International Journal of Applied Ceramic Technology*, 8(2):423–429, 2011.
- <sup>181</sup> Y. Makiuchi, R. Aoyagi, Y. Hiruma, H. Nagata, and T. Takenaka.  $(\text{Bi}_{1/2}\text{Na}_{1/2})\text{TiO}_3\text{-(Bi}_{1/2}\text{K}_{1/2})\text{TiO}_3\text{-BaTiO}_3$ -Based Lead-Free Piezoelectric Ceramics. *Japanese Journal of Applied Physics Part 1-regular Papers Brief Communications & Review Papers*, 44(6B):4350, 2005.
- <sup>182</sup> S. Zhang and H. Hiruma Y. Tadashi T. Shrouf, T.R. Nagata. Piezoelectric Properties in  $(\text{K}_{0.5}\text{Bi}_{0.5})\text{TiO}_3\text{-(Na}_{0.5}\text{Bi}_{0.5})\text{TiO}_3\text{-BaTiO}_3$  Lead-Free Ceramics. *IEEE Transactions on Ultrasonics, Ferroelectrics and Frequency Control*, 54(5), 2007.
- <sup>183</sup> J. U. Rahman, A. Hussain, A. Maqbool, G. H. Ryu, T. K. Song, W.-J. Kim, and M. H. Kim. Field Induced Strain Response of Lead-Free  $\text{BaZrO}_3$ -Modified  $\text{Bi}_{0.5}\text{Na}_{0.5}\text{TiO}_3\text{-BaTiO}_3$  Ceramics. *Journal of Alloys and Compounds*, 593(1):97 – 102, 2014.

- <sup>184</sup> C. Peng, J. F. Li, and W. Gong. Preparation and Properties of  $(\text{Bi}_{1/2}\text{Na}_{1/2})\text{TiO}_3\text{-Ba}(\text{Ti},\text{Zr})\text{O}_3$  Lead-Free Piezoelectric Ceramics. *Materials Letters*, 59(12):1576–1580, 2005.
- <sup>185</sup> F. Wang, M. Xu, Y. Tang, T. Wang, W. Shi, and C. M. Leung. Large Strain Response in the Ternary  $\text{Bi}_{0.5}\text{Na}_{0.5}\text{TiO}_3\text{-BaTiO}_3\text{-SrTiO}_3$  Solid Solutions. *Journal of the American Ceramic Society*, 95(6):1955–1959, 2012.
- <sup>186</sup> D. Lin, K.W. Kwok, and H.L.W. Chan. Structure and Electrical Properties of  $\text{Bi}_{0.5}\text{Na}_{0.5}\text{TiO}_3\text{-BaTiO}_3\text{-Bi}_{0.5}\text{Li}_{0.5}\text{TiO}_3$  Lead-Free Piezoelectric Ceramics. *Solid State Ionics*, 178(37-38):1930–1937, 2008.
- <sup>187</sup> A. Maqbool, A. Hussain, J. U. Rahman, T. K. Song, J. Kim W.-Y. and Lee, and Kim M. H. Enhanced Electric Field-Induced Strain and Ferroelectric Behavior of  $(\text{Bi}_{0.5}\text{Na}_{0.5})\text{TiO}_3\text{-BaTiO}_3\text{-SrZrO}_3$  Lead-Free Ceramics. *Ceramics International*, 40(8, Part A):11905 – 11914, 2014.
- <sup>188</sup> W. Jo, S. Schaab, E. Sapper, L. A. Schmitt, H.-J. Kleebe, A. J. Bell, and J. Rödel. On the Phase Identity and its Thermal Evolution of Lead Free  $(\text{Bi}_{1/2}\text{Na}_{1/2})\text{TiO}_3\text{-6 mol\% BaTiO}_3$ . *Journal of Applied Physics*, 110(7):074106, 2011.
- <sup>189</sup> X. Tan, E. Aulbach, W. Jo, T. Granzow, J. Kling, M. Marsilius, H. J. Kleebe, and J. Rödel. Effect of Uniaxial Stress on Ferroelectric Behavior of  $(\text{Bi}_{1/2}\text{Na}_{1/2})\text{TiO}_3$  Based Lead-Free Piezoelectric Ceramics. *Journal of Applied Physics*, 106(4):044107–7, 2009.
- <sup>190</sup> G. Viola, R. McKinnon, V. Koval, A. Adomkevicius, S. Dunn, and H. Yan. Lithium-Induced Phase Transitions in Lead-Free  $\text{Bi}_{0.5}\text{Na}_{0.5}\text{TiO}_3$ . *Journal of Physical Chemistry C*, 118(16): 8564–8570, 2014.
- <sup>191</sup> S. T. Zhang, A. B. Kouna, E. Aulbach, H. Ehrenberg, and J. Rödel. Giant Strain in Lead-Free Piezoceramics  $\text{Bi}_{0.5}\text{Na}_{0.5}\text{TiO}_3\text{-BaTiO}_3\text{-K}_{0.5}\text{Na}_{0.5}\text{NbO}_3$  System. *Applied Physics Letters*, 91(11):112906, 2007.
- <sup>192</sup> S. T. Zhang, A. B. Kouna, E. Aulbach, W. Jo, T. Granzow, H. Ehrenberg, and J. Rödel. Lead-free Piezoceramics with Giant Strain in the System  $\text{Bi}_{0.5}\text{Na}_{0.5}\text{TiO}_3\text{-BaTiO}_3\text{-K}_{0.5}\text{Na}_{0.5}\text{NbO}_3$ . II. Temperature Dependent Properties. *Journal of Applied Physics*, 103(3):034108, 2008.
- <sup>193</sup> E. V. Colla, E. Y. Koroleva, N. M. Okuneva, and S. B. Vakhruhev. Long-Time Relaxation of the Dielectric Response in Lead Magnoniobate. *Physical Review Letters*, 74(9):1681–1684, 1995.
- <sup>194</sup> J. Kling, W. Jo, R. Dittmer, S. Schaab, and H.-J. Kleebe. Temperature-Dependent Phase Transitions in the Lead-Free Piezoceramics  $(1-x-y)(\text{Bi}_{1/2}\text{Na}_{1/2})\text{TiO}_3\text{-xBaTiO}_3\text{-y}(\text{K}_{0.5}\text{Na}_{0.5})\text{NbO}_3$  Observed by in situ Transmission Electron Microscopy and Dielectric Measurements. *Journal of the American Ceramic Society*, 96(10):3312–3324, 2013.

- <sup>195</sup> M. Hinterstein, M. Knapp, M. Hölzel, W. Jo, A. Cervellino, and H. Ehrenberg. Field Induced Phase Transition in Lead-Free 0.92BNT-0.06BT-0.02KNN. *Journal of Applied Crystallography*, 43(6):1314–1321, 2010.
- <sup>196</sup> T. Tani and T. Kimura. Reactive-Templated Grain Growth Processing for Lead Free Piezoelectric Ceramics. *Advances in applied ceramics*, 105(1):55–63, 2006.
- <sup>197</sup> E. A. Patterson, D. P. Cann, J. Pokorny, and I. M. Reaney. Electromechanical Strain in  $\text{Bi}(\text{Zn}_{1/2}\text{Ti}_{1/2})\text{O}_3$ - $(\text{Bi}_{1/2}\text{Na}_{1/2})\text{TiO}_3$ - $(\text{Bi}_{1/2}\text{K}_{1/2})\text{TiO}_3$  Solid Solutions. *Journal of Applied Physics*, 111(9):094105, 2012.
- <sup>198</sup> R. Dittmer, W. Jo, J. Daniels, S. Schaab, and J. Rödel. Relaxor Characteristics of Morphotropic Phase Boundary  $(\text{Bi}_{1/2}\text{Na}_{1/2})\text{TiO}_3$ - $(\text{Bi}_{1/2}\text{K}_{1/2})\text{TiO}_3$  Modified with  $\text{Bi}(\text{Zn}_{1/2}\text{Ti}_{1/2})\text{O}_3$ . *Journal of the American Ceramic Society*, 94(12):4283–4290, 2011.
- <sup>199</sup> A. Ullah, C. W. Ahn, and I. W. Kim. Dielectric, Piezoelectric Properties and Field-Induced Large Strain of  $\text{Bi}(\text{Zn}_{0.5}\text{Ti}_{0.5})\text{O}_3$ -Modified Morphotropic Phase Boundary  $\text{Bi}_{0.5}(\text{Na}_{0.82}\text{K}_{0.18})_{0.5}\text{TiO}_3$  Piezoelectric Ceramics. *Japanese Journal of Applied Physics*, 51:09MD07, 2012.
- <sup>200</sup> D. S. Lee, D. H. Lim, M. S. Kim, K. H. Kim, and S. J. Jeong. Electric Field-Induced Deformation Behavior in Mixed  $\text{Bi}_{0.5}\text{Na}_{0.5}\text{TiO}_3$  and  $\text{Bi}_{0.5}(\text{Na}_{0.75}\text{K}_{0.25})_{0.5}\text{TiO}_3$ - $\text{BiAlO}_3$ . *Applied Physics Letters*, 99(6):062906, 2011.
- <sup>201</sup> A. Ullah, C. Q. Ahn, A. Hussain, S. Y. Lee, and I. W. Kim. Phase Transition, Electrical Properties, and Temperature-Insensitive Large Strain in  $\text{BiAlO}_3$ -Modified  $\text{Bi}_{0.5}(\text{Na}_{0.75}\text{K}_{0.25})_{0.5}\text{TiO}_3$  Lead-Free Piezoelectric Ceramics. *Journal of the American Ceramic Society*, 94(11):3915–3921, 2011.
- <sup>202</sup> A. Ullah, C. W. Ahn, A. Hussain, S. Y. Lee, H. J. Lee, and I. W. Kim. Phase Transitions and Large Electric Field-Induced Strain in  $\text{BiAlO}_3$ -Modified  $\text{Bi}_{0.5}(\text{Na},\text{K})_{0.5}\text{TiO}_3$  Lead-Free Piezoelectric Ceramics. *Current Applied Physics*, 10(4):1174–1181, 2010.
- <sup>203</sup> E. M. Anton, W. Jo, J. Trodahl, D. Damjanovic, and J. Rödel. Effect of  $\text{K}_{0.5}\text{Na}_{0.5}\text{NbO}_3$  on Properties at and off the Morphotropic Phase Boundary in  $\text{Bi}_{0.5}\text{Na}_{0.5}\text{TiO}_3$ - $\text{Bi}_{0.5}\text{K}_{0.5}\text{TiO}_3$  Ceramics. *Japanese Journal of Applied Physics*, 50(5), 2011.
- <sup>204</sup> K. T. P. Seifert, W. Jo, and J. Rödel. Temperature-Insensitive Large Strain of  $(\text{Bi}_{1/2}\text{Na}_{1/2})\text{TiO}_3$ - $(\text{Bi}_{1/2}\text{K}_{1/2})\text{TiO}_3$ - $(\text{K}_{0.5}\text{Na}_{0.5})\text{NbO}_3$  Lead-Free Piezoceramics. *Journal of the American Ceramic Society*, 93(5):1392–1396, 2010.
- <sup>205</sup> J. Hao, B. Shen, J. Zhai, C. Liu, X. Li, and X. Gao. Switching of Morphotropic Phase Boundary and Large Strain Response in Lead-Free Ternary  $(\text{Bi}_{0.5}\text{Na}_{0.5})\text{TiO}_3$ - $(\text{K}_{0.5}\text{Bi}_{0.5})\text{TiO}_3$ - $(\text{K}_{0.5}\text{Na}_{0.5})\text{NbO}_3$  system. *Journal of Applied Physics*, 113(11), 2013.

- <sup>206</sup> A. Ullah, C. W. Ahn, S. Y. Lee, J. S. Kim, and I. W. Kim. Structure, Ferroelectric Properties, and Electric Field-Induced Large Strain in Lead-Free  $\text{Bi}_{0.5}(\text{Na},\text{K})_{0.5}\text{TiO}_3$ - $(\text{Bi}_{0.5}\text{La}_{0.5})\text{AlO}_3$  Piezoelectric Ceramics. *Ceramics International*, 38, Supplement 1(0):S363–S368, 2012.
- <sup>207</sup> N. Kumar, T. Y. Ansell, and D. P. Cann. Role of Point Defects in Bipolar Fatigue Behavior of  $\text{Bi}(\text{Mg}_{1/2}\text{Ti}_{1/2})\text{O}_3$  Modified  $(\text{Bi}_{1/2}\text{K}_{1/2})\text{TiO}_3$ - $(\text{Bi}_{1/2}\text{Na}_{1/2})\text{TiO}_3$  Relaxor Ceramics. *Journal of Applied Physics*, 115(15):–, 2014.
- <sup>208</sup> K. Wang, A. Hussain, W. Jo, and J. Rödel. Temperature-Dependent Properties of  $(\text{Bi}_{1/2}\text{Na}_{1/2})\text{TiO}_3$ - $(\text{Bi}_{1/2}\text{K}_{1/2})\text{TiO}_3$ - $\text{SrTiO}_3$  Lead-Free Piezoceramics. *Journal of the American Ceramic Society*, 95(7):2241–2247, 2012.
- <sup>209</sup> A. Hussain, J. U. Rahman, A. Zaman, R. A. Malik, J. S. Kim, T. K. Song, W. J. Kim, and M. H. Kim. Field-Induced Strain and Polarization Response in Lead-Free  $\text{Bi}_{1/2}(\text{Na}_{0.80}\text{K}_{0.20})_{1/2}\text{TiO}_3$ - $\text{SrZrO}_3$  Ceramics. *Materials Chemistry and Physics*, 143(3):1282 – 1288, 2014.
- <sup>210</sup> Y. Lu, Y. Li, D. Wang, T. Wang, and Q. Yin. Lead-Free Piezoelectric Ceramics of  $(\text{Bi}_{1/2}\text{Na}_{1/2})\text{TiO}_3$ - $(\text{Bi}_{1/2}\text{K}_{1/2})\text{TiO}_3$ - $(\text{Bi}_{1/2}\text{Ag}_{1/2})\text{TiO}_3$  System. *Journal of Electroceramics*, 21(1-4):309–313, 2008.
- <sup>211</sup> V. D. N. Tran, T. H. Dinh, H. S. Han, W. Jo, and J. S. Lee. Lead-Free  $\text{Bi}_{1/2}(\text{Na}_{0.82}\text{K}_{0.18})_{1/2}\text{TiO}_3$  Relaxor Ferroelectrics with Temperature Insensitive Electrostrictive Coefficient. *Ceramics International*, 39(1):S119–S124, 2013.
- <sup>212</sup> R. Dittmer, W. Jo, E. Aulbach, T. Granzow, and J. Rödel. Frequency Dependence of Large-Signal Properties in Lead-Free Piezoceramics. *Journal of Applied Physics*, 112(1):014101, 2012.
- <sup>213</sup> D. S. Lee, Jeong S.J., M. S. Kim, and K. H. Kim. Effect of Sintering Time on Strain in Ceramic Composite Consisting of  $0.94\text{Bi}_{0.5}(\text{Na}_{0.75}\text{K}_{0.25})_{0.5}\text{TiO}_3$ - $0.06\text{BiAlO}_3$  with  $(\text{Bi}_{0.5}\text{Na}_{0.5})\text{TiO}_3$ . *Japanese Journal of Applied Physics*, 52(2R):021801, 2013.
- <sup>214</sup> V.V. Shvartsman and A.L. Kholkin. Nanoscale Investigation of Polycrystalline Ferroelectric Materials via Piezoresponse Force Microscopy. In *Multifunctional Polycrystalline Ferroelectric Materials*, volume 140, pages 409–468. Springer Netherlands, 2011.
- <sup>215</sup> P. Ebert. *Probing the Nanoworld, Microscopies, Scattering and Spectroscopies of the Solid State*, chapter Scanning Probe Microscopy Overview. Institute of solid state research, 2007.
- <sup>216</sup> K. Szot. *Probing the Nanoworld, Microscopies, Scattering and Spectroscopies of the Solid State*, chapter Piezoresponse Force Microscopy. Institute of Solid State Research, Jülich, 2007.
- <sup>217</sup> B. J. Rodriguez, S. Jesse, K. Seal, N. Balke, S.V. Kalinin, and R. Proksch. *Scanning Probe Microscopy of Functional Materials*, chapter Dynamic and Spectroscopic Modes and Multivariate Data Analysis in Piezoresponse Force Microscopy, pages 491–528. Springer, 2010.

- <sup>218</sup> A.L. Kholkin, S.V. Kalinin, A. Roelofs, and A. Gruverman. Review of Ferroelectric Domain Imaging by Piezoresponse Force Microscopy. In S. Kalinin and A. Gruverman, editors, *Scanning Probe Microscopy*, pages 173–214. Springer New York, 2007. ISBN 978-0-387-28667-9.
- <sup>219</sup> S. V. Kalinin, B. J. Rodriguez, S. Jesse, E. Karapetian, B. Mirman, E. A. Eliseev, and A. N. Morozovska. Nanoscale Electromechanics of Ferroelectric and Biological Systems: A New Dimension in Scanning Probe Microscopy. *Annu. Rev. Mater. Res.*, 37(1):189–238, 2007.
- <sup>220</sup> S. V. Kalinin, S. Jesse, B. J. Rodriguez, J. Shin, A. P. Baddorf, H. N. Lee, A. Borisevich, and S. J. Pennycook. Spatial Resolution, Information Limit, and Contrast Transfer in Piezoresponse Force Microscopy. *Nanotechnology*, 17(14):3400, 2006.
- <sup>221</sup> S. Jesse, P. Maksymovych, and S. V. Kalinin. Rapid Multidimensional Data Acquisition in Scanning Probe Microscopy Applied to Local Polarization Dynamics and Voltage Dependent Contact Mechanics. *Applied Physics Letters*, 93(11), 2008.
- <sup>222</sup> S. V. Kalinin and D. A. Bonnell. Imaging Mechanism of Piezoresponse Force Microscopy of Ferroelectric Surfaces. *Physical Review B*, 65(12):125408, 2002.
- <sup>223</sup> S. V. Kalinin, B. J. Rodriguez, S. Jesse, J. Shin, A. P. Baddorf, P. Gupta, H. Jain, D. B. Williams, and A. Gruverman. Vector Piezoresponse Force Microscopy. *Microscopy and Microanalysis*, 12(3):206–220, 2006.
- <sup>224</sup> S. Hong, J. Woo, H. Shin, J. U. Jeon, Y. E. Pak, E. L. Colla, N. Setter, E. Kim, and K. No. Principle of Ferroelectric Domain Imaging Using Atomic Force Microscope. *Journal of Applied Physics*, 89(2):1377–1386, 2001.
- <sup>225</sup> E. Soergel. Piezoresponse Force Microscopy (PFM). *Journal of Physics D: Applied Physics*, 44(46):464003, 2011.
- <sup>226</sup> F. Peter, A. Rüdiger, R. Waser, K. Szot, and B. Reichenberg. Comparison of In-Plane and Out-Of-Plane Optical Amplification in AFM Measurements. *Review of Scientific Instruments*, 76(4):046101, 2005.
- <sup>227</sup> S. Jesse, A. P. Baddorf, and S. V. Kalinin. Dynamic Behaviour in Piezoresponse Force Microscopy. *Nanotechnology*, 17(6):1615, 2006.
- <sup>228</sup> H. Y. Guo, J. B. Xu, I. H. Wilson, Z. Xie, E. Z. Luo, S. B. Hong, and H. Yan. Study Of Domain Stability on  $(\text{Pb}_{0.76}\text{Ca}_{0.24})\text{TiO}_3$  Thin Films Using Piezoresponse Microscopy. *Applied Physics Letters*, 81(4):715–717, 2002.
- <sup>229</sup> S.V. Kalinin, B. J.J. Rodriguez, S. Jesse, P. Maksymovych, K. Seal, M. Nikiforov, A. Baddorf, A. L. Kholkin, and R. Proksch. Local Bias-Induced Phase Transitions. *Materials Today*, 11(11):16 – 27, 2008.

- <sup>230</sup> C. Harnagea, A. Pignolet, M. Alexe, D. Hesse, and U. Gösele. Quantitative Ferroelectric Characterization of Single Submicron Grains in Bi-Layered Perovskite Thin Films. *Applied Physics A-materials Science & Processing*, 70(3):261–267, 2000.
- <sup>231</sup> D. Ricinschi, L. Mitoseriu, A. Stancu, P. Postolache, and M. Okuyama. Analysis of the Switching Characteristics of PZT Films by First Order Reversal Curve Diagrams. *Integrated Ferroelectrics*, 67:103–115, 2004.
- <sup>232</sup> D. Ricinschi, M. Noda, M. Okuyama, Y. Ishibashi, M. Iwata, and L. Mitoseriu. A Landau-Theory-Based Computational Study of In-Plane and Out-Of Plane Polarization Components Role in Switching of Ferroelectric Thin Films. *Journal of the Korean Physical Society*, 42: S1232–S1236, 2003.
- <sup>233</sup> D. Ricinschi and M. Okuyama. Nanoscale Spatial Correlation of Piezoelectric Displacement Hysteresis Loops of PZT Films in the Fresh and Fatigued States. *Integrated Ferroelectrics*, 50(1):149–158, 2002.
- <sup>234</sup> T. Jungk. *Untersuchung der Abbildungsmechanismen Ferroelektrischer Domänen mit dem Rasterkraftmikroskop*. PhD thesis, Mathematisch-Naturwissenschaftliche Fakultät Rheinische Friedrich-Wilhelms-Universität Bonn, 2006.
- <sup>235</sup> A. Mandelis. Signal-to-Noise Ratio in Lock-In Amplifier Synchronous Detection: A Generalized Communications Systems Approach with Applications to Frequency, Time, and Hybrid (Rate Window) Photothermal Measurements. *Review of Scientific Instruments*, 65(11):3309–3323, 1994.
- <sup>236</sup> T. Jungk, A. Hoffmann, and E. Soergel. Impact of the Tip Radius on the Lateral Resolution in Piezoresponse Force Microscopy. *New Journal of Physics*, 10(1):013019, 2008.
- <sup>237</sup> B. Meyer and D. Vanderbilt. *Ab Initio* Study of Ferroelectric Domain Walls in  $\text{PbTiO}_3$ . *Physical Review B*, 65(10):104111, 2002.
- <sup>238</sup> B. J. Rodriguez, S. Jesse, A. P. Baddorf, and S. V. Kalinin. High Resolution Electromechanical Imaging of Ferroelectric Materials in a Liquid Environment by Piezoresponse Force Microscopy. *Phys. Rev. Lett.*, 96:237602, 2006.
- <sup>239</sup> S. Jesse, R. K. Vasudevan, L. Collins, E. Strelcov, M. B. Okatan, A. Belianinov, A. P. Baddorf, R. Proksch, and S. V. Kalinin. Band Excitation in Scanning Probe Microscopy: Recognition and Functional Imaging. *Annual review of physical chemistry*, 65(1):519–536, 2014.
- <sup>240</sup> F. Griggio, S. Jesse, A. Kumar, D. M. Marincel, D. S. Tinberg, S. V. Kalinin, and S. Trolier-McKinstry. Mapping Piezoelectric Nonlinearity in the Rayleigh Regime Using Band Excitation Piezoresponse Force Microscopy. *Applied Physics Letters*, 98(21):212901, 2011.

- <sup>241</sup> R. Garcia and R. Perez. Dynamic Atomic Force Microscopy Methods. *Surface Science Reports*, 47(6-8):197–301, 2002.
- <sup>242</sup> Y. Dai, X. Zhang, and G. Zhou. Phase Transitional Behavior in  $K_{0.5}Na_{0.5}NbO_3$ -LiTaO<sub>3</sub> Ceramics. *Applied Physics Letters*, 90(26), 2007.
- <sup>243</sup> E. Hollenstein, M. Davis, D. Damjanovic, and N. Setter. Piezoelectric Properties of Li- and Ta-Modified  $(K_{0.5}Na_{0.5})NbO_3$  Ceramics. *Applied Physical Letters*, 87(18):1835–1842, 2005.
- <sup>244</sup> K. Wang and J.-F. Li. Domain Engineering of Lead-Free Li-Modified  $(K,Na)NbO_3$  Polycrystals with Highly Enhanced Piezoelectricity. *Advanced Functional Materials*, 20(12):1924–1929, 2010.
- <sup>245</sup> J. Fu, R. Z. Zuo, and Z. K. Xu. High Piezoelectric Activity in  $(Na,K)NbO_3$  Based Lead-Free Piezoelectric Ceramics: Contribution of Nanodomains. *Applied Physics Letters*, 99(6):062901, 2011.
- <sup>246</sup> K. Wang and J.-F. Li. Analysis of Crystallographic Evolution in  $(Na, K)NbO_3$ -Based Lead-Free Piezoceramics by X-Ray Diffraction. *Applied Physics Letters*, 91(26), 2007.
- <sup>247</sup> S. J. Zhang, R. Xia, T. R. Shroud, G. Z. Zang, and J. F. Wang. Piezoelectric Properties in Perovskite  $0.948(K_{0.5}Na_{0.5})NbO_3$ - $0.052LiSbO_3$  Lead-Free Ceramics. *Journal Of Applied Physics*, 100(10), 2006.
- <sup>248</sup> T. A. Skidmore, T. P. Comyn, and S. J. Milne. Temperature Stability of  $([Na_{0.5}K_{0.5}NbO_3]_{0.93}$ - $[LiTaO_3]_{0.07})$  Lead-Free Piezoelectric Ceramics. *Applied Physics Letters*, 94(22):222902, 2009.
- <sup>249</sup> K. Wang, J. F. Li, and N. Liu. Piezoelectric Properties of Low-Temperature Sintered Li-Modified  $(Na, K)NbO_3$  Lead-Free Ceramics. *Applied Physics Letters*, 93(9):3, 2008.
- <sup>250</sup> D. W. Baker, P. A. Thomas, N. Zhang, and A. M. Glazer. A Comprehensive Study of the Phase Diagram of  $K_xNa_{1-x}NbO_3$ . *Applied Physics Letters*, 95(9):091903, 2009.
- <sup>251</sup> N. Klein, E. Hollenstein, D. Damjanovic, H. J. Trodahl, N. Setter, and M. Kuball. A Study of the Phase Diagram of  $(K,Na,Li)NbO_3$  Determined by Dielectric and Piezoelectric Measurements, and Raman Spectroscopy. *Journal of Applied Physics*, 102(1):014112, 2007.
- <sup>252</sup> W. Ge, Y. Ren, J. Zhang, C. P. Devreugd, J. Li, and D. Viehland. A Monoclinic-Tetragonal Ferroelectric Phase Transition in Lead-Free  $(K_{0.5}Na_{0.5})NbO_3$ -x *Journal of Applied Physics*, 111(10):103503, May 2012.
- <sup>253</sup> J. G. Wu, D. Q. Xiao, Y. Y. Wang, W. J. Wu, B. Zhang, and J. G. Zhu. Improved Temperature Stability of CaTiO<sub>3</sub>-modified  $[(K_{0.5}Na_{0.5})(0.96)Li_{0.04}](Nb_{0.91}Sb_{0.05}Ta_{0.04})O_3$  Lead-Free Piezoelectric Ceramics. *Journal of Applied Physics*, 104(2):024102, 2008.

- <sup>254</sup> K. Wang, F. Z. Yao, W. Jo, D. Gobeljic, V. V. Shvartsman, D. C. Lupascu, J. F. Li, and J. Rödel. Temperature-Insensitive (K,Na)NbO<sub>3</sub>-Based Lead-Free Piezoactuator Ceramics. *Advanced Functional Materials*, 23(33):4079–4086, 2013.
- <sup>255</sup> J. S. Kim, I. R. Hwang, S. H. Hong, J. H. Lee, B. H. Park, A. C. Woo, and N. Sahn. Piezoelectric Properties of Highly Oriented Lead-Free Na<sub>0.5</sub>K<sub>0.5</sub>NbO<sub>3</sub> Films as Determined Using Piezoelectric Force Microscopy. *Journal of the Korean Physical Society*, 48(6):1583–1587, 2006.
- <sup>256</sup> R. P. Herber, G. A. Schneider, S. Wagner, and M. J. Hoffmann. Characterization of Ferroelectric Domains in Morphotropic Potassium Sodium Niobate with Scanning Probe Microscopy. *Applied Physics Letters*, 90(25):252905, 2007.
- <sup>257</sup> R. Rai, I. Coondoo, R. Rani, I. Bdikin, S. Sharma, and A. L. Kholkin. Impedance Spectroscopy and Piezoresponse Force Microscopy Analysis of Lead-Free (1-x) K<sub>0.5</sub>Na<sub>0.5</sub>NbO<sub>3</sub> - xLiNbO<sub>3</sub> Ceramics. *Current Applied Physics*, 13(2):430–440, 2013.
- <sup>258</sup> I. Coondoo, N. Panwar, R. Rai, H. Amorin, and A. L. Kholkin. Synthesis and Physical Properties of Ca- and Ta-Modified (K,Na)NbO<sub>3</sub> Lead-Free Piezoelectric Ceramics. *Phase Transitions*, 86(11):1130–1140, 2013.
- <sup>259</sup> R. Rai, R. Rani, S. Sharma, and A. L. Kholkin. Influence of Li and La Content on Phase Structures and Electrical Properties of K<sub>0.5</sub>Na<sub>0.5</sub>NbO<sub>3</sub> Lead-Free Piezoelectric Ceramics. *Journal of Alloys and Compounds*, 577:575–580, 2013.
- <sup>260</sup> D. Gobeljic, V. V. Shvartsman, K. Wang, F. Z. Yao, J. F. Li, W. Jo, J. Rödel, and D. C. Lupascu. Temperature Dependence of the Local Piezoresponse in (K,Na)NbO<sub>3</sub>-Based Ceramics with Large Electromechanical Strain. *Journal of Applied Physics*, 116(6):066811, 2014.
- <sup>261</sup> I. Horcas, R. Fernandez, J. M. Gomez-Rodriguez, J. Colchero, J. Gomez-Herrero, and A. M. Baro. WSXM: A Software for Scanning Probe Microscopy and a Tool for Nanotechnology. *Review of Scientific Instruments*, 78(1):013705, 2007.
- <sup>262</sup> S. E. Park and T. R. ShROUT. Ultrahigh Strain and Piezoelectric Behavior in Relaxor Based Ferroelectric Single Crystals. *Journal of Applied Physics*, 82(4):1804–1811, 1997.
- <sup>263</sup> D. Wang, Y. Fotinich, and G. P. Carman. Influence of Temperature on the Electromechanical and Fatigue Behavior of Piezoelectric Ceramics. *Journal of Applied Physics*, 83(10):5342–5350, 1998.
- <sup>264</sup> E. Sapper, S. Schaab, W. Jo, T. Granzow, and J. Rödel. Influence of Electric Fields on the Depolarization Temperature of Mn-Doped BNT-xBT. *Journal of Applied Physics*, 111(1):014105, 2012.



- <sup>265</sup> K. Kuwata, J. Uchino and S. Nomura. Electrostrictive Coefficients of  $\text{Pb}(\text{Mg}_{1/3}\text{Nb}_{2/3})\text{O}_3$  Ceramics. *Japanese Journal of Applied Physics*, 19(11):2099–2103, 1980.
- <sup>266</sup> K. Uchino, S. Nomura, L. Cross, R. Newnham, and S. Jang. Electrostrictive Effect in Perovskites and its Transducer Applications. *Journal of Materials Science*, 16(3):569–578, 1981.
- <sup>267</sup> S. J. Zhang, H. J. Lee, C. Ma, and X. L. Tan. Sintering Effect on Microstructure and Properties of  $(\text{K},\text{Na})\text{NbO}_3$  Ceramics. *Journal of the American Ceramic Society*, 94(11):3659–3665, 2011.
- <sup>268</sup> J. J. Yao, J. F. Li, D. Viehland, Y. F. Chang, and G. L. Messing. Aging Associated Domain Evolution in the Orthorhombic Phase of  $\langle 001 \rangle$  Textured  $(\text{K}_{0.5}\text{Na}_{0.5})\text{Nb}_{0.97}\text{Sb}_{0.03}\text{O}_3$  Ceramics. *Applied Physics Letters*, 100(13):132902, 2012.
- <sup>269</sup> K. A. Schönau, L. A. Schmitt, M. Knapp, H. Fuess, R. A. Eichel, H. Kungl, and M. J. Hoffmann. Nanodomain Structure of  $\text{Pb}[\text{Zr}_{1-x}\text{Ti}_x]\text{O}_3$  at its Morphotropic Phase Boundary: Investigations From Local to Average Structure. *Physical Review B*, 75(18):184117, 2007.
- <sup>270</sup> R. Theissmann, L. A. Schmitt, J. Kling, R. Schierholz, K. A. Schonau, H. Fuess, M. Knapp, H. Kungl, and M. J. Hoffmann. Nanodomains in Morphotropic Lead Zirconate Titanate Ceramics: On the Origin of the Strong Piezoelectric Effect. *Journal of Applied Physics*, 102(2):024111, 2007.
- <sup>271</sup> T. Sluka, A. K. Tagantsev, D. Damjanovic, M. Gureev, and N. Setter. Enhanced Electromechanical Response of Ferroelectrics due to Charged Domain Walls. *Nature Communications*, 3:748, 2012.
- <sup>272</sup> F. M. Bai, J. F. Li, and D. Viehland. Domain Engineered States Over Various Length Scales in  $(001)$ -Oriented  $\text{Pb}(\text{Mg}_{1/3}\text{Nb}_{2/3})\text{O}_3$ -xCrystals: Electrical History Dependence of Hierarchical Domains. *Journal of Applied Physics*, 97(5):054103, 2005.
- <sup>273</sup> G. A. Rossetti, A. G. Khachaturyan, G. Akcay, and Y. Ni. Ferroelectric Solid Solutions with Morphotropic Boundaries: Vanishing Polarization Anisotropy, Adaptive, Polar Glass, and Two-Phase States. *Journal of Applied Physics*, 103(11):114113, 2008.
- <sup>274</sup> S. Jesse, A. P. Baddorf, and S. V. Kalinin. Switching Spectroscopy Piezoresponse Force Microscopy of Ferroelectric Materials. *Applied Physics Letters*, 88(6):062908, 2006.
- <sup>275</sup> L. Wu, D. Q. Xiao, D. M. Lin, J. G. Zhu, and P. Yu. Synthesis and Properties of  $[\text{Bi}_{0.5}(\text{Na}_{1-x}\text{Ag}_x)_{0.5}]_{1-y}\text{Ba}_y\text{TiO}_3$  Piezoelectric Ceramics. *Japanese Journal Of Applied Physics*, 44(12):8515–8518, 2005.
- <sup>276</sup> J. Y. Li, R. C. Rogan, E. Ustundag, and K. Bhattacharya. Domain Switching in Polycrystalline Ferroelectric Ceramics. *Nature Materials*, 4(10):776–781, 2005.

- <sup>277</sup> J. Lee and R. Ramesh. Imprint of  $(\text{Pb,L a})(\text{Zr,T i})\text{O}_3$  Thin Films With Various Crystalline Dualities. *Applied Physics Letters*, 68(4):484–486, 1996.
- <sup>278</sup> J. F. Scott, C. A. Araujo, B. M. Melnick, L. D. Mcmillan, and R. Zuleeg. Quantitative Measurement of Space-charge Effects In Lead Zirconate-titanate Memories. *Journal of Applied Physics*, 70(1):382–388, 1991.
- <sup>279</sup> M. Alexe, C. Harnagea, D. Hesse, and U. Gosele. Polarization Imprint and Size Effects in Mesoscopic Ferroelectric Structures. *Applied Physics Letters*, 79(2):242–244, 2001.
- <sup>280</sup> A. Deyneka, G. Suchanek, L. Jastrabik, and G. Gerlach. Phase Transitions in  $\text{PbZr}_{1-x}\text{Ti}_x\text{O}_3$  Ceramics Prepared by Different Techniques. *Japanese Journal of Applied Physics Part 1-regular Papers Short Notes & Review Papers*, 41(11B):6966–6968, 2002.
- <sup>281</sup> X. Y. Liu, Y. M. Liu, S. Takekawa, K. Kitamura, F. S. Ohuchi, and J. Y. Li. Nanopolar Structures and Local Ferroelectricity of  $\text{Sr}_{0.61}\text{Ba}_{0.39}\text{Nb}_2\text{O}_6$  Relaxor Crystal Across Curie Temperature by Piezoresponse Force Microscopy. *Journal of Applied Physics*, 106(12):124106, 2009.
- <sup>282</sup> W. Jo, R. Dittmer, M. Acosta, J. Zang, C. Groh, E. Sapper, K. Wang, and J. Rödel. Giant Electric-Field-Induced Strains in Lead-Free Ceramics for Actuator Applications - Status and Perspective. *Journal of Electroceramics*, 29(1):71–93, 2012.
- <sup>283</sup> A. J. Royles, A. J. Bell, A. P. Jephcoat, A. K. Kleppe, S. J. Milne, and T. P. Comyn. Electric-Field-Induced Phase Switching in the Lead Free Piezoelectric Potassium Sodium Bismuth Titanate. *Applied Physics Letters*, 97(13):132909, 2010.
- <sup>284</sup> W. Kleemann, J. Dec, V. V. Shvartsman, Z. Kutnjak, and T. Braun. Two-Dimensional Ising Model Criticality in a Three-Dimensional Uniaxial Relaxor Ferroelectric with Frozen Polar Nanoregions. *Physical Review Letters*, 97(6), 2006.
- <sup>285</sup> L. Boltzmann. On Some Questions in the Kinetic Theory of Gases. *Akademie der Wissenschaften, Wien Ber.*, 96:891–918, 1887.
- <sup>286</sup> K. Binder and A. P. Young. Spin-Glasses - Experimental Facts, Theoretical Concepts, and Open Questions. *Reviews of Modern Physics*, 58(4):801–976, 1986.
- <sup>287</sup> R. Dittmer, D. Gobeljic, W. Jo, V.V. Shvartsman, D. C. Lupascu, J. L. Jones, and J. Rödel. Ergodicity Reflected in Macroscopic and Microscopic Field-Dependent Behavior of BNT-Based Relaxors. *Journal of Applied Physics*, 115, 2014.
- <sup>288</sup> D. Gobeljic, R. Dittmer, J. Rödel, V. V. Shvartsman, and D. C. Lupascu. Macroscopic and Nanoscopic Polarization Relaxation Kinetics in Lead-Free Relaxors  $\text{Bi}_{1/2}\text{Na}_{1/2}\text{TiO}_3$ - $\text{Bi}_{1/2}\text{K}_{1/2}\text{TiO}_3$ - $\text{BiZn}_{1/2}\text{Ti}_{1/2}\text{O}_3$ . *Journal of the American Ceramic Society*, 97(12):3904–3912, 2014.

- <sup>289</sup> S. Schaab. *Influence of Charged Defects on the Polarization Dynamics and Phase Transitions in the Relaxor Ferroelectric PLZT*. PhD thesis, 2011.
- <sup>290</sup> E.-M. Anton, L. A. Schmitt, M. Hinterstein, J. Trodahl, B. Kowalski, W. Jo, H. Kleebe, J. Rödel, and J. Jones. Structure and Temperature-Dependent Phase Transitions of Lead-Free  $\text{Bi}_{1/2}\text{Na}_{1/2}\text{TiO}_3$ - $\text{Bi}_{1/2}\text{K}_{1/2}\text{TiO}_3$ - $\text{K}_{0.5}\text{Na}_{0.5}\text{NbO}_3$  Piezoceramics. *Journal of Materials Research*, 27(19):2466–2478, 2012.
- <sup>291</sup> D. Wang, X. Ke, Y. Wang, J. Gao, Y. Wang, L. Zhang, S. Yang, and X. Ren. Phase Diagram of Polar States in Doped Ferroelectric Systems. *Physical Review B*, 86(5):054120, 2012.
- <sup>292</sup> S. V. Kalinin, B. J. Rodriguez, S. Jesse, A. N. Morozovska, A. A. Bokov, and Z. G. Ye. Spatial Distribution of Relaxation Behavior on the Surface of a Ferroelectric Relaxor in the Ergodic Phase. *Applied Physics Letters*, 95:142902, 2009.
- <sup>293</sup> V. V. Shvartsman and A. L. Kholkin. Polar Structures of  $\text{PbMg}_{1/3}\text{Nb}_{2/3}\text{O}_3$ - $\text{PbTiO}_3$  Relaxors: Piezoresponse Force Microscopy Approach. *Journal of Advanced Dielectrics*, 02(02):1241003, 2012.
- <sup>294</sup> P. Lehnen, J. Dec, W. Kleemann, TH. Woike, and R. Pankrath. Relaxor Properties of SBN:Ce. *Ferroelectrics*, 240(1):1547–1554, 2000.
- <sup>295</sup> P. Bonneau, P. Garnier, G. Calvarin, E. Husson, J.R. Gavarri, A.W. Hewat, and A. Morell. X-Ray and Neutron Diffraction Studies of the Diffuse Phase Transition in  $\text{PbMg}_{1/3}\text{Nb}_{2/3}\text{O}_3$  Ceramics. *Journal of Solid State Chemistry*, 91(2):350 – 361, 1991.
- <sup>296</sup> A. H. Meitzler and H. M. O'Bryan. Polymorphism and Pseudoferroelectricity in PLZT Ceramics. *Proceedings of the IEEE*, 61(7):959–966, 1973.
- <sup>297</sup> G. O. Jones, J. Kreisel, and P. A. Thomas. A Structural Study of the  $(\text{Na}_{1-x}\text{K}_x)_{0.5}\text{Bi}_{0.5}\text{TiO}_3$  Perovskite Series as a Function of Substitution ( $x$ ) and Temperature. *Powder Diffraction*, 17(4):301–319, 2002.
- <sup>298</sup> E. Aksel, J. S. Forrester, J. L. Jones, P. A. Thomas, K. Page, and M. R. Suchomel. Monoclinic Crystal Structure of Polycrystalline  $\text{Na}_{0.5}\text{Bi}_{0.5}\text{TiO}_3$ . *Applied Physics Letters*, 98(15):152901, 2011.
- <sup>299</sup> V. V. Shvartsman and A. L. Kholkin. Evolution of Nanodomains in  $0.9\text{PbMg}_{1/3}\text{Nb}_{2/3}\text{O}_3$ - $0.1\text{PbTiO}_3$  Single Crystals. *Journal of Applied Physics*, 101(6):064108, 2007.
- <sup>300</sup> V. V. Shvartsman, A. L. Kholkin, M. Tyunina, and J. Levoska. Relaxation of Induced Polar State in Relaxor  $\text{PbMg}_{1/3}\text{Nb}_{1/3}\text{O}_3$  Thin Films Studied by Piezoresponse Force Microscopy. *Applied Physics Letters*, 86(22):222907, 2005.

- <sup>301</sup> D. I. Woodward, R. Dittmer, W. Jo, D. Walker, D. S. Keeble, M. W. Dale, J. Rödel, and P. A. Thomas. Investigation of the Depolarisation Transition in Bi-Based Relaxor Ferroelectrics. *Journal of Applied Physics*, 115(11):114109, 2014.
- <sup>302</sup> A. Kholkin, I. Bdikin, D. Kiselev, V. Shvartsman, and S. H. Kim. Nanoscale Characterization of Polycrystalline Ferroelectric Materials for Piezoelectric Applications. *Journal of Electroceramics*, 19(1):83–96, 2007.
- <sup>303</sup> D. C. Lupascu, S. Fedosov, C. Verdier, J. Rödel, and H. von Seggern. Stretched Exponential Relaxation in Perovskite Ferroelectrics after Cyclic Loading. *Journal of Applied Physics*, 95(3):1386–1390, 2004.
- <sup>304</sup> W. Jo, J. Daniels, D. Damjanovic, W. Kleemann, and J. Rödel. Two-Stage Processes of Electrically Induced-Ferroelectric to Relaxor Transition in  $0.94(\text{Bi}_{1/2}\text{Na}_{1/2})\text{TiO}_3$ - $0.06\text{BaTiO}_3$ . *Applied Physics Letters*, 102(19):192903, 2013.
- <sup>305</sup> C. C. Huang and D. P. Cann. Phase Transitions and Dielectric Properties in  $\text{Bi}(\text{Zn}_{1/2}\text{Ti}_{1/2})\text{O}_3$ - $\text{BaTiO}_3$  Perovskite Solid Solutions. *Journal of Applied Physics*, 104(2):024117, 2008.
- <sup>306</sup> B. Xiong, H. Hao, S. Zhang, H. Liu, and M. Cao. Structure, Dielectric Properties and Temperature Stability of  $\text{BaTiO}_3$ - $\text{Bi}(\text{Mg}_{1/2}\text{Ti}_{1/2})\text{O}_3$  Perovskite Solid Solutions. *Journal of the American Ceramic Society*, 94(10):3412–3417, 2011.
- <sup>307</sup> N. Raengthon, T. Sebastian, D. Cumming, Reaney. I. M., and D. P. Cann.  $\text{BaTiO}_3$ - $\text{Bi}(\text{Zn}_{1/2}\text{Ti}_{1/2})\text{O}_3$ - $\text{BiScO}_3$  Ceramics for High-Temperature Capacitor Applications. *Journal of the American Ceramic Society*, 95(11):3554–3561, 2012.
- <sup>308</sup> G. Arlt. Domain Contributions to Piezoelectricity in Ceramics. In *Ultrasonics Symposium, 1990. Proceedings., IEEE 1990*, pages 733–742 vol.2, 1990.
- <sup>309</sup> A. V. Turik. Elastic, Piezoelectric, and Dielectric Properties of Single Crystals of  $\text{BaTiO}_3$  with a Laminar Domain Structure. *Soviet Physics Solid State*, 12(3):688, 1970.
- <sup>310</sup> D. Lupascu and J. Rödel. Fatigue in Bulk Lead Zirconate Titanate Actuator Materials. *Advanced Engineering Materials*, 7(10):882–898, 2005.
- <sup>311</sup> S.-Y. Choi, S.-J. Jeong, D.-S. Lee, M.-S. Kim, J.-S. Lee, J. H. Cho, B. I. Kim, and Y. Ikuhara. Gigantic Electrostrain in Duplex Structured Alkaline Niobates. *Chemistry of Materials*, 24(17):3363–3369, 2012.
- <sup>312</sup> D. S. Lee, D. H. Lim, M. S. Kim, K. H. Kim, and S. J. Jeong. Electric Field-Induced Deformation Behavior in Mixed  $\text{Bi}_{0.5}\text{Na}_{0.5}\text{TiO}_3$  and  $\text{Bi}_{0.5}(\text{Na}_{0.75}\text{K}_{0.25})_{0.5}\text{TiO}_3$ - $\text{BiAlO}_3$ . *Applied Physics Letters*, 99(6):062906, 2011.

- <sup>313</sup> D. S. Lee, S. J. Jeong, E. C. Park, and J. S. Song. Characteristic of Grain Oriented  $(\text{Bi}_{0.5}\text{Na}_{0.5})\text{TiO}_3\text{-BaTiO}_3$  Ceramics. *Journal of Electroceramics*, 17(2-4):505–508, 2006.
- <sup>314</sup> T. Shrout, W. A. Schulze, and J. V. Biggers. Electromechanical Behavior of Antiferroelectric-Ferroelectric Multilayer PZT Based Composites. *Ferroelectrics*, 29(1):129–134, 1980.
- <sup>315</sup> D. E. Dausch, E. Furman, F. Wang, and G. H. Haertling. PLZT-Based Multilayer Composite Thin Films, Part I: Experimental Investigation of Composite Film Structures. *Ferroelectrics*, 177(1):221–236, 1996.
- <sup>316</sup> D. E. Dausch, E. Furman, F. Wang, and G. H. Haertling. PLZT-Based Multilayer Composite Thin Films, Part II: Experimental Investigation of Composite Film Structures. *Ferroelectrics*, 177(1):237–253, 1996.
- <sup>317</sup> A. Yoneda, T. Takenaka, and K. Sakata. Composite Piezoelectric Ceramics of  $(\text{LiBi})_{1/2}$ -Modified PZT System. *Japanese Journal of Applied Physics Part 1-regular Papers Short Notes & Review Papers*, 28(S2):95–97, 1989.
- <sup>318</sup> H. Komiya, Y. Naito, T. Takenaka, and K. Sakata. Piezoelectric and Pyroelectric Composite Ceramics of the Multilayer Type by Tape Casting. *Japanese Journal of Applied Physics Part 1-regular Papers Short Notes & Review Papers*, 28(S2):114, 1989.
- <sup>319</sup> O. Furukawa, M. Harata, M. Imai, Y. Yamashita, and S. Mukaeda. Low Firing and High Dielectric-Constant X7R-Ceramic Dielectric For Multilayer Capacitors Based On Relaxor and Barium-Titanate Composite. *Journal of Materials Science*, 26(21):5838–5842, 1991.
- <sup>320</sup> C. Groh, D. J. Franzbach, W. Jo, K. G. Webber, J. Kling, L. A. Schmitt, H. J. Kleebe, S.-J. Jeong, J.-S. Lee, and J. Rödel. Relaxor/Ferroelectric Composites: A Solution in the Quest for Practically Viable Lead-Free Incipient Piezoceramics. *Advanced Functional Materials*, 24(3):356–362, 2014.
- <sup>321</sup> N. H. Khansur, C. Groh, W. Jo, C. Reinhard, J. A. Kimpton, K. G. Webber, and J. E. Daniels. Tailoring of Unipolar Strain in Lead-Free Piezoelectrics Using the Ceramic/Ceramic Composite Approach. *Journal of Applied Physics*, 115(12):124108, 2014.
- <sup>322</sup> M. Seul, L. R. Monar, L. Ogorman, and R. Wolfe. Morphology and Local-Structure in Labyrinthine Stripe Domain Phase. *Science*, 254(5038):1616–1618, 1991.
- <sup>323</sup> M. Seul and R. Wolfe. Evolution of Disorder in 2-Dimensional Stripe Patterns- Smectic Instabilities and Disclination Unbinding. *Physical Review Letters*, 68(16):2460–2463, 1992.
- <sup>324</sup> V. V. Shvartsman, B. Dkhil, and A. L. Kholkin. Mesoscale Domains and Nature of the Relaxor State by Piezoresponse Force Microscopy. *Annual Review of Materials Research*, 43(1):423–449, 2013.

- <sup>325</sup> A. Kholkin, A. Morozovska, D. Kiselev, I. Bdikin, B. Rodriguez, P. P. Wu, A. Bokov, Z. G. Ye, B. Dkhil, L. Q. Chen, M. Kosec, and S. V. Kalinin. Surface Domain Structures and Mesoscopic Phase Transition in Relaxor Ferroelectrics. *Advanced Functional Materials*, 21(11):1977–1987, 2011.
- <sup>326</sup> B. Kaplan. Analysis of Checkerboard Pattern in Ultrathin Magnetic Films. *Journal of Magnetism and Magnetic Materials*, 303(1):9–13, 2006.
- <sup>327</sup> J. Castro, G. A. Gehring, and S. J. Robinson. On the Stripe Domain Structure of Ferromagnetic Ultrathin Films. *Journal of Magnetism and Magnetic Materials*, 214(1-2):85–92, 2000.
- <sup>328</sup> Y. Yafet and E. M. Gyorgy. Ferromagnetic Strip-Domains in an Atomic Monolayer. *Physical Review B*, 38(13):9145–9151, 1988.
- <sup>329</sup> A. L. Sukstanskii and K. I. Primak. Domain Structure in an Ultrathin Ferromagnetic Film. *Journal of Magnetism and Magnetic Materials*, 169(1-2):31–38, 1997.
- <sup>330</sup> E. I. Shishkin, V. Y. Shur, F. Schlaphof, and L. M. Eng. Observation and Manipulation of the as-Grown Maze Domain Structure in Lead Germanate by Scanning Force Microscopy. *Applied Physics Letters*, 88(25):252902, 2006.
- <sup>331</sup> I. K. Bdikin, V. V. Shvartsman, and A. L. Kholkin. Nanoscale Domains and Local Piezoelectric Hysteresis in  $\text{Pb}(\text{Zn}_{1/3}\text{Nb}_{2/3})\text{O}_3$ -4.5% $\text{PbTiO}_3$  Single Crystals. *Applied Physics Letters*, 83(20):4232–4234, 2003.
- <sup>332</sup> P. Paruch, T. Giamarchi, and J. M. Triscone. Domain Wall Roughness in Epitaxial Ferroelectric  $\text{PbZr}_{0.2}\text{Ti}_{0.8}\text{O}_3$  Thin Films. *Physical Review Letters*, 94(19):197601, 2005.
- <sup>333</sup> S. I. Wright and D. P. Field. Recent Studies of Local Texture and its Influence on Failure. *Materials Science and Engineering: A*, 257(1):165–170, 1998.
- <sup>334</sup> S. I. Wright, B. L. Adams, and K. Kunze. Application of a New Automatic Lattice Orientation Measurement Technique to Polycrystalline Aluminum. *Materials Science and Engineering: A*, 160(2):229–240, 1993.
- <sup>335</sup> C. A. Michaluk, D. P. Field, K. A. Nibur, S. I. Wright, and R. A. Witt. Effects of Local Texture and Grain Structure on the Sputtering Performance of Tantalum. In *Materials Science Forum*, volume 408, pages 1615–1620, 2002.
- <sup>336</sup> D. P. Field, S. I. Wright, and P. Trivedi. Microtextural Analysis of Grain Fragmentation in Aluminum. In *Materials Science Forum*, volume 426, pages 3739–3744, 2003.
- <sup>337</sup> S. I. Wright, D. P. Field, and M. M. Nowell. The Applicability of Conventional Fiber Texture Analysis Techniques in Electron Backscatter Diffraction. In *Materials Science Forum*, volume 426, pages 3685–3690, 2003.

- <sup>338</sup> N.T. Tsou, P.R. Potnis, and J.E. Huber. Classification of Laminate Domain Patterns in Ferroelectrics. *Physical Review B*, 83(18):184120, 2011.
- <sup>339</sup> S. V. Kalinin, A. Rar, and S. Jesse. A Decade of Piezoresponse Force Microscopy: Progress, Challenges, and Opportunities. *IEEE Transactions on Ultrasonics, Ferroelectrics, and Frequency Control*, 53(12):2226–2252, 2006.
- <sup>340</sup> E. Cross. Materials Science: Lead-Free at Last. *Nature*, 432(7013):24–25, 2004.
- <sup>341</sup> W. Liu and X. Ren. Large Piezoelectric Effect in Pb-Free Ceramics. *Physical Review Letters*, 103(25):257602, 2009.
- <sup>342</sup> V. V. Shvartsman, J. Dec, T. Lukasiewicz, A. L. Kholkin, and W. Kleemann. Evolution of the Polar Structure in Relaxor Ferroelectrics Close to the Curie Temperature Studied by Piezoresponse Force Microscopy. *Ferroelectrics*, 373(1):77–85, 2008.
- <sup>343</sup> V. V. Shvartsman and A. L. Kholkin. Domain Structure of  $0.8\text{Pb}(\text{Mg}_{1/3}\text{Nb}_{1/3})\text{O}_3$ - $0.2\text{PbTiO}_3$  Studied by Piezoresponse Force Microscopy. *Physical Review B: Condensed Matter*, 69(1):014102, 2004.
- <sup>344</sup> K. S. Wong, J. Y. Dai, X. Y. Zhao, and H. S. Luo. Time- and Temperature-Dependent Domain Evolutions in Poled (111)-cut  $(\text{Pb}(\text{Mg}_{1/3}\text{Nb}_{2/3})\text{O}_3)_{(0.7)}(\text{PbTiO}_3)_{(0.3)}$  Single Crystal. *Applied Physics Letters*, 90(16):162907, 2007.
- <sup>345</sup> P. Bourke. Polygons and Meshes, <http://paulbourke.net/geometry/polygonmesh/>.
- <sup>346</sup> S. Y Choi, S. J. Jeong, D. S. Lee, M. S. Kim, J. S. Lee, J. H. Cho, B. I. Kim, and Y. Ikuhara. Gigantic Electrostrain in Duplex Structured Alkaline Niobates. *Chemistry of Materials*, 24(17):3363–3369, 2012.
- <sup>347</sup> D. A. Kiselev, I. K. Bdikin, E. K. Selezneva, K. Bormanis, A. Sternberg, and A. L. Kholkin. Grain Size Effect and Local Disorder in Polycrystalline Relaxors via Scanning Probe Microscopy. *Journal of Physics D: Applied Physics*, 40(22):7109–7112, 2007.
- <sup>348</sup> A. M. Bratkovsky and A. P. Levanyuk. Effects of Anisotropic Elasticity in the Problem of Domain Formation and Stability of Monodomain State in Ferroelectric Films. *Physical Review B*, 84(4):045401, 2011.
- <sup>349</sup> R. O. Duda, P. E. Hart, et al. *Pattern Classification and Scene Analysis*, volume 3. Wiley New York, New York, 1973.
- <sup>350</sup> U. M. Fayyad, G. Piatetsky-Shapiro, P. Smyth, and R. Uthurusamy. Advances in Knowledge Discovery and Data Mining, <http://www.citeulike.org/group/2902/article/1550195>, accessed 2015-02-16, 1996.

- 
- <sup>351</sup> T. Kanungo, D. M Mount, N. S Netanyahu, C. D. Piatko, R. Silverman, and A. Y. Wu. An Efficient k-Means Clustering Algorithm: Analysis and Implementation. *Pattern Analysis and Machine Intelligence, IEEE Transactions on*, 24(7):881–892, 2002.
- <sup>352</sup> B. Yang, N. J. Park, B. I. Seo, Y. H. Oh, S. J. Kim, S. K. Hong, S. S. Lee, and Y.-J. Park. Nanoscale Imaging of Grain Orientations and Ferroelectric Domains in  $(\text{Bi}_{1-x}\text{La}_x)_4\text{Ti}_3\text{O}_{12}$  Films for Ferroelectric Memories. *Applied Physics Letters*, 87(6):062902, 2005.
- <sup>353</sup> A. K. Tagantsev, L. E. Cross, and J. Fousek. *Domains in Ferroic Crystals and Thin Films*. Springer Science+Business Media, LLC, Heidelberg, 2010.



# List of Figures

2.1	Different mechanisms of microscopic polarization. . . . .	4
2.2	Schematic representation of the frequency dependence of the real and imaginary part of the dielectric permittivity. . . . .	5
2.3	Classification of dielectrics. . . . .	6
2.4	Schematic on the temperature evolution of lattice parameters, unit cell, and spontaneous polarization of barium titanate. . . . .	8
2.5	Free energy, polarization, and susceptibility at a first order and a second order phase transition. . . . .	9
2.6	Principle of the formation of 180° and non-180° domains in a tetragonal, ferroelectric crystal. . . . .	11
2.7	Electric field dependence of polarization and respective local domain structure. . . . .	12
2.8	Schematic representation of the electric-field induced strain hysteresis loop. . . . .	13
2.9	Schematic representation of the domain wall potential landscape in a ferroelectric material with randomly distributed point defects. . . . .	14
2.10	Polarization switching process. . . . .	14
2.11	Comparison of field-induced polarization, temperature-dependent polarization, and relative permittivity typically observed in ferroelectrics and relaxor ferroelectrics. . . . .	16
2.12	Dielectric permittivity as a function of temperature for different relaxor structures. . . . .	19
2.13	Electric field-temperature phase diagram as suggested for PMN. . . . .	21
2.14	Phase diagram proposed for KNN. . . . .	22
2.15	Phase diagram of BNT-BT. . . . .	27
2.16	Experimental setup of piezoresponse force microscope. . . . .	34
2.17	In-phase and out-of phase piezoresponse signal. . . . .	36
2.18	Piezoelectric effect investigated by PFM. . . . .	37
2.19	Piezoresponse force spectroscopy. . . . .	39
2.20	Working principle of a lock-in amplifier. . . . .	41
2.21	Schematic representation of band excitation piezoresponse force microscopy. . . . .	43
3.1	Experimental custom-built setup for <i>in situ</i> measurements of small-signal piezoelectric coefficient. . . . .	49
3.2	XRD diffraction pattern for CZ5. . . . .	52
3.3	Unipolar strain as function of electric field measured at room temperature for CZ5. . . . .	53
3.4	Temperature dependence of permittivity and dielectric loss for a poled CZ5 sample. . . . .	54
3.5	Unipolar strain of CZ5 at different temperatures. Temperature evolution of strain normalized to its room temperature value. . . . .	54

3.6	Temperature evolution of <i>in situ</i> measured small- and large-signal piezoelectric coefficient. . . . .	55
3.7	TEM image, vertical piezoresponse force microscopy (VPFM) image, and lateral piezoresponse force microscopy (LPFM) image of CZ5 domain structure. . . . .	56
3.8	Piezoresponse force microscopy images of the unpoled CZ5 domain structure at different temperatures. . . . .	58
3.9	VPFM and LPFM images of the poled CZ5 sample as function of temperature. . . . .	59
3.10	A local VPFM hysteresis loop at different temperatures at the same location of the CZ5 sample. . . . .	60
3.11	Comparison of temperature dependence of normalized strain for various piezoceramics. . . . .	62
3.12	Polarization and bipolar strain hysteresis loops of CZ5 at different temperatures. . . . .	63
3.13	Temperature dependence of various hysteresis loop parameters. . . . .	64
3.14	A typical histogram for the VPFM signal at room temperature. The width of the histograms of the VPFM and LPFM signals as function of temperature. . . . .	66
3.15	The VPFM signal profile across two neighboring antiparallel domains and thermal evolution of the local piezoresponse for several individual domains. . . . .	68
3.16	A typical hysteresis loop for CZ5 acquired at room temperature with marked parameters. . . . .	69
3.17	Temperature dependence of the local VPFM hysteresis loop parameters. . . . .	70
3.18	Piezoelectricity of CZ5 as function of temperature on macroscopic and microscopic length scales. . . . .	72
4.1	A simplified example of ergodicity and nonergodicity. . . . .	75
4.2	Schematic representation of the Sawyer-Tower experimental setup used for the measurements of large-signal polarization and strain. . . . .	77
4.3	Experimental setup for the optical measurement of field-induced strain. . . . .	78
4.4	Strain and polarization as function of electric field for (a) 2BZT, (b) 3BZT, and (c) 4BZT measured at increasing fields. . . . .	80
4.5	Piezoelectric coefficient and relative permittivity as a function of electric field. . . . .	81
4.6	The surface topography and PFM images of unpoled BNT-BKT-BZT ceramics. . . . .	83
4.7	VPFM images of the BNT-BKT-BZT ceramics obtained after local poling at different bias voltages. . . . .	84
4.8	Dependence of remanent polarization and remanent strain on maximum electric field amplitude. . . . .	86
4.9	Full width at half maximum (FWHM) of the peak as a function of rotation angle as determined by single peak fitting. . . . .	87
4.10	Autocorrelation function image of VPFM image from Figure 4.6 obtained for (a) 2BZT, (b) 3BZT, and (c) 4BZT. . . . .	89

4.11	Autocorrelation function of the VPFM images obtained for the different BZT contents. . . . .	89
4.12	Evolution of absolute values of the average piezoresponse for the poled region with poling voltage. Lines are plotted as guide to the eye. . . . .	90
4.13	The small-signal piezoelectric coefficient after poling at different temperatures for (a) BNT-19BKT-2BZT, (b) BNT-19BKT-3BZT, and (c) BNT-19BKT-4BZT ceramics as function of time. . . . .	92
4.14	PFM images of locally poled BNT-BKT-2BZT taken at different times on heating to (a)-(c) 30 °C, (d)-(f) 43 °C, (g)-(i) 57 °C, and (j)-(l) 71 °C. . . . .	94
4.15	PFM images of locally poled BNT-BKT-3BZT taken at different times on heating to (a)-(c) 30 °C, (d)-(f) 43 °C, (g)-(i) 57 °C, and (j)-(l) 71 °C. . . . .	95
4.16	PFM images of locally poled BNT-BKT-4BZT taken at different times on heating to (a)-(c) 30 °C, (d)-(f) 43 °C, (g)-(i) 57 °C, and (j)-(l) 71 °C. . . . .	96
4.17	The average piezoresponse of the poled area as a function of time for (a) BNT-BKT-2BZT, (b) BNT-BKT-3BZT, and (c) BNT-BKT-4BZT. . . . .	97
4.18	The normalized macroscopic piezoelectric coefficient and the normalized averaged piezoresponse of the induced phase for (a, b) BNT-19BKT-2BZT, (c, d) BNT-19BKT-3BZT, and (e, f) BNT-19BKT-4BZT ceramics as a function of time after poling, performed at different temperatures. . . . .	101
4.19	Schematic representation on the change of the field-induced state with time: (a) electric-field induced long-range order, (b) their breaking into nanodomains after electric field is turned off, (c) relaxed ergodic state with uncorrelated PNRs, and (d) paraelectric phase with no polar entities above Burns temperature. . . . .	103
5.1	Schematic presentation of the polarization processes in polycrystalline composite materials. . . . .	106
5.2	Unipolar strain of 0 %- and 10 %-BNT-7BT compositions. The effective piezoelectric coefficient as a function of BNT-7BT content (after Ref. [312]). . . . .	107
5.3	Amplitude and phase PFM images of the BNT-6BT-2KNN / BNT-7BT ceramic/ceramic composites with different content of nonergodic relaxor 93BNT-7BT. . . . .	112
5.4	Electron backscatter diffraction diffraction images of 0%NE, 30%NE, and 100%NE samples. . . . .	113
5.5	PFM and EBSD images obtained at the same position for the ergodic relaxor BNT-6BT-2KNN. Overlap of the PFM phase image and EBSD map. Overlap of the PFM amplitude image and EBSD map. . . . .	115
5.6	PFM and EBSD images obtained at the same position for the composite ceramics with 30 % of BNT-7BT phase. Overlap of the PFM phase image and EBSD map. Overlap of the PFM amplitude image and EBSD map. . . . .	116

5.7	PFM and EBSD images obtained at the same position for the nonergodic relaxor BNT-7BT. Overlap of the PFM phase image and EBSD map. Overlap of the PFM amplitude image and EBSD map. . . . .	117
5.8	Spatially averaged local hysteresis loops for composites with different content of 93BNT-7BT. . . . .	118
5.9	Compositional diversity: 93BNT-7BT content dependence of the averaged hysteresis loops parameters: maximal and remanent piezoresponse, coercive voltage and work of switching. . . . .	119
5.10	Constituents diversity: PFM phase image of the composite ceramic with 30 % of BNT-7BT phase and intragrain averaged local hysteresis loops for grains with 'labyrinth' and 'checkerboard' domain patterns. . . . .	120
5.11	Proximity effect: variation of the hysteresis loops parameters: maximum and remanent piezoresponse, coercive voltage and work of switching inside a relaxor grain for the composite sample with 30 % of 93BNT-7BT. . . . .	121
5.12	Binarization of an image. Boundary detection in <i>LoS</i> using radial rays. . . . .	124
5.13	The principle of Line-of-Sight domain analysis. . . . .	126
5.14	Binary PFM images, corresponding line-of-sight domain area maps, and line-of-sight domain angle maps of the BNT-6BT-2KNN / BNT-7BT ceramic/ceramic composites with different contents of nonergodic relaxor BNT-7BT. . . . .	127
5.15	The autocorrelation functions of <i>LoS</i> domain area maps. . . . .	129
5.16	The k-means clustering method. An iterative process of defining the cluster centers and associated data. . . . .	132
5.17	The PFM phase image and the corresponding k-means clustering map for the composite ceramic with 30 % of BNT-7BT phase. The k-means maps for the representative clusters. The local hysteresis loops of characteristic clusters. . . . .	134
5.18	Comparison of the maximum and remanent piezoresponse and coercive voltages of the different clusters. . . . .	135
5.19	The PFM phase image and the corresponding k-means clustering map for the nonergodic relaxor BNT-7BT sample. The k-means maps for the representative clusters. The local hysteresis loops of characteristic clusters. . . . .	136
5.20	The PFM phase image and the corresponding k-means clustering map for the ergodic relaxor BNT-6BT-2KNN. The k-means maps for the representative clusters. The local hysteresis loops of representative clusters. . . . .	138
A.1	LPFM images of BNT-BKT-BZT ceramics obtained after local poling. . . . .	145
A.2	The superlattice reflections for (a) 2BZT, (b) 3BZT, and (c) 4BZT presented with the superlattice reflections before and after exposure to the electric field. . . . .	146
A.3	Neutron diffraction patterns for poled (a) 2BZT, (b) 3BZT, and (c) 4BZT in respect to diffraction angle . . . . .	146

# List of Tables

2.1	Crystallographic point groups in short Hermann-Mauguin notation (after Ref. [9]).	6
2.2	Summary of properties of KNN and its compounds. . . . .	23
2.3	Summary of properties for the BNT-based binary system BNT-xBT in the vicinity of the MPB. . . . .	28
2.4	Summary of properties for the BNT-based binary BNT-xBKT system. . . . .	29
2.5	Summary of properties of BNT-based ternary BNT-xBT-yX (x,y) systems. The field amplitude in kV/mm utilized for $S_{max}/E_{max}$ is indicated as a corresponding footnote. . . . .	30
2.6	Summary of properties for BNT-based ternary BNT-xBKT-yX (x,y) system. The field amplitude in kV/mm utilized for $S_{max}/E_{max}$ is indicated as a corresponding footnote. . . . .	32
4.1	Parameters of the best stretched exponential function fit of the time dependence of macroscopic and local piezoresponse. . . . .	100
5.1	The largest, $A_{max}$ , and the average, $A_{avr}$ , domain area for the different composite samples computed by $LoS$ . . . . .	128



# Erklärung

Ich versichere an Eides statt durch meine Unterschrift, dass ich die vorstehende Arbeit selbständig und ohne fremde Hilfe angefertigt und alle Stellen, die ich wörtlich oder annähernd wörtlich aus Veröffentlichungen entnommen habe, als solche kenntlich gemacht habe, mich auch keiner anderen als der angegebenen Literatur oder sonstiger Hilfsmittel bedient habe. Die Arbeit hat in dieser oder ähnlicher Form noch keiner anderen Prüfungsbehörde vorgelegen.

Essen,

---

Danka Dittmer-Gobeljic





# Acknowledgments

I would like to express the deepest appreciation to Prof. Dr. rer. nat. habil. Doru C. Lupascu for the given opportunity to work in his group at the Institute for material science. Without his guidance and inspirational approach to science and research this dissertation would not have been possible.

I owe a deep sense of gratitude to my supervisor Dr. Vladimir V. Shvartsman. His keen interest on me at every stage of my research, his prompt inspirations, outstanding expertise, his commitment to science and timely suggestions with enthusiasm and dynamism have helped me to cope with scientific problems and enable me crossing my own limits.

I would like to thank Prof. Dr. Andrei A. Kholkin for being the second reviewer of my doctoral dissertation.

I would like to express my deep and sincere gratitude to the many collaborators with whom I was privileged to work with. Firstly, I would like to thank Prof. Dr.-Ing. Jürgen Rödel for the great support during my research stay in his work group Nichtmetallisch-Anorganische Werkstoffe (University of Technology Darmstadt). That unique opportunity enabled me stepping into the world of ceramic processing and macroscopic material testing. Besides, I had a great pleasure to work with Dr. Robert Dittmer and Dr. Claudia Groh whose great samples and expertise gave a special direction to my work. Therefore, I would here like to express particular thanks to both of them.

Furthermore, I would like to give a special thanks to Dr. Sergei V. Kalinin and his group from the Center for Nanophase Materials Sciences (Oak Ridge National Laboratory). Working with Sergei opened up for me many new scientific horizons in the world of piezoresponse force microscopy and large data processing. In addition, our inspirational talks about beauty of research, innovation, and life will never be forgotten. I also appropriate the help and guidance of Sergei's scientific gang: Dr. Alex Belianinov, Dr. Stephen Jesse, and Dr. Evgheni Strelcov.

I would like to express my gratitude to Green for taking so much time to read and correct my writings. Danke for all articles, correction of Serboenglish, and scientific suggestions, but also for the literature support (wink).

I would like to thank Mr. Hans-Joachim Keck, Mr. Patrick Dubray, and Mrs. Sabine Kriegel for the technical support I got during the past years. Without their help my work would be much more difficult to cope with. Special thanks go to Herr Keck for his humor, fashion moments, and communication over the wall. You are the best!

In addition, I want to thank my Naz, Gabriel, and Naveed for spicing the period of my PhD studies. My work got a special dimension with you, guys. I also want to thank all my dear UDEMAT

colleagues. I thank Kevin, Frau Vadala, Morad, Lucky, Irina, Schicky-Mickey, Ling, Maryam, Trivedi, Ana Luiza, Tommy, and Stefi for all the beautiful moments we had during the past time.

Finally, I would not be here without the encouragement of my beloved parents Dragisa and Nata and the one I love the most, my sister Nevenka. Their support and love make my work and life joyful and accomplished. Hvala, porodico moja!

I would like to acknowledge the financial help of the European Initial Training Network Marie Curie NANOMOTION (grant agreement number 290158).

Danka Dittmer-Gobeljic  
Essen, July 2015

# Curriculum Vitae

## Personal Details

---

Name	Danka Dittmer-Gobeljic, born Gobeljic
Date of birth	25 July 1985
Place of Birth	Belgrade
Nationality	Serbian

## Basic Education

---

1992–2000	Primary School (Osnovna škola Dule Karaklajic, Lazarevac)
2000–2004	High School (Gimnazija, Lazarevac)

## Higher Education

---

2004–2009	Student of School of Electrical Engineering at University of Belgrade, majoring in nanoelectronic, optoelectronic, and laser technique
-----------	--

## Work Experience

---

2009–2010	Researcher of CNR-IFN Institute for Photonics and Nanotechnologies, Italy
2010–2011	Researcher at Department of Chemistry, University of Bari, Italy
since 2012	PhD Student at Institut für Materialwissenschaft, Prof. Dr. rer. nat. Doru C. Lupascu, Universität Duisburg-Essen

## Refereed Publications

---

M. Escobar Castillo, V. V. Shvartsman, D. Gobeljic, Y. Gao, J. Landers, H. Wende, and D. C. Lupascu, "Effect of Particle Size on Ferroelectric and Magnetic Properties of BiFeO<sub>3</sub> Nanopowders," *Nanotechnology*, **24**[35] 355701 (2013).

K. Wang, F.-Z. Yao, W. Jo, D. Gobeljic, V. V. Shvartsman, D. C. Lupascu, J.-F. Li, and J. Rödel, "Temperature-Insensitive (K,Na)NbO<sub>3</sub>-Based Lead-Free Piezoactuator Ceramics," *Adv. Funct. Mater.*, **23**[33] 4079-4086 (2013).

M. D. Angione, M. Magliulo, S. Cotrone, A. Mallardi, D. Altamura, C. Giannini, N. Cioffi, L. Sabbatini, D. Gobeljic, G. Scamarcio, G. Palazzo, L. Torsi, "Volatile General Anesthetic Sensing with Organic Field-Effect Transistors Integrating Phospholipid Membranes," *Biosens. Bioelectron.*, **40**[1] 303-307 (2013).

G. Palazzo, M. Magliulo, A. Mallardi, M. D. Angione, D. Gobeljic, G. Scamarcio, E. Fratini, F. Ridi, and L. Torsi, "Electronic Transduction of Proton Translocations in Nanoassembled Lamellae of Bacteriorhodopsin," *ACS Nano*, **8**[8] 7834-7845 (2014).

D. Gobeljic, V. V. Shvartsman, K. Wang, F. Yao, J.-F. Li, W. Jo, J. Rödel, and D. C. Lupascu, "Temperature Dependence of the Local Piezoresponse in (K,Na)NbO<sub>3</sub>-Based Ceramics with Large Electromechanical Strain," *J. Appl. Phys.*, **116**[1] 066811 (2014).

R. Dittmer, D. Gobeljic, W. Jo, V. V. Shvartsman, D. C. Lupascu, J. L. Jones, and J. Rödel, "Ergodicity Reflected in Macroscopic and Microscopic Field-Dependent Behavior of BNT-Based Relaxors," *J. Appl. Phys.*, **115**[1] 084111 (2014).

D. Gobeljic, R. Dittmer, J. Rödel, V. V. Shvartsman, and D. C. Lupascu, "Macroscopic and Nanoscopic Polarization Relaxation Kinetics in Lead-Free Relaxors Bi<sub>1/2</sub>Na<sub>1/2</sub>TiO<sub>3</sub>-Bi<sub>1/2</sub>K<sub>1/2</sub>TiO<sub>3</sub>-BiZn<sub>1/2</sub>Ti<sub>1/2</sub>O<sub>3</sub>," *J. Am. Ceram. Soc.*, **97**[12] 3904-12 (2014).

D. Gobeljic, V. V. Shvartsman, A. Belianinov, S. Jesse, S. V. Kalinin, C. Groh, J. Rödel, and D. C. Lupascu, "Mapping of Nanoscale Heterogeneity of the Polarization Reversal in Huge Strain Lead-Free Relaxor-Ferroelectric Ceramic/Ceramic Composites," submitted to *Nanoscale* (2015).

D. Gobeljic, V. V. Shvartsman, S. V. Kalinin, A. Belianinov, S. Jesse, and D. C. Lupascu, "Real Space Morphological Analysis of Multilevel Domain Structures in Polycrystalline Ferroelectric Relaxor Composite Materials," not published

### Conference Contributions

---

D. Gobeljic, V. V. Shvartsman, and D. C. Lupascu, "Piezoresponse Force Microscopy of Lead-Free Piezoelectrics," Workshop School of PFM and nanoscale electromechanics, Center for Nanoscale Material, Oak Ridge National Laboratory, Tennessee, USA, 4-8 March 2013

D. Gobeljic, V. V. Shvartsman, K. Wang, W. Jo, J.-F. Li, J. Rödel, and D. C. Lupascu, "Piezoresponse Force Microscopy Studies of (K,Na)NbO<sub>3</sub>-Based Ceramics for Piezoactuator Applications," Deutsche Physikalische Gesellschaft Spring Meeting, Regensburg, 10-15 March 2013

D. Gobeljic, V. V. Shvartsman, R. Dittmer, C. Groh, W. Jo, J. Rödel, and D. C. Lupascu, "Piezoresponse Force Microscopy of BNT-Based Ceramics," International Workshop on Relaxor Ferroelectrics, St. Petersburg, Russia, 1-6 July 2013

D. Gobeljic, V. V. Shvartsman, K. Wang, W. Jo, J.-F. Li, J. Rödel, and D. C. Lupascu, "Piezoresponse Force Microscopy Study of Doped (K,Na)NbO<sub>3</sub>-Based Ceramics for Piezoactuator Applications," 2013 Joint UFFC, EFTF and PFM Symposium, Prague, Czech Republic, 21-25 July 2013

D. Gobeljic, V. V. Shvartsman, R. Dittmer, W. Jo, J. Rödel, and D. C. Lupascu, "Piezoresponse Force Microscopy of Lead-Free Piezoelectrics," Nanomotion workshop at Bosch, Stuttgart, Germany, 30 January 2014

D. Gobeljic, V. V. Shvartsman, C. Groh, W. Jo, J. Rödel, S. Kalinin, and D. C. Lupascu, "Nanoscale Heterogeneity of the Polarization Reversal in Huge Strain Lead-Free Relaxor-Ferroelectric Composite Ceramics," 2014 Joint IEEE International Symposium on the Applications of Ferroelectric, International Workshop on Acoustic Transduction Materials and Devices & Workshop on Piezoresponse Force Microscopy, State College, Pennsylvania, USA, 12-16 May 2014

D. Gobeljic, V. V. Shvartsman, R. Dittmer, W. Jo, J. Rödel, and D. C. Lupascu, "Ergodicity Reflected in Microscopic Behavior of BNT-Based Relaxors," 2014 Joint IEEE International Symposium on the Applications of Ferroelectric, International Workshop on Acoustic Transduction Materials and Devices & Workshop on Piezoresponse Force Microscopy, State College, Pennsylvania, USA, 12-16 May 2014

D. Gobeljic, V. V. Shvartsman, C. Groh, W. Jo, J. Rödel, S. Kalinin, and D. C. Lupascu, "Real Space Morphological Analysis of Multilevel Domain Structures in Polycrystalline Ferroelectric Relaxors," Materials Science and Engineering, Darmstadt, 23-25 September 2014

D. Gobeljic, V. V. Shvartsman, C. Groh, W. Jo, J. Rödel, S. Kalinin, and D. C. Lupascu, "PFM Study of Local Piezoelectric Properties of Giant Strain Lead-Free Relaxor-Ferroelectric Composite Ceramics," 2015 Joint IEEE International Symposium on ISAF-ISIF-PFM, Singapore, 24-27 May 2015

